TEMPERATURE SWING ADSORPTION PROCESSES FOR GAS SEPARATION

A Dissertation
Presented to
The Academic Faculty

By

Darshan Gopalrao Pahinkar
`

In Partial Fulfillment
Of the Requirements for the Degree
Doctor of Philosophy in Mechanical Engineering

Georgia Institute of Technology

December 2016

TEMPERATURE SWING ADSORPTION PROCESSES FOR GAS SEPARATION

Approved by:

Dr. Srinivas Garimella, Chair
George W. Woodruff School of
Mechanical Engineering
Georgia Institute of Technology

Dr. Sheldon Jeter
George W. Woodruff School of
Mechanical Engineering
Georgia Institute of Technology

Dr. Samuel Graham
George W. Woodruff School of
Mechanical Engineering
Georgia Institute of Technology

Dr. William Koros
School of Chemical and Biomolecular
Engineering
Georgia Institute of Technology

Dr. Satish Kumar
George W. Woodruff School of
Mechanical Engineering
Georgia Institute of Technology

Date Approved: September 19, 2016

To my wife, Neha for her unconditional love, support and sacrifices

ACKNOWLEDGEMENTS

I feel extremely elated to express my deep sense of respect and appreciation towards my advisor Dr. Srinivas Garimella. I have enjoyed every moment of my association with him and learned from him the academic discipline, research leadership skills and professional ethics. I sincerely thank him for his guidance, constructive criticism and support.

I would also like to thank all the current and past members of the Sustainable Thermal Systems Laboratory for their friendship and valuable assistance. Long and fruitful discussions with them have helped me in solving challenges and difficulties in this work. Especially, Bryce Moore, Daniel Boman, Dr. Malcolm MacDonald and Dhruv Hoysall kindly assisted in the research and technical writing. This research could not have materialized without valuable suggestions and timely inputs from Dr. Robert Johnson and Mr. Tracy Fowler from ExxonMobil, the sponsors of this work. I would like to also thank my Ph.D. reading committee members, Drs. Samuel Graham, Satish Kumar, Sheldon Jeter, and William Koros for their suggestions and patient review of my dissertation.

I must take this opportunity to acknowledge my friends and family. I thank my numerous friends for their continuous support and camaraderie. I thank my uncle Shivaji for his encouragement and continued interest in my ventures. I truly appreciate my brother Deven for showing remarkable understanding and maturity over these years and for holding the strings, even though I could not be with him at times, when he needed me the most. I would also like to thank my parents-in-law Dileep and Swati, for their

blessings and generous support towards my academic pursuit. No words could ever express my pious feelings for my parents, Gopal and Rekha. Their immense love, teachings and unconditional support are the sole source of all my inspiration and determination. Thanking notes are indeed insufficient to acknowledge my wife, Neha's role in my life. I cannot imagine how she sacrificed her promising career just to support my decision of pursuing Ph.D. I could not have come this far without her. In fact, this pursuit made us closest friends. Finally, it will not be inappropriate to mention Brian Silas, Madan Mohan, Naushad, Mohammad Rafi, Thomas Newman, and John Williams for keeping me motivated through stressful times.

TABLE OF CONTENTS

ACKNOWLEDGEMENTS ..... **IV**

LIST OF TABLES ..... **IX**

LIST OF FIGURES ..... **XI**

LIST OF SYMBOLS AND ABBREVIATIONS ..... **XVI**

Symbols xvii

Greek xxii

Superscripts and Subscripts xxii

SUMMARY ..... **XXVI**

1 INTRODUCTION **1**

1.1 Natural gas as a fuel 1

1.2 Thermally driven energy systems 4

1.3 Motivation for the present work 5

1.4 Research objectives 8

1.5 Dissertation outline 9

2 PROCESS MODELING METHODOLOGY **11**

2.1 Introduction 11

2.2 Modeling Methodology 22
2.2.1 Adsorption stage model 23
2.2.2 Displacement models 28
2.2.3 Desorption model 33
2.2.4 Cooling stage model 34
2.2.5 Purge stage model 34
2.2.6 Sequential coupling and full process simulation methodology 37
2.2.7 Microchannel boundary and initial conditions 39

2.2.8 Product purity and yield 40

2.3 Optimization of geometry and material selection 41
2.3.1 Adsorbent microchannel geometry 41
2.3.2 Adsorbent and HTF material selection 49

2.4 Results 56

2.5 Conclusions 65

3 PERFORMANCE ASSESSMENT 68

3.1 Introduction 68

3.2 System design selection and results 69
3.2.1 Liquid HTF recirculation and absorption 69

3.3 Process performance prediction 74

3.4 Energy requirements and operating cost 79

3.5 Reduction in operating energy requirement 82

3.6 Heat recovery from the cooling stage 86

3.7 Discussion 89

3.8 Multistage purification process 94

3.9 Summary and Conclusions 96

4 EXPERIMENTS AND MODEL VALIDATION 98

4.1 Introduction 98

4.2 Experimental set-up and procedure 102

4.3 Experimental results and discussion 107

4.4 Model development 115
4.4.1 Adsorbent-coated microchannel equations 116
4.4.2 Header equations 126
4.4.3 Valve equations 128
4.4.4 Source and sink models 128
4.4.5 Simulation procedure 128

4.5 Model validation 129

4.6 Model validation with adsorbent-coated microchannels 136

4.7 Conclusions 153

5 CONCLUSIONS AND RECOMMENDATIONS 158

APPENDICES 166

A. 2-D AXISYMMETRIC HEAT AND MASS TRANSFER MODELING 167

A.1 Modeling methodology 167

B. DECOUPLED MOMENTUM APPROACH AND PROPERTY VARIATION 175

C. SAMPLE CALCULATIONS FOR PROCESS MODEL DATA POINT 177

C.1 Instantaneous heat and mass transfer resistance calculation 180

C.2. Governing equations 184

C.3 – Fluid property calculations and process performance parameters 191

C.4 – Energy requirement calculation for overall process operation in cyclic steady state 195

D. SAMPLE CALCULATIONS FOR LABORATORY SCALE MODELS 198

E. HEAT TRANSFER COEFFICIENTS IN THE TEST ENVIRONMENT 210

REFERENCES 213

LIST OF TABLES

Table 2.1. Simulation parameters and material properties (Mark, 1999; Lee, 2007; Determan *et al.*, 2011) 24

Table 2.2. Purification cycle simulation criteria and monitored variables. 39

Table 2.3. Boundary Conditions for the microchannel species and energy equations. 40

Table 2.4. Coefficients for the Langmuir equations with competitive adsorption (Babarao *et al.*, 2007; Lee, 2007) 42

Table 2.5. Effect of microchannel diameter on adsorption stage performance 46

Table 2.6.Effect of adsorbent layer thickness on adsorption stage performance 49

Table 2.7. Comparison of properties of water and PAO (Process Systems Enterprise, 1997-2015; Chevron, 2008) 52

Table 2.8. Comparison of stage times with silicalite-water and zeolite 5A – PAO for a temperature swing of 75°C 53

Table 2.9. Final stage times and total cycle time selected for the full process simulation 57

Table 2.10. Single-point process performance comparison with the literature 65

Table 3.1. Stage times and total cycle time selected for the full process simulation 69

Table 3.2. Effect of reduction in ΔP on purification cycle time. 85

Table 3.3. Effect of reduction in ΔP on energy required for process components 86

Table 3.4. Heat recovery during cooling stage. 88

Table 4.1. Calculated uncertainties for sensors 114

Table 4.2. Numerical values of parameters used for simulation 118

Table 4.3. Auxiliary parameters for competitive DSL equation used for estimation of zeolite 5A adsorbent capacity and intra-crystalline diffusion coefficient (Gholami and Talaie, 2009) 122

Table 4.4. Governing equations and their boundary and initial conditions.....127
Table 4.5. Calculation of packing properties of adsorbent layer 137
Table C.1 Calculation of geometrical parameters (not iterative variables…… 178
Table C.2 Calculation of heat and mass transfer coefficients……..182
Table C.3 Sample calculations for the governing conservation equations……..185
Table C.4. Sample calculations for fluid property an process performance parameters.191
Table C.5. Sample calculations for energy requirement for the process operation.
…….....195
Table D.1. Calculation of heat and mass transfer resistances……..200
Table D.2. Sample calculations for governing equations in the laboratory scale models……...203
Table E.1. Variation of heat loss parameters for fused silica temperature extremes observed in the experiments…….…210

LIST OF FIGURES

Figure 1.1. Fractions of non-renewable fuels as USA primary energy (EIA, 2015).....2

Figure 1.2. Globally increasing natural gas consumption (Schaal, 2013). 2

Figure 1.3. Sequential purification of natural gas (Brooks, 2013) 3

Figure 1.4. Prudhoe bay natural gas processing plant in Alaska (White, 2014) 4

Figure 1.5. Adsorbent bed design with alternate rows of adsorbent-coated and HTF microchannels (Pahinkar *et al.*, 2016). 7

Figure 2.1. Improvements in selectivity of mixed matrix membranes by increasing adsorbent loading in polymers (Koros and Mahajan, 2000; Bernardo *et al.*, 2009). 15

Figure 2.2. CO_2 adsorption isotherms for MOFs, activated carbon zeolites and silicalite at 25°C (Lee, 2007; Gholami and Talaie, 2009; Shao *et al.*, 2011; Herm *et al.*, 2012; Xiang *et al.*, 2012) 17

Figure 2.3. Schematics of the stages in the proposed TSA based purification cycle. Red dots indicate adsorbent crystals in the gray hollow binder matrix and small yellow dots indicate CO_2 impurity in pure CH_4 shown as yellow background. 21

Figure 2.4. Computational modeling architecture of the purification process.....22

Figure 2.5. Illustration of (a) Initial convective diffusive flow and (b) subsequent slow diffusive flow 33

Figure 2.6. (a) Schematic representation of water evaporation as it is exposed to concentration gradient (b) Illustration of an instant in time during water removal.....35

Figure 2.7. Effect of variation of microchannel diameter on (a) product purity and (b) CO_2 adsorbed concentration for a constant adsorbent layer thickness of 30 µm. 45

Figure 2.8. Effect of variation of adsorbent layer thickness on (a) product purity and (b) CO_2 adsorbed concentration for a constant diameter of 530 µm. 48

Figure 2.9 Competitive adsorption isotherms for zeolite 5A and silicalite at 25°C and 100°C for CH_4-CO_2 gas mixture (70/30 by mole).....51

Figure 2.10. Cyclic CO_2 adsorbed concentration with silicalite – water and zeolite 5A – PAO pairs 52

Figure 2.11. Variation of adsorbent layer temperature during (a) desorption (b) cooling with PAO and water as HTFs.....55

Figure 2.12. (a) Adsorbed concentrations in the adsorbent layer during the adsorption stage (b) Component gas densities during displacement of gas (c) Adsorbed concentrations during displacement of gas 58

Figure 2.13. (a) Component gas densities in the adsorbent layer and (b) Adsorbed concentrations during extended desorption (c) Axial temperature variation during cooling stage showing rapid thermal wave 60

Figure 2.14. Progress of liquid water removal from the adsorbent layer 62

Figure 2.15. Total adsorbed concentration in the adsorbent layer predicted for two cycles 63

Figure 2.16. Product collection per cycle showing transient variation for adsorption and purge stages.....64

Figure 3.1. Component architecture considered for modeling the TSA-based purification process. Also shown are the recirculation loops for purge gas and HTF. 71

Figure 3.2. (a) HTF sink absorption capacity for component gases during desorption stage normalized with adsorbent mass (b) Saturation of HTF with selected stage times. 74

Figure 3.3. Schematic showing limits of product recovery from the purification process. 75

Figure 3.4. Product purity vs. process capacity compared with PSA and TSA processes (Kapoor and Yang, 1989; Olajossy *et al.*, 2003; Pahinkar *et al.*, 2016). 77

Figure 3.5. Product purity vs. CH_4 recovery compared with the PSA and TSA processes in the literature (Kapoor and Yang, 1989; Olajossy *et al.*, 2003; Pahinkar *et al.*, 2016) 78

Figure 3.6. Component-wise energy requirement for the baseline case. 80

Figure 3.7. Variation of energy ratio plotted with process capacity for variable feed times. 81

Figure 3.8. (a) Effect of reduction in desorption temperature on operating adsorption swing capacity, seen as the difference between adsorption stage peak value near 1 s and lowest value after cooling stage at 7 s. (b) Effect of drop in temperature on product purity. 84

Figure 3.9. Water temperature at the microchannel outlet for the TSA cycle for the baseline case (100 kPa). Green region shows the 0.69 s for which the water exits the microchannel at 200°C, while cooling has already commenced near the microchannel inlet. 88

Figure 3.10. Modified energy ratio calculations with reduced pressure drop cases. More than 50% reduction in the energy ratio is possible with reduction of ΔP by 75%. 89

Figure 3.11. (a) Process capacity vs. product purity (b) CH_4 recovery vs. product purity (c) CO_2 separation capacity vs. CO_2 specific energy requirement with the updated operating process conditions (Kapoor and Yang, 1989; Olajossy *et al.*, 2003; Bounaceur *et al.*, 2006; Clausse *et al.*, 2011; Pirngruber *et al.*, 2013; Krishnamurthy *et al.*, 2014; Luis, 2016; Pahinkar *et al.*, 2016). 92

Figure 3.12. Implementation of the microchannel TSA-based purification process for multistage operation. Numerical values show calculated purity and product collected normalized with mass of adsorbent.....95

Figure 4.1. (a) Schematic of the test facility used for breakthrough experiments (b) Test facility photograph.....104

Figure 4.2. (a) Heat transfer (b) mass transfer results from the adsorption experiments on PLOT column (ΔP = 18 kPa, L = 2 m).....109

Figure 4.3. Mass transfer (left) and heat transfer (right) results for a repeating set of adsorption experiments showing water saturating the adsorption sites gradually.....111

Figure 4.4. Adsorption experiment results for PLOT columns (a) Adsorption time vs. ΔP (b) average ΔT vs. ΔP (c) average ΔT vs. adsorption time.....113

Figure 4.5. Lab scale model architecture.....116

Figure 4.6. (a) Knudsen number variation with adsorbent layer pore size (b) Comparison of Ordinary and Knudsen diffusion coefficients and their variation with pore sizes.....120

Figure 4.7. (a) Heat transfer resistance networks from microchannel gas node to the ambient temperature node (b) Dimensions of the thermal mass nodes. 125

Figure 4.8. Heat (top) and mass transfer (bottom) model validation with (a) ε = 0.60 and MF = 0.60 (b) ε = 0.8 and MF = 0.54 for L = 2 m, ΔP = 18 kPa. Thin lines in the heat transfer validation are for model results, while thicker lines indicate test results.....130

Figure 4.9. Test matrix model validation for PLOT columns for (a) Adsorption time (b) ΔT.....132

Figure 4.10. Error analysis for PLOT columns for (a) Adsorption time (b) ΔT (c) ΔT_{Max} 135

Figure 4.11. Microscopic images of inner surfaces of the PLOT columns at different axial locations. The brown background is the fused silica cover and while clusters are adsorbent particles. 136

Figure 4.12. Microscopic images of the adsorbent-coated microchannel inner surfaces at different axial locations showing a contiguous adsorbent layer. 138

Figure 4.13. (a) Heat transfer (b) mass transfer test results for sample no. 6 (L = 0.9 m) for a ΔP of 49 kPa.....139

Figure 4.14. Adsorption experiment results on customized adsorbent-coated microchannels (a) Adsorption time vs. ΔP (b) average ΔT vs. ΔP (c) average ΔT vs. adsorption time 141

Figure 4.15. SEM images of zeolite 5A adsorbent particles used for fabrication of custom-made adsorbent-coated microchannels.....142

Figure 4.16. (a) Heat and (b) mass transfer model validation for sample no. 6 (L = 0.9 m) using adsorbent particle size of 7 µm. (c) heat and (d) mass transfer model validation using adsorbent particle size of 2 µm. The solid lines represent the experimental results, whereas the dashed lines represent the modeling results. 143

Figure 4.17. Predicted temperature variation with local adsorbent particle diameter varying axially (inlet to outlet) (a) linearly from 2 µm to 7 µm (b) linearly from 7 µm to 2 µm (c) decreasing quadratically from 7 µm at the inlet to 2 µm at the axial midpoint, and then back to 7 µm at the outlet. 148

Figure 4.18. Test matrix model validation for adsorbent-coated microchannels for (a) adsorption time (b) ΔT. The dashed lines in ΔT validation represent ΔT_{Max} and the dash-dotted lines represent ΔT_{min} for the corresponding adsorbent-coated microchannel. 150

Figure 4.19. Comparison between predicted and measured values for adsorbent-coated microchannels for (a) Adsorption time (b) ΔT (c) ΔT_{Max} 151

Figure 4.20. Drop in adsorption time with test time for repeated baking and because of water adsorption 156

Figure A.1. Adsorbed CO_2 concentration contour plots during adsorption stage……...170

Figure A.2. Adsorbent layer temperature contour plots during adsorption stage. ……172

Figure A.3. Product purity variation with two heat and mass transfer modeling approaches……173

Figure B.1. Instantaneous density variation during displacement of gas assuming a homogeneous mixture……..175

Figure B.2. Time lapse image of displacement of gas showing clean displacement showing a distinct gas-liquid interface (Moore, 2012). ……...176

Figure B.3. Instantaneous density variation during displacement of gas with decoupled approach. ……....176

Figure C.1. Adsorbent-coated microchannel cross section showing geometrical parameters……...177

Figure C.2. Initial and final states of the displacement of gas used for the sample calculation……180

Figure D.1 Cross section of the microchannel assembly with surrounding insulation and temperature nodes. ……..198

Figure D.2. A schematic showing initial and final states considered for sample calculations with a 0.22 m long channel with a ΔP of 16 kPa. Dark orange represents impure gas and light yellow represents pure gas. ……..…199

Figure E.1. Comparison of temperature curves predicted by models for a ΔTamb of 1.77°C, 1°C and 0.23°C (Corresponding to the total temperature difference of 10°C, 5°C and 1°C between the fused silica cover and the ambient). Solid lines, dashed lines and dash-dotted lines represent these three cases, respectively. ……..……212

LIST OF SYMBOLS AND ABBREVIATIONS

Symbols

A	Area [m^2]
a,b	Line fitting coefficients in type-B uncertainty
A_1, A_2…	DSL coefficients [mol kg^{-1} or mol kg^{-1} K]
b,B	DSL coefficients [kPa^{-1}]
BC	Boundary condition
C	Concentration [kg m^{-3}]
C_A	Adsorbed concentration [mol m^{-3}]
$C_{A,Eq}$	Equilibrium concentration [mol m^{-3}]
c_P	Heat capacity [J kg^{-1} K^{-1}]
C_T	Valve actuation constant [s^{-1}]
C_v	Valve flow coefficient [kg s^{-1} kPa^{-1}]
d,D	DSL coefficients [kPa^{-1}]
d_{pore}	Macropore (void) size in adsorbent layer [m]
D_A	Axial dispersion coefficient [m^2 s^{-1}]

D_{AB}	Binary diffusion coefficient [$m^2\ s^{-1}$]
$D_{crystal}$	Intra-crystalline diffusion coefficient [$m^2\ s^{-1}$]
D_{eff}	Effective diffusion coefficient [$m^2\ s^{-1}$]
D_h	Hydraulic diameter [m]
ΔH	Heat of adsorption [$J\ mol^{-1}$]
E	Activation energy [$J\ mol^{-1}$]
$\dot{E}$	Specific power [$kJ\ kg\text{-}ads^{-1}\ hr^{-1}$]
eps	Gas channel surface roughness [m]
f	Friction factor [-]
h	Enthalpy density [$J\ m^{-3}$]
H	Enthalpy [$kJ\ kg^{-1}$]
h_{free}	Free or natural convection coefficient [$W\ m^{-2}\ K^{-1}$]
h_m	Mass transfer coefficient [$m\ s^{-1}$]
h_T	Heat transfer coefficient [$W\ m^{-2}\ K^{-1}$]
HTF	Heat transfer fluid
k	Thermal conductivity [$W\ m^{-1}\ K^{-1}$]
K_{LDF}	Linear driving force constant [s^{-1}]

Kn	Knudsen number [m m^{-1}]
l	Length of water column (purge stage) [m]
L	Length [m]
LHV	Lower heating value [kJ kg^{-1}]
M	Mass [kg]
$\dot{m}$	Mass flowrate [kg s^{-1}]
$\dot{M}$	Mass collection rate [kg kg^{-1} hr^{-1}]
M_B	Langmuir equation coefficient [mol kg^{-1}]
MF	Adsorbent loading [kg kg-polymer^{-1}]
MW	Molecular weight [kg $kmole^{-1}$]
N	Sample size [-]
N_{nodes}	Number of nodes [-]
$\dot{N}_{cyc}$	Cycles per hour [cycles hr^{-1}]
N_{ch}	Number of channels made using 1 kg adsorbent [kg^{-1}]
P	Pressure [kPa]
Pe	Peclet number [-]
Pe_{grid}	Grid Peclet number [-]

Peri	Channel perimeter [m]
Pr	Prandtl number [-]
$Q_{B/D}$	Heat of adsorption in DSL equation [J mol^{-1}]
R or R_{eq}	Radius [m]
$r_{crystal}$	Adsorbent crystal size [m]
Re	Reynolds number [-]
R	Overall transport resistance [m^{-2} s or m-K W^{-1}]
R_0	Distance of adsorbent layer midpoint from center [m]
R_1	Distance of adsorbent layer endpoint from center [m]
R_2	Distance of fused silica midpoint from center [m]
R_3	Distance of fused silica endpoint from center [m]
R_h	Hydraulic radius of microchannel [m]
Ru	Universal gas constant [J mol^{-1} K^{-1}]
S	Switch
t	Time [s]
th	Adsorbent layer thickness [m]
th_{FS}	Monolith wall thickness [m]

T	Temperature [K or °C]
u	Velocity [m s^{-1}]
U	Total uncertainty
U_A	Type-A uncertainty
U_B	Type-B uncertainty
U_g	Nodal internal energy density [J m^{-3}]
v	Specific volume [m^3 kg^{-1}]
V	Volume [m^3]
VI	Virtual instrument
V_p	Valve position [-]
X	Sensor reading
X	Switch for gas/liquid phases
$\overline{X}$	Mean sensor reading
y	Mass fraction [-]
Y_i	Sensor reading used for type-B calibration
z	Axial position [m]

Greek

ε	Adsorbent matrix void fraction [m^3 m^{-3}]
ε_r	Radiation emissivity [-]
η	Recovery factor or efficiency [-]
λ	Mean free path [m]
μ	Viscosity [kg m^{-1} s^{-1}]
ρ	Density [kg m^{-3}]
σ	Stefan-Boltzmann constant [W m^{-2} K^{-4}]
τ	Tortuosity factor [m m^{-1}]
ω	Adsorbent volume fraction [m^3 m^{-3}]

Superscripts and Subscripts

abs	Absorbed
ads	Adsorbent layer or adsorption stage
ads	Adsorption
amb	Ambient
binder	silica binder
CH_4	Methane

CO_2	Carbon dioxide
Com	Compressor
conv	Convection
cool	Cooling
deso	Desorption
FS	Fused silica
g	Microchannel
G	Gas phase
GDL	Gas displacing liquid
h	Hydraulic
Heat	Related to heat transfer
HTF	Heat transfer fluid
i	Assigned species (He, N_2, CO_2)
in	Inlet
ini	Initial
ins	Insulation
Knudsen	Knudsen diffusion

Mass	Related to mass transfer
mid	Midpoint
mix	Mixture
L	Liquid phase
LDG	Liquid displacing gas
ordinary	Molecular or ordinary diffusion
out	Outlet
p	Constant pressure
poly	Polymer material
prod	Product
recir	Recirculation
sat	Saturation pressure
sens	Sensible
s	Surface
sys	System
rad	Radiation
total	Total (net) diffusion

v	Valve
w	Adsorbent layer or wall

SUMMARY

Natural gas has become increasingly important as a fuel source with lower environmental impact; therefore, there is a growing need for scalable natural gas purification systems with small footprints. Current industrial purification systems are based on absorption, membrane separation, or adsorption techniques; however, each of these technologies requires large capital costs or suffers from scalability issues. Adsorption-based separation techniques are categorized into pressure-swing adsorption (PSA) and temperature-swing adsorption (TSA). Among adsorption-based gas purification techniques, PSA has typically been preferred over TSA due to the ease of operation and reliability. TSA processes have not commonly been used for industrial gas separation due to the typically low thermal conductivity of the adsorbent bed, which poses challenges for desorption of impurities and regeneration of the adsorbent. However, the high heat and mass transfer coefficients possible with microchannels offer the potential for using the TSA process for gas purification.

The present work investigates the fluid mechanics and coupled heat and mass transfer processes within a microchannel monolith with a polymer-adsorbent matrix coating the inner walls of the microchannels during TSA-based gas separation. Carbon dioxide is separated from methane by passing the feed gas through microchannels, followed by sequential flow of desorbing hot liquid, cooling liquid, and purge gas through the same microchannels. For selected operating conditions and geometries, the process shows merit when compared to current technologies. A combination of spatially- and temporally-resolved analyses was conducted to assess these processes and select optimal configurations and process parameters. Experimental validation followed,

wherein the temporal and spatial variations of the rates of adsorption and heat releases during the adsorption stage of the separation process in adsorbent-coated microchannels were measured and analyzed using mass spectrometry. This combination of measurements and analyses was used to develop validated models, which are expected to provide design guidance to a wide variety of TSA-based separation and other related industrial processes.

1 INTRODUCTION

The rise in global environmental concerns has resulted in widespread efforts toward investigation of sustainable energy sources and technologies that can deliver clean energy. In the USA, 104 EJ of primary energy is consumed annually, of which 91.2% is from non-renewable sources (EIA, 2015). Combustion of these fossil fuels generates nearly 3.96×10^{12} kg of carbon dioxide (CO_2) in the USA (with a total of 29.43×10^{12} kg on Earth (GCA, 2014)) each year, contributing significantly to global warming. The total CO_2 emission is dependent primarily on four factors (Gates, 2010):

- Global population
- Per capita use of services (e.g., appliances)
- CO_2 produced per unit of energy
- Energy required for each of the services.

Of these factors, the development of ways to moderate the first two factors is a very long term goal and is complicated as they are closely tied with the human development index (HDI). However, tackling the last two causes of CO_2 emission is more tangible and offers opportunities for engineering solutions.

1.1 Natural gas as a fuel

The CO_2 emission coefficient of coal is 96 kg GJ^{-1} of energy, whereas for petroleum-based fuels, it is 70 kg GJ^{-1}. As compared to these fuels, natural gas produces 50 kg GJ^{-1} upon combustion without production of any solid waste, such as soot (EIA, 2015), thus addressing the third factor mentioned above. With continuously increasing proven natural gas reserves and the consequent availability of cleaner energy at a reduced

cost, the use of natural gas as a primary fuel for power generation and in the automobile industry has sharply risen in the last decade. Figure 1.1 shows that the contribution of natural gas as an energy source in the USA has increased by 30% since 2005 (EIA, 2015).

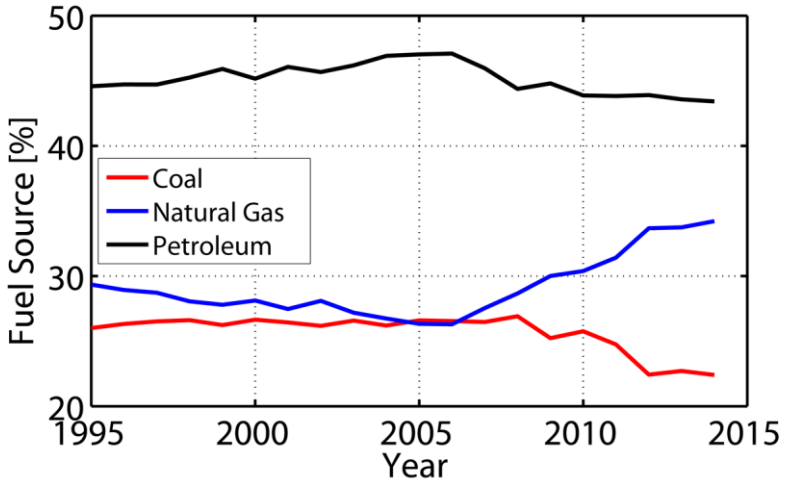

Figure 1.1. Fractions of non-renewable fuels as USA primary energy (EIA, 2015).

Such a trend is also observed globally, which can be seen in Figure 1.2, which shows that natural gas consumption reached 3.14 trillion m^3 per year at the start of this decade.

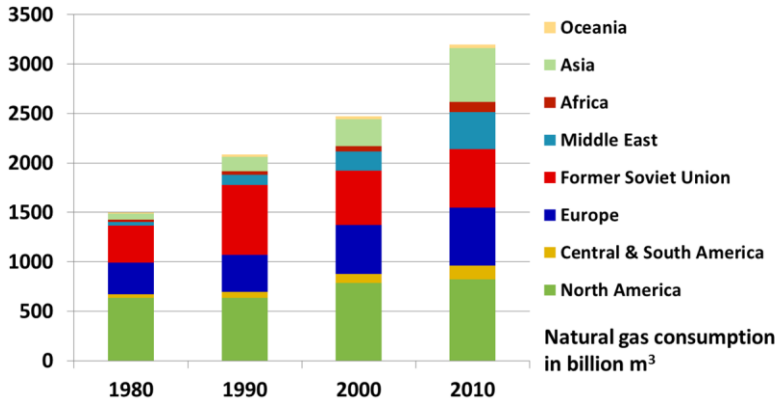

Figure 1.2. Globally increasing natural gas consumption (Schaal, 2013).

Natural gas must be purified to be used as fuel in different energy sectors. Raw natural gas contains 70% to 90% methane (CH_4) depending on the source, whereas the remainder is composed of heavier hydrocarbons, which can be separated as natural gas liquids (NGLs), acid gas impurities including CO_2 and hydrogen sulfide (H_2S), and traces of nitrogen (N_2). It may also contain liquid water immediately after extraction. Different separation techniques are employed to remove impurities from natural gas. Typically, a sequential approach as shown in Figure 1.3 is followed, wherein sediment and liquid water, trace water vapor, acid gases, N_2 and NGLs are removed from CH_4 in successive stages. Contingent on the location of the natural gas reserve (inland vs. off-shore), one or more of these processes can be clustered at a single location to minimize capital and transportation costs. Different grades of gas can be supplied after acid gas removal for end use; therefore, acid gas removal becomes the vital process in the natural gas life cycle.

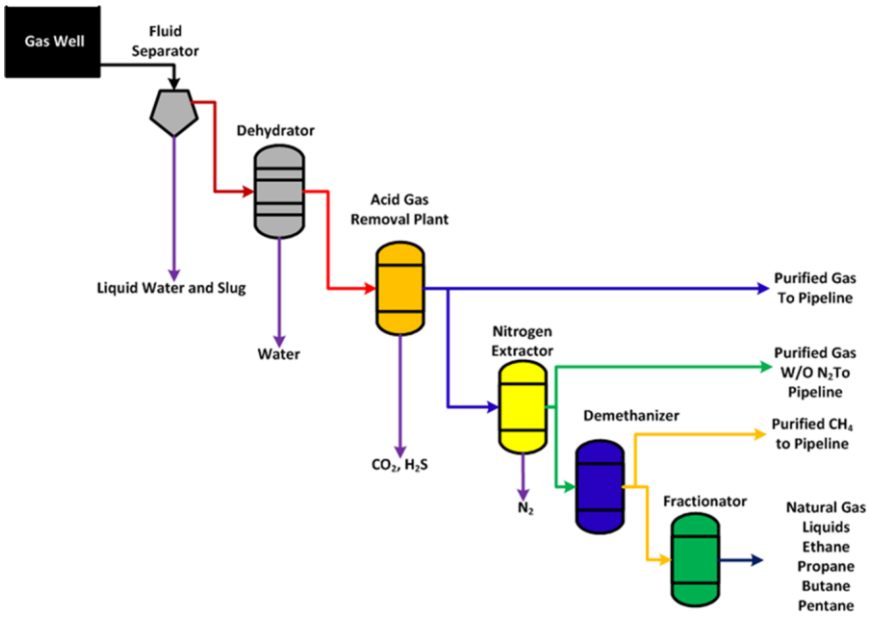

Figure 1.3. Sequential purification of natural gas (Brooks, 2013)

To enhance the quality of the fuel and minimize corrosion of the pipelines, the minimum acceptable natural gas purity is set to 98% (Baker, 2002). Furthermore, when the gas is liquefied (LNG) for transportation and storage, the CO_2 fraction is limited to 100 ppm, to avoid freezing of CO_2 and choking of pipelines (Schaal, 2013).

Because of multiple separation processes, the typical plant size, and the corresponding capital costs are high. As an example, Figure 1.4 shows the large footprint of the Prudhoe Bay processing plant in Northern Alaska, from where the processed gas is sent to the end use via pipelines. To accommodate the growing need of natural gas as a primary fuel and to reduce the cost overhead to improve market penetration, compact and cost-effective natural gas separation and purification processes meeting the purity constraints must be investigated and commercialized.

Figure 1.4. Prudhoe bay natural gas processing plant in Alaska (White, 2014)

1.2 Thermally driven energy systems

Annually, 40 EJ of primary energy is consumed in the USA to produce 14.75 EJ of electricity (EIA, 2015), with 87% coming from fossil and nuclear fuels. The power

conversion loss combined with the waste heat produced from the consumption of direct primary energy amounts to nearly 43 EJ of waste heat available at temperatures greater than 30°C (Rattner and Garimella, 2011). As conventional fuels become more constrained, the need to manage the available primary energy resources intelligently is becoming critical, until renewable energy sources can effectively replace the current energy supply landscape. Judicious management of energy requires the utilization of low-grade waste heat from power and other industries for thermal applications. Accordingly, thermally driven systems can replace electrically driven systems that may increase the carbon load on the environment. This transition will eventually lead to reduced burden on power industries, reduced use of conventional energy sources, and reduced carbon footprint, while retaining overall energy sufficiency, addressing the fourth impacting factor in CO_2 emission mentioned above. One such energy technology pertaining to gas separation that can reduce the use of direct electricity for its operation is the temperature swing adsorption (TSA) process.

1.3 Motivation for the present work

The thermodynamic state of an adsorbent can be manipulated by altering either the partial pressure or the temperature of the surrounding gas adsorbate to cause adsorption or desorption. Existing adsorption-based systems prefer pressure swing adsorption (PSA) over temperature swing adsorption (TSA). Conventional adsorbent beds are prepared by filling the adsorbent pellets in rigid cylinders, allowing porous regions between adsorbent particles for the gases to flow. In a PSA process, compressors are incorporated into the system for pressurization and depressurization of the adsorbent, thus consuming electricity. Additionally, these processes are slow due to large mass

transfer resistances in large adsorbent particles and sluggish gas diffusion through porous gaps (Pahinkar *et al.*, 2015). Nevertheless, PSA processes are preferred due to their ease of operation. TSA processes have not been commonly used for industrial gas separation due to the difficulty in heating the low thermal conductivity adsorbent material to desorb impurities and regenerate the adsorbent (Riemer *et al.*, 1994).

The high heat and mass transfer coefficients possible with microchannels offer the potential for the use of TSA processes for gas purification. The central concept of the present research involves passing of the impure feed gas through a microchannel monolith with an adsorbent layer coated along the inner walls of the microchannel. The adsorbent microchannels not only create convective passages, through which the working fluids flow quickly, but also eliminate difficulties in heating and cooling the adsorbent as a result of excellent heat and mass transfer characteristics. Rapid cycling of the adsorbent is therefore possible with the use of heat transfer fluids (HTFs) that may pass through separate adjacent channels or through the same channels. Multiple microchannels can be stacked together to form a monolith to make the system modular and achieve the required process output for a wide range of capacities. Such natural gas purification systems enable the two important topics discussed earlier: a) the shift toward the use of natural gas as a fuel, and b) the use of thermally driven systems, resulting in a reduction in primary energy consumption.

Figure 1.5 shows a schematic of a monolithic structure employed for TSA-based natural gas purification by Pahinkar *et al.* (2016). Alternate rows of adsorbent-coated microchannels and HTF channels transfer heat across the thin monolith wall, minimizing the heat transfer resistance. Therefore, the desorption and cooling stages of the

purification cycle can be executed quickly, improving the product yield for the same amount of adsorbent mass 15-fold over that of bed-based processes. Due to small mass transfer resistance between the microchannel and the adsorbent layer, adsorption and purge stage wave fronts are sharp, which enhances the product purity and CH_4 recovery to 97% and above. Finally, this process is shown to work with water as the HTF at 90°C, obviating the use of electricity for its core operation. Such thermally driven separation systems can also utilize a part of the purified fuel they produce, reducing the need for subsystems for auxiliary operations.

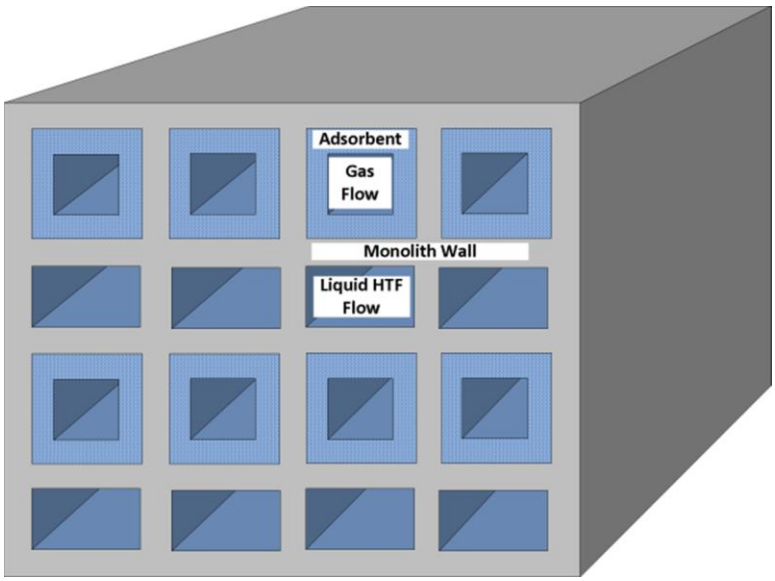

Figure 1.5. Adsorbent bed design with alternate rows of adsorbent-coated and HTF microchannels (Pahinkar *et al.*, 2016).

The primary distinctive feature of the present work is to pass the working and coupling fluids through the same channel, thus eliminating the need for dedicated HTF channels, which makes the purification systems much more compact. This not only reduces the system footprint, but also simplifies header design. This requires the

investigation of the direct and simultaneous interaction of liquid HTFs and working fluids with the adsorbent, which is considered in depth in the present study.

The present work explores several parameters for the design of the system through fluid dynamics and heat and mass transfer modeling. These include the size of the microchannels, thickness of the adsorbent layer, materials for the adsorbent and HTF, and most importantly, appropriate sequencing and timing of the stages based on these parameters. Additional considerations include routing options for the working and coupling fluids, avenues for heat and mass recovery to enhance industrial feasibility, and comparisons between the process performance map under consideration here and those of the conventional separation processes. An experimental investigation of gas separation in microchannels at the laboratory scale is also conducted to validate the process models. The combination of measurements and analyses is used to develop validated models and provide design guidance for TSA processes.

1.4 Research objectives

The primary research objectives of this work are to:

- Develop an experimentally validated computational process model for the TSA cycle with working fluid and coupling fluid flowing in series through microchannels

- Compare process performance with that of other industrial natural gas purification processes

To accomplish these objectives, the following tasks are undertaken:

- Develop heat transfer, mass transfer, and fluid flow models for the adsorption, desorption, cooling, and purge stages of the proposed cycle and identify critical issues in the implementation of the process.

- Couple the individual models sequentially to attain cyclic steady state operation of the process and predict process performance (e.g., product purity, yield and energy efficiency).

- Investigate heat and mass recovery techniques for improvements in process performance.

- Design and construct a test facility and conduct heat and mass transfer experiments on the adsorbent microchannels for a range of pressure drops and microchannel lengths.

- Develop lab-scale models for heat and mass transfer tests, and use experimental results to validate the models.

1.5 Dissertation outline

This dissertation is organized as follows:

- **Chapter 2** describes the concept development for the natural gas purification process through an understanding of the advantages and limitations of conventional gas separation systems. Once the process foundation is laid, computational models for each of the stages for the purification process are developed, followed by a parametric study to select optimum microchannel dimensions and a feasible adsorbent-HTF pair.

Subsequently, full process model development and overall process performance are discussed using a sample set of operating conditions.

- **Chapter 3** describes feasibility of the TSA-based process in the present work by comparison with conventional gas separation processes. A performance map of the process is generated and the relevant performance indicators are compared with the corresponding parameters in the literature to demonstrate the applicability of the concept.

- **Chapter 4** contains a detailed experimental analysis of feed gas adsorption in adsorbent-coated microchannels and the development of laboratory scale models, followed by validation of the heat and mass transfer models. Preferable adsorbent coating structures, manufacturing variability in coating the adsorbent, and the response of the adsorbent to a range of experimental conditions are discussed.

- **Chapter 5** summarizes important conclusions and provides recommendations for future work.

2 PROCESS MODELING METHODOLOGY

2.1 Introduction

Natural gas consumption worldwide is over 3.14 trillion m^3 per year (Schaal, 2013) and continuously increasing. Therefore, natural gas purification is by far the largest industrial gas separation application with a total worldwide market of up to $5 billion per year (Baker, 2002). Natural gas is predominantly methane (CH_4); but also contains impurities such as carbon dioxide (CO_2), hydrogen sulfide (H_2S), nitrogen (N_2) and other hydrocarbons in varying proportions ranging from 10% to 30%. Before supplying the gas via pipelines, removal of these impurities is essential. Gases such as N_2 reduce the combustion efficiency of the fuel without other harmful effects; however, acid gases such as H_2S and CO_2 are corrosive, harmful to the environment, and may lead to excessive maintenance costs. Furthermore, freezing of CO_2 clogs liquefaction pipelines due to its relatively high freezing point. Regulations on CH_4 purity in natural gas are therefore stringent. Pipeline grade purity requirement exceeds 98.0% (Baker, 2002), while the CO_2 content in liquefied natural gas (LNG) is limited to 100 ppm (99.99% pure CH_4) (Schaal, 2013). As natural gas becomes increasingly important as an alternative to conventional fossil fuels, the growing need for inexpensive, multi-utility (large to small scales, on-shore and off-shore platforms), and scalable natural gas purification systems that cater to these product purity requirements must be addressed.

The most widely used large-scale process for the removal of acid gases from CH_4 involves the absorption of gaseous contaminants into liquid solvents that demonstrate

strong chemical affinities for acid gases (Yang *et al.*, 2008). Absorption-based systems are widely employed for not only natural gas purification, but also for CO_2 separation from flue gas (Aaron and Tsouris, 2005). The dynamics of an absorption-based purification system are well understood, and operation and product collection in an absorption process is continuous. However, implementation of absorption-based systems requires large capital costs. As a result of bulk liquid circulation, which is the primary process in the system, the system size is large; therefore, absorption-based systems seldom find applications in off-shore platforms or smaller plants. Continuous operation of the system deteriorates the solvent gradually over time due to irreversible reactions of more strongly reacting impurities with the solvent, and replacement of the solvent is expensive. The reversible energy requirement reported in the literature for absorption-based systems is 0.34 kWh kg^{-1} CO_2, while the same for the adsorption-based processes can be as low as 0.16 kWh kg^{-1} CO_2 (Göttlicher and Pruschek, 1997) for a feed gas mixture with 28% CO_2 by volume. The actual operating costs for the MEA absorption systems (Bounaceur *et al.*, 2006), however, can be up to 1.67 kWh kg-CO_2^{-1}.

The second commonly used separation method – membrane gas separation – relies on preferential sieving of the components in the feed gas mixture based on a combination of gas molecule size, selectivity of membrane material, and membrane sizes (Koros and Mahajan, 2000). Membrane separation processes are gaining importance in small-scale (< 6000 m^3 hr^{-1}) and medium-scale applications (6000 - 50000 m^3 hr^{-1}) applications, at off-shore locations, and in remote locations where energy availability is an issue, because of advantages such as small footprint, simplicity in design, low

environmental impact, and low energy requirements (approximately 0.07 kWh kg^{-1} CO_2 (Göttlicher and Pruschek, 1997) reversible electrical input).

Thorough reviews of membrane gas separation technology and advances have been conducted by Koros and Mahajan (2000), Bernardo *et al.* (2009) and Baker (2002). Since its first commercial implementation, a vast number of membrane materials have been devised and tested for target applications, and they can be broadly classified into the following categories: polymers, reverse selective membranes, molecular sieves, zeolites and mixed matrix membranes. Although polymers and reverse selective membranes are used for conventional separation purposes, molecular sieves and zeolites are considered superior in terms of separation performance and selectivity.

Molecular sieving membranes have CO_2/CH_4 selectivity up to 10 times more than their polymeric counterparts and offer more rigidity and stability. However, due to the greater cost per unit area of molecular sieves compared to polymers, aging effects, pore blocking, and brittleness, molecular sieve membranes are not yet commercially viable (Bernardo *et al.,* 2009). Gas separation in zeolites is driven by molecular diffusion as in molecular sieves as well as by preferential adsorption (Koros and Mahajan, 2000). Favorable attributes such as very high selectivity, high thermal and chemical stability, and moderate cost have driven the use of zeolites in CO_2/N_2, CO_2/CH_4 separation. However due to their inelasticity, formation of standalone zeolites into flat sheets or hollow fibers is difficult.

Lower selectivity and permeability, plasticization in the presence of heavy hydrocarbons and CO_2 in large quantities, and loss of separation properties at elevated

temperatures and pressures are additional challenges for conventional membrane plants. Despite their simple operation, the mass flux of permeate gases remains very small compared to that of amine absorption systems and the large-scale plant is not cost-competitive with absorption systems or with PSA processes. With recent advancements in the manufacturing of mixed matrix membranes (MMM), some of the challenges such as low selectivity and thermal and chemical instability can directly be addressed. It is possible to make such a matrix within the same framework of polymer membrane manufacturing (Koros and Mahajan, 2000). Recent efforts have been directed at successful fabrication of MMMs with a variety of polymers and adsorbents. Among these investigations, studies on the integration of zeolites into rubbery polymers have shown improved selectivity without sacrificing permeability (Bernardo *et al.*, 2009). Figure 2.1 shows the improvement in CO_2/CH_4 selectivity as the adsorbent particles are integrated in the conventional membrane materials without any significant change in polymer permeability.

Although recent development in making MMMs addresses the challenges highlighted above for membrane separation process, it also opens new avenues for investigating the applicability of these membranes in separation systems. While an increase in zeolite content in the polymer matrix increases selectivity, and in turn, the separation performance (Koros and Mahajan, 2000), it must be noted that the membrane gas separation process migrates from the conventional sieving mechanism toward the adsorption-based cyclic process. Determan *et al.* (2011) studied a possible application of MMMs configured by Lively *et al.* (2009) as hollow fiber modules for the removal of CO_2 from flue gas using a TSA process and employed a hot water regeneration stage. In a

similar approach, new hybrid systems incorporating such superior membrane materials can combine the benefits of membrane separation and adsorption systems. Therefore, along with understanding the separation behavior in MMMs from a membrane standpoint, it is also essential to consider the possibility of incorporating them into adsorption-based systems.

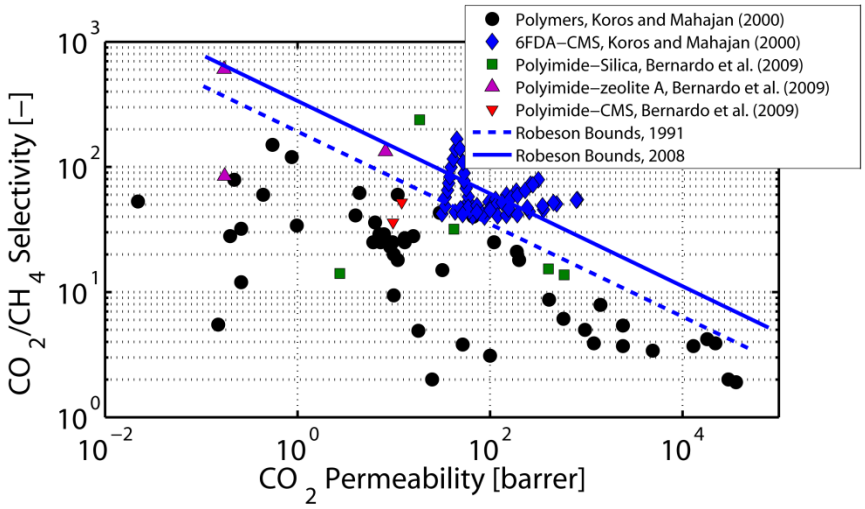

Figure 2.1. Improvements in selectivity of mixed matrix membranes by increasing adsorbent loading in polymers (Koros and Mahajan, 2000; Bernardo *et al.*, 2009).

Adsorption-based gas separation processes employ preferential adsorption of component gases on solid adsorbent materials, and this phenomenon is controlled by manipulating the pressure (PSA) and temperature (TSA) of the gases under consideration. In a typical PSA process, the adsorbent pellets or crystals are packed to form a porous adsorbent bed through which the mixture components pass. In the adsorption stage of the cycle, the bed is pressurized with the feed mixture, and gas separation takes place by selective adsorption. After the bed is saturated with the adsorbate, it is depressurized, in some cases to near-vacuum pressure (Zhang *et al.*, 2009; Liu *et al.*, 2011), which desorbs

the adsorbed species that are subsequently removed from the system. A pressurization stage follows, after which the next batch of feed gas can pass through the bed. In a TSA process, the adsorbate is removed from the adsorbent by increasing the adsorbent temperature. After the adsorbed components are removed, the adsorbent bed is regenerated by cooling the adsorbent, followed by the next feed stage. Although the nature of a typical adsorption process is periodic, commercial viability can be improved by out-of-phase product collection from several adsorbent beds, making the overall process pseudo-continuous (Cen *et al.*, 1985).

Bed-based PSA systems are well established and a vast body of literature describing the flow and adsorption kinetics in the adsorbent bed is available. The research scope in PSA systems has been widened to study different adsorbents and their impacts on adsorbent breakthrough. In particular, interaction of different classes of zeolites such as 13X, 5A, LTA, silicalite, and DDR with gases such as N_2, CO_2, CH_4, and water vapor has been documented in terms of pure gas adsorption isotherms, competitive adsorption isotherms, and heat of adsorption (Cavenati *et al.*, 2004; Delgado *et al.*, 2007; Liang *et al.*, 2009; Palomino *et al.*, 2009; Wang and LeVan, 2009; Morishige, 2011; Peng *et al.*, 2011; Shao *et al.*, 2011; Delgado *et al.*, 2012; Mulgundmath *et al.*, 2012). For metal organic frameworks (MOFs), larger capacities for the component gases than zeolites have been reported, but from a separation cycle perspective, more energy is required to desorb the adsorbed species (Liang *et al.*, 2009; Palomino *et al.*, 2009; Chowdhury *et al.*, 2012; Herm *et al.*, 2012; Askari and Chung, 2013). Figure 2.2 shows an overview of CO_2 adsorption isotherms at 25°C for representative adsorbents. The adsorbents show not only

different capacity at a given partial pressure, but also different patterns of variation in adsorbent capacities with partial pressure, which in turn affects their selectivities.

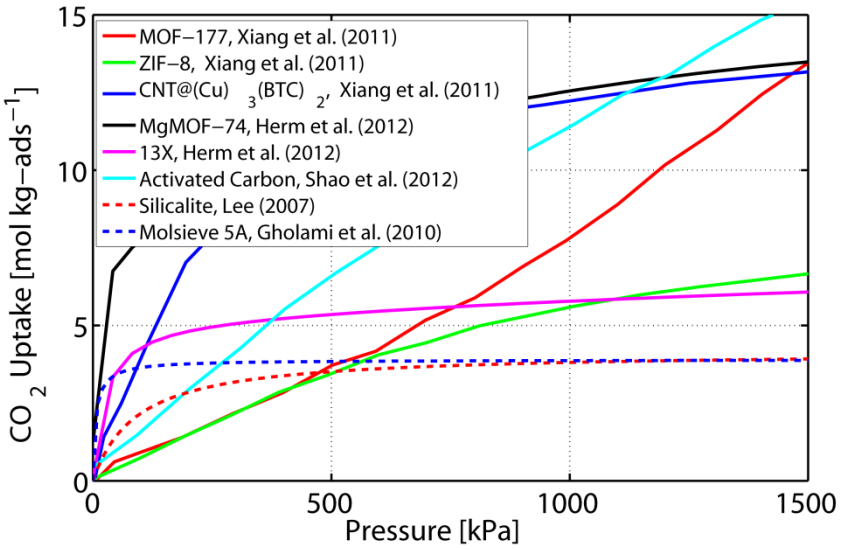

Figure 2.2. CO_2 adsorption isotherms for MOFs, activated carbon zeolites and silicalite at 25°C (Lee, 2007; Gholami and Talaie, 2009; Shao *et al.*, 2011; Herm *et al.*, 2012; Xiang *et al.*, 2012)

Adsorption systems can be less expensive in some aspects compared to absorption systems. Solid adsorbents seldom need replacement as compared to the liquid solvents used in amine absorption systems, which decreases the operating cost. However, a PSA-based process requires complex valve operation and large compressor operation costs. In this aspect, TSA-based processes are favored because large pressure swings are not needed for their operation, which reduces system complexity and compressor power requirements (Moore, 2012). Despite these advantages, however, PSA-based systems have thus far been considered more energy efficient than their TSA counterparts, mainly due to the difficulty in heating adsorbent packed in a bed form (Moate and LeVan, 2010;

Lee *et al.*, 2015). The adsorbent materials used for the removal of CO_2 from natural gas or flue gas mixtures have low thermal conductivities; hence, long durations and heating loads are required for the desorption stage of a TSA-based separation cycle. For the same reason, very few studies in the literature have reported a full process design of TSA-based separation. Li *et al.* (2014) conducted a theoretical analysis of energy required for desorption of CO_2 and reported the ideal values of the total energy required (sum of heat of desorption and sensible heat) for a variety of MOFs. Pirngruber *et al.* (2013) performed a similar feasibility analysis for TSA-based processes on a hypothetical adsorbent for determining optimum conditions for desorption. Mérel *et al.* (2006) investigated an indirect TSA-based CO_2 separation process that utilized finned heating of the adsorbent bed for better heat distribution and reported the process capacity and cyclic energy required. They found that the heat loss fraction is 25% of the total heat required, while the heat of desorption for zeolite 13X, adsorbent sensible heat, and sensible heating of the metal accessories are 11%, 27%, and 37%, respectively. These calculations reinforce the need for a better design of TSA-based separation processes that results in lower parasitic thermal energy consumption by the metal accessories to make TSA processes viable.

Microchannel heat exchangers are attracting increasing attention in the heat exchanger industry due to the high heat and mass transfer coefficients achievable at small hydraulic diameters. Microchannel designs with adsorbent particles coated on the walls can exchange heat and species with the working and coupling fluids very effectively, which helps overcome the limiting challenges associated with large-scale systems. In particular, TSA processes can be greatly improved by configuring the impurity removal

and regeneration processes using convection within microchannels instead of diffusion through the porous bed in the case of bed-based systems.

The hollow fibers constructed from the mixed matrix membrane (MMM) mentioned earlier are suitable candidates for such microchannels, wherein the flow area can be used for the motion of the requisite fluids, while the adsorbent–polymer matrix can be utilized for selective adsorption and desorption. Additionally, these microchannels can be stacked together in arrays to form monoliths to greatly increase product collection (Pahinkar *et al.*, 2015, 2016), which improves scalability of the system. It should also be noted that adsorption process performance depends on heat and mass transfer kinetics only within the microchannel and not on the overall size of the system as in packed bed-based systems. The flue gas CO_2 separation approach studied by Determan *et al.*(2011) utilized a hollow fiber module arranged as a heat exchanger, where the HTF, modeled as water, flows through the center of the hollow fiber. Pahinkar *et al.* (2016) analyzed an equivalent TSA-based process design for CH_4 purification that consists of parallel alternating arrays of adsorbent and HTF channels. Such a structured design results in a reduction of the system footprint compared to the module analyzed by Determan *et al.* (2011) due to elimination of non-uniform space assigned for the flue gas flow over the adsorbent layer. More compact systems can be built using hollow fiber MMMs by flowing the working fluids and HTFs through the same channel. This direct interaction of feed gas mixture and hot and cold HTFs with the adsorbent–polymer matrix presents a new avenue for research.

This Chapter investigates a TSA-based gas separation cycle concept and its underlying heat transfer, mass transfer, and fluid dynamics phenomena in a microchannel

monolith with porous adsorbent-binder matrix coated along the inner walls of each microchannel representing an MMM hollow fiber. This configuration is unique in that both the working fluid and the HTFs flow through the same microchannel, resulting in direct and simultaneous interaction of feed gas mixture and hot and cold HTFs with the adsorbent-polymer matrix. This design reduces heat and mass transfer resistances when compared to configurations in which heat is transferred across separate parallel channels (Pahinkar *et al.*, 2016); thus increasing the possibility of reducing the system footprint with direct contact heat and mass exchange.

The cycle has four stages, the first being the adsorption stage as shown in Figure 2.3(a), where CO_2 is removed from CH_4 by passing the feed gas through the adsorbent microchannel. The adsorption stage is followed by a desorption stage, in which the hot HTF enters the microchannel, heats the adsorbent, and desorbs the adsorbed gases. These desorbed gases are carried away with the hot liquid stream as shown in Figure 2.3(b). This concept could also be an improvement over more conventional PSA and TSA processes because the HTF serves the purpose of heating the adsorbent as well as that of a purge gas for partial pressure reduction and impurity removal, making this a "pressure-enhanced temperature swing" process. After impurities are removed from the adsorbent, cold liquid is sent through the microchannel, which lowers the adsorbent temperature and prepares it for the next adsorption stage. The cooling stage is shown in Figure 2.3(c). After the adsorbent is cooled, the cold liquid is driven out of the microchannel by a purge gas, bled from the product stream. The purge gas is expected to displace the cold liquid in the microchannel and dry it by shearing the liquid attached to the microchannel walls as shown in Figure 2.3(d). In addition, after the liquid displacement is accomplished, the

purge stage is extended further to dry the adsorbent-binder matrix by evaporating any trapped liquid. The implementation of such a system requires a thorough understanding of the alternating flows of the working and coupling fluids through the adsorbent microchannel in a cyclic steady state. Additionally, the effect of the presence of two phases on mass transfer between the adsorbent layer and the microchannel, and on the adsorption into the adsorbent, and the effect of adsorbent microchannel geometry, adsorbent and HTF material on the overall process performance is unclear.

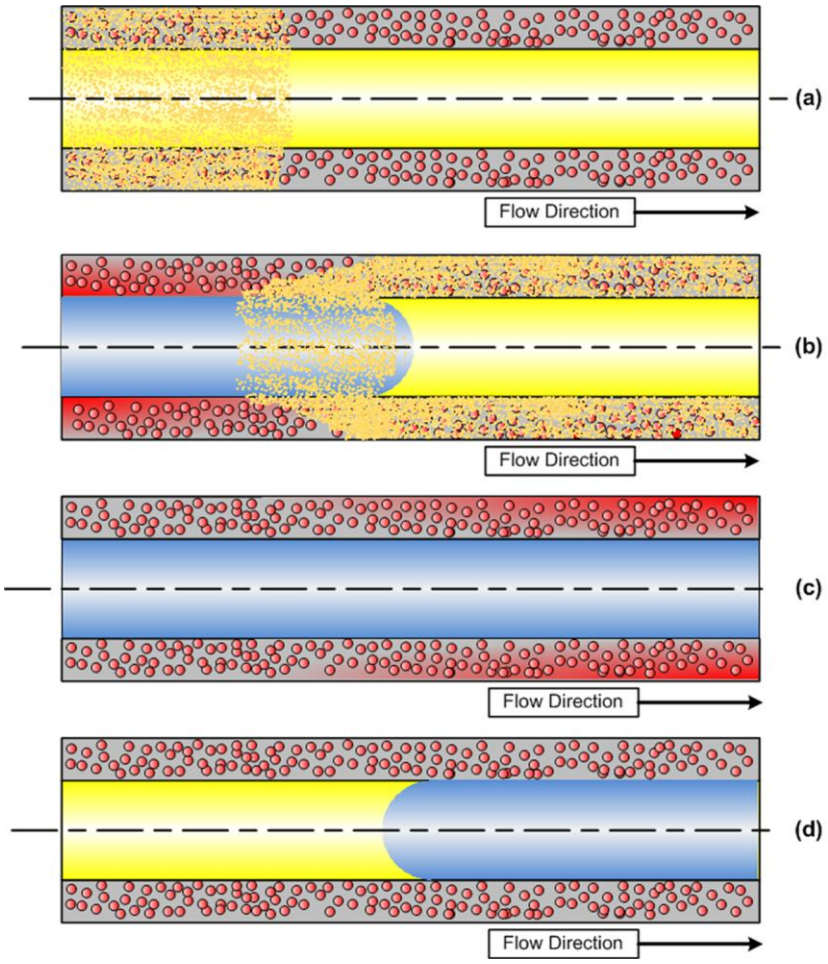

Figure 2.3. Schematics of the stages in the proposed TSA based purification cycle. Red dots indicate adsorbent crystals in the gray hollow binder matrix and small yellow dots indicate CO_2 impurity in pure CH_4 shown as yellow background.

2.2 Modeling Methodology

The computational model of the purification cycle involves analyses of the fluid dynamics (FD), heat transfer (HT), and mass transfer (MT) associated with the microchannel and the adsorbent layer. It is assumed that the mixed matrix membrane (MMM) representing the adsorbent layer is attached to a monolith wall for additional support and to inhibit mass transfer beyond the adsorbent layer. To simplify the modeling efforts, the development of the complete process model is subdivided into a sequence of six different sub-models as shown in Figure 2.4.

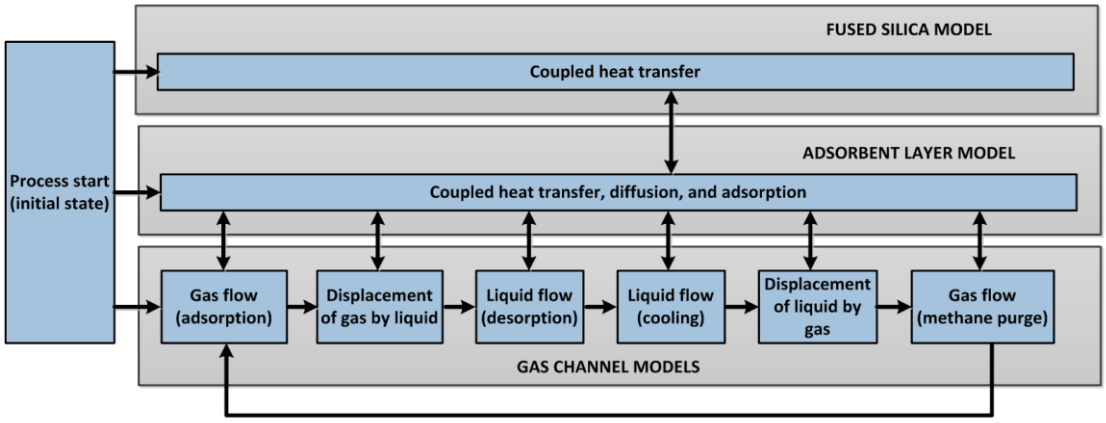

Figure 2.4. Computational modeling architecture of the purification process

The models for each of the stages are developed independently; these individual models are then coupled sequentially to develop a full purification process model operating in a cyclic steady state. The FD/HT/MT models are developed and simulated in gPROMS^{TM} Model Builder (Process Systems Enterprise, 1997-2015), and the material properties of the system components are imported from the Multiflash^{TM} property data package. The monolith wall material is modeled as fused silica with a thickness of 25 µm, which has a low thermal capacity and density, thereby minimizing dynamic heat losses during heat transfer to the adsorbent. The feed gas composition assumed for the

present work is 0.7/0.3 (CH_4/CO_2) by mole. The inlet and outlet pressures for the working fluid gases and the coupling liquid are assumed constant at 5500 and 5400 kPa, respectively. Thus, mass flow rates and velocities of the fluids adjust to match the fixed pressure drop imposed between the microchannel inlet and outlet, based on the chosen microchannel diameter and length. The selection of these pressure extremes is based on typical pressure values used for transportation of natural gas via pipelines (Schaal, 2013). Table 2.1 shows the numerical values of parameters chosen for the model simulation.

The microchannel diameter, adsorbent layer thickness, adsorbent material and the HTF material are chosen to ensure a feasible and realistic process performance; their selection is discussed in detail in later sections.

2.2.1 Adsorption stage model

For the adsorption stage modeling, an approach similar to that used by Pahinkar *et al.* (2015) is used. This approach involves radial lumping of the adsorbent microchannel fluid, adsorbent layer, and monolith wall regions. A 2-D axisymmetric model was also developed and its results are compared with those with the present approach in Appendix A. The heat loss from the microchannel monolith wall to the surroundings is neglected because several microchannels stacked together interact with each other thermally and all are considered to demonstrate a similar thermal state at any instant of the process.

Table 2.1. Simulation parameters and material properties (Mark, 1999; Lee, 2007; Determan *et al.*, 2011)

Parameter	Value
ε	0.55
MF	1
L	1 m
th_{FS}	25 μm
P_{in}	5500 kPa
P_{out}	5400 kPa
T_0	25°C
T_{Deso}	200°C
N_{nodes}	100
k_{ads}	1.2 W m^{-1} K^{-1}
$c_{P,ads}$	800 J kg^{-1} K^{-1}
ρ_{poly}	1270 kg m^{-3}
k_{poly}	0.22 W m^{-1} K^{-1}
$c_{P,poly}$	1460 J kg^{-1} K^{-1}
ρ_{FS}	2200 kg m^{-3}
k_{FS}	1.3 W m^{-1} K^{-1}
$c_{P,FS}$	740 J kg^{-1} K^{-1}
eps	10^{-6} m

2.2.1.1 Mass and heat transfer resistances

For the mass and heat transfer resistance determination, the mass and heat transfer coefficients are calculated using Churchill equations (Churchill, 1977a; Churchill, 1977b) and the effective diffusion coefficient approach, which also involves calculation of the mean free path for the mixture of CH_4 and CO_2 is followed (Cussler, 1997). Equations (2.1) and (2.2) are used to calculate the mass and heat transfer resistances, respectively. The thermo-physical properties of the adsorbent layer, ρ_w, $c_{p,w}$, and k_w are calculated using appropriate weighted average methods from the adsorbent and binding polymer properties (Pahinkar *et al.*, 2015).

$$R_{eq,Mass,i} = \frac{1}{h_m \cdot Peri} + \frac{\ln\left(\frac{R_{w,mid}}{R_h}\right)}{2\pi D_{eff,i}} \qquad (2.1)$$

$$\mathrm{R}_{eq,Heat} = \frac{1}{h_T \cdot Peri} + \frac{\ln\left(\frac{R_{w,mid}}{R_h}\right)}{2\pi k_w} \tag{2.2}$$

2.2.1.2 Governing equations for the microchannel

The governing equations for the microchannel are balances for each species, the momentum balance, and the energy balance for each node, and are shown in Equations (2.3) through (2.5), respectively. The dispersion coefficient D_A in Equation (2.3) is calculated using the Peclet number as shown in Equation (2.6). D_{AB} is the binary diffusion coefficient adjusted for convection as shown in Equation (2.7), which also indicates the difference between the effective diffusion coefficient used for the adsorbent layer, $D_{eff,i}$ and D_{AB}.

$$\frac{\partial C_{g,i}}{\partial t} + \frac{\partial\left(uC_{g,i}\right)}{\partial z} = \frac{\partial}{\partial z}\left(D_{A,i}\frac{\partial C_{g,i}}{\partial z}\right) - \frac{C_{g,i} - C_{w,i}}{A_g \cdot \mathrm{R}_{eq,Mass,i}} \tag{2.3}$$

$$\rho\frac{\partial u}{\partial t} + \rho u\frac{\partial u}{\partial z} - \sum_i \frac{C_{g,i} - C_{w,i}}{A_g \cdot \mathrm{R}_{eq,Mass,i}} u = -\frac{\partial P}{\partial z} + \mu\frac{\partial^2 u}{\partial z^2} - f\frac{\rho u^2}{2D_h} \tag{2.4}$$

$$\frac{\partial\left(h_g\right)}{\partial t} + \frac{\partial\left(u \cdot h_g\right)}{\partial z} = \frac{\partial}{\partial z}\left(k_g\frac{\partial T_g}{\partial z}\right) - \frac{T_g - T_w}{A_g \cdot \mathrm{R}_{eq,Heat}} \tag{2.5}$$

$$Pe_i = \frac{uD_h}{D_{AB,i}}$$
$$D_{A,i} = D_{AB,i}\left(1+\frac{Pe_i^{\,2}}{192}\right) \tag{2.6}$$

$$D_{AB,i} = \frac{D_{AB}}{1-y_i}$$
$$D_{eff,i} = D_{AB,i}\frac{\varepsilon}{\tau} \tag{2.7}$$

2.2.1.3 Governing equations for the adsorbent layer

The governing equations for the adsorbent layer involve the species and energy balance for each adsorbent layer node, which are shown in Equations (2.8) and (2.9), respectively. In these equations, C_A is the adsorbed concentration for the species components, which is dependent on the adsorbent material, gas mass fraction, pressure, and temperature. The method of calculating C_A is addressed later, where criteria for the selection of the adsorbent are discussed.

$$\frac{\partial C_{w,i}}{\partial t} + \frac{\omega}{\varepsilon}\frac{\partial C_{A,i}}{\partial t} = \frac{\partial}{\partial z}\left(D_{eff,i}\frac{\partial C_{w,i}}{\partial z}\right) + \frac{C_{g,i}-C_{w,i}}{A_w \cdot \mathrm{R}_{eq,Mass,i}} \tag{2.8}$$

$$\rho_w c_{p,w}\frac{\partial T_w}{\partial t} = k_w\frac{\partial^2 T_w}{\partial z^2} + \frac{T_g - T_w}{A_w \cdot \mathrm{R}_{eq,Heat}} + \sum_i \omega \cdot \Delta H_{ads,i}\frac{\partial C_{A,i}}{\partial t} - \frac{T_w - T_{FS}}{A_w \cdot \mathrm{R}_{eq,Heat,FS}} \tag{2.9}$$

The source terms in the energy equation include heat transfer from the microchannel to the adsorbent layer, heat transfer from the adsorbent layer to the fused silica wall, and the volumetric rate of heat generation due to adsorption for all component

species. The resistance to heat transfer from the adsorbent layer to the fused silica is calculated using Equation (2.10), in which the conduction heat transfer resistance in the adsorbent layer and that in the fused silica are added (Pahinkar *et al.*, 2015).

$$\mathrm{R}_{eq,FS} = \frac{\ln\left(\frac{R_h + th}{R_{w,mid}}\right)}{2\pi k_w} + \frac{\ln\left(\frac{R_{FS,mid}}{R_h + th}\right)}{2\pi k_{FS}} \tag{2.10}$$

2.2.1.4 Governing equations for the fused silica

The adsorbent layer considered in the present simulation is attached to the fused silica monolith wall. Although the fused silica wall is impermeable to species, the thermal mass of fused silica participates in heat transfer with the adsorbent layer. The energy equation used for the fused silica wall is shown in Equation (2.11), which is coupled with the energy equation for the adsorbent layer shown in Equation (2.9). The thermo-physical properties of fused silica used in Equation (2.11) are listed in Table 2.1.

$$\rho_{FS} c_{p,FS} \frac{\partial T_{FS}}{\partial t} = k_{FS} \frac{\partial^2 T_{FS}}{\partial z^2} + \frac{T_w - T_{FS}}{A_{FS} \cdot \mathrm{R}_{eq,Heat,FS}} \tag{2.11}$$

2.2.1.5 Boundary conditions for the adsorbent layer

The adsorbent layer is assumed to be insulated at the inlet and outlet headers to improve computational stability of the model in presence of changing boundary conditions for the microchannel. The boundary conditions for the species and energy balances can then be identified as shown in Equation (2.12) and (2.13).

$$D_{eff,i} \left.\frac{\partial C_{w,i}}{\partial z}\right|_{z=0} = D_{eff,i} \left.\frac{\partial C_{w,i}}{\partial z}\right|_{z=L} = 0 \tag{2.12}$$

$$k_w \left.\frac{\partial T_w}{\partial z}\right|_{z=0} = k_w \left.\frac{\partial T_w}{\partial z}\right|_{z=L} = 0 \qquad (2.13)$$

2.2.2 *Displacement models*

At the end of the adsorption stage, the hot HTF enters the microchannel to heat the adsorbent and desorb CO_2. The hot HTF accomplishes three tasks: the displacement of the residual gases from the microchannel, heating of the adsorbent layer, desorption of gases from the adsorbent, and the removal of the desorbed gases from the channel.

The model of the residual gas displacement with the hot HTF is separated from the desorption stage model to simplify the implementation of the complete process model. Although the boundary conditions for these two scenarios are identical, the presence of two different phases requires independent analysis of the displacement phenomenon. An approach with decoupled momentum and heat/mass transfer in the microchannel is used, where the displacement of gas by liquid is simulated on a dynamic mesh using simplified momentum equations. The heat and mass transfer in the microchannel and the adsorbent layer, however, are analyzed on a fixed mesh. Logical statements are introduced to distinguish between liquid and gas nodes, so that the heat and mass transfer kinetics are simulated separately for these regions. The liquid-gas interface location is explicitly imported into the heat and mass transfer models. The effect of mass transfer into the microchannel is neglected, because the desorbed gases constitute only 4% of the mass of gas-liquid mixture present in the channel. This methodology accurately simulates heat and mass transfer during displacement while maintaining stability and substantial details in the modeling equations. Details of the fluid displacement modeling and experimental validation are described by Moore *et al.* (2016).

The equations used for modeling displacement in the present study are the incompressible forms of the displacement equations derived by Moore *et al.* (2016) and are listed in Equations (2.14) through (2.16), where the total pressure drop in the channel is calculated as the sum of pressure drops across liquid- and gas-filled regions. The interface location, which marks the boundary between the two phases during displacement, is tracked through the variable *z* in Equation (2.14). The interface velocity defined by Equation (2.17) shows the velocity of the fluids during the displacement stage and is used in the energy and species conservation equations.

$$-\Delta P_{tot} = \left(\frac{dP}{dz}\right)_L \left(z_{IF}\right) + \left(\frac{dP}{dz}\right)_G \left(L - z_{IF}\right) \tag{2.14}$$

$$-\left(\frac{dP}{dz}\right)_L = f_L \frac{\rho_L u^2}{2D_h} + \rho_L \frac{du}{dt} \tag{2.15}$$

$$-\left(\frac{dP}{dz}\right)_G = f_G \frac{\rho_G u^2}{2D_h} + \rho_G \frac{du}{dt} \tag{2.16}$$

$$u = \frac{dz_{IF}}{dt} \tag{2.17}$$

With modifications incorporated for the decoupled momentum approach, the species equation for the microchannel during the displacement stage is given by Equation (2.18). A similar approach is followed for all other governing equations illustrated previously. This modeling approach is applicable for both displacement scenarios (gas by liquid and liquid by gas.) The clean displacement approach adopted for the displacement of gas is justified by the experimental findings of Moore (2012), who observed a liquid slug cleanly displacing residual gas present in the microchannel.

$$X_G\left(\frac{\partial C_{g,i}}{\partial t}+\frac{\partial\left(uC_{g,i}\right)}{\partial z}-D_{A,G,i}\frac{\partial^2 C_{g,i}}{\partial z^2}+\frac{C_{g,i}-C_{w,i}}{A_g\cdot \mathrm{R}_{eq,Mass,G,i}}\right)+$$
$$X_L\left(\frac{\partial C_{g,i}}{\partial t}+\frac{\partial\left(uC_{g,i}\right)}{\partial z}-D_{A,L,i}\frac{\partial^2 C_{g,i}}{\partial z^2}+\frac{C_{g,i}-C_{w,i}}{A_g\cdot \mathrm{R}_{eq,Mass,L,i}}\right)=0 \quad (2.18)$$

In these equations, X_G and X_L are used to switch between the liquid and gas regions. During the displacement of gas, if the axial location for a node is downstream of the interface location, then X_G for that node becomes *one* while X_L becomes *zero*. The axial fluid property variation with this decoupled approach is discussed in Appendix B.

During the desorption stage, gases desorbing out of the adsorbent crystals accumulate in the void spaces, and concentrations of both gases increase locally in the adsorbent layer. The increase in concentration and temperature causes an increase in the total pressure of the gases, which exceeds the pressure of the corresponding microchannel node at the start of desorption. Hence, favorable pressure and concentration gradients drive a convective-diffusive flow of desorbed gases radially inwards. Figure 2.5(a) explains the assumption of convective-diffusive flow during desorption. This quick desorption phenomenon is more likely to be short-lived and to exist during early desorption stage before the loss of desorbing gases to the microchannel, although this mechanism is explained in an exaggerated manner for illustrative purposes in Figure 2.5(a), where desorbing gases are shown as bubbles entering the microchannel from the adsorbent layer. The flow of gases from the adsorbent layer to the microchannel diminishes as a substantial mass of the gases leaves the adsorbent layer and mixes with the HTF stream. At this point, pressure equilibrium is attained between the microchannel and the adsorbent layer. Further desorption and outflow of gases takes place by slow diffusion through the gaseous void space and slow diffusion though the liquid boundary

layer in the microchannel. This condition is depicted in Figure 2.5(b). The total pressure difference in the adsorbent layer and corresponding microchannel node is tracked to differentiate between these two desorption scenarios. In this manner, appropriate changes involving diffusion phenomena (gas diffusion and gas convection during early desorption/gas diffusion and liquid convection during late desorption) are made to the mass transfer resistance shown in Equation (2.1).

It must be noted that surface tension forces become important for the entry of the HTF into the adsorbent layer during desorption and cooling. The presence of void spaces of variable size in the adsorbent layer poses significant challenges in modeling the exact local movement of the HTF. The binder material, modeled as Poly (Ether Imide) (PEI) in the present work is hydrophilic. Therefore, when liquid water is used as the HTF, PEI is more likely to facilitate the entry of water in the adsorbent layer owing to capillary forces acting in the direction from the microchannel core to the adsorbent layer. Simultaneously, as the gases are desorbed and are accumulated in the void spaces, they exert a counteracting force due to pressure difference between the adsorbent layer and the microchannel. However, for the microchannel geometry considered in the present work, capillary forces are not capable of inducing a radially outward motion of the HTF. This is because the outer boundary of the adsorbent layer, i.e., the channel wall, is impervious, and the incoming HTF would encounter the desorbing gases at high pressure. Hence, the surface tension forces can only act to decrease the pressure difference between the adsorbent layer and the microchannel, which is created by the desorption of gases. (In contrast, for designs such as heat pipes, capillary forces are the primary driving agents for the liquid flow from the condenser to the evaporator and for such systems, they do not

encounter a counteracting force that could prevent this refrigerant transfer). The physical effect of surface tension forces in terms of HTF ingress into the adsorbent layer can manifest after substantial mass of gases leaves the adsorbent layer by diffusing through the adsorbent layer, followed by getting dissolved in the liquid HTF. The present model takes the different modes of mass transfer into account to accurately model the species diffusion in gases and liquids. The HTF is not modeled as a mixture component, and conservation of CH_4 and CO_2 is targeted. This approach enables full process simulation without addressing HTF ingress in the adsorbent layer. The interaction of HTF and adsorbent layer in presence of surface tension forces should be investigated in detail in future, using flow visualization and other relevant techniques to characterize the desorption stage phenomenon in the adsorbent layer. Nevertheless, the full process model does consider that due to a combined effect of surface tension forces and impurity removal from the adsorbent layer, the adsorbent layer is completely filled with liquid HTF at the end of the cooling stage, and this liquid must be removed, so that a fresh batch of impure gas can be sent for purification. Modeling techniques used to predict the time required for liquid HTF removal are discussed in a subsequent section.

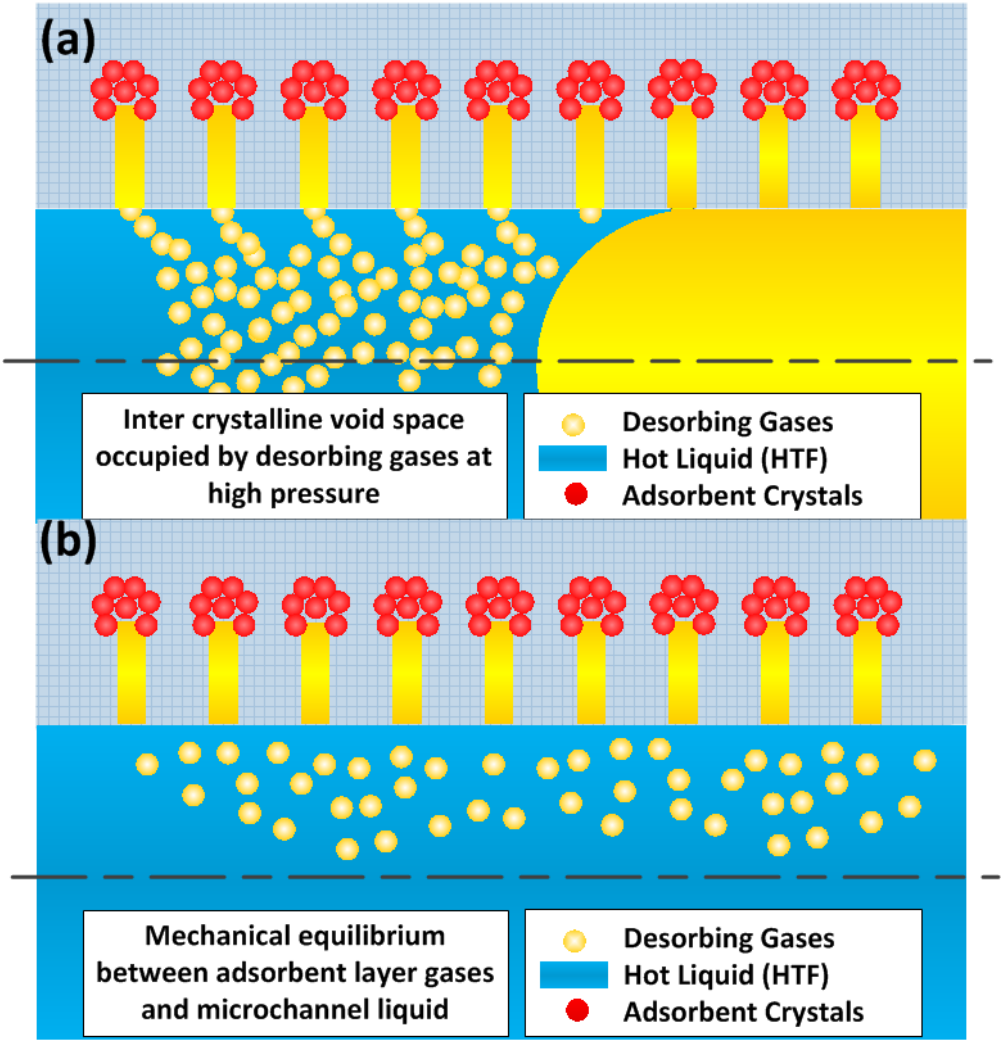

Figure 2.5. Illustration of (a) Initial convective diffusive flow and (b) subsequent slow diffusive flow

2.2.3 Desorption model

The heat and mass transfer models of the extended desorption stage are developed using the assumptions described above for displacement modeling. The desorption model is switched on after the hot HTF sweeps over the entire length of the microchannel. The conservation equations used for the desorption model consist only of the liquid part of the displacement equations because the displacement and desorption models are parts of the larger desorption process model. Additionally, the momentum equation is similar to

Equation (2.4) with appropriate substitutions for liquid phase material properties. Depending on the desired extent of contaminant removal, the desorption stage may be extended beyond the time required for the initial desorption or thermal wave, which is described in the displacement modeling section.

2.2.4 *Cooling stage model*

After the desorption process is complete, the adsorbent layer is brought to room temperature so that adsorbent particles can adsorb impurities again during the next feed gas cycle. Hence, cold HTF is passed through the microchannel. Species and energy equations used for the cooling model are identical to the equations used for the desorption stage. The only change in the equations involves an alteration of the boundary condition for the fluid temperature at the inlet.

2.2.5 *Purge stage model*

The purge stage involves the displacement of the cold HTF in the microchannel. The channel is effectively dried and prepared for the next adsorption stage. The initial liquid displacement modeling methodology is discussed in the previous sections. Once the gas-liquid interface reaches the channel outlet as the purge gas displaces the cold HTF, the purge stage model is activated. Because this stage of the cycle involves purified CH_4 flowing through the microchannel, the governing equations for heat and mass transfer and fluid flow are identical to Equations (2.3) through (2.9).

As a result of the expected re-adsorption of the desorbing gases during the cooling stage, loss of pressure in the void spaces is expected to facilitate the entry of the HTF into the void space. Removal of the HTF trapped in the void spaces is only possible via evaporation as it cannot be physically displaced. If the outer surface of the adsorbent

layer (i.e., the channel wall) were to permit mass transfer, application of a pressure difference across the inner and outer surface of the annular layer with a purge gas would have helped in removal of the liquid. Hence, for estimation of the time required for the HTF to evaporate, an independent kinetic model is developed in gPROMS^{TM}. It is assumed that HTF occupies the entire void space at the end of the cooling stage and the total mass of trapped HTF can be calculated using Equation (2.19). The concept of HTF evaporation in the adsorbent layer void space and vapor-liquid interface movement in the void spaces are illustrated schematically in Figure 2.6(a) and Figure 2.6(b), respectively.

$$M_{L,ini} = \varepsilon V_w \rho_L \tag{2.19}$$

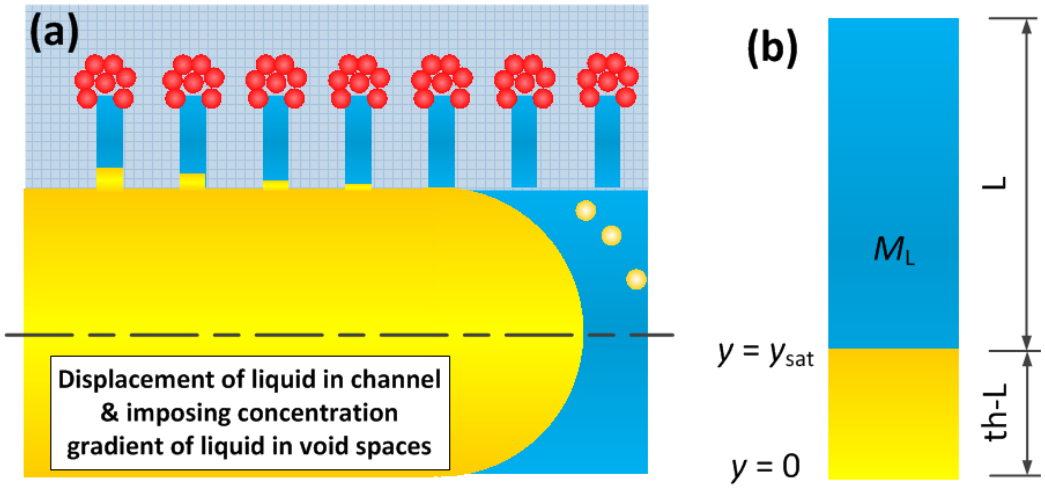

Figure 2.6. (a) Schematic representation of water evaporation as it is exposed to concentration gradient (b) Illustration of an instant in time during water removal

It is assumed that liquid and vapor phases of the HTF are in equilibrium at the interface. The mass fraction of HTF in gas at the vapor-liquid interface can be determined by ratio of the saturation pressure of HTF at the liquid temperature and the total gas pressure in the void space. The evaporated HTF at the interface is exposed to the concentration gradient as purge gas is assumed to contain negligible HTF vapor. Thus,

the rate of removal of evaporated HTF can be determined from Equation (2.20), which is a function of HTF diffusivity and tortuosity of the adsorbent layer.

$$\frac{dM_L}{dt} = -D_{eff,HTF-CH_4} \cdot A_s \cdot \rho_G \frac{dy}{\tau(th-l)} \tag{2.20}$$

With an initial condition of an HTF filled adsorbent layer, the kinetic model is simulated until the total mass of the HTF becomes zero. This kinetic model is also validated analytically as shown in Equation (2.21), where first order differential equation for mass conservation is solved by simple integration.

For the displacement of liquid, the clean displacement approach used for the displacement of gas is not valid, as Moore (2012) observed intermittent, annular and rivulet flow regimes, and in absence of liquid replenishment, these regimes are soon replaced by single-phase gas flow. Because the purge stage continues even after the theoretical time required for the displacement of liquid, this additional purge stage time is utilized to remove the HTF from both domains, the microchannel and the adsorbent layer. It is expected that at the end of the purge stage, not only the adsorbent layer, but also the microchannel flow region, is free of HTF. Furthermore, surface tension does not play an appreciable role during the purge stage, because drying of static liquid due to evaporation is merely dependent on how fast the evaporated liquid can be removed from the adsorbent layer via diffusion.

$$t_{purge} = \frac{(th)^2 \varepsilon\tau}{2D_{eff,HTF-CH_4}} \cdot \frac{\rho_L}{\rho_G} \tag{2.21}$$

2.2.6 *Sequential coupling and full process simulation methodology*

In the complete purification process model, the sub-models (*i.e.*, adsorption, displacement of gas by liquid, desorption, cooling, displacement of liquid by gas, and purge) are coupled sequentially as shown in Figure 2.4. A switching technique is used to activate the relevant governing equations during the transition from one stage to another. The governing heat and mass transfer equations are modified using the binary switches and equivalent resistances. Each stage is assigned a switch that assumes a value of either one or zero, depending on whether the stage is being simulated at that time or not. The overall microchannel domain species equation used for the full process simulation is shown in Equation (2.22), where *S* indicates the switch for a corresponding stage of the process. Similar treatment is given to the other conservation equations for the full process model.

$$\begin{aligned}&\frac{\partial C_{g,i}}{\partial t}+\frac{\partial\left(uC_{g,i}\right)}{\partial z}-\\&\begin{bmatrix}\left(S_{Ads}+S_{LDG}\cdot X_G+S_{GDL}\cdot X_G+S_{Purge}\right)D_{A,G,i}+\\\left(S_{LDG}\cdot X_L+S_{deso}+S_{Cool}+S_{GDL}\cdot X_L\right)D_{A,L,i}\end{bmatrix}\cdot\frac{\partial^2 C_{g,i}}{\partial z^2}+\\&\begin{bmatrix}\left(S_{Ads}+S_{LDG}\cdot X_G+S_{GDL}\cdot X_G+S_{Purge}\right)\dfrac{1}{\mathrm{R}_{eq,Mass,G,i}}+\\\left(S_{LDG}\cdot X_L+S_{deso}+S_{Cool}+S_{GDL}\cdot X_L\right)\dfrac{1}{\mathrm{R}_{eq,Mass,L,i}}\end{bmatrix}\cdot\frac{\left(C_{g,i}-C_{w,i}\right)}{A_g}=0\end{aligned}\tag{2.22}$$

The momentum equation, however, assumes the form shown in Equation (2.23), due to different approaches adapted for single-phase (adsorption, desorption, cooling, and purge) and two-phase flows (displacement of gas and displacement of liquid) to calculate the fluid velocity in the microchannel.

$$
\begin{aligned}
-\frac{\partial P}{\partial z} &= \left(S_{ads} + S_{purge} + S_{deso} + S_{cool}\right) \\
&\left(\begin{array}{l}
\rho\dfrac{\partial u}{\partial t} + \rho u\dfrac{\partial u}{\partial z} - \\
\displaystyle\sum_i \frac{C_{g,i} - C_{w,i}}{A_{cs}\cdot \mathrm{R}_{eq,Mass,i}} u - \mu\frac{\partial^2 u}{\partial z^2} + f\frac{\rho u^2}{2D_h}
\end{array}\right) \\
&+\left(S_{LDG}\right)\left[\begin{array}{l}
\left(f_L\dfrac{\rho_L u^2}{2D_h} + \rho_L\dfrac{du}{dt}\right) z_{IF} + \\
\left(f_G\dfrac{\rho_G u^2}{2D_h} + \rho_G\dfrac{du}{dt}\right)\left(L - z_{IF}\right)
\end{array}\right] \\
&+\left(S_{GDL}\right)\left[\begin{array}{l}
\left(f_L\dfrac{\rho_L u^2}{2D_h} + \rho_L\dfrac{du}{dt}\right)\left(L - z_{IF}\right) + \\
\left(f_G\dfrac{\rho_G u^2}{2D_h} + \rho_G\dfrac{du}{dt}\right)\left(z_{IF}\right)
\end{array}\right]
\end{aligned}
\tag{2.23}
$$

The full process model is simulated with an implicit first-order backward differencing scheme in gPROMS™ by controlling the binary switches explicitly. The stages are simulated ensuring that the grid size mentioned in Table 2.1 results in a grid Peclet number of 0.13, which is much lower than the maximum acceptable limit of two to achieve numerical stability. Hybrid differencing techniques can be employed; however, the additional penalty on the calculation time and simulation failures must be addressed. Additionally, gPROMS™ ModelBuilder offers backward, forward, and central differencing options and hybrid differencing is observed to create computational instabilities in the solution procedure, as the transient built-in solvers are used to solve the differential equations. Appendix C shows detailed sample calculations for a sample data point during the simulation of the overall process in a cyclic steady state.

In the full process model, the execution times for each of these stages are specified. The times required for each stage are calculated using parametric studies, in which important variables for the considered stage are monitored. Table 2.2 shows the

criteria for monitored variables during each stage used for determining the stage times for satisfactory performance of the purification cycle. The adsorption stage is continued until the adsorption wave front reaches the axial midpoint of the microchannel so that, as the HTF stream replaces the feed gas stream at the inlet, the feed gas in the upstream half of the microchannel is adsorbed in the downstream half of the adsorbent layer as the displacement is continued, maximizing product purity and recovery. While the displacement times are calculated based on when the gas-liquid interface reaches the outlet, the desorption stage time depends largely on the magnitude of T_{deso} and is discussed in detail in later sections. The cooling stage time is the time required for the HTF to leave the microchannel at 25°C, which is the inlet HTF temperature. The purge stage time is calculated separately as discussed earlier, and the purge stage is simply simulated for the corresponding time with the purified product being recirculated, without explicitly modeling the HTF leaving the adsorbent layer.

Table 2.2. Purification cycle simulation criteria and monitored variables.

Stage	**Monitored variable and imposed constraint**
Adsorption	$C_{A,CO2} = C_{A,CO2,Max}$ for z ~ 0.5
Displacement of gas	$z_{IF} \leq L$
Desorption	Depends on T_{deso}
Cooling	$T_{g,L} = 25°C$
Displacement of liquid	$z_{IF} \leq L$
Purge	$M_{HTF}=0$

2.2.7 Microchannel boundary and initial conditions

The microchannel inlet is exposed to different species and temperature boundary conditions during the execution of each stage. Table 2.3 lists the boundary conditions at the channel inlet and outlet. The adsorbent microchannel is assumed to be filled with purified CH_4 at T_0 at the start of the process. The mixing header models are not integrated

with the full process model and it is assumed that the requisite species and the temperature values are available at the channel inlet as needed by the corresponding stage. A hypothetical model for valves, with a valve time constant, C_T, of 0.1 s, is inserted in the boundary conditions equation as shown in Equation (2.24), to avoid simulation failures due to a sudden change of equations. The solenoid valve used in the experimental set-up by Moore *et al.* (2016), is found to have a response time of 0.04 s, substantiating the value chosen here for C_T.

$$\frac{d\left(BC\right)_{Actual}}{dt} = \frac{1}{C_T}\left(BC_{Assigned} - BC_{Actual}\right) \tag{2.24}$$

Table 2.3. Boundary Conditions for the microchannel species and energy equations.

Stage of the cycle	BC - channel Inlet	BC - channel Outlet
Adsorption	$y_i\big\|_{z=0} = y_{i,\,feed}$ $T_g\big\|_{z=0} = T_0$	
Displacement of gas and Desorption	$C_{g,i}\big\|_{z=0} = [10^{-2}, 10^{-2}]$ $T_g\big\|_{z=0} = T_{deso}$	$\left.\frac{\partial C_{g,i}}{\partial z}\right\|_{z=L} = 0$
Cooling	$C_{g,i}\big\|_{z=0} = [10^{-2}, 10^{-2}]$ $T_g\big\|_{z=0} = T_0$	$\left.\frac{\partial T_g}{\partial z}\right\|_{z=L} = 0$
Displacement of liquid and Purge	$y_i\big\|_{z=0} = y_{i,\mathrm{Prod}}$ $T_g\big\|_{z=0} = T_0$	

2.2.8 Product purity and yield

The performance indicators for the entire purification process are the bulk methane purity and the methane yield per unit adsorbent mass. These parameters are monitored to evaluate the process performance and to provide a platform for comparison with other existing purification technologies. Equations used to determine the product

yield and mass and mole based product compositions are shown in Equation (2.25) through (2.27).

$$\frac{\partial \overline{M}_i}{\partial t} = \frac{A_g \cdot u \cdot C_{g,i}\Big|_{z=L}}{\rho_{ads} \omega V_w} \tag{2.25}$$

$$Purity_{kg,i} = \frac{\overline{M}_i}{\sum_i \overline{M}_i} \tag{2.26}$$

$$Purity_{mole,i} = \frac{\left(Purity_{kg,i} \Big/ MW_i \right)}{\sum_i \left(Purity_{kg,i} \Big/ MW_i \right)} \tag{2.27}$$

2.3 Optimization of geometry and material selection

2.3.1 Adsorbent microchannel geometry

The appropriate adsorbent microchannel geometry is selected using a parametric study on the microchannel diameter and the adsorbent layer thickness. The microchannel length is kept constant at 1 m, while the binder that holds the adsorbent to form a hollow adsorbent layer is assumed to be made of poly (ether imide) (PEI) (Mark, 1999), which can resist temperatures of up to 482°C. Another reason for selection of PEI is its high glass transition temperature (up to 216°C (Mark, 1999)) and the use of a brittle and glassy polymer eliminates its own resistances to gas flow due to moving linkages, unlike rubbery polymers such as PDMS. Therefore, macroscopic gas diffusion equations based on the Chapman-Enskog theory (or the Knudsen diffusion approach, if applicable) suffice for the calculation of the effective diffusion coefficient used in Equation (2.1) (Cussler, 1997).

The adsorbent material considered for the simulation of this parametric study is silicalite, while the HTF compatible with the adsorbent is water. The adsorbent-HTF pair is selected in such a way that the HTF interacts with the adsorbent only thermally, thereby maximizing the amount of gas adsorbed.

The Langmuir equation is used for calculating the competitive adsorption isotherms for CH_4 and CO_2 in the silicalite adsorbent as shown in Equation (2.28) along with temperature dependence shown in Equation (2.29). Auxiliary parameters and coefficients used in these equations are listed in Table 2.4.

$$C_{A,Eq,i} = \rho_{ads}\left(M_{B,i}\frac{B_i \cdot P_i}{1+\sum_i B_i \cdot P_i}\right) \tag{2.28}$$

$$B_i = b_{0i}e^{\left(\frac{-Q_{B,i}}{RT_w}\right)} \tag{2.29}$$

Table 2.4. Coefficients for the Langmuir equations with competitive adsorption (Babarao *et al.*, 2007; Lee, 2007)

Factor	CH_4	CO_2
M_B, mol kg^{-1}	3.918	4.161
b_0, kPa^{-1}	4.15×10^{-7}	4.506×10^{-7}
Q_B, J mol^{-1}	20000	25400
$D_{crystal,1}$, m^2 s^{-}	1.5×10^{-8}	5.3×10^{-9}
$\rho_{ads,}$ kg m^{-3}	1793	
r, m	10^{-6}	

To model the microporous diffusion and account for intra-crystalline diffusivity, the LDF constant shown in Equation (2.30) is used. This constant, K_{LDF}, is then used in the linear driving force equation, Equation (2.31), to determine the instantaneous rate of adsorption.

$$K_{LDF,i} = \frac{15 \cdot D_{crystal,i}}{r^2} \tag{2.30}$$

$$\frac{\partial C_{A,i}}{\partial t} = K_{LDF,i} \cdot \left(C_{A,Eq,i} - C_{A,i} \right) \tag{2.31}$$

The parametric study on microchannel geometry is performed in two parts. First, the adsorbent layer thickness is kept constant at 30 μm and the microchannel diameter is varied from 150 to 530 μm.

The full process is simulated with the adsorption stage running until the product purity in the product sink drops below 99%, and with a desorption stage time of 20 s. Figure 2.7 shows the effect of microchannel diameter on the time required to saturate the adsorbent layer and subsequently, the time required for removal of CO_2 from the adsorbent layer. For the smallest D_h of 150 μm considered in the present study, it takes nearly 4 s for the feed CO_2 to saturate the adsorbent as a result of low feed mass flow rate. As the diameter increases, the mass flow rate of the feed gas increases, therefore the time required for saturation of the adsorbent layer decreases. The convective heat and mass transfer coefficients from the fluid to the adsorbent layer surface decrease as D_h is increased. This decrease impedes the heat and mass transfer into and out of the adsorbent layer marginally. However, this higher convective resistance is compensated for by the higher mass flow rate possible at the larger diameter. Furthermore, increased heat and mass transfer resistances with increased diameter would only have been a critical factor if Peclet numbers (Pe) were of the order of one. The three possible outcomes that are possible with variation of D_h on relative effects of convection through the microchannel and radial diffusion of heat and species are (a) high heat and mass transfer coefficients but with low mass flow rates, resulting in quick heat and mass transfer to and from the

adsorbent layer with longer stage times (b) moderate heat and mass transfer coefficients at moderately long stage times (c) low heat and mass transfer coefficients but with shorter stage times. Although the present parametric study does not attempt to determine the microchannel geometry for the trade-off between convection and diffusion, it accounts for additional effects, including microporous diffusion and adsorption, to analyze the overall adsorption stage performance. This parametric study focuses on the ability to achieve separation while maintaining a sharp adsorption and thermal wavefront by using the considered geometry within controllable and short stage times. For the adsorption stage with a D_h of 530 µm, heat and mass transfer Pe values are 8193 and 8243, respectively. This clearly indicates that fluid flow in the microchannel considered in the present work is inertia-dominated and marginal changes in the heat and mass transfer resistances, as a result of change in diameter, do not affect the overall adsorption stage performance in terms of purity and product collection. For a diameter of 530 µm, it takes no more than 0.3 s for the adsorbent layer to saturate as seen in Figure 2.7(a).

The adsorbed concentration curves during desorption provide more insight into the effectiveness of adsorption swing with the present concept. As shown in Figure 2.7(b), for the smallest D_h of 150 µm, the velocity of hot water during desorption is small, resulting in a slower heating of the adsorbent layer and a slower CO_2 removal. The CO_2 removal rate is very small; hence, the hot water supply should be continued for a reasonable swing capacity of the adsorbent layer. This results in an increased cycle time and energy requirement. For a D_h of 530 µm, the mass flow rate of hot water through the microchannel is the highest between the cases considered; hence, the adsorbed concentration of CO_2 rises quickly to the maximum CO_2 concentration during adsorption

in 0.3 s and the entire adsorbent layer is nearly regenerated in about 6 s. It should be noted that the maximum CO_2 adsorbed concentration for all the cases is similar, which shows equal adsorbent layer utilization, regardless of the diameter.

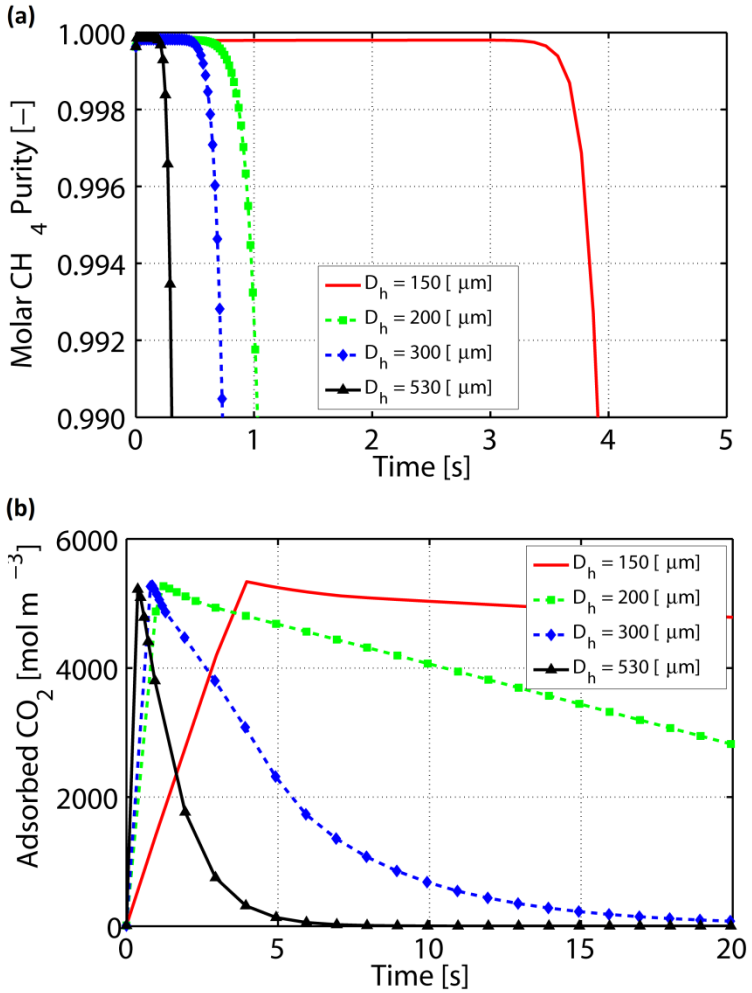

Figure 2.7. Effect of variation of microchannel diameter on (a) product purity and (b) CO_2 adsorbed concentration for a constant adsorbent layer thickness of 30 µm.

Table 2.5 shows the mass of product collected normalized with the adsorbent mass during the adsorption stage for the range of D_h considered. As the diameter increases, the product mass collected increases more sharply than the increase in the

adsorbent mass. Hence, increase in diameter has a favorable effect on the process performance and a diameter of 530 µm is considered for further analysis.

Table 2.5. Effect of microchannel diameter on adsorption stage performance

th **[µm]**	D_h **[µm]**	$V_w \times 10^{-8}$ **[m^3]**	$M_{ads} \times 10^{-6}$ **[kg]**	$M_{prod} \times 10^{-6}$ **[kg]**	M_{prod} **[kg kg^{-1}]**
30	150	1.13	3.18	1.66	0.52
	200	1.60	4.51	2.45	0.54
	300	2.54	7.17	4.63	0.64
	530	4.71	13.3	11.7	0.88

To analyze the effect of adsorbent layer thickness, *th*, on process performance, D_h is fixed at 530 µm, while *th* is varied from 15 to 120 µm. Figure 2.8 shows the results from this parametric study. For a constant D_h, increase in *th* does not add any benefit to the adsorption stage performance. The product purity starts dropping at nearly same time just after 0.2 s; however, at different rates for different *th* values, as seen in Figure 2.8(a). For the thinnest adsorbent layer, the adsorbent layer saturates quickly within 0.2 s, while the CO_2 adsorbed concentration in the adsorbent layer reaches the highest possible value analogous to the cases shown in Figure 2.8(b). However, as *th* increases, the feed gas wave front tends to reach the microchannel outlet without completely filling the adsorbent layer. For the thickest adsorbent layer with a *th* of 120 µm, 34% of the adsorbent layer remains unused as seen in Figure 2.8(b). The dispersed nature of the adsorption wave for thick adsorbent layer is in agreement with the previous experimental findings for the hollow fibers in the literature (Lively *et al.*, 2011; Lively *et al.*, 2012).

Additionally, the desorption stage performance with a thick adsorbent layer deteriorates due to an increased mass transfer resistance to the desorbing gases. While the entire adsorbent layer can be saturated and regenerated within 4 s for a *th* of 15 µm, even

a partly filled 120 μm thick adsorbent layer cannot be regenerated within 20 s as seen in Figure 2.8(b). Such behavior can be attributed to the convection-based design in the present study, where the diffusion in the adsorbent layer in the radial direction must be fast enough to match the feed gas convection in the axial direction in the microchannel. Thinner adsorbent layers can exhibit such behavior, as a result of lower mass transfer resistance within the adsorbent layer. It is found that mass transfer resistance through the adsorbent layer is up to ten times greater than the convection mass transfer resistance at the adsorbent layer wall. Therefore, employing a thin adsorbent layer reduces the overall mass transfer resistance by a significant margin. For thick adsorbent layers, diffusion in the adsorbent layer lags convection in the microchannel, contaminating the product before saturating the adsorbent layer. The reduced slope of the purity curve for a *th* of 120 μm, as shown in Figure 2.8(a), indicates that CO_2 starts to enter the outlet stream after 0.4 s, while the adsorbent layer is not saturated with CO_2 entirely; and even after 1.5 s, only 66% of the adsorbent layer is filled with CO_2. For thinner adsorbent layers, the time required for adsorbent layer saturation matches the time required for the fluid breakthrough of CO_2 closely. For useful operation of this cycle, the cycle times should therefore be based on convection time scales and not diffusion time scales.

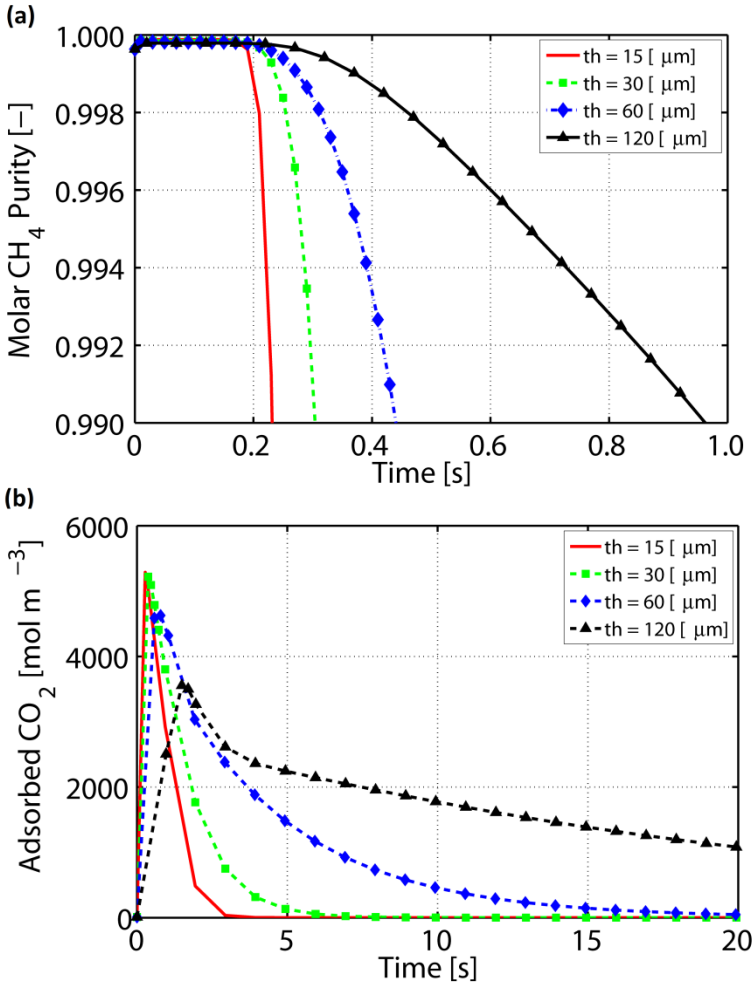

Figure 2.8. Effect of variation of adsorbent layer thickness on (a) product purity and (b) CO_2 adsorbed concentration for a constant diameter of 530 µm.

Although the adsorption and desorption processes are quickest for the 15 µm case, a *th* of 30 µm is selected for further analysis, to enable slightly better process control. Also, it can be seen from Table 2.6 that for a *th* of 30 µm, the absolute product collected is higher than that with a *th* of 15 µm, because of a higher separation capacity. A *th* of 60 µm yields the highest absolute product; however, the desorption time as shown in Figure 2.8(b), exceeds 20 s. For a T_{deso} of 200°C, the regeneration ability stays above 95% as seen in Figure 2.8(b), even when the desorption stage is terminated after 4 s. As *th* increases, the actual product collection saturates, while the adsorbent mass increases

proportionally. Therefore, the normalized product collected during the adsorption stage decreases as *th* increases.

From a process standpoint, choosing a greater D_h and a thinner adsorbent layer results in shorter cycle times. For example, with a D_h of 200 μm and *th* of 100 μm, the total cycle time is estimated to be 2225 s, compared to 203 s with a D_h of 530 μm and *th* of 30 μm, as illustrated later. This enhanced performance is attributed to large mass flow rates through a large microchannel, and to reduced mass transfer resistances through a thin adsorbent layer. It must be noted that this optimization is based on the mass of purified product, whereas the optimization for energy requirement is addressed in a later section.

Table 2.6. Effect of adsorbent layer thickness on adsorption stage performance

D_h [μm]	*th* [μm]	$V_w \times 10^{-8}$ [m^3]	$M_{ads} \times 10^{-6}$ [kg]	$M_{prod} \times 10^{-6}$ [kg]	M_{prod} [kg kg^{-1}]
530	15	2.43	6.83	10.3	1.51
	30	4.71	13.3	11.7	0.88
	60	8.86	24.9	12.3	0.49
	120	1.55	43.5	12.3	0.28

2.3.2 Adsorbent and HTF material selection

The appropriate adsorbent material and HTF are selected based on another parametric study to assess the feasibility of adsorbent-HTF pairs. The full process performance observed with the use of silicalite – water is compared against that of the zeolite 5A – polyalphaolefin (PAO) pair.

Zeolite 5A has a higher selectivity for CO_2 compared to silicalite as shown in Figure 2.9, which shows the competitive adsorption isotherms for zeolite 5A and silicalite for a CH_4-CO_2 mixture (70/30). The dual-site Langmuir equation (DSL) for modeling the

isotherms for zeolite 5A, along with its auxiliary parameters, is explained in Pahinkar *et al.* (2015), and is adapted from Gholami *et al.* (2010).

More favorable isotherms for zeolite 5A at 25°C result in greater adsorption capacity at low CO_2 partial pressures and faster adsorption. This advantage of using zeolite 5A as an adsorbent can only materialize if the HTF does not interfere with CO_2 adsorption. As zeolite 5A has a high affinity for water (Gholami and Talaie, 2009), its use as the HTF adversely affects the adsorption and desorption of CO_2. Therefore, PAO, which has a large molecule size compared to water and CO_2 and does not interfere with CO_2 adsorption, is chosen as the HTF for the zeolite 5A case. Although zeolite 5A has a high capacity for CO_2 that remains constant for a large range of partial pressures, it cannot rely on merely temperature swing for a reasonable adsorbent swing capacity, as seen in Figure 2.9.

Silicalite, on the other hand shows reduced selectivity, as seen in the slope of the capacity curve at zero partial pressure; however, it has a comparable adsorption capacity to that of zeolite 5A. Silicalite is also found to show better response to temperature swing in terms of increased adsorbent swing capacity. Due to negligible water adsorption capacity of silicalite, water can be used as the HTF to heat and cool the adsorbent layer. The full process simulation using this pair is demonstrated in the previous section, where the use of the silicalite–water pair was shown to drive the selection of the appropriate geometry for adsorbent-coated microchannels.

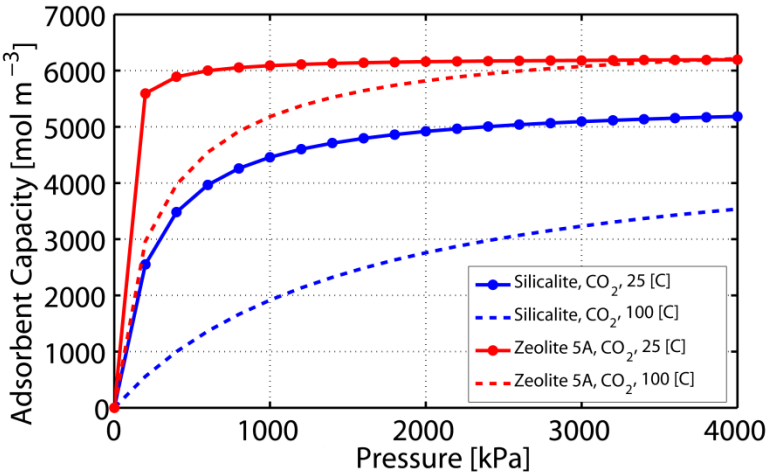

Figure 2.9 Competitive adsorption isotherms for zeolite 5A and silicalite at 25°C and 100°C for CH_4-CO_2 gas mixture (70/30 by mole)

Table 2.7 shows the comparison of the material properties of water and HTF at 25°C and 100°C. It should be noted that the desorption temperature selected for this parametric study is 100°C, considering the safety concerns regarding use of an organic flammable liquid at higher temperatures.

It can be seen that the viscosity of PAO is at least an order of magnitude greater than that of water, which impedes HTF flow during the desorption and cooling stages.

Table 2.7. Comparison of properties of water and PAO (Process Systems Enterprise, 1997-2015; Chevron, 2008)

Property	PAO, 25°C	PAO, 100°C	Water, 25°C	Water, 100°C
μ, kg m^{-1} s^{-1}	7.7×10^{-3}	1.9×10^{-3}	8.9×10^{-4}	2.82×10^{-4}
c_p, J kg^{-1} K^{-1}	2208	2468	4180	4580
k, W m^{-1} K^{-1}	0.154	0.143	0.590	0.670
ρ, kg m^{-3}	808	719	997	958
Pr	110	33	6.18	1.92
σ, Å	45.0		2.64	
MW, g mole^{-1}	336		18	
p_{sat}, kPa	0.133		3.16	
$D_{eff,HTF-CH4}$, m^2 s^{-1}	1.37×10^{-9}		1.05×10^{-7}	

The full process is simulated with the methodology discussed in the previous sections and the two adsorbent-HTF pairs. Based on the extent of completion of each stage, the stage times for both the scenarios are estimated and listed in Table 2.8 with Figure 2.10 showing the overall cycle performance in terms of the adsorbent capacity for CH_4 and CO_2. The adsorption, desorption, cooling and purge stages are marked by the numbers 1, 2, 3, and 4, respectively.

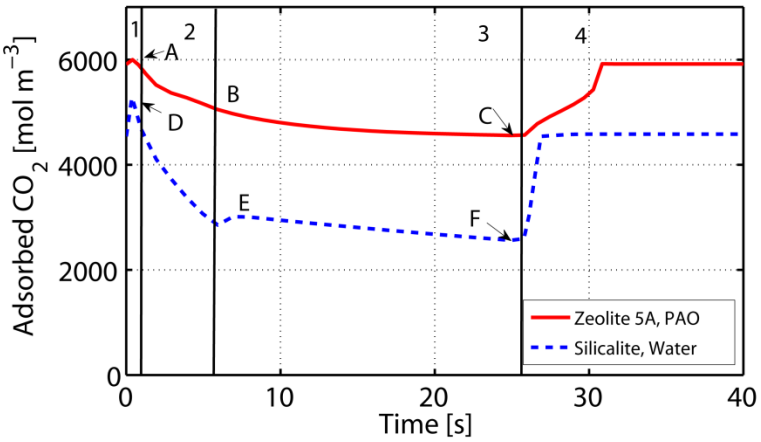

Figure 2.10. Cyclic CO_2 adsorbed concentration with silicalite – water and zeolite 5A – PAO pairs

The adsorption stage times for both the pairs are comparable and are dependent on the adsorbent swing capacity for silicalite and zeolite 5A. It should be noted that the adsorbed CO_2 after the purge stage is already high, because of the high CO_2 mole fraction in the product, and the purge stage in fact involves purification of the product gas. Therefore, enough CO_2 from the feed stage cannot be accommodated in the adsorbent layer, especially in zeolite 5A. This is attributed to the reduced operating capacity at a reduced temperature swing of 75°C. At the end of the adsorption stage, the CO_2 adsorbed concentrations for zeolite 5A and silicalite rise from the equilibrium desorbed values at the start to the values at A and D, respectively.

Table 2.8. Comparison of stage times with silicalite-water and zeolite 5A – PAO for a temperature swing of 75°C

Stage	Zeolite 5A - PAO	Silicalite - Water
Adsorption [s]	0.16	0.19
Displacement of gas [s]	1.40	0.55
Desorption [s]	5.00	5.00
Cooling [s]	23.00	3.00
Displacement of liquid [s]	5.00	0.70
Purge [s]	320400	195.00
Total time [s]	**320434.56**	**204.44**

The desorption stage time is kept constant at 5 s for both the HTFs to assess desorption effectiveness. The desorption stage time with silicalite-water pair with T_{deso} of 200°C discussed in the previous section is 4 s with a 95% regeneration. However, the desorption stage time with T_{deso} of 100°C should be higher than 5.5 s. As shown in Figure 2.11(a), water is able to raise the temperature of the adsorbent layer within 3 s, while the temperature rise with PAO is slower and not all the axial locations reach 100°C after 5 s.

As mentioned before, the high viscosity of PAO limits its mass flow rate through the microchannel. Therefore, rate of energy input into or removal from the microchannel is significantly lower, in turn decreasing the rate of heating or cooling of the adsorbent layer. Therefore, the rate of decrease in CO_2 adsorbed concentration with PAO is smaller than that with water. The CO_2 concentrations at the end of the desorption stage are depicted as points B and E, respectively, for zeolite 5A and silicalite. The cooling stage time, which is primarily dependent on heat transfer from the adsorbent layer to the HTF, is affected adversely by the high viscosity of PAO, as shown in Figure 2.11(b). It takes more than 23 s for PAO to cool the adsorbent layer to 25°C, while water does so in only 3 s. Because the Reynolds number during the cooling stage does not exceed 5, heat transfer coefficients for this laminar flow also remain small (1326 W m^{-2} K^{-1}) due to the low thermal conductivity of PAO. The corresponding heat transfer coefficient for the flow of water during the cooling stage is 6215 W m^{-2} K^{-1}. The final values of adsorbed CO_2 at the end of the cooling stages are depicted by points C and F for the zeolite 5A and silicalite cases, respectively. The adsorbent swing capacities for the zeolite 5A–PAO and silicalite–water pairs for a temperature swing of 75°C are then calculated as the vertical distances between A and C, and D and F in Figure 2.10, which are 1450 and 2650 mol m^{-3}, respectively.

Additional problems arise during the displacement of liquid and purge stages with PAO as the HTF. Not only does it take longer to be displaced from the microchannel compared to water, but it also takes an unreasonable amount of time to be removed from the adsorbent layer. These results are due to the low volatility of PAO (one order of magnitude lower than water) and diffusion coefficient (two orders of magnitude lower

than water) as a result of greater molecular weight. Hence, once PAO enters the adsorbent layer void spaces during desorption and the cooling stage as a result of adsorbed CO_2 removal, it cannot be practically removed as seen from the purge stage time values shown in Table 2.8.

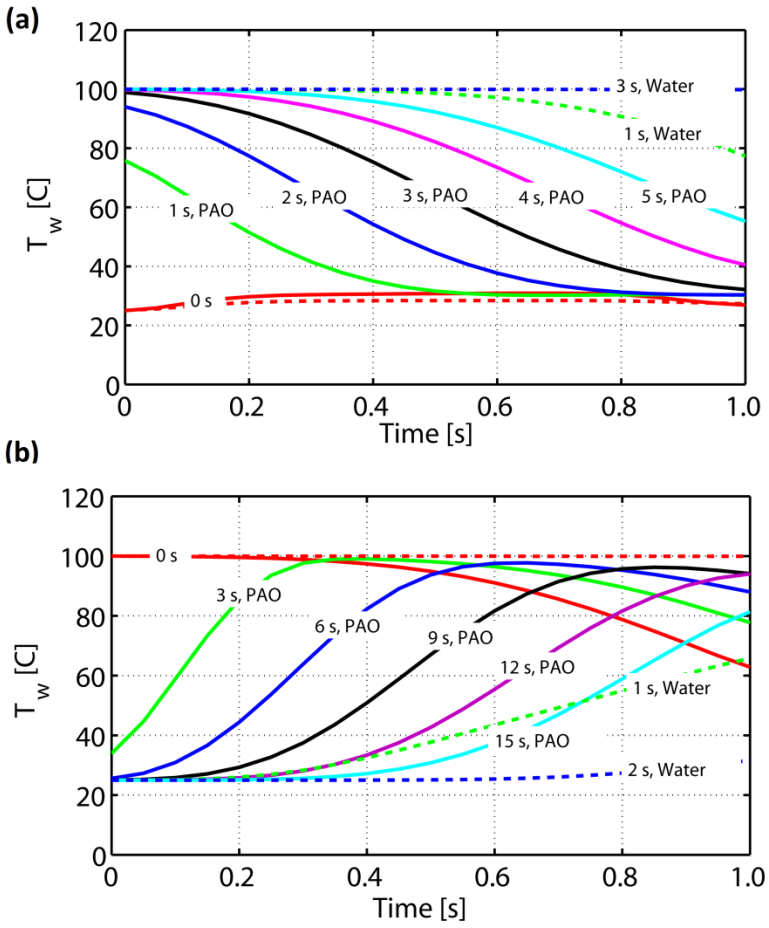

Figure 2.11. Variation of adsorbent layer temperature during (a) desorption (b) cooling with PAO and water as HTFs

Water, on the other hand, not only flows through the microchannel rapidly with high heat and mass transfer coefficients, thereby improving process effectiveness, but also offers smaller resistance to evaporation and diffusion through the adsorbent layer. It

takes 195 s for the adsorbent layer to be free of water and ready for the next feed stage as seen in Table 2.8.

Therefore, due to a higher adsorption swing capacity and regeneration ability of silicalite and the excellent heat and mass transfer characteristics of water as the HTF, the silicalite–water pair is selected for further analysis.

2.4 Results

Once the adsorbent microchannel geometry and the adsorbent–HTF pair is selected, the full process is simulated using the key parameters listed in Table 2.1. The final stage times selected for the process simulation are shown in Table 2.9. Because T_{deso} selected for the optimized version of the full process simulation is 200°C, the displacement of gas and desorption stage patterns for CO_2 average adsorbed concentrations follow the trend shown in Figure 2.7(b). The stage times then differ from those shown in Table 2.8, due to reduced viscosity of water at 200°C compared to that at 100°C (55% decrease), in turn increasing the velocity. Therefore, the displacement of gas at 200°C is faster by 5% than at 100°C, and a 4 s desorption stage results in 95% regeneration ability as seen in Figure 2.7(b).

This section explains the adsorbent layer and the microchannel heat and mass transfer kinetics in a cyclic steady state, and discusses the transient variation in the adsorbed and gaseous concentrations for both CH_4 and CO_2 through the various stages.

Table 2.9. Final stage times and total cycle time selected for the full process simulation

Stage	Time [s]
Adsorption [s]	0.19
Displacement of gas [s]	0.52
Desorption [s]	4.00
Cooling [s]	3.00
Displacement of liquid [s]	0.70
Purge [s]	195.00
Total time [s]	**203.41**

Figure 2.12(a) shows the adsorbed concentration of CH_4 and CO_2 during the adsorption stage. It can be seen that the CH_4 concentration in the adsorbent layer decreases as the adsorption wave front progresses. CO_2, on the other hand, diffuses and is adsorbed as it travels through the channel. The feed gas supply is stopped at 0.19 s to prevent contamination of the collected product. It should be noted that the adsorption stage duration affects the CH_4 yield and purity. More advanced control of the supply and collection times should yield a broad spectrum of product purity to meet varying end use requirements.

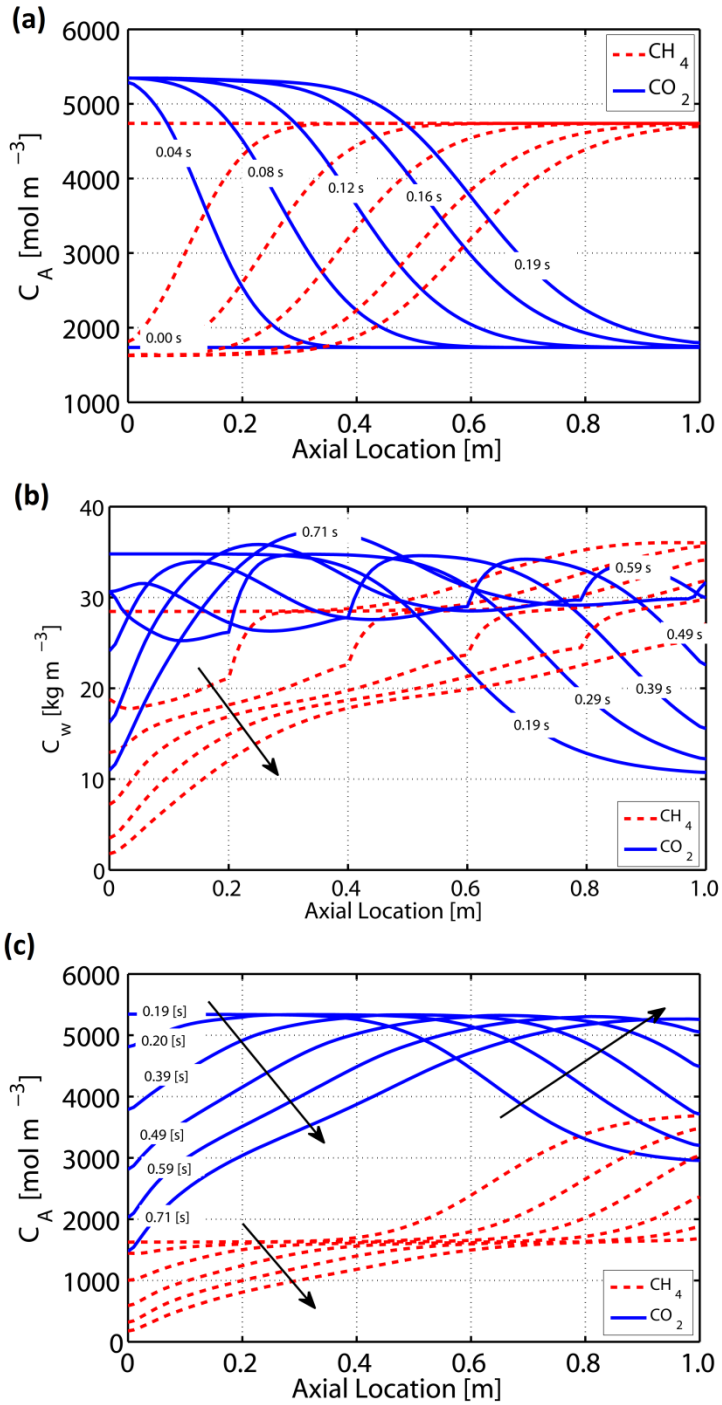

Figure 2.12. (a) Adsorbed concentrations in the adsorbent layer during the adsorption stage (b) Component gas densities during displacement of gas (c) Adsorbed concentrations during displacement of gas

Figure 2.12(b) shows the density of trapped gases in the adsorbent layer during the displacement of gas by liquid. The initial reduction of CO_2 density as a result of convective-diffusive flow can be seen over the duration of the displacement stage. As the

adsorbent is heated to the desorption temperature, more gaseous CO_2 accumulates in the void spaces and increases the total pressure, aiding quick removal of the gases. A wave of rising CO_2 pressure can be observed in Figure 2.12(b) in the form of a distinct concentration peak followed by a rapid loss of mass in upstream regions. CH_4 density, however, falls rapidly without any local peaks as the amount of CH_4 adsorbed in the previous stage is small compared to that of CO_2. Figure 2.12(c), which shows the corresponding adsorbed concentrations, indicates a continuous decrease in the adsorbed concentrations of both gases. It is also interesting to note that the residual feed gas gets adsorbed into the adsorbent downstream while the desorption process has started in the upstream adsorbent as a result of selection of premature termination of feed to prevent product contamination.

Figure 2.13(a) shows the progress of gas removal from the adsorbent layer during the extended desorption stage. The CO_2 desorption wave in the form of a gas density peak, which initiates with the start of the displacement stage and reaches the axial midpoint of the microchannel at 0.71 s, reaches the outlet in about the next 0.5 s. Continued decrease in both gas densities is seen as a result of slow diffusive flow afterwards, which is a result of the change in the mode of mass transfer from advective-diffusive to diffusive. As the desorption stage concludes at 4.71 s, CH_4 density in the adsorbent layer is negligible, while CO_2 density remains below 5% of the initial value at the start of desorption. Similar patterns are observed for the adsorbed concentration graph shown in Figure 2.13(b). The adsorbed concentration levels of both the component gases fall uniformly as a result of desorption from the adsorbent pores and removal from the void spaces through diffusion. The residual adsorbed concentration of CO_2 at the end of

the desorption stage remains below 5% of the maximum CO_2 adsorption capacity of silicalite.

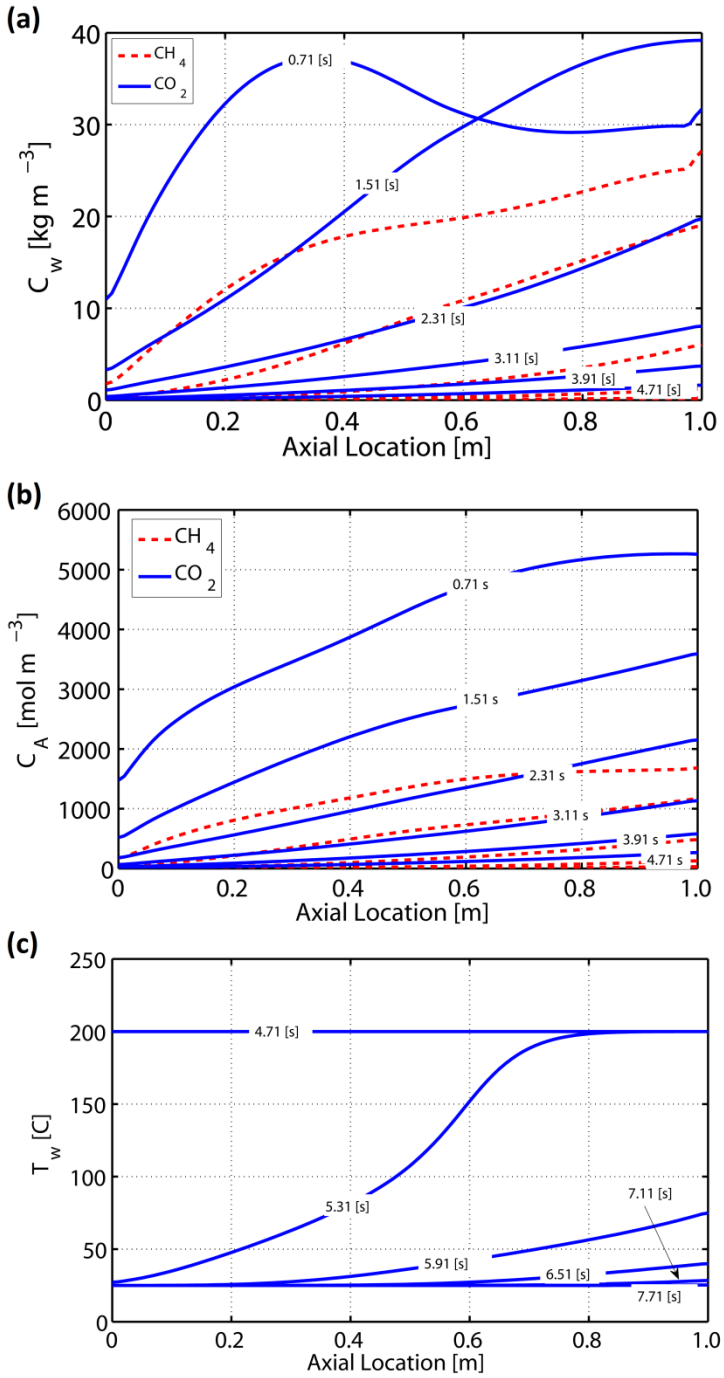

Figure 2.13. (a) Component gas densities in the adsorbent layer and (b) Adsorbed concentrations during extended desorption (c) Axial temperature variation during cooling stage showing rapid thermal wave

As the desorption process concludes, the hot water supply at the microchannel inlet is replaced by a cold water supply. However, the reduction in temperature causes silicalite to adsorb gases trapped at the end of desorption stage and increase the adsorbed CO_2 concentration by a small margin. Figure 2.13(c) shows the temperature variation of the adsorbent layer during the cooling stage. It takes approximately 3 s for water to cool the entire adsorbent layer to 25°C from 200°C. Due to small thermal mass of the adsorbent layer and fused silica monolith wall, the cooling thermal wave breakthrough occurs nearly at the same instant as the cooling fluid breakthrough.

Figure 2.14 shows the progress of water removal from the adsorbent layer as a result of evaporation. As water is removed, the gases in the purge stream diffuse and adsorb into the adsorbent, and the process is highly dependent on localized resistance offered by the remnant water in the void spaces. However, an overall estimate of the time when the adsorbent layer is free of liquid water can be acquired from Figure 2.14. This time estimate also covers the time required for drying the water films existing on the microchannel walls at the end of displacement of liquid, documented by Moore *et al.* (2016). After the liquid evaporation is complete, the adsorbed concentrations of species in the adsorbent layer are assumed to have reached the equilibrium concentration level, corresponding to the product tank mole fractions; and the process may be followed by sending a fresh batch of feed gases through the microchannels for purification, continuing the cycle.

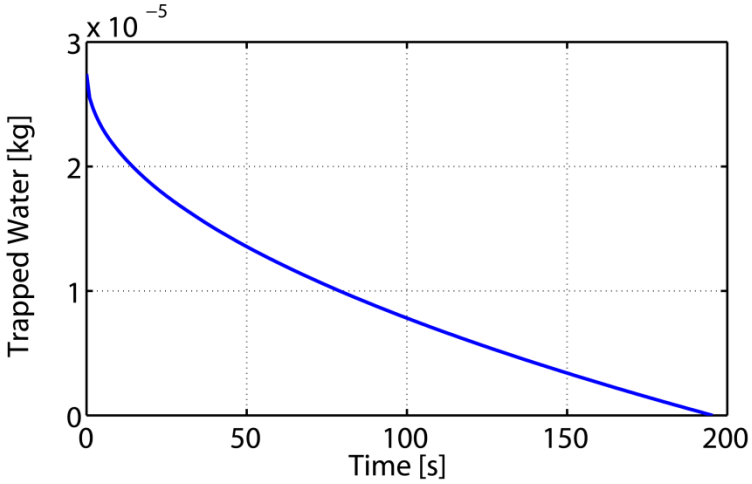

Figure 2.14. Progress of liquid water removal from the adsorbent layer

The integrated adsorbed concentration of CO_2 in the adsorbent layer varies over two entire cycles as shown in Figure 2.15. Two consecutive cycles are considered to explain the cyclic steady state of the process with the operating capacity of the adsorbent ranging from point A to C. A partial increase in adsorbed CO_2 concentration during the purge stage results in purification of product gas (up to point B) without any feed, while a further increase in adsorbed concentration is observed during the feed/adsorption stage as more CO_2 enters the microchannel for separation (up to point C). An insignificant re-adsorption of trapped CO_2 during the cooling stage is also observed (just before point A). As explained previously, the precise rate of regeneration of the adsorbent layer during the purge stage is difficult to determine. Nevertheless, the dotted lines shown in Figure 2.15 represent a possible pattern of variation of adsorbed concentrations, as water is removed from the adsorbent layer.

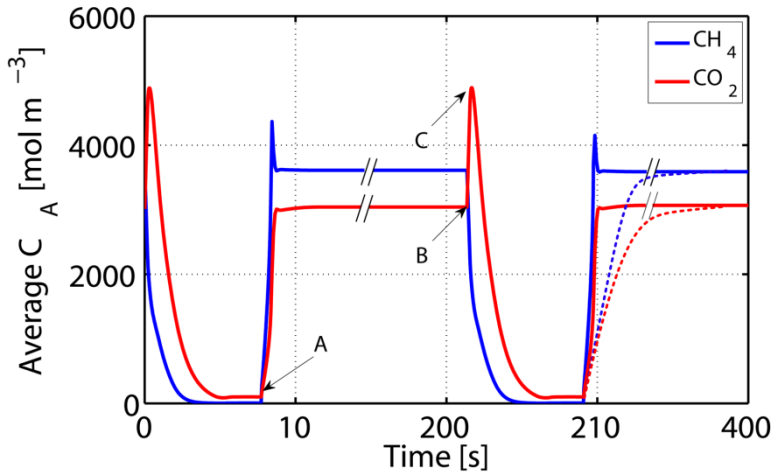

Figure 2.15. Total adsorbed concentration in the adsorbent layer predicted for two cycles

The performance of the purification process is analyzed by monitoring the product yield and purity. Figure 2.16 shows the product collection from a process operating in cyclic steady state. For this simulation, it is assumed that although the feed stage only lasts for 0.19 s, the product collection continues until the displacement of gas is complete, so that the product recovery remains high. The initial increase in product gases seen in Figure 2.16 is due to the collection of gases from the adsorbent microchannel present previously before the start of the feed stage and the feed gases. At the end of the cooling stage, the adsorbed concentrations of both the component gases, CH_4 and CO_2 are the lowest, which are subsequently compensated by the product purge. This essentially reduces the total product by the amount required to replenish the adsorbed concentrations in the adsorbent and gaseous concentrations in the void spaces.

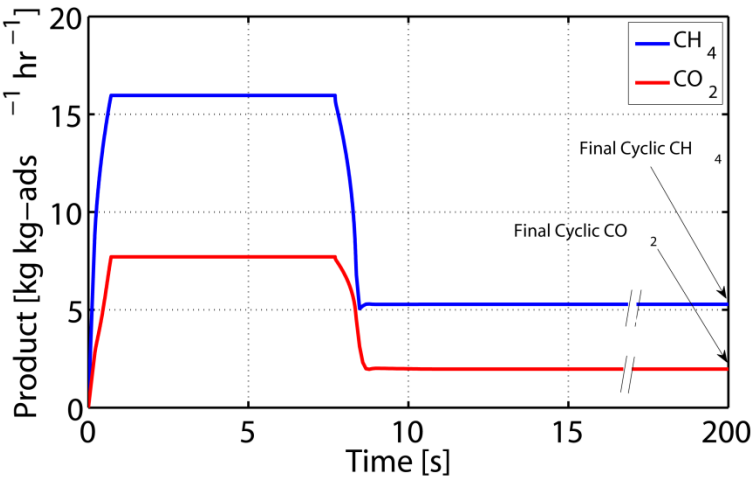

Figure 2.16. Product collection per cycle showing transient variation for adsorption and purge stages

Based on the collected CH_4 and CO_2 seen in Figure 2.16(b), the purity of collected product in this case is 90% by mole. The calculated CH_4 recovery, which compares the CH_4 in the product and CH_4 in the feed, is 82%. The total product collection from the process is 7.4 kg kg-ads^{-1} hr^{-1} (9118 LSTP kg-ads^{-1} hr^{-1}) for the stage times listed in Table 2.9. The single point performance data are comparable with those in the literature as shown in Table 2.10, in terms of product purity and recovery. While the process capacity for the system under consideration is ~100-fold better than the values for bed-based PSA processes reported in the literature, it is four times better than the TSA-based process studied by Pahinkar *et al.* (2016), who studied a monolithic design with separate alternating rows of gas and liquid HTF microchannels.

Table 2.10. Single-point process performance comparison with the literature

Parameter	Present Study	Kapoor and Yang (1989)	Olajossy *et al.* (2003)	Pahinkar *et al.* (2016)
CH_4 Molar Purity [%]	**90**	82-95	86-98	~ 97
CH_4 Mass Recovery [%]	**82**	40-94	86-93	> 94
Process capacity [LSTP kg-ads^{-1} hr^{-1}]	**9118**	< 121	< 167	< 2750

It must be noted that the calculations presented in this section refer to a single adsorption stage time based on the criteria shown in Table 2.2. A comprehensive investigation of the purification cycle is reported in Chapter 3, wherein further improvements in the process performance through variation of stage times and heat and mass recovery are also reported.

2.5 Conclusions

A novel TSA process cycle involving adsorbent microchannels for natural gas purification is proposed and the underlying fluid dynamics and heat and mass transfer are analyzed computationally. Comprehensive HT/MT/FD models are developed for the adsorption, desorption, cooling and purge stages of the process cycle to investigate species exchange and adsorption phenomena in the adsorbent layer in a cyclic steady state process.

It is found that the adsorption stage is fast, resulting in adsorbent layer saturation within 0.2 s as a result of the convection-governed process, unlike the diffusion-governed process in the case of adsorbent beds. Due to the presence of two different phases in the microchannel during the desorption stage, species exchange is subjected to varying mass transfer resistances. Nevertheless, the desorption stage does not take more than 4 s for a near complete regeneration of the adsorbent layer. As a result of the small thermal mass

of the microchannel geometry, the cooling stage is also rapid, lasting only 3 s. One of the areas of further improvement is the purge stage, where the microchannel configuration with a prescribed constant pressure drop results in small rate of liquid water removal from the adsorbent layer. The options of mechanisms by which water can be removed from the adsorbent layer are limited. However, the overall cycle time for the TSA process proposed is smaller than the PSA processes documented in the literature (600 - 1200 s) (Kapoor and Yang, 1989; Olajossy *et al.*, 2003).

Parametric studies on microchannel geometry are conducted, which show that a larger diameter channel with a thinner adsorbent layer results in short and efficient purification cycles. In particular, the cycle time is estimated to be 203 s for a D_h of 530 μm and *th* of 30 μm, which increases to 2225 s for a D_h of 200 μm and *th* of 100 μm. Large mass flow rates as a result of the large microchannel diameter, and reduction in mass transfer resistances within the adsorbent layer as a result of the thinner adsorbent layer result in fast execution of each of the stages. The full process model is simulated with two adsorbent-HTF pairs, silicalite–water and zeolite 5A–PAO. Although zeolite 5A is an excellent CO_2 adsorbent, it cannot be used with water, because of its greater affinity for water. The use of PAO, which does not interfere with CO_2 adsorption in zeolite 5A, results in a very slow process due to its high viscosity. Additionally, because of its low volatility, it cannot be evaporated out of the adsorbent layer. The silicalite–water pair, however, yields excellent process performance, due to higher temperature sensitivity of silicalite and excellent heat and mass transfer characteristics offered by water. Therefore, silicalite–water is the preferred adsorbent–HTF pair for this system.

With the silicalite–water pair and a D_h of 530 μm and *th* of 30 μm, the proposed concept can produce high purity output with a moderate CH_4 recovery in purification cycles of 203 s duration. The estimated process capacity of the present study is not only about two orders of magnitude greater than the capacity of the bed-based PSA processes, but is also an improvement over a design with separate alternating microchannels for gas and HTF flow. Chapter 3 reports a comprehensive investigation of this process for a range of attainable purities, recovery factors and energy efficiencies to determine its viability for an actual large scale installation.

3 PERFORMANCE ASSESSMENT

3.1 Introduction

In Chapter 2, a temperature swing adsorption (TSA) process in adsorbent-coated microchannels for natural gas purification, with the flow of working and coupling fluids through the same microchannels, was investigated. A review of existing industrial natural gas purification techniques was conducted to identify the advantages and limitations of MEA absorption (Göttlicher and Pruschek, 1997; Aaron and Tsouris, 2005; Yang *et al.*, 2008; Pirngruber *et al.*, 2013), membrane separation (Koros and Mahajan, 2000; Baker, 2002; Bernardo *et al.*, 2009) and bed-based PSA systems (Cen *et al.*, 1985; Kapoor and Yang, 1989; Olajossy *et al.*, 2003; Liu *et al.*, 2011; Shao *et al.*, 2011; Mulgundmath *et al.*, 2012), which are extensively investigated and used for commercial gas separation plants. TSA-based purification processes, however, are difficult to implement (Riemer *et al.*, 1994) due to the low thermal conductivity of the adsorbent packed in an adsorbent bed, except for the recent studies with microchannel heat and mass exchangers (Lively *et al.*, 2009; Determan *et al.*, 2011). It was also demonstrated that with the recent developments in manufacturing of hollow fiber or mixed matrix membranes (MMM), adsorption-based gas separation systems can be designed to effectively utilize high heat and mass transfer coefficients in microchannels to enhance product collection and reduce system footprint (Pahinkar *et al.*, 2015, 2016).

In Chapter 2, adsorption, desorption, cooling and purge stages of the TSA-based cycle were analyzed in detail and the microchannel geometry was optimized. The

silicalite-water adsorbent-HTF pair was selected based on detailed analyses of the heat and mass transfer processes in each stage.

This Chapter uses the model developed in Chapter 2 to investigate the complete performance spectrum of the purification process in terms of product purity, process capacity, CH_4 recovery, and operating energy requirement. These performance parameters are compared with those reported in the literature for existing purification processes. Methods to enhance product purity and reduce energy requirements are also investigated.

3.2 System design selection and results

3.2.1 Liquid HTF recirculation and absorption

Detailed stage-wise fluid dynamics, heat and mass transfer modeling is described in Chapter 2; however, for the full process simulation, additional consideration must be given to gas solubility in water and absorption to ensure a realistic operation. The estimated stages times and the total cycle time used for the simulation are shown in Table 3.1.

Table 3.1. Stage times and total cycle time selected for the full process simulation

Stage	Time [s]
Adsorption [s]	0.19
Displacement of gas [s]	0.52
Desorption [s]	4.00
Cooling [s]	3.00
Displacement of liquid [s]	0.70
Purge [s]	195.00
Total time [s]	**203.41**

The modeling architecture considered for the process is shown in Figure 3.1, which also shows purge gas recirculation and HTF recirculation paths. The HTF is recirculated to avoid the need of a fresh batch of HTF to be sent through the monolith for each cycle. This requires an investigation of the effect of liquid absorption on cyclic steady state of the process and its influence on product collection.

The governing equations used for modeling the absorption of gas in the HTF are based on condensability of gases in the presence of a pressurized liquid. As gases are pressurized at the system temperature, the mass of gases that changes phase and mixes with the liquid HTF can be calculated by using Equations (3.1) and (3.2) (Reid *et al.*, 1986).

$$x_{i,abs} = x_{i,G} \cdot \frac{P_{sys}}{P_{i,G,sat}} \tag{3.1}$$

$$C_{g,i,abs} = y_{i,G,abs} \cdot \rho_L \tag{3.2}$$

The saturation pressures of CH_4 and CO_2 in Equation (3.1) as a function of temperature can be calculated using Equations (3.3) and (3.4), respectively (Reid *et al.*, 1986). These curves are fitted based on the variation of the saturation pressure of each of the component gases with temperature (Klein, 2016). The dissolved species are considered to be in equilibrium with the liquid.

$$P_{CH_4,G,sat} = e^{\left(\frac{-1023.41}{T_g}+13.78\right)} \tag{3.3}$$

$$P_{CO_2,G,sat} = e^{\left(\frac{-2012.41}{T_g}+15.522\right)} \tag{3.4}$$

The species conservation equation derived in Chapter 2 is modified to account for the absorbed fraction of gases in the HTF liquid. The rate of change of absorbed gas concentration in the HTF, derived in Equation (3.2), and the rate of change of gas concentration that is not absorbed and remains suspended in the HTF, constitute the overall species balance for the microchannel node. After this modification, the governing species balance equation used for microchannel flow is shown in Equation (3.5).

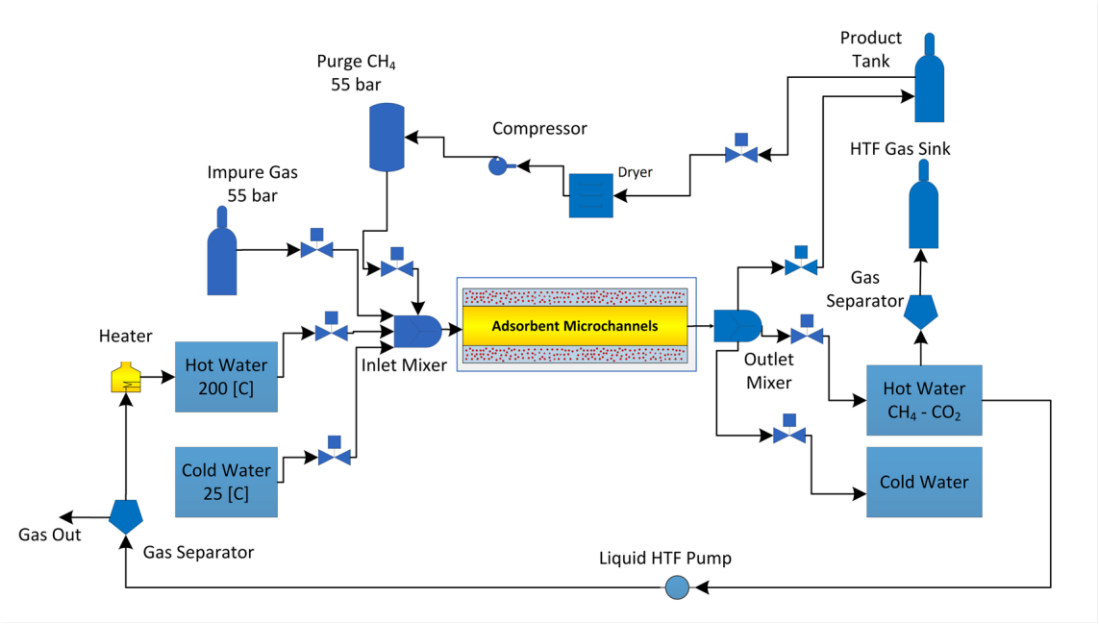

Figure 3.1. Component architecture considered for modeling the TSA-based purification process. Also shown are the recirculation loops for purge gas and HTF.

$$\frac{\partial C_{g,i}}{\partial t}+\frac{\partial C_{g,i,abs}}{\partial t}+\frac{\partial\left(uC_{g,i}\right)}{\partial z}-\left[\begin{array}{l}\left(S_{ads}+S_{LDG}\cdot X_{G}+S_{GDL}\cdot X_{G}+S_{Purge}\right)D_{A,G,i}+\\ \left(S_{LDG}\cdot X_{L}+S_{deso}+S_{cool}+S_{GDL}\cdot X_{L}\right)D_{A,L,i}\end{array}\right]\cdot\frac{\partial^{2}C_{g,i}}{\partial z^{2}}+$$
$$\left[\begin{array}{l}\left(S_{ads}+S_{LDG}\cdot X_{G}+S_{GDL}\cdot X_{G}+S_{Purge}\right)\dfrac{1}{\mathrm{R}_{eq,Mass,G,i}}+\\ \left(S_{LDG}\cdot X_{L}+S_{deso}+S_{cool}+S_{GDL}\cdot X_{L}\right)\dfrac{1}{\mathrm{R}_{eq,Mass,L,i}}\end{array}\right]\cdot\frac{\left(C_{g,i}-C_{w,i}\right)}{A_{g}}=0 \tag{3.5}$$

Simulation of the entire cycle can become unstable due to instantaneous transfer of a large mass of species from the gaseous phase to the dissolved phase, if a pure liquid is assumed to enter the microchannel. A first-order time delay is unable to prevent simulation failure unless it completely damps the absorption source term. To address this challenge, the mixture is sampled only at the microchannel outlet. Species desorbing out of the adsorbent and mixing with the liquid stream reach the outlet by convection, regardless of absorption in water. Additionally, as shown in Chapter 2, the quality of the two-phase mixture in the microchannel does not exceed 0.04 during the desorption stage. Hence, heat and mass transfer resistances are conservatively predicted using liquid properties for the microchannel flows. Once the two-phase mixture reaches the outlet node, Equation (3.5) is solved locally, while the axially discretized heat and mass transfer equations without the absorption term can be solved at all the other nodes. After the mixture is collected in the desorption sink, the maximum gas absorption capacity of water as a function of the transient variation of the local mole fraction of gases and temperature is shown in Figure 3.2(a).

For a desorption stage HTF-gas collection of 4 s, the mass of water is 73 kg kg-ads^{-1}, while the amounts of CO_2 and CH_4 that water can absorb are 8.6 kg kg-ads^{-1} and 1.2 kg kg-ads^{-1} respectively. As shown in Figure 3.2(b) for both species, the mass separated in the microchannel and accumulated in the desorption tank in each cycle is less than the maximum capacity that water can absorb per cycle. Hence, gases cannot be recovered from the desorption sink without heating the collected water in a single cycle further (the desorption sink is already at T_{deso}, 200°C), unless the same HTF mass is recirculated for several cycles until the cumulative mass of absorbed gases reaches the

maximum absorption capacity. Once water is fully saturated with both species, the desorbing gases cannot be absorbed into the liquid and can be easily separated from the desorption sink using a gas separator without additional energy input. This rationale is based on the assumption that the amount of carbonic acid produced as a result of reaction of CO_2 with water is small and does not react with the walls of the system components and the microchannel adsorbent layer. Another important underlying assumption in modeling desorption with saturated water is non-interaction of the absorbed gas in water and the adsorbent. This assumption can be justified by considering the direction of gas flow, which is from adsorbent to the microchannel and remains so at the beginning of the desorption stage. Additionally, for adsorbents like silicalite, the adsorption isotherms at high partial pressures are more sensitive to temperature than partial pressure (Palomino *et al.*, 2009). Hence, in the later stages of desorption, even if fully saturated water reaches the adsorbent through void spaces and creates a scenario in which absorbed gases contribute to the partial pressure for adsorption, its effect on adsorption capacity is minimal.

With water recirculation, as shown in Figure 3.2(b), gas recovery is estimated to initiate from the desorption sink only after 4000 s or after 20 cycles. This leads to an important simplification in process modeling: if fully saturated hot water is used for desorption, the operation of a real cycle is analogous to a case without absorption of gases and near-complete recovery of gases lost to the HTF stream is possible.

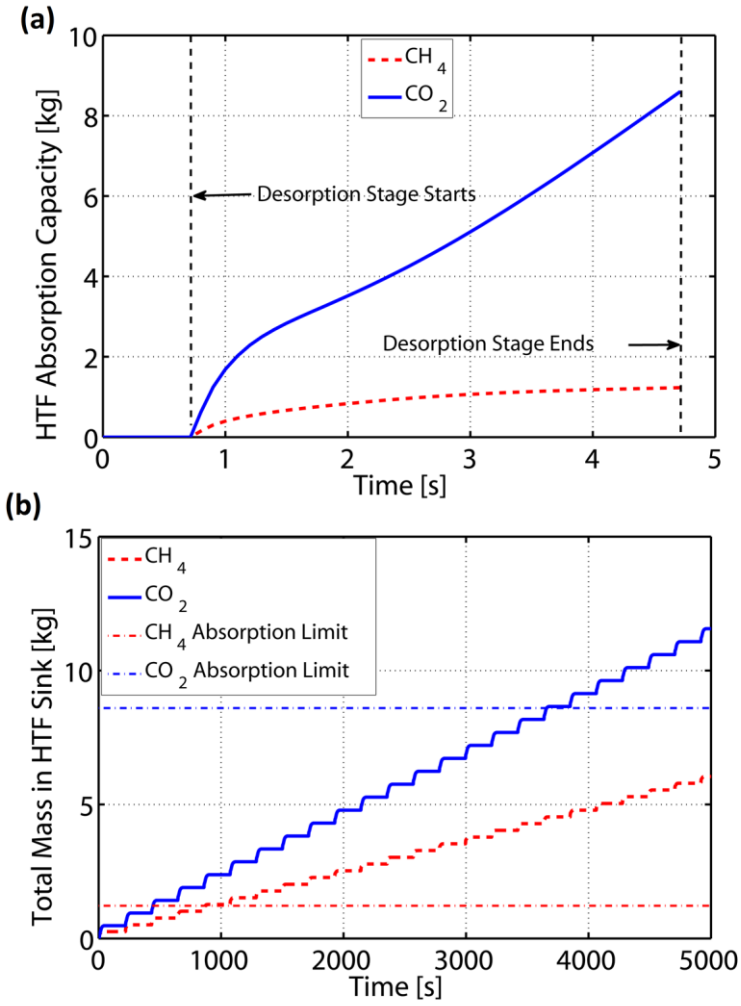

Figure 3.2. (a) HTF sink absorption capacity for component gases during desorption stage normalized with adsorbent mass (b) Saturation of HTF with selected stage times.

3.3 Process performance prediction

During cyclic operation of the purification process, feed gas enters the microchannel at the start of the adsorption stage, and collection of the purified product can commence. The process capacity and the product purity change as the feed time and the product collection time vary. A wide range of product purity and recovery is achieved by changing the feed and collection times. Figure 3.3 shows schematics of the two extremes of product collection scenarios while keeping the feed time constant.

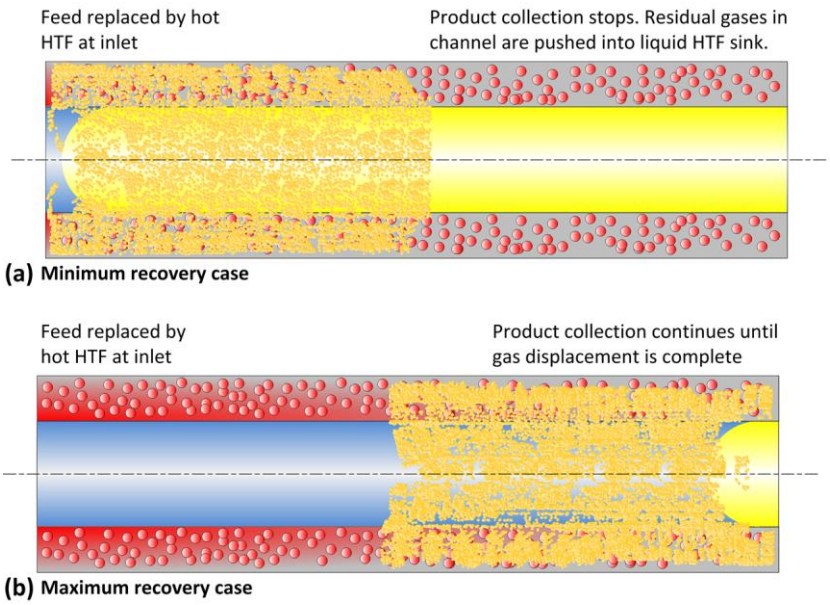

Figure 3.3. Schematic showing limits of product recovery from the purification process.

Figure 3.3(a) shows the adsorption stage scenario resulting in the least possible product collection from the process. If the feed gas supply continues for a small duration after the start of the adsorption stage, and both the inlet and outlet gas valves are turned off simultaneously afterwards, no feed gas can enter the product resulting in negligible net product collection. In contrast, Figure 3.3(b) shows the case when product collection is the highest. This is possible as a result of continued product collection until the liquid-gas interface reaches the microchannel outlet, even after the feed supply is cut off. Depending on the selection of feed times and product collection times in between the two extremes shown in Figure 3.3(a) and Figure 3.3(b), a performance matrix can be generated. The purity calculation in the product tank is shown in Equations (2.25) through (2.27), while CH_4 recovery is calculated as shown in Equation (3.9).

$$\frac{\partial \overline{M}_i}{\partial t} = \frac{A_g \cdot u \cdot C_{g,i}\big|_{z=L}}{\rho_{ads} \omega V_w} \tag{3.6}$$

$$Purity_{kg,i} = \frac{\overline{M}_i}{\sum_i \overline{M}_i} \tag{3.7}$$

$$Purity_{mole,i} = \frac{\left(Purity_{kg,i} \Big/ MW_i \right)}{\sum_i \left(Purity_{kg,i} \Big/ MW_i \right)} \tag{3.8}$$

$$\eta_{CH_4} = \frac{\overline{M}_{CH_4,product} - \overline{M}_{CH_4,purge}}{\overline{M}_{CH_4,feed}} \tag{3.9}$$

Figure 3.4 shows the variation of product purity with process capacity evaluated for different feed and collection times. As feed time is increased, more CO_2 enters the microchannel, reducing product purity as seen in Figure 3.4. Additionally, as the collection time is increased, process capacity increases at the cost of purity. Nevertheless, the purity values do not fall below 87% for the operating conditions considered here. More importantly, process capacity with the use of adsorbent-coated microchannels is found to be up to 100-fold greater than that for the bed-based PSA processes at similar product purities. The reasons for such very high predicted process capacities are: (a) extremely small requirement of adsorbent mass per microchannel, (b) higher intra-crystalline diffusivity values as a result of smaller adsorbent particles (~1 μm) and (c) high heat and mass transfer coefficients as a result of a convection-based design, unlike the diffusion-based designs of bed-based PSA systems. For the void fraction and adsorbent loading considered here, the adsorbent mass per microchannel is only 1.325×10^{-5} kg, whereas for example, the adsorbent mass required for construction of the bed studied by Olajossy *et al.* (2003) is 3.9 kg.

Additionally, for similar product purities, the purification process capacity in the present work is at least 50% greater than those from the TSA-based process studied by Pahinkar *et al.* (2016), who investigated gas separation using separate alternating parallel microchannels for the flow of working fluids and HTFs. The system footprint decreases by an even greater margin (> 82%) when the product is normalized with system volume, due to the elimination of additional channels for the HTF.

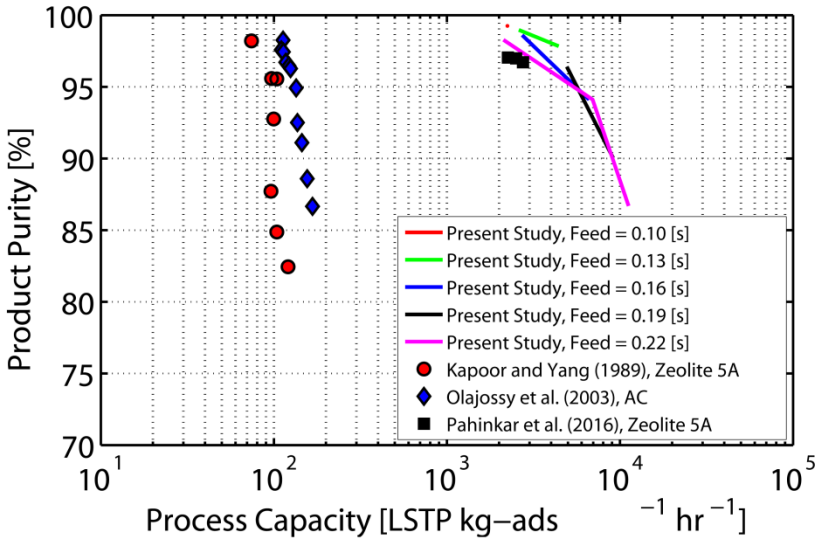

Figure 3.4. Product purity vs. process capacity compared with PSA and TSA processes (Kapoor and Yang, 1989; Olajossy *et al.*, 2003; Pahinkar *et al.*, 2016).

Figure 3.5 shows the variation of product purity with CH_4 recovery. The CH_4 recovery factor is directly proportional to process capacity, as seen from a comparison of Figure 3.4 and Figure 3.5. As more product gas is collected, the fraction of CH_4 in the product increases. The recovery factor predicted for the concept investigated here does not exceed 83%, resulting in the loss of at least 17% CH_4 to the desorption HTF sink. This value cannot be enhanced directly, because the gases desorbing out of the adsorbent and mixing with the HTF during desorption contain CH_4, in addition to CO_2. With the

saturated liquid HTF recirculation approach illustrated in the previous section, it is possible to recover CH_4 from the desorption sink without a parasitic heat load; however, an independent treatment of the collected gas collected is needed as it would have different gas mole fractions than the product mole fractions. This is also why CH_4 recovery values in the present work are lower than those of Pahinkar *et al.* (2016), because the gases recovered from the desorption sink are not considered for calculation of recovery in the present work. Nevertheless, the product purity remains comparable to those of Pahinkar *et al.* (2016). The CH_4 recovery values reported here are also competitive with those from the bed-based PSA system investigated by Kapoor and Yang (1989). The similarity in recovery factors and the greater process capacity indicates the potential for large-scale feasibility of the system considered here.

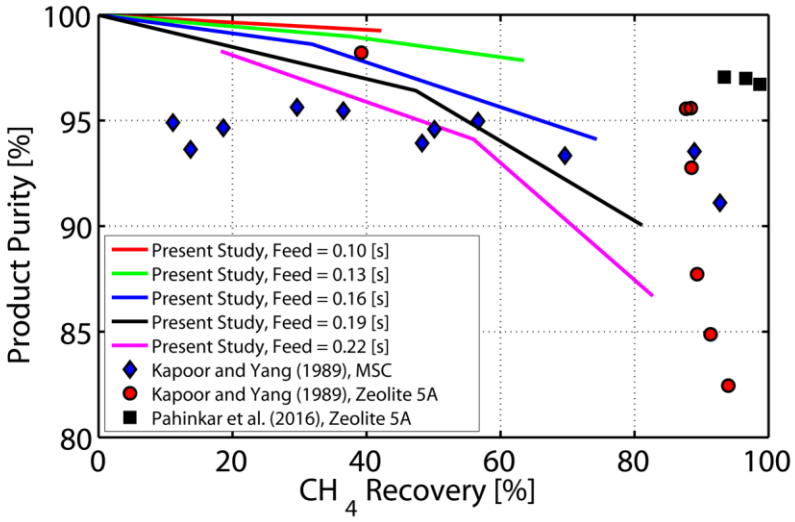

Figure 3.5. Product purity vs. CH_4 recovery compared with the PSA and TSA processes in the literature (Kapoor and Yang, 1989; Olajossy *et al.*, 2003; Pahinkar *et al.*, 2016)

3.4 Energy requirements and operating cost

As illustrated in Figure 3.1, the purge gas compressor and HTF recirculation pump require electrical input for their operation, while the HTF heater requires heat input. The microchannel monolith requires sensible heat for heating the monolith from 25°C to 200°C and heat of desorption for the removal of impurities from the adsorbent. For a process operating in repeating cycles, Equation (3.10) is used to calculate the sensible heat required for heating the adsorbent layer and the fused silica monolith wall. For a 203.41 s long cycle and 1 kg of silicalite used to construct a monolith, $\dot{N}_{\mathrm{cyc}}$ and N_{ch} are calculated to be 17.7 cycles hr^{-1} and 75,500 kg-ads^{-1}, respectively. It should be noted that the sensible heat is calculated based on the thermal mass of the monolith and not the thermal mass of the HTF, due to the HTF recirculation approach discussed in the previous section. The only energy the recirculating HTF is assumed to lose every cycle is the sensible heat required to heat the monolith and the heat of desorption. Hence, it is not necessary to heat the entire mass of the HTF entering in the microchannel every cycle from T_0 to T_{deso}.

$$\dot{E}_{Sens} = \dot{N}_{cyc} \cdot N_{ch} \left(\rho_w \cdot c_{p,w} \cdot A_w + \rho_{FS} \cdot c_{FS} \cdot A_{FS} \right) \cdot L \cdot \Delta T \tag{3.10}$$

The heat of desorption for the same monolith size is calculated using Equation (3.11). For a temperature swing of 175°C and system pressure of 5500 kPa, the operating adsorption capacity of silicalite for CO_2 is determined to be 4900 mol m^{-3}, while it is 3600 mol m^{-3} for CH_4.

$$\dot{E}_{Deso} = \dot{N}_{cyc} \cdot N_{ch} A_w \cdot L \cdot \sum_i \omega \cdot \Delta H_{ads,i} \cdot \Delta C_{A,i} \tag{3.11}$$

The electrical input required for recirculation of the HTF is calculated using Equation (3.12). After separating the mixture components in gaseous form in the desorption sink, the HTF, which also carries dissolved component gases, is recirculated to the monolith inlet neglecting losses from the pipelines.

$$\dot{E}_{HTF,recir} = \dot{N}_{cyc} \cdot N_{ch} \cdot M_{HTF,cyc} \cdot \nu_{HTF} \cdot \Delta P \tag{3.12}$$

Finally, the compressor input power required to recirculate the purge gas from the product gas tank to the monolith inlet for the entire duration of the purge stage is calculated as shown in Equation (3.13) (assuming isentropic compression.)

$$\dot{E}_{purge} = \dot{N}_{cyc} \cdot N_{ch} \cdot \Delta H_{Com} \tag{3.13}$$

For the standard operating case with the stage times shown in Table 3.1, the predicted energy requirements for each of the components are shown in Figure 3.6. It can be seen that the heat of desorption is only 10.3 % of the sensible heat requirement, while the sensible heat itself is about 42% of the total energy required.

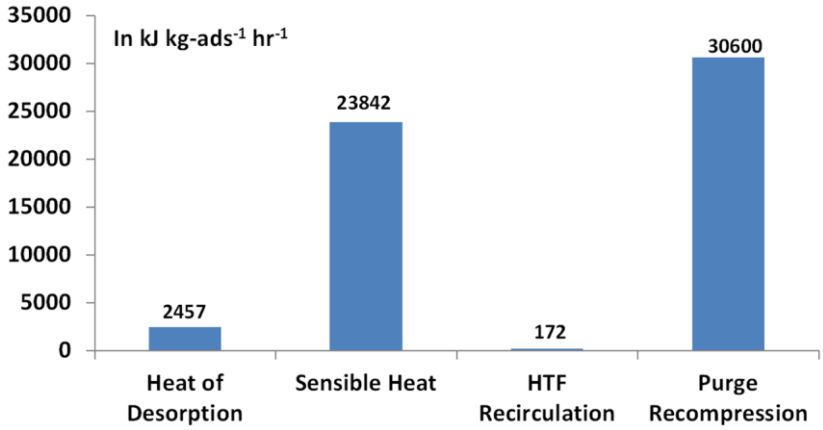

Figure 3.6. Component-wise energy requirement for the baseline case.

From Figure 3.6, it can also be seen that the highest power input is required for compression of the purge gas from 5400 kPa to 5500 kPa: the purge gas compressor consumes up to 53% of the total energy required for process operation.

Figure 3.7 shows the variation of the total energy requirement in terms of energy ratio shown in Equation (3.14). The energy ratio is defined as the ratio of total energy required for the operation of the purification process to combustion potential of the product. The product collection in the denominator is varied by changing the feed and collection times, while the total energy required in the numerator remains unaffected with any change in these times, as the energy required is a function of the monolith mass, temperature swing and the purge stage time.

$$Ratio_{Energy} = \frac{\dot{E}_{Deso} + \dot{E}_{Sens} + \dot{E}_{HTF,recir} + \dot{E}_{purge}}{Purity_{CH_4}\, \dot{M}_{prod} \cdot LHV} \tag{3.14}$$

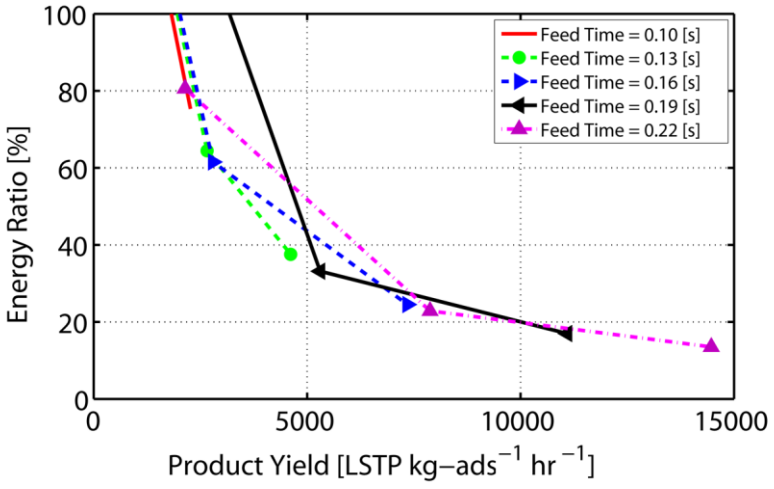

Figure 3.7. Variation of energy ratio plotted with process capacity for variable feed times.

It is also important to note that a higher process capacity results in a lower energy ratio, enhancing the economic viability. The lowest energy ratio calculated for the baseline case is 14%. An increase in the adsorption stage duration beyond 0.22 s may result in lower values of energy ratios, but at the cost of significant drop in product purity. This value of energy ratio is equivalent to 1.6 kWh kg-product^{-1} absolute operating power input and is higher than the reversible electrical energy requirement predicted for chemical absorption (0.34 kWh kg^{-1}) and that for cryogenic distillation (1.0 kWh kg^{-1}) (Göttlicher and Pruschek, 1997). However, the actual operating energy requirement for the MEA absorption system is reported (Bounaceur *et al.*, 2006) to be up to 1.67 kWh kg-product^{-1}, making the process analyzed in the present study comparable to absorption systems in terms of energy consumption. Avenues for energy reduction are discussed in the next section.

3.5 Reduction in operating energy requirement

As shown in Figure 3.6, energy utilization is dominated by the sensible heat required to raise the temperature of the monolith and power input to the purge gas compressor, requiring 42% and 53% of the total energy input, respectively.

The sensible heat required can be reduced by decreasing the desorption temperature, thereby reducing the temperature swing available for the process. Simulations are conducted with three desorption temperatures (200°C, 100°C, 50°C), while keeping the rest of the parameters the same as the baseline case described in Chapter 2. Figure 3.8(a) shows variation of cyclic CO_2 adsorbed concentrations as a function of temperature. As expected, the operating adsorption capacity drops significantly with temperature swing, affecting the product purity accordingly. For a

temperature swing of 175°C, the adsorbent swing capacity is up to 95% of the maximum adsorbent capacity (from point S to C). However, with a reduction of temperature swing to 75°C and 25°C, the adsorbent swing capacity decreases to the distance from points S to B and S to A (39% and 18% of the swing in the baseline case with 175°C), respectively. Therefore, with a desorption temperature of 50°C, up to 85% of the sensible energy can be saved; however, the adsorption capacity drops to 18% of the capacity with a desorption temperature of 200°C. This results in negligible product purity increment over the feed gas as shown in Figure 3.8(b), which shows the energy ratio-product purity curves for the maximum product collection times for a given feed time, as illustrated in Figure 3.3(b). Marginal improvement in product purity is possible by using a shorter adsorption stage, but the total process capacity is reduced by a substantial margin, negating the predicted compactness and high process capacity of the purification cycle illustrated in Figure 3.4. Thus, it is concluded that reducing the available temperature swing is not a viable option for reducing the total energy required, as it considerably deteriorates process performance without commensurate benefits.

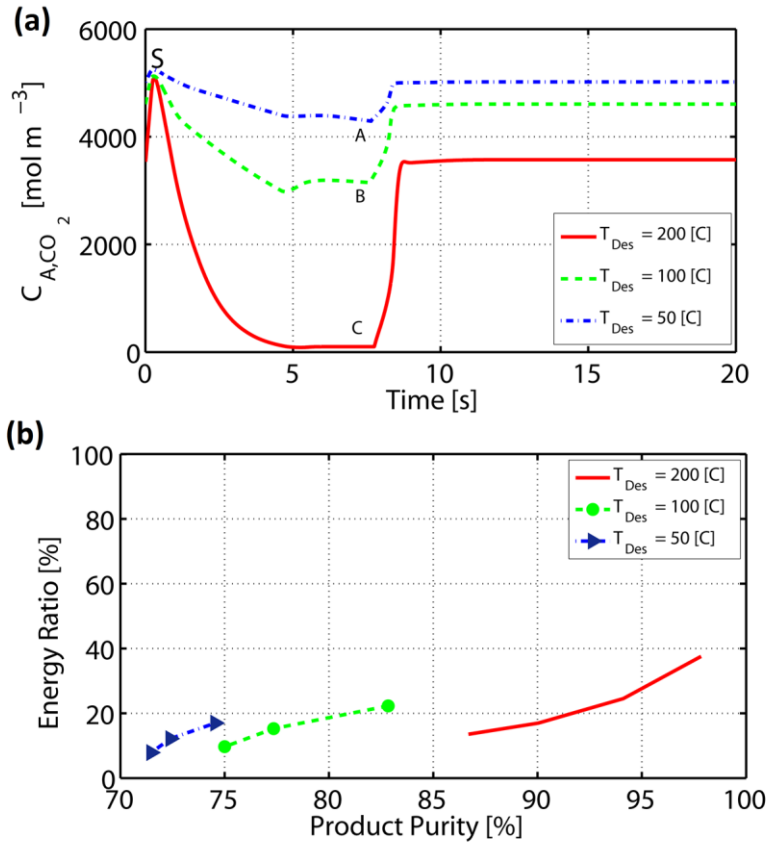

Figure 3.8. (a) Effect of reduction in desorption temperature on operating adsorption swing capacity, seen as the difference between adsorption stage peak value near 1 s and lowest value after cooling stage at 7 s. (b) Effect of drop in temperature on product purity.

The other major energy consumption of the cycle is by the purge gas compressor, and is more critical because it is in the form of electrical energy input. The baseline case imposes a 100 kPa pressure drop across the microchannel. This pressure drop can be reduced to decrease the compressor power by reducing not only the specific volume change, but also the mass flow rate through the compressor. The reduced pressure drop, however, decreases the mass flow rate though the microchannel for all the stages, and not just for the purge stage. Hence, all the stage times must be recalculated, as the times in Table 3.1 change depending on flowrates of the component mixture and the HTF through

the microchannel. For this parametric study, 25 kPa and 10 kPa are chosen as the lower pressure drop values. Table 3.2 shows the revised values of all the stage times for the three pressure drop cases considered. As the pressure drop decreases, it takes longer for CO_2 to saturate the adsorbent during adsorption. Additionally, it takes longer to remove the CO_2 from the adsorbent layer with the resulting slower liquid flows. Cooling stage time is also affected accordingly; however, the extended purge stage time remains unaffected. This is because the removal of liquid water from the adsorbent layer is governed by diffusion of evaporated water through the porous layer and not by convection through the microchannel. It can be seen from Table 3.2 that the total cycle time increases by only 15% even though the pressure drop is reduced by 90% as a result of a constant purge stage time, which constitutes up to 96% of the total cycle time for the baseline case.

Table 3.2. Effect of reduction in ΔP on purification cycle time.

Stage times [s]	**ΔP = 100 kPa**	**ΔP = 25 kPa**	**ΔP = 10 kPa**
Adsorption	0.19	0.35	0.50
Displacement of gas	0.52	0.90	1.30
Desorption	4.00	15.00	20.00
Cooling	3.00	8.00	10.00
Displacement of liquid	0.70	2.65	6.60
Purge	195.00	195.00	195.00
Complete cycle	203.41	221.90	233.40

For a constant baseline temperature swing of 175°C, the sensible heat and heat of desorption remain unchanged, because equal adsorbent layer saturation and operating capacity is ensured when the adsorption and desorption stage times are calculated. The

calculated values of power inputs to the liquid HTF recirculation pump and the purge gas compressor are shown in Table 3.3. The power required for liquid HTF pump is only 0.30% of the total energy input for a 100 kPa pressure drop, and further decreases to 0.07% for a pressure drop of 10 kPa. More importantly, a significant change in compressor power is observed for the reduced pressure drop cases. A reduction of up to 97% in compressor power is observed with a 10 kPa pressure drop. The total energy requirement, therefore, decreases to 48% of the total energy required in the baseline case with a 100 kPa pressure drop.

Table 3.3. Effect of reduction in ΔP on energy required for process components

ΔP	HTF pump power [kJ kg-ads^{-1} hr^{-1}]	% Saving	Purge gas recompression power [kJ kg-ads^{-1} hr^{-1}]	% Saving
100 kPa	172	-	30600	-
25 kPa	86	**50**	3704	**88**
10 kPa	19	**89**	991	**97**

3.6 Heat recovery from the cooling stage

Partial heat recovery from the cooling stage is possible by collecting hot HTF in the desorption sink, which exits the microchannel at 200°C even after the desorption stage is terminated. As the cold HTF enters the microchannel, it displaces the hot HTF by simultaneously being heated because of heat exchange from the microchannel. If the microchannel outlet valve to the desorption sink is closed with a delay after the cold HTF enters the microchannel, the hot HTF can be collected in the desorption sink, resulting in a significant heat recovery. Figure 3.9 explains this based on the HTF outlet temperature. The duration for which the hot HTF can be collected after the end of the desorption stage is estimated to be 0.69 s for the baseline case (100 kPa). For the reduced pressure drop

cases, these times and the hot HTF mass flow rates and corresponding heat recovery calculations are shown in Table 3.4. Considering the component-wise energy requirements shown in Figure 3.6, the energy recovered during the cooling stage is significant (14.6% of the original value for the baseline case with 100 kPa without heat recovery from the cooling stage) and decreases the energy ratio to 12% from 14%. The lower pressure drop cases show more gains, because the total energy required has already decreased by nearly 52% of the energy requirement for the baseline case. The energy ratio calculations are repeated for the revised stage times and pressure drops, and the results are plotted in Figure 3.10, which shows reduced energy consumption over the baseline case, shown in Figure 3.7.

It can be seen that the energy ratio falls to 5.7% and 6.1% for the 25 kPa and 10 kPa pressure drop cases, respectively as compared to 14% for the 100 kPa pressure drop case, with a sensible heat fraction of 96.2%. This means that the high-grade electricity requirement is only 3.8% of the total operating cost, while the source for the rest of the energy need not be electricity.

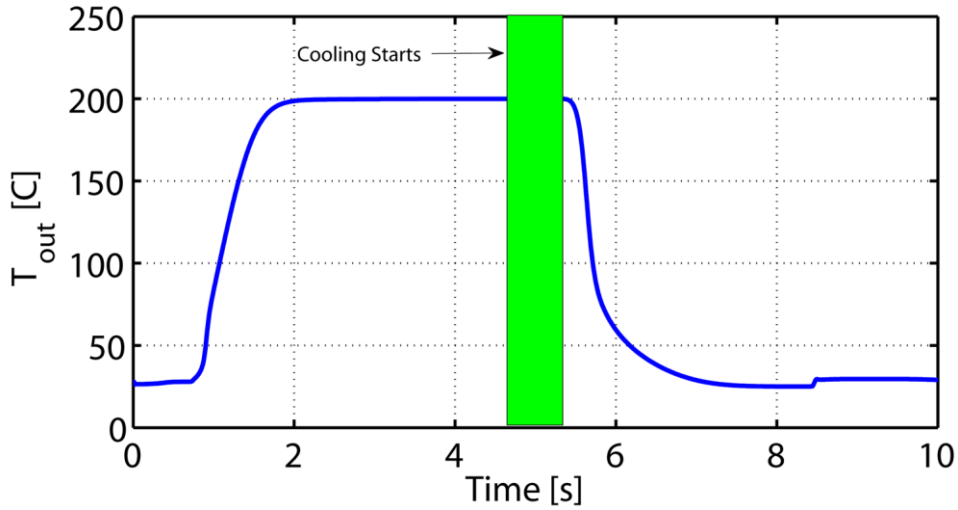

Figure 3.9. Water temperature at the microchannel outlet for the TSA cycle for the baseline case (100 kPa). Green region shows the 0.69 s for which the water exits the microchannel at 200°C, while cooling has already commenced near the microchannel inlet.

Table 3.4. Heat recovery during cooling stage.

ΔP	**Useful time for heat recovery [s]**	**Water mass flow rate [kg s^{-1}]**	**Integrated heat recovered [MJ kg-ads^{-1}]**	**Energy savings with heat recovery [%]**
100 kPa	0.69	20.1×10^{-4}	8364	14.6
25 kPa	1.10	13.2×10^{-4}	8682	28.7
10 kPa	2.21	7.07×10^{-5}	9316	33.9

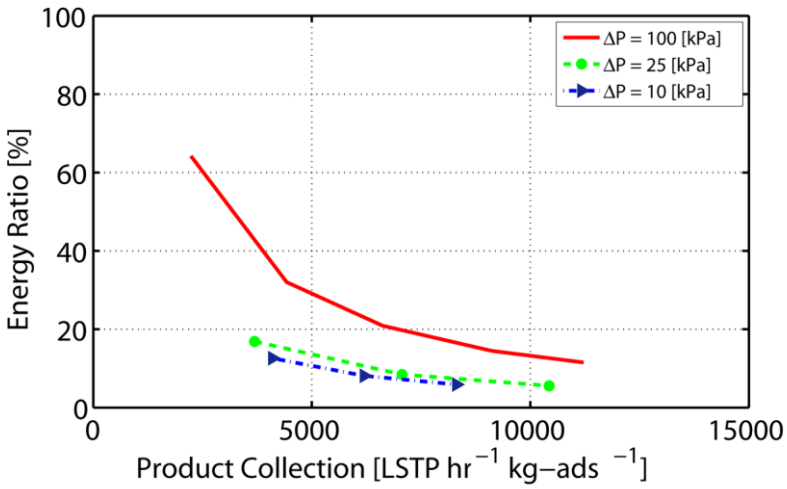

Figure 3.10. Modified energy ratio calculations with reduced pressure drop cases. More than 50% reduction in the energy ratio is possible with reduction of ΔP by 75%.

3.7 Discussion

The revised process capacities, product purities and CH_4 recoveries are shown in Figure 3.11(a) and (b) which show improved process performance compared to those seen in Figure 3.4 and Figure 3.5, respectively. These data account for both the reduced pressure drop approach and the heat recovered from the cooling stage. Figure 3.11(c) shows the revised total absolute energy requirement for process operation. While the process capacities, product purities and CH_4 recoveries can be compared with those reported in the CH_4 separation studies by Kapoor and Yang (1989) and Olajossy *et al.* (2003) as in Figure 3.4 and Figure 3.5, energy requirement values normalized with purified CH_4 are not reported in these studies. However, energy requirement for CO_2 separation from N_2 is reported by Clausse *et al.* (2011) and Mérel *et al.* (2006) for an indirect TSA process using adsorbent beds with fins. Kulkarni and Sholl (2012) reported the energy requirement for CO_2 separation from air using a TSA process employing a

structured monolith contactor. Krishnamurthy *et al.* (2014) reported a wide range of energy utilization as a function of process capacity for a bed-based vacuum-pressure swing adsorption (VPSA). CO_2 separation costs for MEA absorption-based systems are reported by Luis (2016), Pirngruber *et al.* (2013) and Bounaceur *et al.* (2006). To enable a comparison of the energy requirement of the present concept with these studies, the energy requirement estimated for the present concept for removal for CH_4 is recalculated as energy requirement for separating CO_2 from the feed mixture. The mass of CO_2 removed during the adsorption stage is used to normalize the actual energy requirement per cycle, and the energy requirement values are plotted against the mass of CO_2 removed per unit adsorbent mass per hour in Figure 3.11(c).

From Figure 3.11(a), it is clear that process performance remains superior to that of the bed-based PSA processes, and also of the TSA-process that uses separate alternating microchannels for the flow of working fluids and HTFs (Kapoor and Yang, 1989; Olajossy *et al.*, 2003; Pahinkar *et al.*, 2016). A marginal reduction in product output with a reduction in pressure drop across the microchannel is seen; however, this change is insignificant compared to the gains predicted over the systems discussed in the literature. As seen in Figure 3.4, process capacity remains up to two orders of magnitude greater than that of the bed-based systems and up to 4 times greater than the capacity of the TSA-process with separate alternating microchannels. From the product purity–CH_4 recovery graph shown in Figure 3.11(b), CH_4 recovery is observed to improve from a maximum of 82.8% to 87.9% and 88.05% without compromising product purity as the pressure drop across the microchannel decreases from 100 kPa to 25 kPa and 10 kPa, respectively. This improvement is attributed to the sharper adsorption wave at lower fluid

velocities. The revised product purities and recoveries are competitive with the relevant studies in the literature, although the gas recovery from the desorption sink is not considered.

The CO_2-specific energy requirement for the present concept is found to be better than that of the bed-based TSA processes as shown in Figure 3.11(c). For better economic viability, the lower right corner of Figure 3.11(c) is desired, which indicates higher gas removal capacities with low energy requirements. The baseline case with 100 kPa is expected to yield higher process capacity, but at the expense of higher energy penalty. However, the performance predicted for the low pressure drop cases (25 kPa and 10 kPa) is in a competitive operating cost region. Thus, the reduction in pressure drop across the microchannel significantly increases the energy effectiveness of the present concept. The energy requirement for the present concept is not only lower than that of bed-based TSA systems, but also smaller than commonly used MEA absorption systems. At reduced pressure drop values, the process performance is better than that of the TSA process reported by Pahinkar *et al.* (2016).

The present concept yields a better performance when compared with the bed-based PSA process studied by Krishnamurthy *et al.* (2014) for which the energy requirement is marginally lower; however, the process capacity is smaller by at least an order of magnitude than that estimated for the present concept. The present concept yields at least an order of magnitude greater CO_2 removal capacity than bed-based PSA and TSA processes at similar or competitive operating costs.

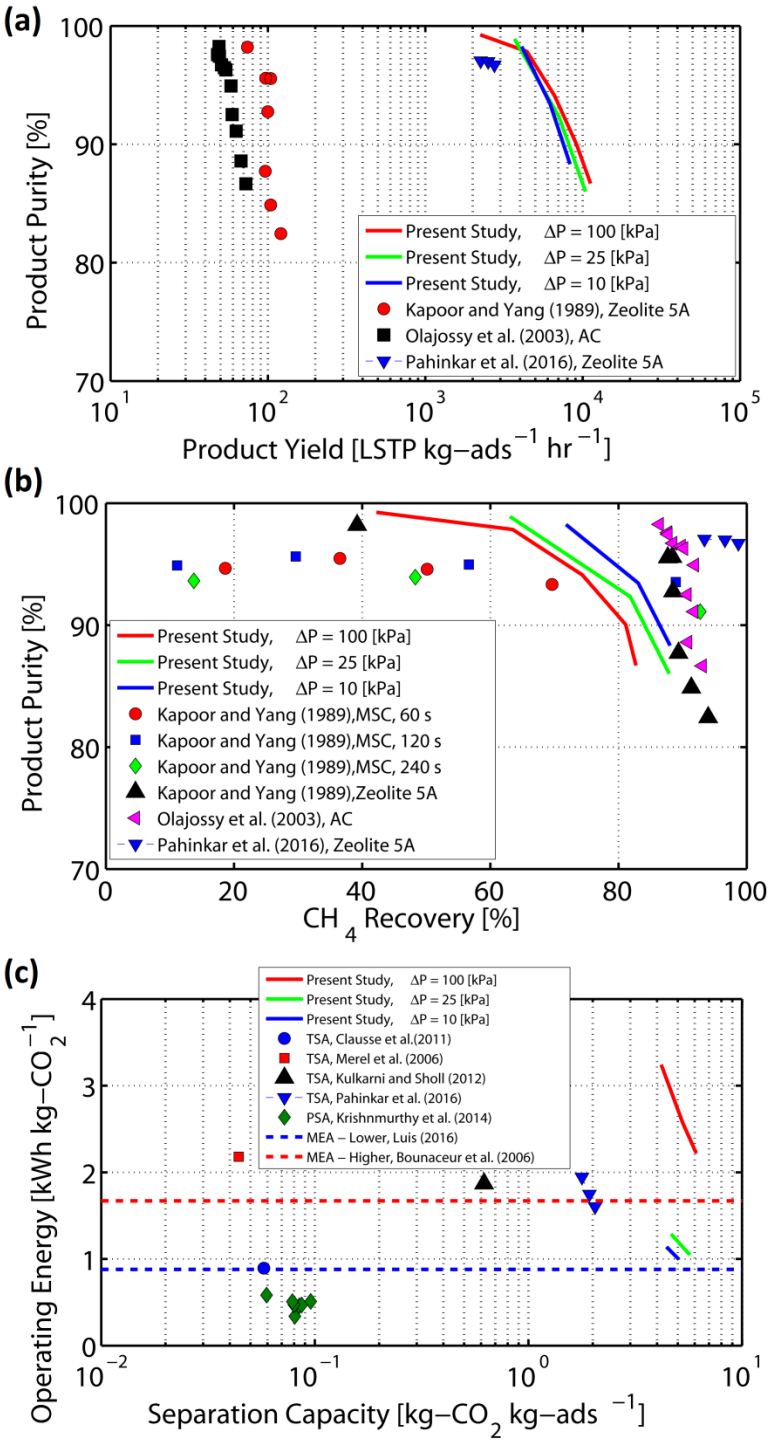

Figure 3.11. (a) Process capacity vs. product purity (b) CH_4 recovery vs. product purity (c) CO_2 separation capacity vs. CO_2 specific energy requirement with the updated operating process conditions (Kapoor and Yang, 1989; Olajossy *et al.*, 2003; Bounaceur *et al.*, 2006; Clausse *et al.*, 2011; Pirngruber *et al.*, 2013; Krishnamurthy *et al.*, 2014; Luis, 2016; Pahinkar *et al.*, 2016).

Because MEA absorption systems operate continuously and are scalable, the specific gas processing capacity is dependent on the MEA recirculation rate and the total volume of MEA used in these systems, the data for which are unavailable in the relevant studies. Luis (2016) reported a range of energy requirement from 0.88 to 1.52 kWh kg-CO_2^{-1}. Pirngruber *et al.* (2013) reported the energy requirement to be 1.03 kWh kg-CO_2^{-1} for advanced MEA systems, while Bounaceur *et al.* (2006) documented it to be 1.67 kWh kg-CO_2^{-1}. This discussion shows that a direct comparison of specific CO_2 removal capacity in the present concept and that of absorption systems is difficult. However, with the availability of CO_2 specific energy requirement for these systems, it can be seen that the performance of the present concept approaches the performance of the most economical absorption system. Furthermore, the use of solid adsorbents instead of liquid absorbent makes the system durable, thereby reducing maintenance costs of absorbent replacement. As the system is modular, with its gas processing capacity dependent on number of microchannels, the concept is expected to be more versatile for a wider range of applications. As mentioned previously, the process consumes up to 97% of its energy as sensible heat, enhancing its utility in remote applications, where electricity infrastructure is limited but low-grade heat supply is available.

The nominal energy requirement values, when normalized with mass of CH_4-rich product are even smaller than those of the absorption systems utilized for CO_2 removal. The specific energy utilization for a 25 kPa pressure drop and 6% energy ratio is 0.68 kWh kg-product^{-1}, which is lower than the reversible electrical input for the cryogenic distillation process for CO_2 removal (1.0 kWh kg-CO_2^{-1}) (Göttlicher and Pruschek, 1997) and the advanced MEA absorption systems (1.03 kWh kg-CO_2^{-1}). Therefore, the energy

utilization for the purification process under consideration here is competitive with existing large-scale gas separation systems. In summary, the present concept offers very high process capacity, high CH_4 recovery, high product purities, and competitive energy utilization.

3.8 Multistage purification process

To further explore the possibility of enhancing the product purity beyond those reported in Figure 3.10, multistage purification scenarios are considered. Figure 3.12 shows a schematic of a staged purification setup based on present purification concept. The monoliths are arranged in series such that the two sink tanks from the first stage are modeled as the source tanks for the two second-stage monoliths. For this calculation, the intermediate mixing of streams is not considered and the flow of gas is assumed to follow a branching as shown in Figure 3.12. The first stage feed time is kept at the baseline value of 0.19 s, and product collection is assumed to continue until the liquid-gas interface in each monolith reaches the outlet, resulting in the highest possible recovery factors. The process model designed for one microchannel monolith is simulated for three microchannel monoliths with modified boundary conditions as shown in Figure 3.12.

The two intermediate sink tanks, the product gas tank and the desorption gas tank, are designed to release the same amount of gas for the next adsorption stage as that collected from the first stage, so that the thermodynamic equilibrium between the stages is maintained. As an example, of 0.8242 kg kg-ads^{-1} of total feed gas supplied to the first stage monolith in a 0.19 s feed, gas collected in the intermediate product tank is 0.397 kg kg-ads^{-1}, while rest of the gas is collected in the HTF sink tank. For a pressure drop of 100 kPa in the second stage, it takes 0.11 s to send the exact same amount of gas (0.397

kg) into the second monolith; hence, the second stage adsorption time is fixed to 0.11 s. Using this approach, adsorption times for the two monoliths in the second stage are fixed, thereby reducing the total number of degrees of freedom. The intermediate HTF tank contains the gaseous fraction of the component mixture separated from the HTF. Although, this staged purification scenario requires three times the mass of adsorbent and energy than the single stage case; it is possible to achieve product purities as high as 99.8% at a recovery factor of 31.6% at the end of the second stage. By reducing the amount of CO_2 entering the system in the first stage, which is possible by selecting a shorter first stage adsorption time of 0.16 s, the second stage product purity can be increased to 99.9%.

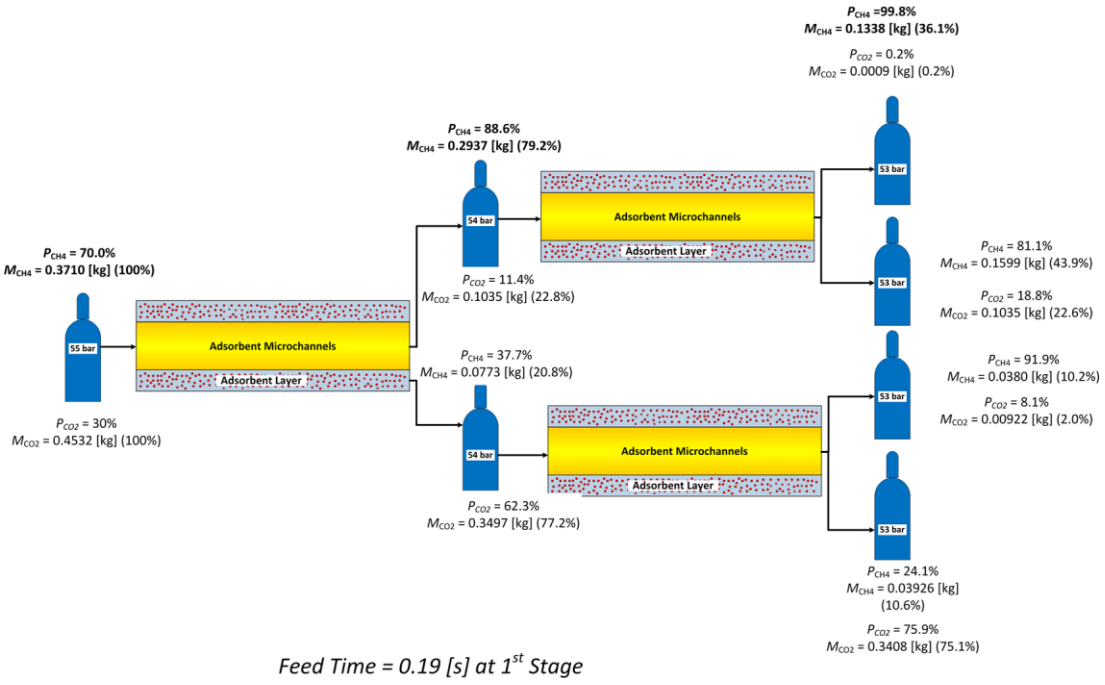

Figure 3.12. Implementation of the microchannel TSA-based purification process for multistage operation. Numerical values show calculated purity and product collected normalized with mass of adsorbent.

It must be noted that with a multistage purification process, the degrees of freedom in the system increase directly with the number of stages and hence, the multistage process performance prediction is highly dependent on the selection of first stage process times, intermediate and final tank pressures, and mixing of gases in the intermediate tanks to maintain a high recovery factor.

3.9 Summary and Conclusions

A novel temperature swing adsorption-based natural gas purification cycle using a monolith consisting of adsorbent-coated microchannels is investigated in Chapters 2 and 3. In Chapter 2, the development of a full process simulation model, and selection of geometric parameters and adsorbent and heat transfer fluid were reported. This Chapter develops a comprehensive performance map of the process that involves determination of ranges of product purity, CH_4 recovery and process capacity, and energy requirements.

The process capacity is found to be up to two orders of magnitude greater than those reported for the adsorbent bed-based PSA systems by Kapoor and Yang (1989) and Olajossy *et al.* (2003) with a competitive set of product purity and CH_4 recovery factors. With a 203.41 s cycle time, and an initial mole fraction of 70% CH_4, a range of product purities from 87% to 99% CH_4 is possible, simultaneously recovering up to 83% CH_4 from the feed stream. Thus, the process capacity and purification performance of the cycle under consideration are found to be better than those of bed-based PSA processes.

The energy requirement for the process is found to be 14% of the product combustion potential and by reducing the pressure drop across the microchannel and recovering heat from the cooling stage, this energy ratio can be further decreased to 6%.

The specific energy utilization predicted for the present work is 0.68 kWh kg-product^{-1} and is found to be lower than the actual energy requirement for MEA absorption systems and the reversible electrical input for cryogenic distillation installations (Göttlicher and Pruschek, 1997). The CO_2-specific energy requirement is also found competitive with the existing adsorption- and MEA absorption-based systems. The TSA-based process in the present study is assessed to be suitable for large-scale industrial applications and can be powered primarily with low-grade heat. The use of microchannels utilizing a small amount of adsorbent per microchannel in addition to convection based fluid dynamics within the microchannel increase the compactness and scalability of the system drastically over existing PSA-based systems. For a single stage purification process, a favorable process performance region is predicted, which yields very high process capacity, moderate CH_4 recovery, high product purities, and moderate energy utilization.

Product purity enhancement by staged purification is also possible with the present concept without affecting cycle design and scalability. Product purities up to 99.9% are possible through appropriate timing of the process stages and by maintaining the necessary thermodynamic equilibrium between the stages. Such an implementation, however, would require a comparative feasibility assessment of utilizing a second stage TSA-based monolith over other processes like cryogenic separation, which also produce high product purity at an increased operating cost.

4 EXPERIMENTS AND MODEL VALIDATION

This chapter starts with a brief review of the prior feasibility analyses of using microchannels for gas separation applications, followed by a discussion of an experimental investigation of gas separation in microchannels. The experimental approach, test procedure and observed trends are discussed. Laboratory scale models are developed to replicate the experimental procedure, followed by heat and mass transfer model validation using the observed data. Finally, findings from the experiments are used to improve designs of adsorption systems.

4.1 Introduction

Adsorption-based gas separation processes utilized for natural gas purification and carbon dioxide capture from flue gas have been shown to benefit from the use of adsorbent-coated microchannels, which yields a greater process capacity, and competitive product purities and gas recoveries when compared with other conventionally used geometries, as discussed in Chapters 2 and 3. Due to high heat and mass transfer coefficients in microchannels, the execution of the various stages of the adsorption-based gas separation cycle is faster than that of adsorbent beds, and a sharp wave front is maintained for the adsorption and regeneration stages of the cycle.

Pressure swing adsorption (PSA) in microchannels is found to be effective because of unimpeded transmission of pressure waves along its length. In a PSA process, the depressurization in microchannels is found very effective when the stage performance is compared with the fixed bed depressurization processes in the literature. Pahinkar *et al.*

(2015) conducted a computational investigation of depressurization in microchannels and reported up to four times greater CO_2 removal capacities, when compared with equilibrium-based CH_4-CO_2 separation studies by Kapoor and Yang (1989) using zeolite 5A and N_2-CO_2 separation studies by Shen *et al.* (2011) using activated carbon. They also predicted up to 25 times greater process capacity with adsorbent-coated microchannels as compared with the PSA process investigated by Krishnamurthy *et al.* (2014).

PSA processes utilizing fixed adsorbent beds are commonly used for gas separation applications, as bed-based temperature swing adsorption (TSA) processes are deemed difficult to implement due to the low thermal conductivity of the adsorbent material as well as due to the presence of void spaces in the bed (Riemer *et al.*, 1994). Therefore, heat duties and process times are expected to be large and heat distribution is found to be ineffective (Moate and LeVan, 2010), negating the large-scale viability of such a system. However, TSA processes in microchannels are enhanced due to high heat and mass transfer coefficients and the small thermal mass of the adsorbent. Lively *et al.* (2009) demonstrated the fabrication of sub-millimeter mixed matrix membrane hollow fibers (MMM), which combine the advantages of polymeric membranes and adsorbent particles (Bernardo *et al.*, 2009), thereby opening up potential avenues for revisiting the use of TSA processes for gas separation. These MMMs can be fabricated within frameworks already available for making conventional polymeric membranes, emphasizing the low capital costs associated with their use. Pahinkar *et al.* (2016) investigated a TSA process for natural gas purification using an adsorbent-polymer matrix based on the hollow fibers reported by Lively *et al.* (2009) with the flow of

working fluids and HTFs through separate, alternating parallel channels. They found that process capacity was improved over bed-based PSA processes by up to an order of magnitude at similar values of purity and recoveries. Subsequently, by sending the process gases and HTF through the same microchannels, they reduced the system footprint considerably while achieving up to five times greater product capacity compared to the design with separate channels, as seen in Chapter 3.

These promising predictions from gas separation process models that use adsorbent-coated microchannels warrant experimental investigations of the heat and mass transfer processes during gas separation and validation of the models with the data. Recently, Lively *et al.* conducted studies to analyze hollow fiber response during gas separation and rapid temperature swing adsorption processes. Lively *et al.* (2009) described a spinning technique to fabricate hollow fibers with high adsorbent fraction to improve separation performance and reported its use to separate CO_2 from N_2 in a flue gas stream. They documented the adsorption capacity and degree of spreading of the breakthrough curve as a function of gas flow rates and module void fractions. They also investigated the effect of cooling water on adsorption stage performance in terms of increase in CO_2 adsorption capacity and reduction of CO_2 breakthrough velocity. Additionally, an effect of cooling water velocity on the amount of the heat of adsorption that can be captured was analyzed (Lively *et al.*, 2009; Lively *et al.*, 2010; Lively *et al.*, 2011; Lively *et al.*, 2012).

Kalyanaraman *et al.* (2015) compared results from experiments on the adsorption stage using hollow fibers with corresponding model results using different flow rates, hollow fiber lengths, and packing fractions. They used sequential flows of flue gas with

helium (He) as tracer, and purged the system with pure N_2. Their results for the CO_2 breakthrough curve for a variety of test conditions are in agreement with the corresponding model results. However, temperature responses noted by Lively *et al.* (2012) and Kalyanaraman *et al.* (2015) were recorded using a single thermocouple located near the axial midpoint of the test section. While its response provides qualitative information in terms of comparative temperature rise for a variety of mass flow rates and packing fractions, the numerical values of the temperature rise for these hollow fibers and a comparison with corresponding model results have been inconsistent (Kalyanaraman *et al.*, 2015). The fixed adsorbent bed breakthrough experiments using metal organic frameworks (MOFs) by Casas *et al.* (2013), however, show consistent agreement between data and adsorption stage models for five axial locations for the temperature measurement and the outlet concentration measurement. Because Casas *et al.* (2013) performed breakthrough experiments on fixed adsorbent beds, one-to-one comparison of the data with adsorbent-coated microchannels and hollow fibers used by Lively *et al.* (2009) is not possible.

The important difference between the hollow fiber configuration investigated in the literature and the adsorbent-coated microchannel monolith considered here is the orientation of working fluid flow. Flue gas typically flows over the hollow fibers in cross flow arrangement, while the water flows axially through the central bore. The CO_2 in the flue gas stream gets adsorbed into the hollow fiber, when cold water flows through the central bore. As the cold water flow is replaced by the hot water flow during desorption, CO_2 is desorbed and is accumulated at the bottom of the module, because it is heavier than other flue gas components. It can be removed from the module thereafter.

The use of adsorbent-coated microchannels simplifies the header and system design due to the use of only one set of microchannels for fabricating a monolith, in a scalable manner, based on design duty. In cross flow arrangements, the number of parallel channels and baffling arrangements used (if any) affects the gas-side pressure drop and heat transfer, while in a microchannel monolith, the performance parameters scale directly with the number of channels in a simple manner.

This Chapter investigates the heat and mass transfer response in the adsorbent layer of a microchannel during batch adsorption (breakthrough) tests under a range of imposed pressure drops (or mass flow rates) and microchannel lengths, which are used to validate the corresponding coupled fluid flow, heat transfer, and mass transfer models.

4.2 Experimental set-up and procedure

The experimental facility constructed for these experiments on the adsorbent-coated microchannels is shown in Figure 4.1. The microchannel is laid out between two fiberglass insulation sheets in a serpentine fashion. This arrangement helps to vary the microchannel length without major modifications in the test set-up. For the first phase of the experiments, PLOT capillary gas chromatograph (GC) columns from Sigma-Aldrich with a 530 μm internal diameter and an average adsorbent layer thickness of 30 μm are used. Zeolite 5A is selected as the adsorbent because of its high affinity and adsorption capacity for CO_2 at near-ambient pressure, leading to a definite capacity gain for CO_2 over other gases in the mixture. The microchannel is made of 60 μm thick fused silica, which provides support to the coated adsorbent layer on the inner circumference of the microchannel.

Bare-wire thermocouples (Omega, TT-T-40, and Type T) are used for temperature measurement over the fused silica coating of the microchannel to track the adsorption thermal wave and heights of the temperature peaks during adsorption. Thermocouples are calibrated using a temperature bath at 5°C, 15°C, 35°C and 50°C. Although the overall size of the thermocouple does not exceed 400 µm, it is impractical to pierce the PLOT column and insert thermocouples in the adsorbent layer, as it would disrupt the adsorption thermal wave and potentially dislodge parts of the adsorbent layer. Hence, these thermocouple wires are attached to the fused silica coating at ten equally spaced axial locations, which also enables easy setup and disassembly to facilitate a variety of channels. These bare-wire thermocouples are coiled and tied onto the outer surface of the microchannel to maximize the contact area and enhance the contact pressure. Application of a thermal sealing agent for this purpose is not found to yield good results, because the thermal mass of the sealant itself is found to absorb a significant amount of energy in the adsorption thermal wave, yielding an incorrect pattern for the fused silica wall temperature. For a copper- copper constantan thermocouple making contact with the wall without any thermal seal, the contact thermal resistance without any application of contact pressure is 0.04 K-m W^{-1} (Dassault Systems, 2011). This value is 3% of the heat transfer resistance from the adsorbent layer to the microchannel and is expected to decrease further as the thermocouple wire is coiled around the wall and its end is forced to make contact with the wall. Therefore, the contact resistance is neglected. The thermocouple hot end is manually fabricated to be as small as possible, to reduce the thermal resistance of the thermocouple itself. For measurement of the absolute pressure at the microchannel inlet, a Rosemount 2088A pressure transducer (Range: 0 to 5500 kPa,

accuracy: ±4.1 kPa) is installed, while an extremely low-flow Coriolis (LF3M series, range: 0 to 0.4 kg hr^{-1}, accuracy: ±1% of the mass flow rate) flow meter from Micro Motion® is used to track the mass flow rate of gases entering the microchannel.

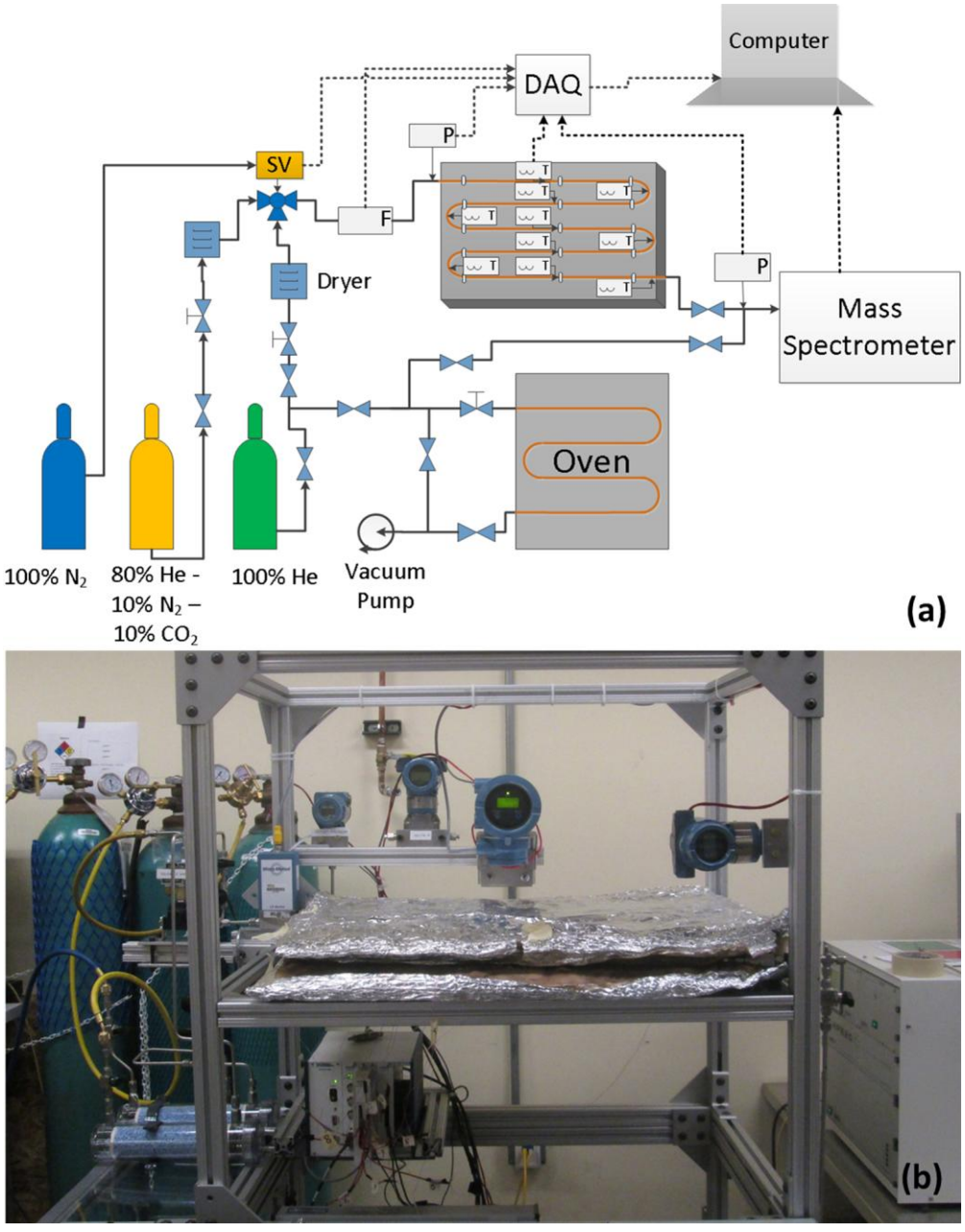

Figure 4.1. (a) Schematic of the test facility used for breakthrough experiments (b) Test facility photograph

A research grade gas cylinder from Airgas® simulates the impure feed mixture (80% He-10% N_2-10% CO_2); while a research grade pure He cylinder is used as the purge gas, which desorbs CO_2 out of the adsorbent and regenerates the microchannel. The N_2 in the feed stream is selected as a tracer gas, which exits the microchannel after insignificant interaction with the adsorbent. The difference in time between when CO_2 exits the microchannel and when N_2 exits is deemed to be the useful adsorption time and is monitored for all experiments. For switching between the feed gas stream and the purge gas stream, a solenoid-controlled, pneumatically actuated T-valve (MAC Valves Inc., external pilot, Pressure range: 170 – 1020 kPa) is used. This T-valve has a measured actuation time of 38 ms and ensures rapid switching of the gas streams, in addition to communicating the time instant at which switching occurs. The analog outputs from each of these instruments are monitored using a National Instruments SCXI-1000 data acquisition system via a 32-channel SCXI-1102 card module and an SCXI-1303 terminal block. Solenoid valve operation is controlled by the same data acquisition system using an SCXI-1161 power relay switch module. The SCXI-1000 system is connected via USB to a computer running a LabVIEW VI, which is responsible for synchronization of the data. A fraction of the gas reaching the microchannel outlet is fed to a Hiden HPR-20 transient mass spectrometer with a temporal resolution of 0.05 s to monitor the gas composition. The signal from the mass spectrometer is synchronized via an Ethernet cable with the same LabVIEW VI.

The experimental procedure consists of sequential flow of impure feed gas and purge gas. Impure gas flow is continued for 40 s, although it takes lesser time for CO_2 in the feed stream to saturate the entire adsorbent layer for all the experiments. Following

this, the solenoid valve is switched to activate the purge gas stream. The purge gas flow is continued for approximately 60 s. The purge stage time is deliberately varied by ±5 s to observe its effects on the adsorption time and temperature rise during adsorption. The solenoid valve is switched to the impure feed gas stream again after the end of the purge duration.

A forced convection oven with a maximum attainable temperature of 225°C (Rickly Hydrological Company) and a vacuum pump (JB Platinum® series, DV-200N) are used to remove trace water from the adsorbent-coated microchannels for 10 hours before each experiment. All the components and sensors are connected using stainless steel Swagelok ¼" fittings along with ball valves to shut-off and needle valves to restrict the gas flows at appropriate locations as shown in Figure 4.1(a). Additionally, laboratory Drierite™ units are installed in the paths of feed gas and purge gas streams to remove trace water vapor present in the gas mixture, before the streams enter the microchannel. The rationale behind the use of desiccants in the experiments, despite the use of research grade cylinders, is explained in a later section. The PLOT column section of the chosen length is cut without causing any damage to it from the procured column of 30 m length for each experiment. This column is then carefully attached to the fittings, which are installed in the oven as shown in Figure 4.1. For the preparation of the test section, an end of the PLOT column is closed, while another end is connected to the vacuum pump. The PLOT column is heated in the oven at 225°C for about 10 hours, and the vacuum pump decreases the pressure in the column to 10 Pa absolute. Due to a very low pressure and high temperature, any contaminants and water vapor that may have entered the test section previously are removed. Once this first regeneration is complete, the PLOT

column is carefully removed from the oven with its ends sealed and is placed between the insulation sheets. During this process, best efforts are made not to disturb the adsorbent layer at the ends of the test section, while the adsorbent layer between the two ends is protected by the fused silica coating. The thermocouples are attached at marked equidistant locations and then the experiment starts by connecting the PLOT column with the plumbing lines allowing the pure gas to flow through the test section. The same test section is not used for a repeated set of experiments, except to study the effects of repeated baking and adsorption.

The adsorption experiments on the GC PLOT columns are conducted for a range of imposed pressure drops (ΔP) from 5 kPa to 55 kPa and microchannel lengths (L) from 1 m to 4 m. The pressure, temperature, mass flow rate and mole fraction readings obtained in breakthrough experiments are analyzed and used for model validation.

4.3 Experimental results and discussion

Figure 4.2 shows sample heat and mass transfer results from the breakthrough experiments for a 2 m long PLOT column and an 18 kPa ΔP without the use of Drierite^{TM} drying units. The results are shown for the entire duration of the feed stage in the experiment. A time of 0 s on the x-axis shows switching of the solenoid valve. At the start of the feed stage, the microchannel is filled with pure He, as seen in Figure 4.2(b). As the solenoid valve is switched, the feed gas enters the microchannel through the auxiliary volume and mass flow meter at the inlet. The delay of about 4 s in the feed mixture reaching the microchannel outlet (point C in Figure 4.2(b)) is attributed to the flow of feed gas through the auxiliary volume at the inlet and then flow of separated He-N_2 through the microchannel. CO_2 on the other hand, travels with the He-N_2 mixture

(point C) to the microchannel inlet, after which it diffuses into the adsorbent and gets adsorbed. Thermocouple readings for the 10 equidistant axial locations in Figure 4.2(a) show a gradual progression of the CO_2 adsorption thermal wave along the microchannel axis. As CO_2 is adsorbed in zeolite 5A, the temperature of the fused silica coating rises quickly locally, and then gradually drops due to heat loss to the ambient through the insulation sheets. The temperature rise (ΔT), however, is not uniform at all locations because of local variations in adsorbent mass fraction and adsorbent layer thickness. As an example, the ΔT between points A and B, for the thermocouple located at 2.0 m downstream of the microchannel inlet, is 2.1°C. However, the average ΔT for all thermocouples is 1.8°C, and enables prediction of the overall heat transfer process during adsorption, instead of relying on a single thermocouple to estimate the heat of adsorption. Once CO_2 saturates the entire adsorbent layer, it exits the microchannel and is detected by the mass spectrometer. After this time, marked by point D in Figure 4.2(b), further influx of feed gas into the microchannel does not change the concentration. The horizontal distance between points C and D, 12.3 s, indicates the useful adsorption time for the experimental conditions and PLOT column being tested.

The results in Figure 4.2 are discussed for illustration of the experimental procedure; however additional PLOT columns are used for a comprehensive set of adsorption experiments, by varying the ΔP and L. The adsorption experiment is repeated to obtain ten readings for each combination of ΔP and L by sequential switching of the solenoid valve as explained previously.

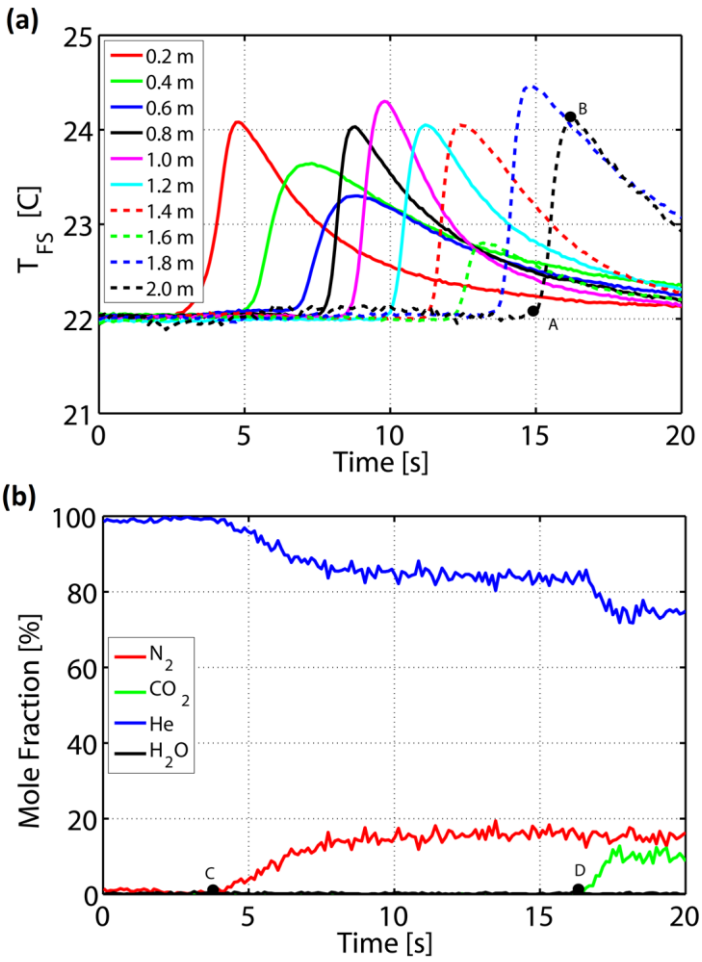

Figure 4.2. (a) Heat transfer (b) mass transfer results from the adsorption experiments on PLOT column (ΔP = 18 kPa, L = 2 m)

Figure 4.2(b) also shows that trace amount of water vapor is present at the microchannel outlet, which complicates the repeatability analysis. Although present in trace quantities, it suppresses CO_2 adsorption and shows a resistance to desorption in presence of a pure He purge. It is known that zeolite 5A has a greater affinity and adsorption capacity for water than for CO_2 (Gholami and Talaie, 2009); therefore, in a competitive adsorption situation of water and CO_2, water precludes any CO_2 adsorption and is the dominant adsorbate. The trace water is not able to generate an adsorption

temperature peak like those generated by the adsorption of 10% CO_2 by volume, nevertheless a gradual saturation of adsorption sites can be seen in Figure 4.3.

In Figure 4.3, the top two charts (labeled as Test 1) show the mass and heat transfer performance illustrated in Figure 4.2. As the experiment is repeated by switching the solenoid valve (40 s for the feed stage, and 60 s for the purge stage), the CO_2 adsorption temperature peaks start to gradually disappear from the heat transfer data (right), simultaneously decreasing the adsorption time (left). The adsorption sites become unresponsive to the change in concentration of CO_2 in the microchannel, reflected by the minimal change in temperature. Once CO_2 adsorption is suppressed in the upstream sites, the net adsorption capacity of the adsorbent layer decreases and therefore the feed CO_2 appears in the outlet stream earlier than in the preceding experiment. For the experimental conditions illustrated in Figure 4.3, it is found that after 32 repetitions, all the adsorption sites are blocked by water and no CO_2 can be adsorbed by the PLOT column. This observation leads to the conclusion that trace water present in the gas cylinder must be entirely removed to obtain a repeatable set of heat and mass transfer data that can be correlated with the model results. To achieve this, Drierite^{TM} units are installed upstream of the microchannel.

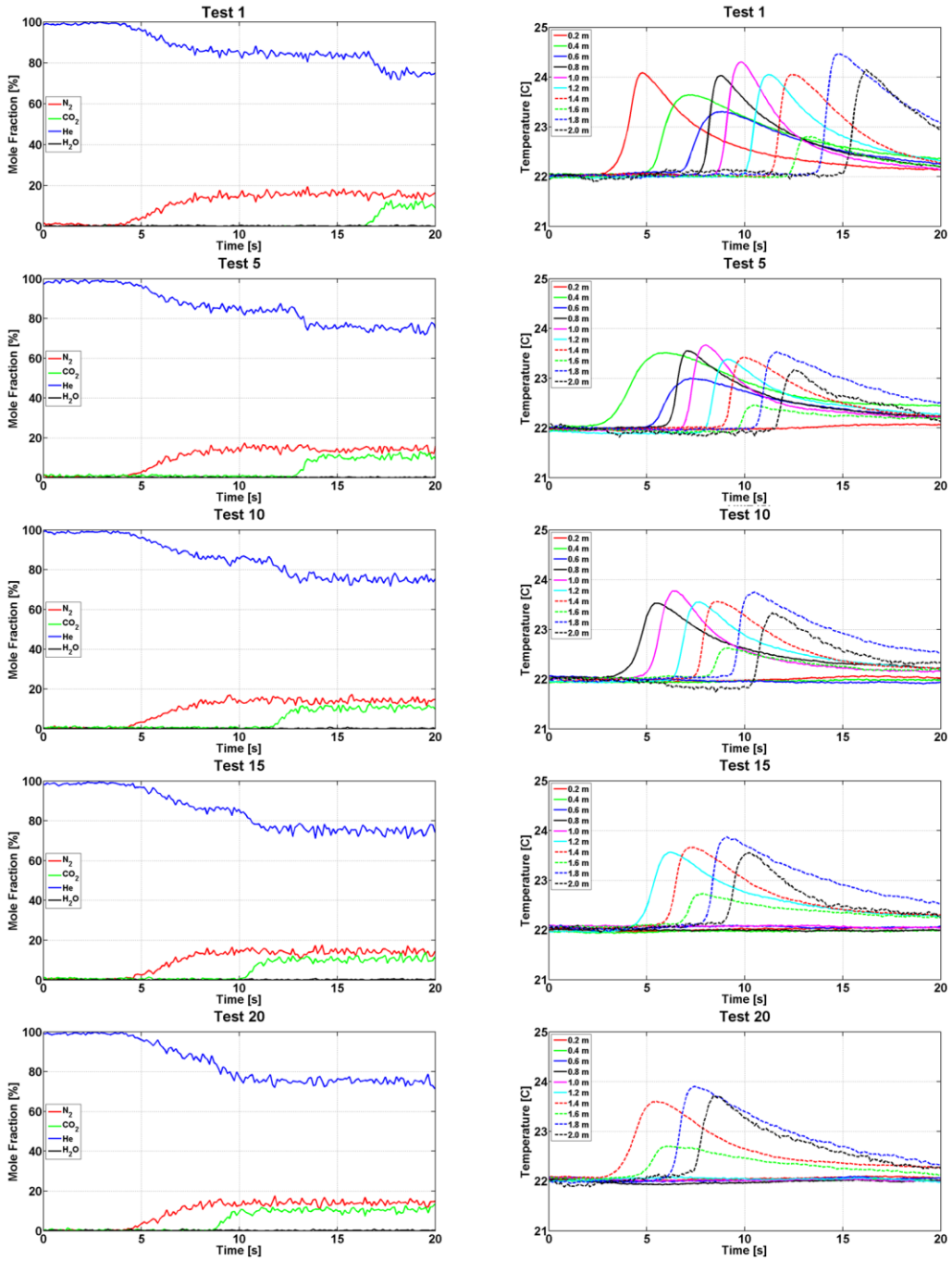

Figure 4.3. Mass transfer (left) and heat transfer (right) results for a repeating set of adsorption experiments showing water saturating the adsorption sites gradually.

The adsorption experiments are then repeated for a range of imposed ΔP from 5 kPa to 55 kPa and L from 1 m to 4 m, and the adsorption times and the average and the maximum ΔT for each of the readings are noted. The summary of the adsorption experiments with the PLOT columns is shown in Figure 4.4. Figure 4.4(a) shows the variation of adsorption time with ΔP for L ranging from 1 to 4 m. Each of the clusters has 10 points, as the experiments are repeated ten times for each combination of ΔP and L.

As shown in Figure 4.4(a), as the ΔP across the microchannel increases for a given L, the time required to saturate the PLOT column adsorbent decreases. Additionally, for the same ΔP, an increase in L delays the saturation of the adsorbent, which again is in accordance with the expected pattern. Figure 4.4(b) shows the average ΔT as a function of ΔP. As the ΔP across the PLOT column increases for a value of L, the average ΔT during adsorption increases slightly. This increase is due to the marginal increase in the capacity of the adsorbent with an increase in partial pressure. This observation is also demonstrated in the ΔT vs. adsorption time graph shown in Figure 4.4(c). From the clusters of data points representing one test condition, it can be seen that as the adsorption time increases, the average ΔT increases, indicating increased adsorbent capacity. However, no pattern confirming the interdependence of L and ΔT can be discerned.

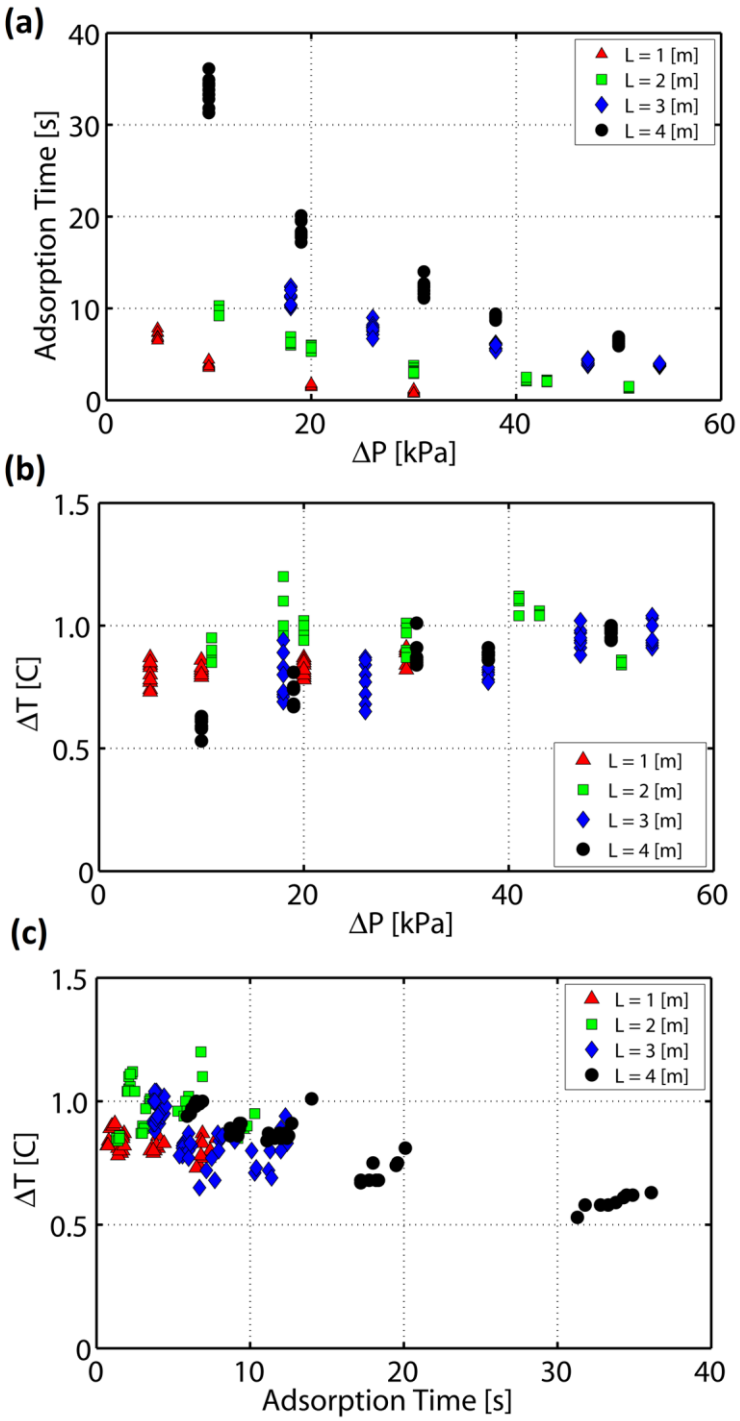

Figure 4.4. Adsorption experiment results for PLOT columns (a) Adsorption time vs. ΔP (b) average ΔT vs. ΔP (c) average ΔT vs. adsorption time

The uncertainties associated with the measurement of pressure, temperature, mass flow rate and mole fractions affect the heat and mass transfer results discussed in Figure 4.4. Type-A uncertainty, which considers random variation of the measured variable around the sample mean is represented by the standard deviation of the mean and is calculated using Equation (4.1) (Coleman and Steele, 1989).

$$U_A = \left[\frac{1}{N(N-1)} \sum_{i=1}^{N} \left(X_i - \bar{X} \right)^2 \right]^{1/2} \tag{4.1}$$

Type-B uncertainty is the systematic error or the manufacturer specified uncertainty for the specific component. Equation (4.2) is used to calculate systematic error in the measurement by sensors. Total uncertainties for all the components are calculated using Equation (4.3) and are listed in Table 4.1 (Coleman and Steele, 1989).

$$U_B{}^2 = \frac{\sum_{i=1}^{N} \left[Y_i - (aX_i + b) \right]^2}{N-2} \tag{4.2}$$

$$U^2 = U_A{}^2 + U_B{}^2 \tag{4.3}$$

Table 4.1. Calculated uncertainties for sensors

Sensor	Type A	Type B	Total
Pressure [kPa]	0.0080	4.1000	4.100
Mass flow rate [kg hr^{-1}]	0.0070	0.0040	0.008
Temperature [C]	0.0003	0.0307	0.031
Mass spectrometer [%]	0.0680	1.0800	1.082

Calculated Type-B uncertainties and absolute total uncertainties for the monitored variables are also listed in Table 4.1. Engineering Equation Solver (EES) software (Klein, 2016) is employed to calculate uncertainty propagation in the adsorption time. The uncertainty in adsorption time [s], i.e., the lag time between fluid breakthrough and

adsorbent breakthrough, is a function of uncertainty in gas velocity [m s^{-1}], *th* [m] and *L* [m]. The uncertainty variation in adsorption time is not reported uniquely, because the uncertainty in adsorption time has different values for different tests, based on the feed velocity and length. For a ΔP of 10 kPa across a 4 m long channel, the absolute uncertainty in adsorption time is calculated as 13.8 s, while the measured adsorption time is 33.6 s (41% relative uncertainty). For the same length, a ΔP of 50 kPa results in an absolute uncertainty of 0.6 s for the measured adsorption time of 6.6 s (9% relative uncertainty). For the range of tests conducted in this study, the minimum, maximum and average uncertainties in adsorption times are 0.03 s, 13.8 s, and 1.37 s (relative uncertainties of 6.83%, 41% and 22.52%), respectively. These uncertainties are discussed in greater detail in subsequent sections, in conjunction with comparisons between the measurements and model predictions.

4.4 Model development

Fluid flow, heat and mass transfer models are developed for the laboratory adsorption tests described above. Figure 4.5 shows a schematic of the model architecture used for development of the adsorption stage model in gPROMS ModelBuilder™ (Process Systems Enterprise, 1997-2015).

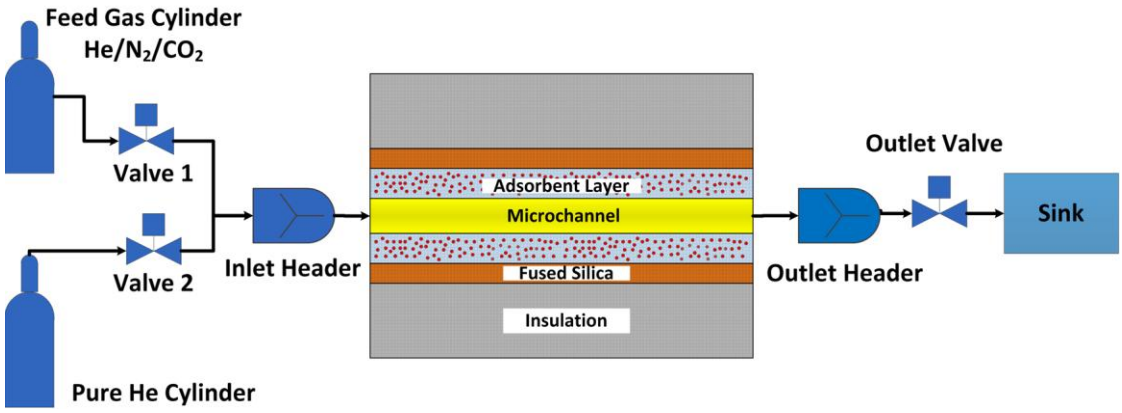

Figure 4.5. Lab scale model architecture

4.4.1 Adsorbent-coated microchannel equations

While the adsorbent-coated microchannel simulated in the adsorption stage model uses the exact dimensions of the PLOT columns used for adsorption experiments (530 µm diameter, 30 µm adsorbent layer thickness, and variable L), a few considerations are necessary for conceptualizing the adsorption process in PLOT columns. The composite matrix approach used by Pahinkar *et al.* (2015) can be used for modeling adsorption in PLOT columns; however, the binder used for holding the adsorbent onto the inner surface of the fused silica cover needs to be differentiated from the glassy polymer, PEI selected by Pahinkar *et al.* (2015). The adsorbent-binder matrix used in the present work is zeolite 5A- silica. The overall material properties of the adsorbent layer are estimated using appropriate weighted averages discussed by Pahinkar *et al.* (2015). The additional adsorbent layer properties, the adsorbent layer void fraction (ε) and adsorbent loading (ratio of adsorbent mass to binder mass, MF) are important to predict the breakthrough time and ΔT. However, these properties are proprietary to the manufacturer and must be estimated using a combined test-modeling approach, illustrated in later sections. The values of other parameters and material properties used for the simulation are given in

Table 4.2. For modeling ternary diffusion of gases in the adsorbent layer, an approach illustrated by Pahinkar *et al.* (2016) is adapted. This approach consists of calculation of an effective ordinary (molecular) diffusion coefficient using Chapman-Enskog theory as shown in Equation (4.4).

$$D_{ij,eff,ordinary} = \frac{1.858\times10^{-27}\cdot T^{1.5}}{Pd^2\Omega}\sum_i\left(\frac{1}{MW_i}\right)^{0.5}\frac{\varepsilon}{\tau} \tag{4.4}$$

The effective diffusion coefficient is then used to calculate the diffusion coefficient of a species in the ternary mixture using Equation (4.5) (Hines and Maddox, 1985).

$$D_{i,mix,eff,ordinary} = \frac{1-x_i}{\sum_{j\neq i}\frac{x_j}{D_{ij,eff,ordinary}}} \tag{4.5}$$

At the pressure at which the tests were conducted, Knudsen diffusion is also expected to be important. The Knudsen diffusion coefficient is calculated using Equation (4.6) (Cussler, 1997).

$$D_{eff,Knudsen} = \frac{d_{pore}}{3\tau}\sqrt{\frac{8R_uT_w}{\pi MW_{mix}}} \tag{4.6}$$

The effective total diffusion coefficient is thus calculated using Equation (4.7) from the ordinary diffusion coefficient and the Knudsen diffusion coefficient (Gholami and Talaie, 2009).

$$\frac{1}{D_{i,eff,total}} = \frac{1}{D_{i,mix,eff,Ordinary}} + \frac{1}{D_{eff,Knudsen}} \tag{4.7}$$

Table 4.2. Numerical values of parameters used for simulation

Parameter	Value
T_0	22°C
N_{nodes}	500
ρ_{FS}	2200 kg m^{-3}
k_{FS}	1.3 W m^{-1} K^{-1}
$c_{P,\,FS}$	740 J kg^{-1} K^{-1}
eps	2×10^{-5} m
ρ_{ads}	1480 kg m^{-3}
k_{ads}	1.2 W m^{-1} K^{-1}
$c_{p,ads}$	800 J kg^{-1} K^{-1}
ρ_{binder}	2648 kg m^{-3}
k_{binder}	1.3 W m^{-1} K^{-1}
$c_{p,binder}$	730 J kg^{-1} K^{-1}
$r_{crystal}$	10^{-6} m
C_T	20 s^{-1}
C_v	10^{-7} kg s^{-1} kPa^{-1}
V_{in}	5.87×10^{-7} m^3
V_{out}	2.13×10^{-7} m^3
τ	2
D_h	530 μm
th	30 μm
th_{FS}	60 μm
th_{ins}	13 mm
ε_r	0.1

Figure 4.6 shows a comparative assessment of ordinary and Knudsen diffusion coefficients for the pressure ranges considered in the present work. The Knudsen number (*Kn*), which compares the mean free path of the gases in the adsorbent layer and the pore size, is calculated using Equation (4.8), while Equation (4.9) is used to calculate the mean free path of the gases.

$$Kn = \frac{\lambda}{d_{pore}} \tag{4.8}$$

$$\lambda = \frac{K_B \cdot T}{\sqrt{2}\pi {d_{molecule}}^2 \cdot P} \tag{4.9}$$

For the laboratory scale experiments conducted at atmospheric conditions, the mean free path of the gases in the ternary mixture is estimated to be 80 nm. The macroporous void size in the adsorbent layer then becomes comparable with the mean free path, which means that the gas molecules are equally likely to collide with the adsorbent layer as with themselves. As shown in Figure 4.6(a), *Kn* and d_{pore} have a hyperbolic relationship, and Knudsen diffusion is usually ignored if $Kn < 0.05$. For the present scenario, Knudsen diffusion can be neglected if d_{pore} were greater than 1550 nm for 100 kPa. For small adsorbent particles of size 1000 nm, it is unlikely that the size of the pore connecting the adsorbent particles exceeds 1500 nm for a realistic porous binder-adsorbent crystal packing arrangement. Therefore, incorporation of both mechanisms – Knudsen diffusion and molecular diffusion as shown in Equation (4.7) is essential for accurate mass transfer resistance calculation in the present study. Also, as seen in Figure 4.7(b), the magnitudes of both the diffusion coefficients are comparable.

As the pressure increases, the ordinary diffusion coefficient decreases as compared to the Knudsen diffusion coefficient, thereby forming the path of greater resistance to gas flow and the governing factor in gas transport. A simultaneous reduction in *Kn* with an increase in pressure decreases the importance of the Knudsen mechanism accordingly. Such a behavior is only possible at high gas pressures, such as those utilized in the process modeling described in Chapter 2. For the present experimental work, however, the use of Equation (4.7) is justified in the present work and an average value of $d_{pore} = 1000$ nm is chosen for simulation.

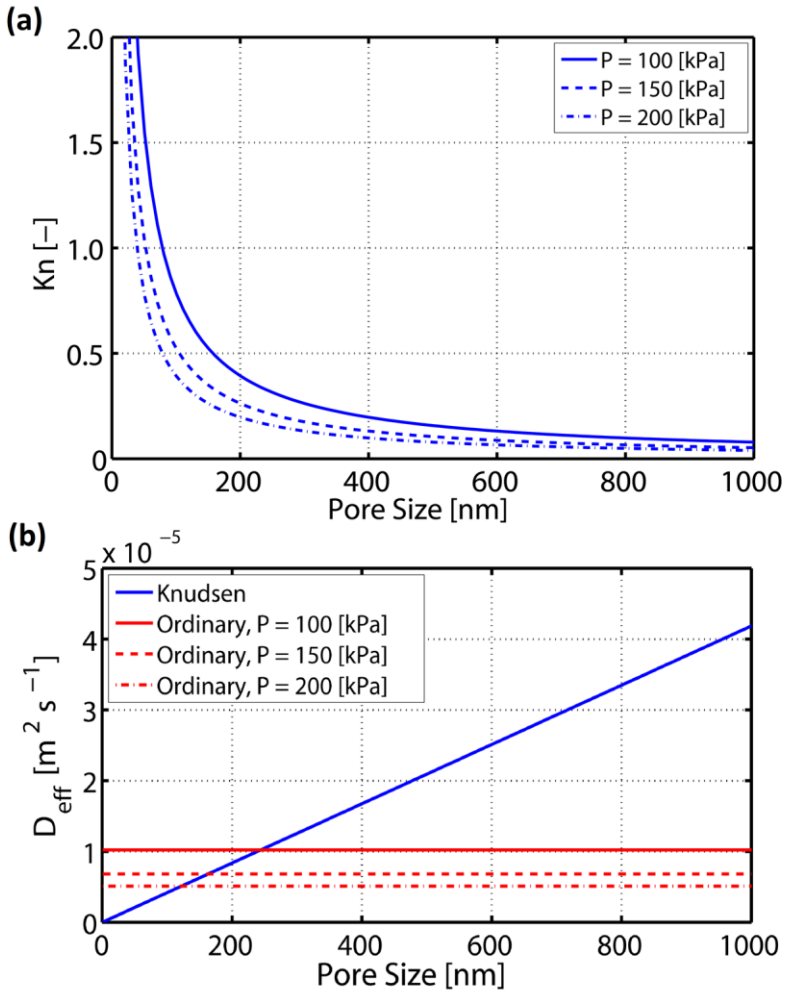

Figure 4.6. (a) Knudsen number variation with adsorbent layer pore size (b) Comparison of Ordinary and Knudsen diffusion coefficients and their variation with pore sizes

Finally, the total diffusion coefficient is substituted in the mass transfer resistance analogy as shown in Equation (4.10), as described by Pahinkar *et al.* (2015). The film or convective mass transfer coefficient, h_m, in Equation (4.10) is estimated using the Churchill (Churchill, 1977a; Churchill, 1977b) correlations. This mass transfer resistance is substituted in the governing conservation equations, which are discussed in later sections.

$$\mathrm{R}_{Mass,i} = \frac{1}{h_m \cdot Peri} + \frac{\ln\left(\frac{R_{w,mid}}{R_h}\right)}{2\pi D_{i,eff,total}} \tag{4.10}$$

The dual-site Langmuir (DSL) equation is used for calculating the competitive adsorption isotherms for N_2 and CO_2 in the zeolite 5A adsorbent crystals as shown in Equation (4.11) along with temperature dependence shown in Equations (4.12) through (4.15) . Helium is assumed to be non-interacting with zeolite 5A. Auxiliary parameters and coefficients used in the DSL equations are listed in Table 4.3 (Gholami and Talaie, 2009).

$$C_{A,Eq,i} = \rho_{ads}\left(M_{B,i}\frac{B_i \cdot P_i}{1+\sum_i B_i \cdot P_i} + M_{D,i}\frac{D_i \cdot P_i}{1+\sum_i D_i \cdot P_i}\right) \tag{4.11}$$

$$B_i = b_{0i}\exp\left(\frac{-Q_{B,i}}{RT_w}\right) \tag{4.12}$$

$$D_i = d_{0i}\exp\left(\frac{-Q_{d,i}}{RT_w}\right) \tag{4.13}$$

$$M_{B,i} = \frac{A_{1,i}}{T_w} + A_{2,i} \tag{4.14}$$

$$M_{D,i} = \frac{A_{3,i}}{T_w} + A_{4,i} \tag{4.15}$$

To model the microporous diffusion and account for intra-crystalline diffusivity, the LDF constant shown in Equation (4.16) is used. Intra-crystalline diffusivity of the gases in the adsorbent is a function of activation energy and adsorbent layer temperature and can be determined using Equation (4.17). The constant, K_{LDF}, is then used in Equation (4.18) to determine the instantaneous rate of adsorption. The heat of adsorption

of component gases on zeolite 5A crystals is calculated using Equation (4.19) (Gholami and Talaie, 2009).

$$K_{LDF,i} = \frac{15 \cdot D_{crystal,i}}{r_{crystal}^{\ 2}} \tag{4.16}$$

$$D_{crystal,i} = D_{o,crystal,i} e^{\left(-\frac{E_i}{RT_w}\right)} \tag{4.17}$$

$$\frac{\partial C_{A,i}}{\partial t} = K_{LDF,i} \cdot \left(C_{A,Eq,i} - C_{A,i}\right) \tag{4.18}$$

$$\Delta H_{ads,i} = \frac{-Q_{B,i} \cdot M_{B,i} \cdot B_i \cdot \left(1 + D_i \cdot P_i\right)^2 - Q_{D,i} \cdot M_{D,i} \cdot D_i \cdot \left(1 + B_i \cdot P_i\right)^2}{M_{B,i} \cdot B_i \cdot \left(1 + D_i \cdot P_i\right)^2 + M_{D,i} \cdot D_i \cdot \left(1 + B_i \cdot P_i\right)^2} \tag{4.19}$$

Table 4.3. Auxiliary parameters for competitive DSL equation used for estimation of zeolite 5A adsorbent capacity and intra-crystalline diffusion coefficient (Gholami and Talaie, 2009)

Factor	CO_2	N_2
A_1, mol K kg^{-1}	516.743	605.423
A_2, mol kg^{-1}	-0.794	-0.582
A_3, mol K kg^{-1}	-932.131	605.423
A_4, mol kg^{-1}	6.083	-0.582
b_0, kPa^{-1}	3.32×10^{-7}	3.73×10^{-7}
Q_B, J mol^{-1}	-41077.1	-7528.09
d_0, kPa^{-1}	6.43×10^{-7}	3.18×10^{-7}
Q_D, J mol^{-1}	-29812.29	-7941.248
$D_{o,crystal}$, m^2 s^{-1}	5.9×10^{-11}	5.2×10^{-13}
E, J mol^{-1}	26334	6275

Estimation of the heat transfer resistance in the experiments is critical to establish a correlation with the data. In the experimental set-up, the adsorbent-coated microchannel is laid between two fiberglass insulation sheets, which are coated with aluminum foil to reduce the radiation heat loss as shown in Figure 4.1(b). The heat transfer resistance network is shown in Figure 4.7. As CO_2 is adsorbed into zeolite 5A in the adsorbent layer (shown in green in Figure 4.7), heat of adsorption is released. This heat is partially picked up by the adjoining gas stream in the microchannel (yellow region in Figure 4.7(b)), and

partially absorbed by the fused silica cover (brown region in Figure 4.7(b)). This heat, in turn, is lost to the ambient by conduction through the insulation and by convection and radiation simultaneously.

The heat transfer resistances required for the conservation equations are calculated as shown in Equations (4.20) through (4.25). Calculation of heat transfer resistances from the microchannel node to the adsorbent layer node and that from adsorbent layer node to the fused silica node is straightforward and adapted from the work by Pahinkar *et al.* (2015). Heat transfer from the fused silica cover to the ambient is calculated using Equation (4.22).

$$\mathrm{R}_{Heat,g\leftrightarrow w} = \frac{1}{h_T \cdot Peri} + \frac{\ln\left(\frac{R_{w,mid}}{R_h}\right)}{2\pi k_w} \tag{4.20}$$

$$\mathrm{R}_{Heat,w\leftrightarrow FS} = \frac{\ln\left(\frac{R_h + th}{R_{w,mid}}\right)}{2\pi k_w} + \frac{\ln\left(\frac{R_{FS,mid}}{R_h + th}\right)}{2\pi k_{FS}} \tag{4.21}$$

$$\mathrm{R}_{Heat,FS\leftrightarrow\infty} = R_{Heat,ins} + \left(\frac{1}{\mathrm{R}_{Heat,conv}} + \frac{1}{R_{Heat,rad}}\right)^{-1} \tag{4.22}$$

Heat is assumed to flow through the insulation sheet followed by losses to the ambient by convection and radiation. The individual heat transfer resistances in Equation (4.22) are calculated using Equations (4.23) through (4.25).

$$\mathrm{R}_{Heat,conv} = \frac{1}{h_{free} Peri_{ins}} \tag{4.23}$$

$$\mathrm{R}_{Heat,rad} = \frac{1}{h_{rad} Peri_{ins}} \tag{4.24}$$

$$R_{Heat,ins} = \frac{\ln\left(\frac{R_{FS,mid}}{R_{Ins,inner}}\right)}{2\pi k_{FS}} \tag{4.25}$$

Equations (4.26) and (4.27) show the calculation of convection (Churchill and Chu, 1975) and radiation heat transfer coefficients (Incropera *et al.*, 2011) for the experimental environment. For the convection heat transfer coefficient, the empirical correlation for a horizontal cylinder is used. Additional details about the calculation of natural convection and radiative heat transfer coefficients, insulation surface temperature, and rate of heat loss for a range of temperature differences between the fused silica cover and the ambient are provided in Appendix E. Although the test section is laid between two large flat surfaces, use of the Nusselt number correlation for flat plate over-predicts the heat transfer coefficient by 20% because the adsorbent-coated microchannels do not make contact with the fiber glass plates at all locations, as shown in Figure 4.1(a). Regardless, the convective and radiative heat transfer coefficients remain very small in the test environment (2.8 and 0.6 W m^{-2} K^{-1}, respectively).

$$h_{free} = \frac{k_{air}}{D_{ins}}\left[0.60 + \frac{0.387 \times Ra_D^{\left(\frac{1}{6}\right)}}{\left[1+\left(\frac{0.559}{\mathrm{Pr}}\right)^{\left(\frac{9}{16}\right)}\right]^{\left(\frac{8}{27}\right)}}\right]^2 \tag{4.26}$$

$$h_{rad} = 4\varepsilon_r \sigma T_0^{\,3} \tag{4.27}$$

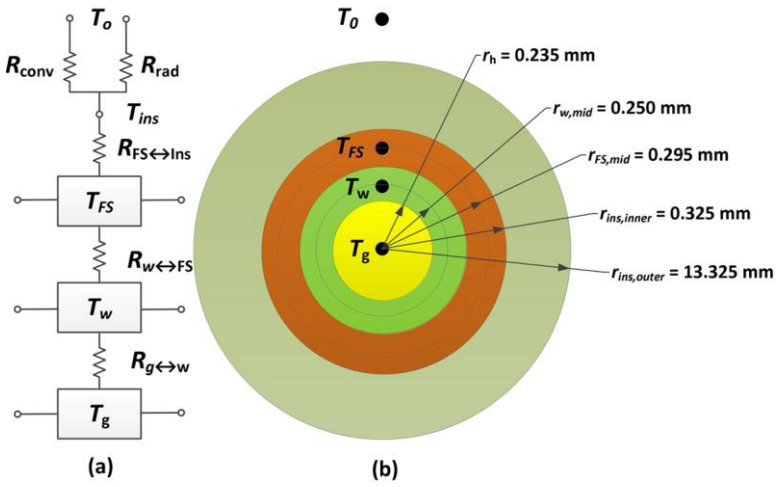

Figure 4.7. (a) Heat transfer resistance networks from microchannel gas node to the ambient temperature node (b) Dimensions of the thermal mass nodes.

The mass transfer resistance calculated in Equation (4.10) and the heat transfer resistances calculated using Equations (4.20) through (4.22) are substituted in the total mass, species, momentum and energy conservation equations for the adsorbent-coated microchannel nodes, adsorbent layer nodes, and fused silica cover nodes and are coupled with each other, as shown in Table 4.4. This coupling helps in predicting the fused silica coating temperature, which can be compared with the measured temperatures. The axial dispersion coefficient, $D_{A,i}$, in the species balance equation for the microchannel is calculated as shown in Equation (4.28) (Cussler, 1997). The boundary conditions and initial conditions for the governing equations are also listed in Table 4.4. The conservation equations for the adsorbent-coated microchannel assembly are coupled with the inlet and outlet headers as shown in Figure 4.5.

$$Pe_i = \frac{uD_h}{D_{AB,i}}$$
$$D_{A,i} = D_{AB,i}\left(1+\frac{Pe_i^{\,2}}{192}\right) \tag{4.28}$$

4.4.2 Header equations

Inlet and outlet header models simulate the mixing of gases in the experiments. Although the switching of the solenoid valve in the experiments changes the concentration at the valve outlet almost instantaneously, the auxiliary volume at the inlet causes the pure and feed streams to mix and decrease the sharpness of the concentration front. Due to axial dispersion of the gas, a plug flow type gas displacement is not observed. In a similar fashion, the concentration wave during adsorption may weaken due to the presence of auxiliary volume at the outlet as the front reaches the microchannel outlet.

Therefore, the adsorption stage model incorporates inlet and outlet header models, which for a given header volume calculate the density, pressure, mass fractions, and enthalpy of the mixture after gas mixing. These variables are then coupled to the corresponding boundary variables of the adsorbent-coated microchannel. The estimated header volumes in the test set-up are listed in Table 4.2. Equations (4.29) through (4.31) show the total mass, species and energy balance equations for the headers. Equation (4.32) relates instantaneous density and the header volume.

$$\frac{dM}{dt} = \sum_{Inlet,\,ports} \dot{m} - \sum_{Outlet,\,ports} \dot{m} \tag{4.29}$$

$$\frac{dM_i}{dt} = \sum_{Inlet,\,ports} \dot{M} \cdot y_i - \sum_{Outlet,\,ports} \dot{M} \cdot y_i \tag{4.30}$$

$$\frac{dU}{dt} = \sum_{Inlet,\,ports} \dot{m} \cdot h_{in} - \sum_{Outlet,\,ports} \dot{m} \cdot h_{out} \tag{4.31}$$

$$M = \rho \cdot V \tag{4.32}$$

Table 4.4. Governing equations and their boundary and initial conditions

Description	Equations
Microchannel - Total Mass Balance	$\frac{\partial \rho}{\partial t}+\frac{\partial(\rho u)}{\partial z}=-\sum_i \frac{C_{g,i}-C_{w,i}}{A_g \cdot \mathrm{R}_{Mass,i}}$ **BCs** $\left.\frac{\partial(\rho u)}{\partial z}\right\|_{z=0}=\left.\frac{\partial(\rho u)}{\partial z}\right\|_{z=L}=0$, **IC** $u=\sqrt{\frac{\Delta P}{L}\frac{2D_h}{\rho f}}$
Microchannel - Species balance	$\rho\frac{\partial y_{g,i}}{\partial t}+\rho u\frac{\partial y_{g,i}}{\partial z}-y_{g,i}\sum_i\frac{C_{g,i}-C_{w,i}}{A_g\cdot \mathrm{R}_{Mass,i}}=D_{A,i}\frac{\partial}{\partial z}\left(\frac{\partial C_{g,i}}{\partial z}\right)+\frac{C_{g,i}-C_{w,i}}{A_g\cdot \mathrm{R}_{Mass,i}}$ **BCs** $\left.\frac{\partial(\rho y_i)}{\partial z}\right\|_{z=0}=\left.\frac{\partial(\rho y_i)}{\partial z}\right\|_{z=L}=0$, **IC** $y_{i,g}=y_{i,product}$
Microchannel - Momentum balance	$\rho\frac{\partial u}{\partial t}+\rho u\frac{\partial u}{\partial z}-\sum_i\frac{C_{g,i}-C_{w,i}}{A_g\cdot \mathrm{R}_{Mass,i}}u=-\frac{\partial P}{\partial z}+\mu\frac{\partial^2 u}{\partial z^2}-f\frac{\rho u^2}{2D_h}$ **BCs** $P\|_{z=0}=P_{v1,out}$, $P\|_{z=L}=P_{v2,in}$; **IC** $P=P_{feed}-(P_{feed}-P_{vacuum})\frac{z}{L}$
Microchannel - Energy Balance	$\frac{\partial(U_g)}{\partial t}+\frac{\partial(u\cdot h_g)}{\partial z}=\frac{\partial}{\partial z}\left(k_g\frac{\partial T_g}{\partial z}\right)-\frac{T_g-T_w}{A_g\cdot \mathrm{R}_{Heat,g\leftrightarrow w}}$ **BCs** $\left.\frac{\partial(h_g)}{\partial z}\right\|_{z=0}=\left.\frac{\partial(h_g)}{\partial z}\right\|_{z=L}=0$, **IC** $T_g=T_0$
Adsorbent layer – Species balance	$\frac{\partial C_{w,i}}{\partial t}+\frac{\omega}{\varepsilon}\frac{\partial C_{A,i}}{\partial t}=\frac{\partial}{\partial z}\left(D_{eff,i}\frac{\partial C_{w,i}}{\partial z}\right)+\frac{C_{g,i}-C_{w,i}}{A_w\cdot \mathrm{R}_{Mass,i}}$ **BCs** $D_{eff,i}\left.\frac{\partial C_{w,i}}{\partial z}\right\|_{z=0}=D_{eff,i}\left.\frac{\partial C_{w,i}}{\partial z}\right\|_{z=L}=0$, **IC** $y_{i,w}=y_{i,product}$
Adsorbent layer – Energy balance	$(1-\varepsilon)\rho_w C_{p,w}\frac{\partial T_w}{\partial t}=(1-\varepsilon)k_w\frac{\partial^2 T_w}{\partial z^2}+\frac{T_g-T_w}{A_w\cdot \mathrm{R}_{Heat,g\leftrightarrow w}}+\sum_i\omega\cdot h_{ads,i}\frac{\partial C_{A,i}}{\partial t}+\frac{T_{FS}-T_w}{A_w\cdot \mathrm{R}_{Heat,w\leftrightarrow FS}}$ **BCs** $k_w\left.\frac{\partial T_w}{\partial z}\right\|_{z=0}=k_w\left.\frac{\partial T_w}{\partial z}\right\|_{z=L}=0$, **IC** $T_w=T_0$
Fused silica cover – Energy balance	$\rho_{FS}C_{p,FS}\frac{\partial T_{FS}}{\partial t}=k_{FS}\frac{\partial^2 T_{FS}}{\partial z^2}+\frac{T_w-T_{FS}}{A_{FS}\cdot \mathrm{R}_{Heat,w\leftrightarrow FS}}+\frac{T_\infty-T_{FS}}{A_{FS}\cdot \mathrm{R}_{Heat,FS\leftrightarrow\infty}}$ **BCs** $k_{FS}\left.\frac{\partial T_w}{\partial z}\right\|_{z=0}=k_{FS}\left.\frac{\partial T_w}{\partial z}\right\|_{z=L}=0$, **IC** $T_{FS}=T_0$

4.4.3 Valve equations

Simple linear opening type valves are used for the simulation of the adsorption stage experiments, so that the valves themselves do not impose a significant additional pressure drop on the flow, and the breakthrough patterns are analyzed primarily based on the pressure drop constraints, which are measured by the pressure sensors in the test facility. Equation (4.33) shows the flow model for the valves (Pahinkar *et al.*, 2015), whereas the values for the valve time constant C_T and flow coefficient, C_v are listed in Table 4.2.

$$\begin{aligned} \dot{m}_v &= V_{p,actual} \cdot C_v \cdot \Delta P \\ \frac{dV_{p,actual}}{dt} &= C_T \left(V_{p,assigned} - V_{p,actual} \right) \end{aligned} \tag{4.33}$$

4.4.4 Source and sink models

Source and sink models, which simply list the feed and outlet pressures, gas inlet and outlet temperatures, and feed composition are also incorporated and connected with the valve models. The outlet pressure is atmospheric pressure, while the inlet pressure is chosen based on the experimental value in the test matrix. The feed and purge gas compositions are the same as the feed (80% He, 10% N_2, 10% CO_2 by volume) and purge cylinder (pure He) chosen for the experiments.

4.4.5 Simulation procedure

The models for the components, shown in Figure 4.5, are coupled with each other by equating the corresponding flow variables (pressure, mass fraction, mass flow rate and enthalpy). The operation of a single solenoid valve in the test set-up is simulated by simultaneous operation of valves 1 and 2 at the inlet. The model is implemented and solved in gPROMS ModelBuilder^{TM}, while the gas thermo-physical properties are

imported from the Multiflash property package (Process Systems Enterprise, 1997-2015). A second order central differencing scheme with an implicit time step calculation is used for simulation of the governing equations. The grid Peclet number, shown in Equation (4.34), which must be less than two for computational stability, is maintained below 0.65. Appendix D shows sample calculations for a time instant when the adsorption stage is in progress and the thermal wave is approximately at the center of the microchannel.

$$Pe_{grid} = \frac{uL}{ND_{A,i}} \tag{4.34}$$

4.5 Model validation

The adsorption stage model is simulated for the known values of ΔP, L from the experiments and other parameters listed in Table 4.2. The parameters critical to the determination of the adsorbent layer capacity but not known explicitly are the adsorbent layer void fraction, ε, and the adsorbent mass loading, MF. To determine these parameters, repeated adsorption experiments are conducted on different 2 m long PLOT columns with an imposed ΔP of 18 kPa. The manufacturing variability of the PLOT columns results in a range of adsorption times and ranges of the local and average ΔT. Hence, to correlate the temperature rise pattern and the adsorption time simultaneously, the adsorption stage model is simulated using a range of chosen values of ε and MF. Figure 4.8(a) shows a representative validation of the model for the data shown in Figure 4.2 using ε = 0.60 and MF = 0.60, while Figure 4.8(b) shows a validation for another test section with ε = 0.80 and MF = 0.54. However, it is impractical to conduct such validations for each of the 175 readings in Figure 4.4.

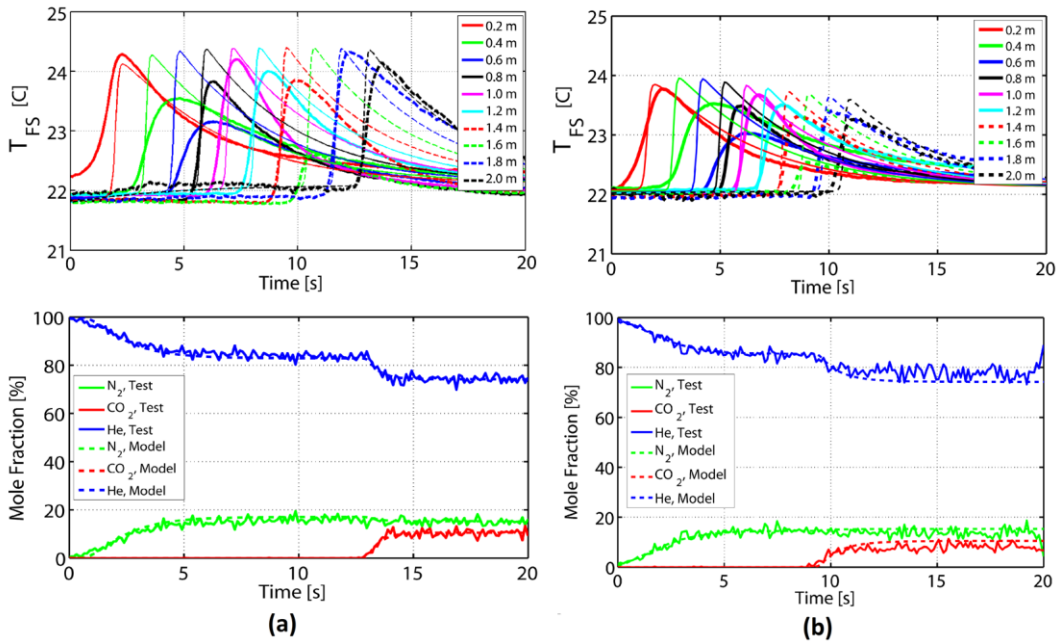

Figure 4.8. Heat (top) and mass transfer (bottom) model validation with (a) ε = 0.60 and MF = 0.60 (b) ε = 0.8 and MF = 0.54 for L = 2 m, ΔP = 18 kPa. Thin lines in the heat transfer validation are for model results, while thicker lines indicate test results.

Therefore, the test results for adsorption times and ΔT for 2 m long PLOT columns with a ΔP of 18 kPa are averaged; so that a single value of adsorption time and ΔT are reported. The adsorption stage model is then simulated for a variety of combinations of ε and MF to yield best fits for the averaged data for the 2 m PLOT column of ε = 0.80 and MF = 0.54, respectively. These values of ε and MF are used for further model validation, wherein adsorption time and ΔT values for the other combinations of the L and ΔP shown in Figure 4.4 are compared with the model results.

Figure 4.9 shows a comprehensive model validation for the averaged values of the data shown in Figure 4.4 along with the corresponding uncertainties. The agreement of the model results and data for the adsorption time is good for smaller values of L. As L

increases, the model over-predicts the adsorption time; nevertheless, the results are within the uncertainty range of the experimental values. The ΔT validation, however, does not yield a close agreement, due to not only fixed values of ε and MF for all the data points, but also local variations in ΔT magnitudes in a single reading. Figure 4.2 and Figure 4.8 show that temperatures increase quickly with nearly similar slopes; however, the magnitudes of temperature peaks are different. This local variation is attributed to uneven distribution of adsorbent particles axially and circumferentially, as well as local variations of the adsorbent layer void fraction. The model can only assume an adsorbent layer of constant thickness with constant packing properties; therefore, ΔT predictions with the model are nearly similar for all axial locations for a combination of ΔP and L as shown in Figure 4.8 and the predicted ΔT is usually greater than the observed ΔT.

Nevertheless, it can be inferred that the qualitative trends of heat and mass transfer results from the models match the corresponding measured trends, with a reasonable accuracy agreement in adsorption time.

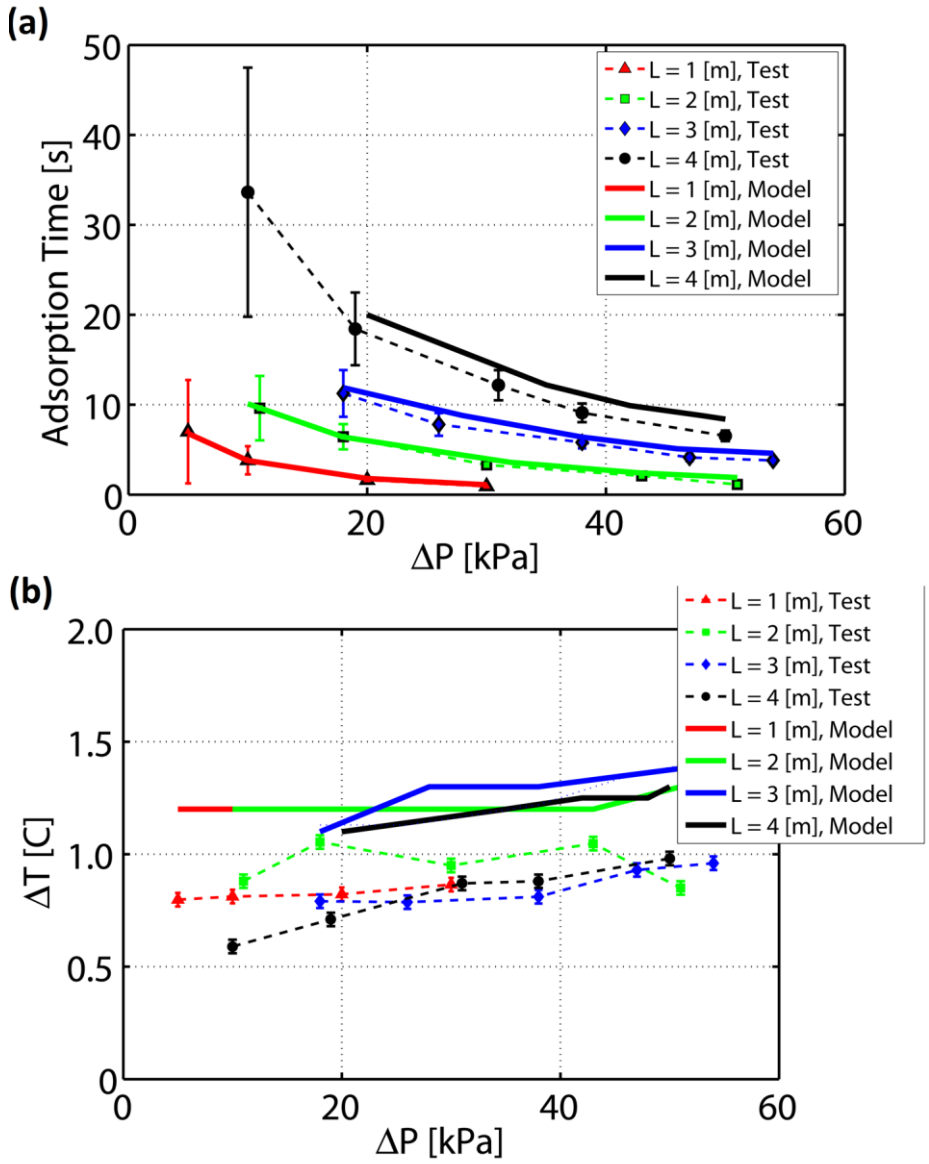

Figure 4.9. Test matrix model validation for PLOT columns for (a) Adsorption time (b) ΔT

Figure 4.10 shows a comparison of the model predictions and the data for adsorption time, ΔT, and ΔT_{Max}, where ΔT_{Max} is the height of the highest peak among the obtained heat transfer data for the 10 thermocouples. Equation (4.35) shows the calculation of error in model predictions for the monitored variables, represented by Q.

$$Error = \frac{Q_{model} - Q_{test}}{Q_{test}} \times 100 \tag{4.35}$$

As shown in Figure 4.10(a), 90% of the predicted adsorption times fall within ±20% of the observed data points, with an average absolute deviation (AAD) of 14%. The agreement for ΔT is not as good, with an AAD of 41% as seen from Figure 4.10(b), due to the reasons discussed previously. However, as shown in Figure 4.10(c), predicted ΔT and observed ΔT_{Max} are in good agreement, with an AAD of 13%. Thus, for a constant *th, ε,* and *MF* of 30 μm, 0.80, and 0.54, respectively, the observed ΔT values would agree well with the predicted ΔT. It appears that the primary reason for the somewhat poor agreement between the predicted and observed ΔTs is manufacturing variability and reduced loading of adsorbent, which lead to shorter temperature peaks than those predicted. Furthermore, the average deviation (AD) and AAD for ΔT are the same 41%, confirming the systematic bias of the model results towards predicting higher ΔT than the average ΔT that is observed. This bias is clearly because of the manufacturing variability in the test sections, where the lack of adsorbent particles and insufficient loading contribute a reduced local ΔT, thereby affecting the average ΔT for all thermocouple locations.

The effect of uneven adsorbent distribution and manufacturing variability in the PLOT columns used for the experiments is also corroborated by Figure 4.11(a), which shows a photograph of the PLOT column adsorbent layer at three different axial locations. At some locations, adsorbent particles are completely absent. The azimuthal variation in adsorbent loading is also seen in these images. The repeatability and uniformity of data are affected because of the uncertainty in the thermal path between the

thermocouple and the adsorbent particles, given this uneven loading. Explicit control over the adsorbent mass and further knowledge of adsorbent layer packing properties could not be achieved for PLOT columns, due to the proprietary nature of the fabrication of these columns. When a thermocouple makes contact with a reduced adsorbent loading region, short temperature peaks are observed as seen in Figure 4.2 and Figure 4.8.

For a repeatable data set with uniform readings, precise information on void fraction, adsorbent mass loading and adsorbent layer thickness is needed, and its uniformity must be ensured. Therefore, another set of experiments are conducted with model validation, using adsorbent-coated microchannels with well-defined properties and a more uniform adsorbent layer.

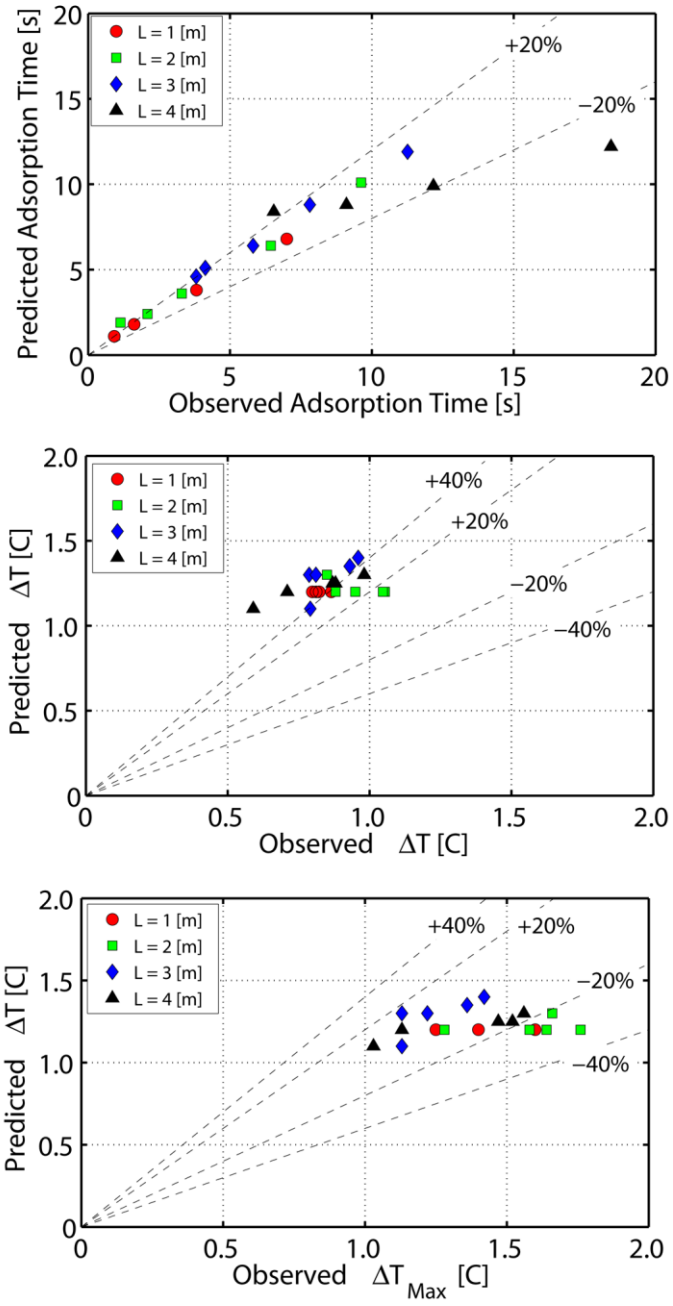

Figure 4.10. Error analysis for PLOT columns for (a) Adsorption time (b) ΔT (c) ΔT_{Max}

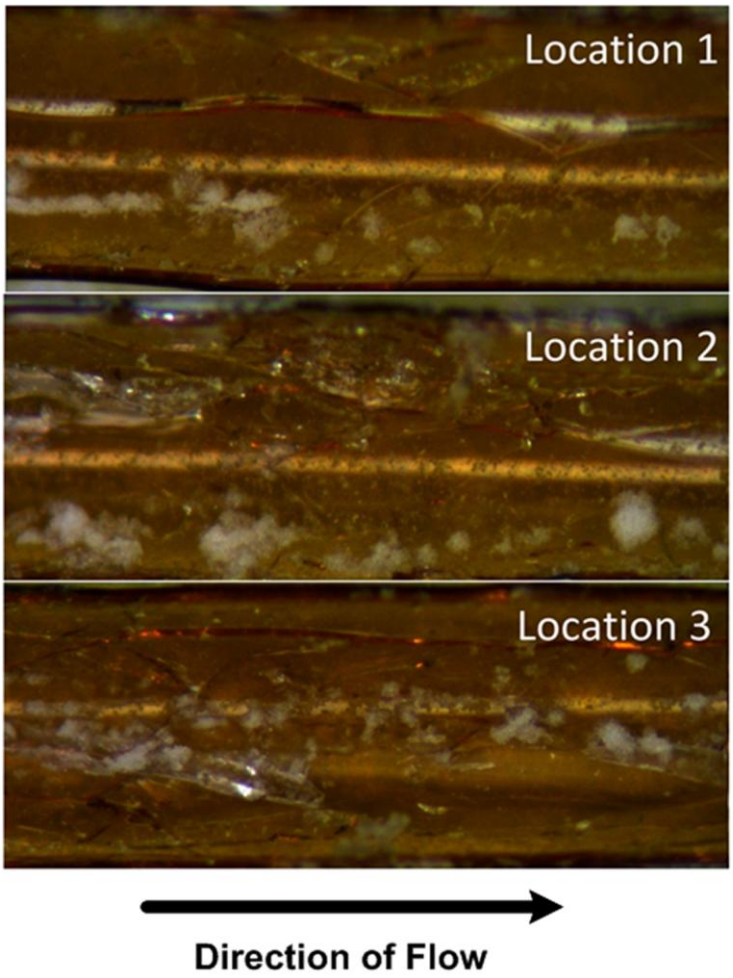

Figure 4.11. Microscopic images of inner surfaces of the PLOT columns at different axial locations. The brown background is the fused silica cover and while clusters are adsorbent particles.

4.6 Model validation with adsorbent-coated microchannels

The customized adsorbent-coated microchannels are fabricated using zeolite 5A as an adsorbent and silica as binder, with known information on *MF*, *th* and the total mass of adsorbent – binder matrix (Courtesy of ExxonMobil Research and Engineering). This adsorbent layer is coated on the fused silica coating of the same diameter (D_h = 530 µm) used previously for the PLOT column experiments. The only unknown parameter, ε, is determined by using Equation (4.36). Table 4.5 shows *th* and total mass of adsorbent-binder used for fabrication of each of the adsorbent-coated microchannels and also shows

calculated ε and ω, which are critical in the species conservation equation (Table 4.4). The adsorbent mass loading, *MF* for all these microchannels is constant at 15.67 (94% adsorbent mass compared to 6% binder mass). This value of *MF* is 29 times greater than the curve fitted value of 0.54 for the PLOT columns discussed above and is expected to generate a pronounced heat of adsorption as well as greater adsorbent capacity in the experiments.

$$\omega = \frac{\rho_{binder} \cdot MF_{ads} \cdot (1-\varepsilon)}{(\rho_{ads} + \rho_{binder} \cdot MF_{ads})}$$
$$V_w = \frac{\pi}{4}\left(D_h^{\,2} - (D_h - 2\times th)^2\right) \cdot L \qquad (4.36)$$
$$M_{total} = V_w \cdot \rho_{ads} \cdot \omega + V_w \cdot \rho_{binder} \cdot (1-\omega-\varepsilon)$$

Table 4.5. Calculation of packing properties of adsorbent layer

Test section #	***th*** **[µm]**	**Adsorbent-binder mass per unit length×10^{-6} [kg m^{-1}]**	***L*** **[m]**	**Calculated** ε **[-]**	**Calculated** ω **[-]**
1		22.12	0.22	0.686	0.303
2		28.48	0.25	0.603	0.384
3	30		0.25		
4		11.46	0.60	0.765	0.227
5			0.66		
6	20	9.61	0.90	0.802	0.190

From Table 4.5, it can be seen that ε for these adsorbent-coated microchannels ranges from 0.6 to 0.8, while it was estimated to be 0.8 for the PLOT columns tested for breakthrough. Additionally, the range of ω for the adsorbent-coated microchannels is from 0.190 to 0.384, while it was estimated to be 0.09 for the tested PLOT columns. These quantitative data show a definite improvement in adsorbent layer packing

properties, which is also corroborated by the microscopic images in Figure 4.12. The longitudinal cross section of the adsorbent-coated microchannels at three different axial locations shows the presence of a distinct and contiguous adsorbent layer as compared to the empty spots in the PLOT column longitudinal cross sections shown in Figure 4.11. It must be noted that the photographs shown in Figure 4.11 and Figure 4.12 are taken after the experiments are conducted and these samples are not used for experiments after the photographs are taken. The photographs are shown only for illustration purposes.

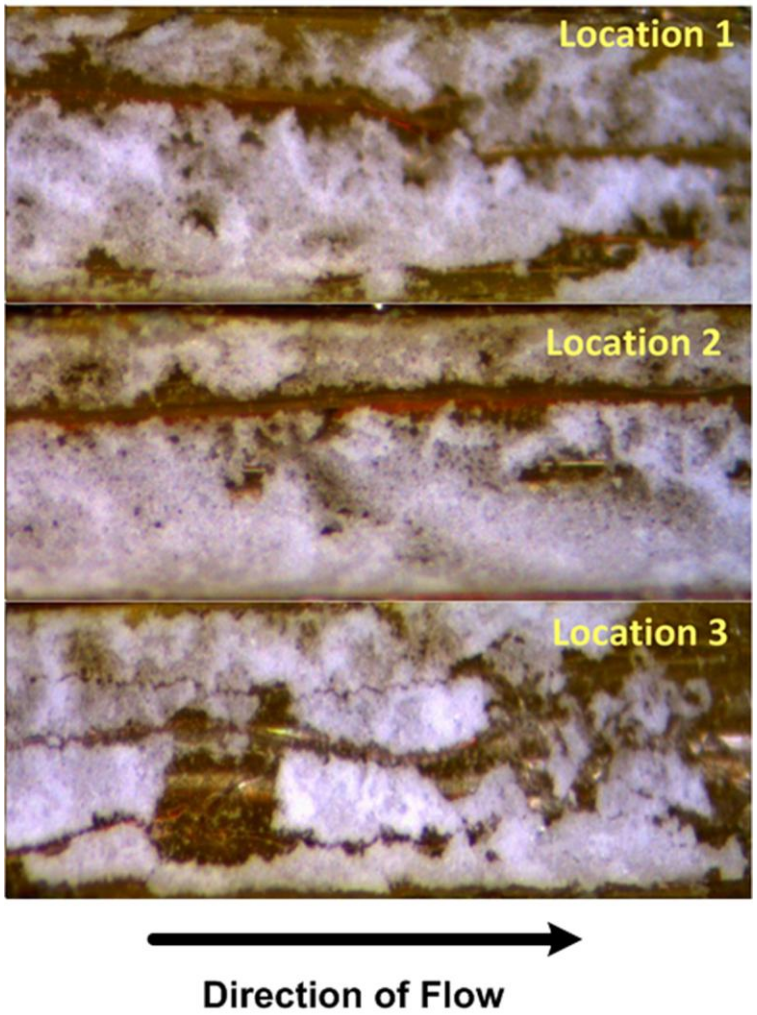

Figure 4.12. Microscopic images of the adsorbent-coated microchannel inner surfaces at different axial locations showing a contiguous adsorbent layer.

The adsorption experiments are then repeated for these adsorbent-coated microchannels to obtain adsorption times and ΔTs for lengths listed in Table 4.5 and for a range of ΔP. Figure 4.13 shows sample heat and mass transfer results for adsorbent-coated microchannel (#6) for a ΔP of 49 kPa. Nine thermocouples placed at equidistant intervals of 0.1 m show the progression of the adsorption thermal wave. The adsorption time in this case is 2.3 s with an average ΔT of 2.5°C and ΔT_{Max} of 5.0°C. Some non-uniformity in temperature peak heights is also seen; nevertheless, the average ΔT is greater than that observed for the PLOT columns due to greater CO_2 adsorption capacity.

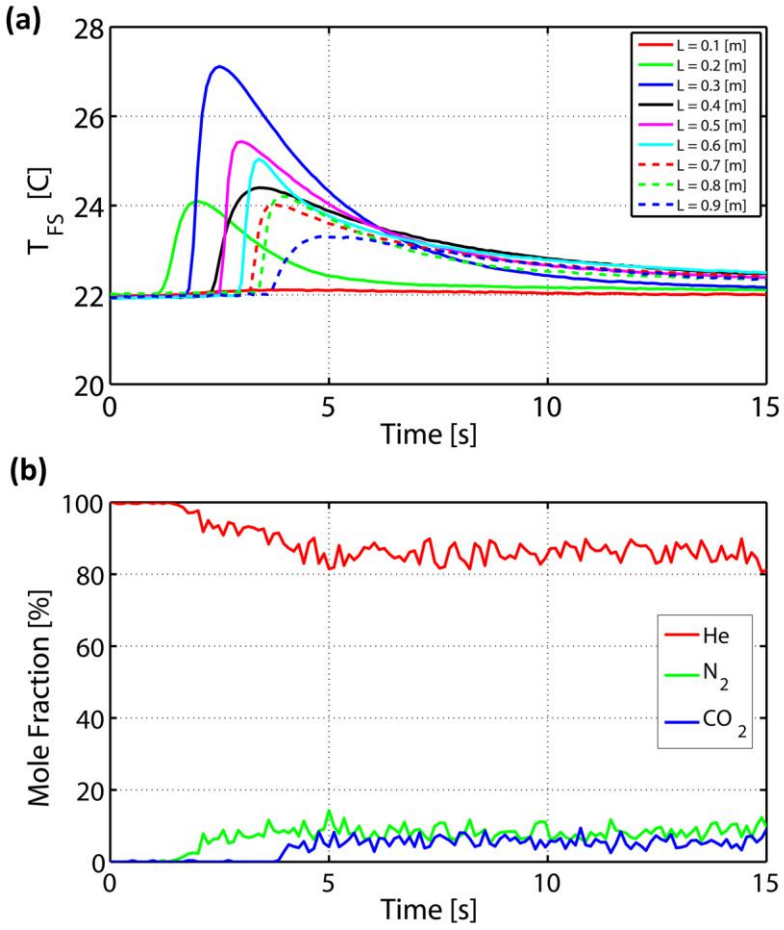

Figure 4.13. (a) Heat transfer (b) mass transfer test results for sample no. 6 (L = 0.9 m) for a ΔP of 49 kPa

Experiments are conducted for the six samples listed in Table 4.5 for a range of ΔP from 5 kPa to 130 kPa, and the observed adsorption times and ΔTs for a total of 62 breakthrough experiments are reported in Figure 4.14. The trends showing a decrease in adsorption time with an increase in ΔP (Figure 4.14(a)) and marginal increase in ΔTs with an increase in ΔP (Figure 4.14(b)) are similar to the trends observed in case of PLOT columns. Additionally, for similar ΔPs, the highest ΔTs are observed for the highest adsorbent volume fraction, ω and lowest void fraction, ε as seen in Figure 4.14(b) and (c). With ε and MF known with higher certainty for the adsorbent-coated microchannels, the model results and observed data can be compared without the use of estimated packing fraction properties. The effect of adsorbent particle size (diameter), which was assumed constant at 2 μm for the model validation for PLOT columns, on heat and mass transfer results can also be analyzed. Figure 4.15 shows Scanning Electron Microscope (SEM) images of the adsorbent particles used for fabrication of the microchannels. It can be seen that the adsorbent particle size ranges from 2 μm to 7 μm in diameter. Variation of adsorbent particle size can affect heat and mass transfer results significantly. Comprehensive information on the adsorbent particle size distribution is unavailable; therefore, it is difficult to select the specific size of the adsorbent particles, based on the variation seen in the two SEM images in Figure 4.15. In the absence of more detailed information, a mean value of the adsorbent particle size was estimated from Figure 4.15, although a single value of the adsorbent particle size estimated based on insufficient data may not be a good representation for the entire test matrix. Therefore, simulations are conducted for a range of adsorbent particle sizes to assess the mass and heat transfer results and compare them with the observed experimental results.

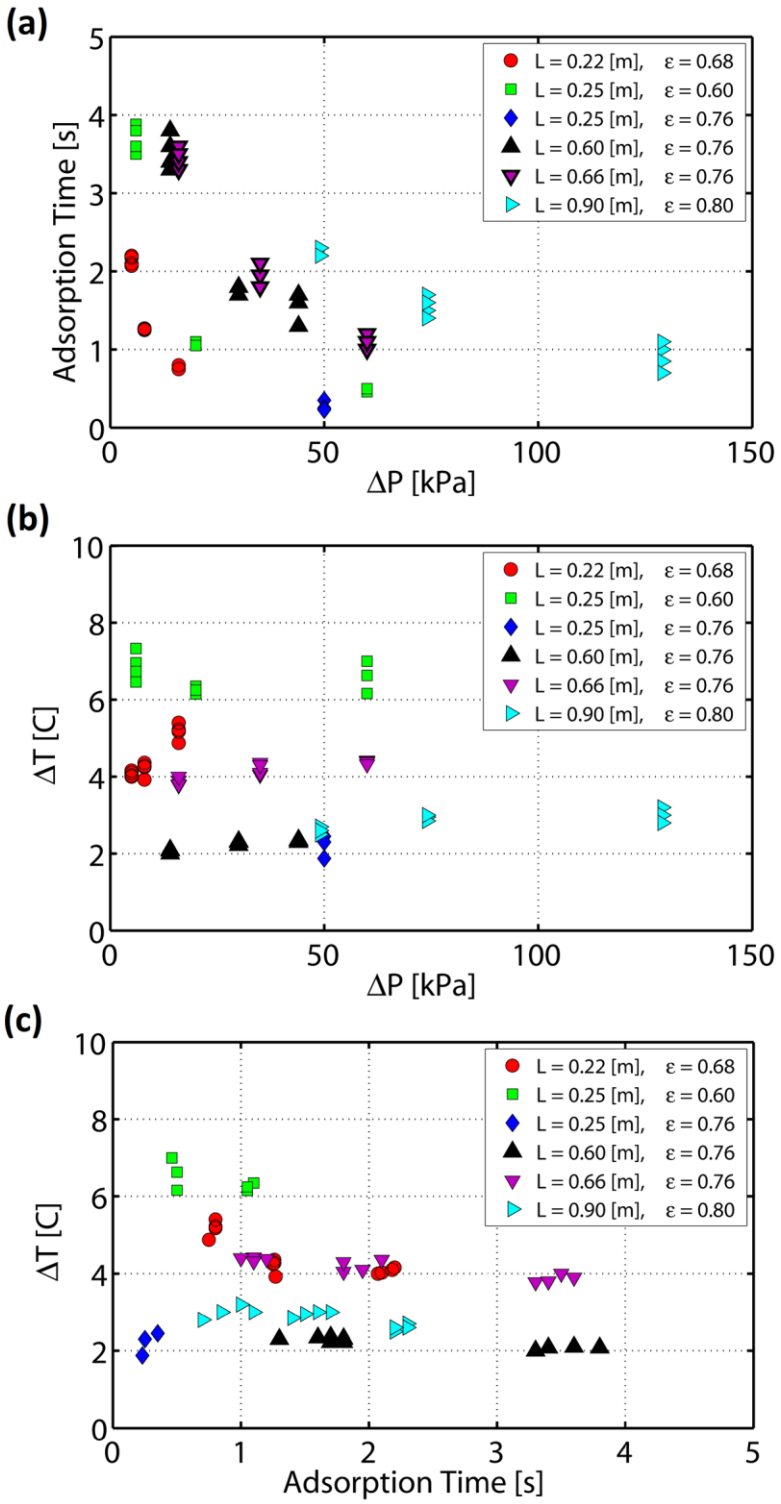

Figure 4.14. Adsorption experiment results on customized adsorbent-coated microchannels (a) Adsorption time vs. ΔP (b) average ΔT vs. ΔP (c) average ΔT vs. adsorption time

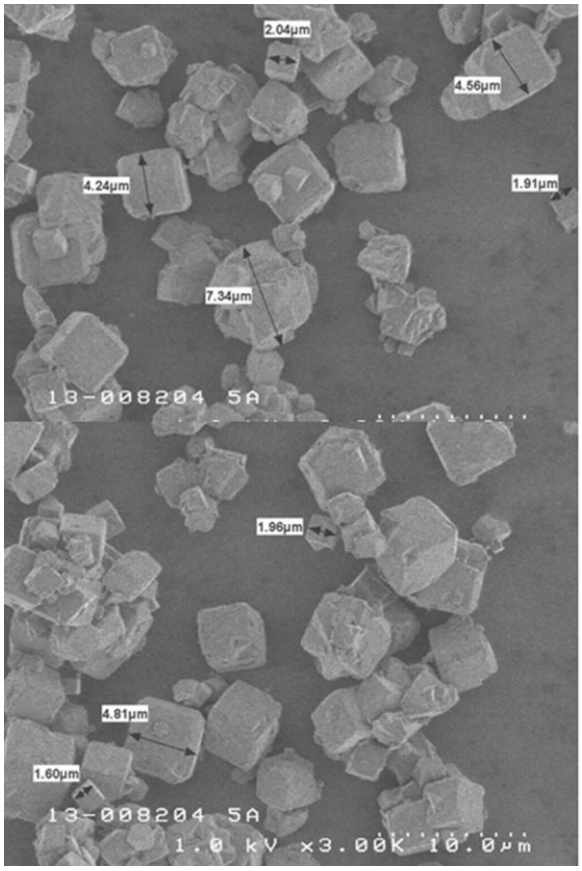

Figure 4.15. SEM images of zeolite 5A adsorbent particles used for fabrication of custom-made adsorbent-coated microchannels

Figure 4.16 shows model validation for the test results shown in Figure 4.13 for an assumed particle sizes of 7 µm (Figure 4.16(a) and (b)) and 2 µm (Figure 4.16(c) and (d)). The temperature rise trends are significantly affected with a change in adsorbent particle size. With a greater adsorbent particle size, the rate of adsorption into the adsorbent decreases in accordance with Equation (4.16). The rate of adsorption directly affects the rate of temperature rise as seen from the energy conservation equation for the adsorbent layer shown in Table 4. Therefore, for an adsorbent size of 7 µm, the rate of temperature increase is low (Figure 4.16(a).) Fluid flow within the microchannel is not affected with changes in adsorbent particles size; therefore, while the adsorption in the adsorbent layer continues at a lower rate, the feed gas wave front reaches the

microchannel outlet without saturating the adsorbent layer entirely (Figure 4.16 (b)). Such behavior detracts from the benefits of using adsorbent-coated microchannels for gas separation.

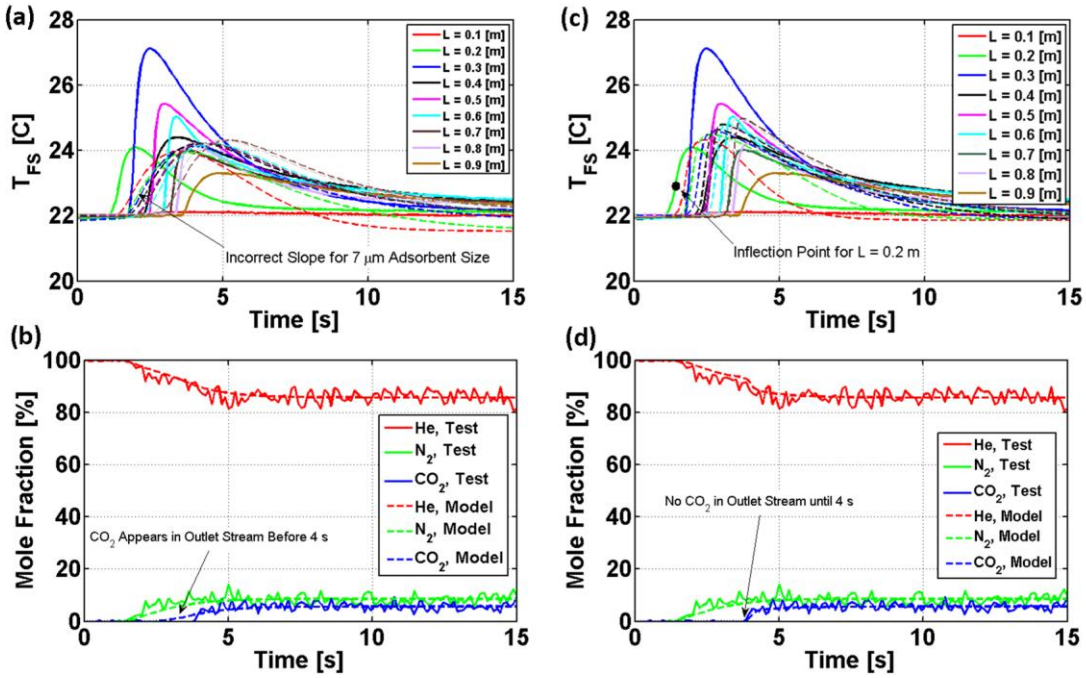

Figure 4.16. (a) Heat and (b) mass transfer model validation for sample no. 6 (L = 0.9 m) using adsorbent particle size of 7 µm. (c) heat and (d) mass transfer model validation using adsorbent particle size of 2 µm. The solid lines represent the experimental results, whereas the dashed lines represent the modeling results.

However, with the use of finer adsorbent particles (2 µm) in heat and mass transfer modeling equations, the slopes of the predicted temperature curves are in agreement with the observed temperature slopes as shown in Figure 4.16(c). This slope in the temperature curves is governed by the heat of adsorption, which is a function of rate of adsorption, which in turn heavily depends on the size of adsorbent particles. As seen in Equation (4.16), rate of adsorption is inversely proportional to square of the adsorbent particle diameter. Therefore, as adsorbent particle size in the models is decreased to 2 µm

from 7 µm in the models, the slopes of the predicted temperature curves increase to match the slopes of the observed temperature curves. This qualitative agreement is seen in Figure 4.16 (c). This rate of change in temperature with time is modeled for every axial location as well as for the temperature readings supplied by each thermocouple. As seen in Figure 4.16(a) and (c), each temperature curve (predicted and observed) exhibits an inflection point (a sample point is shown in Figure 4.16(c)). Before this inflection point, the rate of adsorption at the corresponding location shows a continuous increase. The rate of adsorption achieves a maximum for each temperature curve at the corresponding inflection point, followed by a gradual drop. The slopes of all temperature curves at their corresponding inflection points are measured. The average maximum slope of experimental temperature curves is 8.38°C s^{-1}, while the value predicted by the adsorption models using adsorbent particle size of 7 µm is 1°C s^{-1}. The agreement is much better for a particle size of 2 µm used in the models, which has an average temperature slope of 8.8°C s^{-1}. The heat and mass transfer models use a fixed value of the adsorbent particle size. Therefore, the maximum slopes of the temperature curves predicted by the models are identical for all axial locations. The maximum slopes of the predicted temperature curves for an adsorbent particle diameter of 7 µm stay uniform at 1°C s^{-1}, whereas for an adsorbent particle diameter of 2 µm, they remain uniform at 8.8°C s^{-1}. However, the distribution of adsorbent particles in the experiments is not uniform, as seen from the experimental readings in Figure 4.13(a) and Figure 4.16(a) and (c). The calculated maximum slopes from the experiments vary from 0.22 °C s^{-1} for the first thermocouple location at 0.1 m from the inlet to 17.8°C s^{-1} at 0.3 m from the

microchannel inlet. This variation clearly indicates the variation in adsorbent particle size. The average of maximum slopes for all nine experimental readings is 8.38°C s^{-1}.

Simulation of the models with different adsorbent particle sizes provides insight into relative time scales for the adsorption in the adsorbent layer and convection in the microchannel. For an adsorbent particle size of 7 µm, the adsorbent particles at all locations are still undergoing adsorption and the corresponding temperature rise, while CO_2 starts appearing in the outlet stream. However, this observation is not in agreement with the experimental findings, which can be confirmed by comparing the time instances when CO_2 appears in the outlet stream (Figure 4.16(d)) and the starting instant of CO_2 saturating the last adsorbent layer location, which is seen as the last temperature peak (solid brown line in Figure 4.16(c)). The last adsorbent layer location at 0.9 m may be loaded with a set of larger adsorbent particles because of a smaller local temperature slope compared to the sharp temperature curves for the upstream locations. End effects such as acceleration of the flow and mixing in the headers may not be the cause for this phenomenon, because not all the local readings exhibit a temperature peak with reduced slope (Figure 4.2 for example). Additionally, the laboratory scale model is simulated for predetermined patterns of adsorbent particle size variation. The SEM image in Figure 4.15 shows that the nominal maximum and minimum sizes (approximated as diameters) of the adsorbent particles are 7 µm and 2 µm, respectively. A thorough mean value analysis cannot be performed, because of lack of extensive data on the variation of size of adsorbent particles used in the present study. With the availability of nominal maximum and nominal minimum sizes, three axial profiles of particle size distribution, from channel inlet to outlet: linearly varying diameter from 2 µm to 7 µm, linearly varying

diameter from 7 µm to 2 µm, particle diameter distributions approximated by a quadratic equation, with a diameter of 7 µm at the inlet, 2 µm at the midpoint of the channel length, and 7 µm at the channel outlet, are employed for simulation of the laboratory scale models and for the assessment of their effect on the slopes of temperature peaks and detection of patterns. The variations of temperatures are shown in Figure 4.17.

As shown in Figure 4.17(a) and (b), the axial particle size distribution has a significant effect on the temperature peaks and adsorption stage progress. For the case with linearly increasing adsorbent particle size, the upstream adsorbent particles exhibit a sharp adsorption wavefront and thereby a quick response to the incoming mass of CO_2. These particles are responsible for adsorption of most of the CO_2 and for improving the adsorption time. As the CO_2 wavefront reaches the downstream nodes, where the adsorbent size is larger than that in the upstream region, the rate of adsorption decreases. Therefore, while the adsorption continues at a reduced rate in the downstream region, CO_2 appears in the outlet stream. This pattern results in an adsorption time of 2 s, which is less than the 2.3 s predicted by the models for a constant adsorbent particle diameter of 2 µm and also observed in the experiments for the same boundary conditions. This deviation can be attributed to the reduced rate of adsorption overall with the linearly increasing adsorbent particle diameter. The average slope of temperature profiles with time at their inflection points is 4.9°C s^{-1}, which is much smaller than the 8.38°C s^{-1} observed in the experiments.

The adsorption stage performance worsens for the case of the adsorbent particle diameter decreasing linearly and also deviates from the observed experimental observations significantly, as shown in Figure 4.17(b). Due to the presence of large

particles in the upstream region, the rate of adsorption at local sites is small due to high intraparticle resistance, allowing the CO_2 that is not adsorbed in the upstream region to flow toward the downstream region. Although the smaller adsorbent particle size in the downstream region enhances the rate of adsorption, the overall adsorbent uptake is not improved. Therefore, CO_2 appears in the outlet stream within 1 s, which is much faster than the observed adsorption time of 2.3 s, although the average slope of the temperature curves remains 4.9°C s^{-1} as in the case of the linearly increasing particle diameter discussed above. Thus, in this case, despite the particle diameters decreasing to 2 μm toward the outlet, the adsorption rates achieved are only about as good as those seen with particles of diameter 7 μm uniformly spread along the length of the channel.

For the third case described above, with an initially decreasing particle size from 7 μm diameter at the inlet to 2 μm diameter at the midpoint of the channel, followed by an increase to 7 μm at the outlet, the temperature variations are shown in Figure 4.17(c). In the upstream region, the larger adsorbent particles hinder adsorption locally, thereby allowing most of the CO_2 mass, which should have been adsorbed, to flow downstream. As the particle size decreases toward the axial midpoint of the microchannel, the rate of adsorption improves, the CO_2 wavefront decelerates, and the adsorption time increases due to improved adsorbent capacity. Beyond the axial midpoint, the rate of adsorption decreases again, due to increasing particle diameters, resulting in an overall adsorption time of 2.2 s. Therefore, the adsorption stage performance approaches shown in Figure 4.16(c) and (d), which is based on a constant adsorbent size of 2 μm. These predicted local variations provide insights into the effects of the actual particle size distribution in the channels.

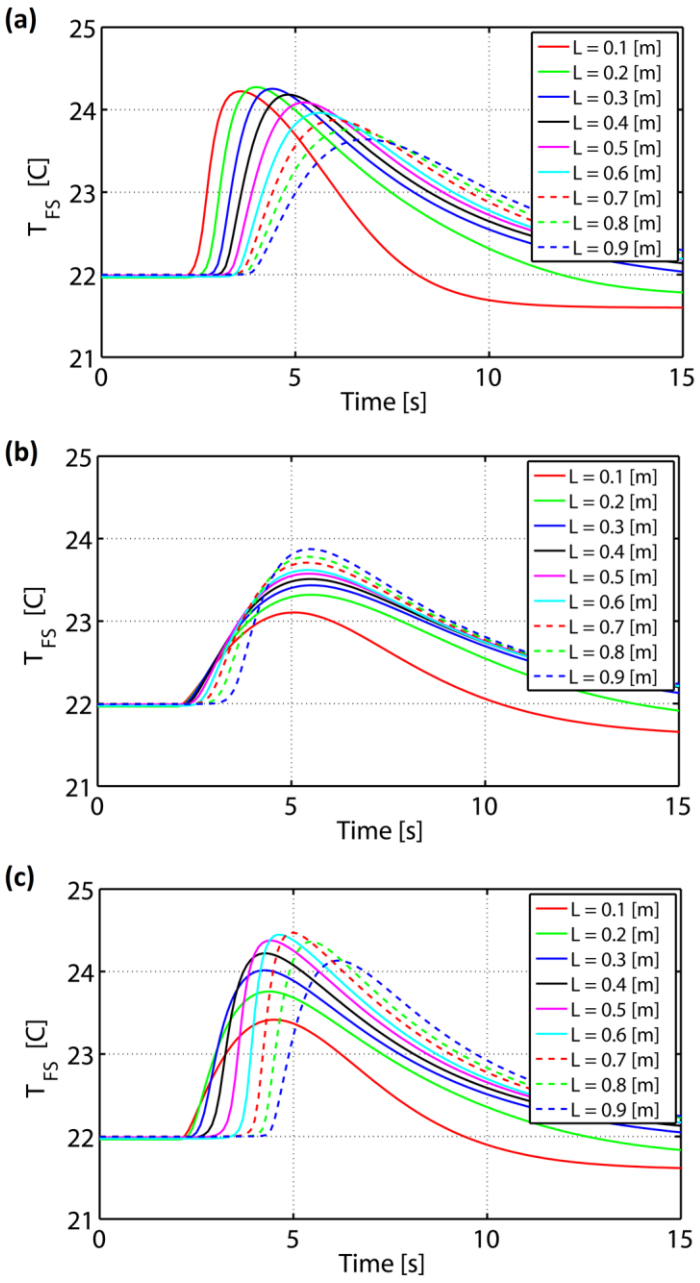

Figure 4.17. Predicted temperature variation with local adsorbent particle diameter varying axially (inlet to outlet) (a) linearly from 2 µm to 7 µm (b) linearly from 7 µm to 2 µm (c) decreasing quadratically from 7 µm at the inlet to 2 µm at the axial midpoint, and then back to 7 µm at the outlet.

As shown in Figure 4.15, the particle size is not constant in the fabricated microchannels. In the absence of knowledge of the actual particle size distribution, the above analyses are conducted to estimate bounding values of adsorption rates and times. A constant adsorbent particle size of 2 μm is chosen for the analyses in the present study because the predicted adsorption time (2.3 s) matches well with the experimentally observed value. Additionally, along with local variations in the slopes, the average slope of the predicted temperature curves matches well with those observed experimentally.

Based on these results, an adsorbent particle size of 2 μm is selected for further simulation of the breakthrough experiments for the rest of the microchannel samples listed in Table 4.5. Figure 4.18(a) shows the model validation for adsorption time, for which the data shown in Figure 4.14(a) are averaged for a combination of ΔP and L. Because of more precise information on ε and MF, the experimentally observed adsorption times match well with the adsorption times predicted by the models. Figure 4.18(b) shows plots the ΔT, with the model once again predicting the experimental values well. It is worth noting that the predicted ΔTs fall between the observed ΔT and ΔT_{Max}, implying that some manufacturing variability also persists in the adsorbent-coated microchannels. For sample 1 with L = 0.22 m, the predicted ΔT matches closely with the observed ΔT_{Max}, while they match more closely with observed ΔT for sample 6 with L = 0.9 m.

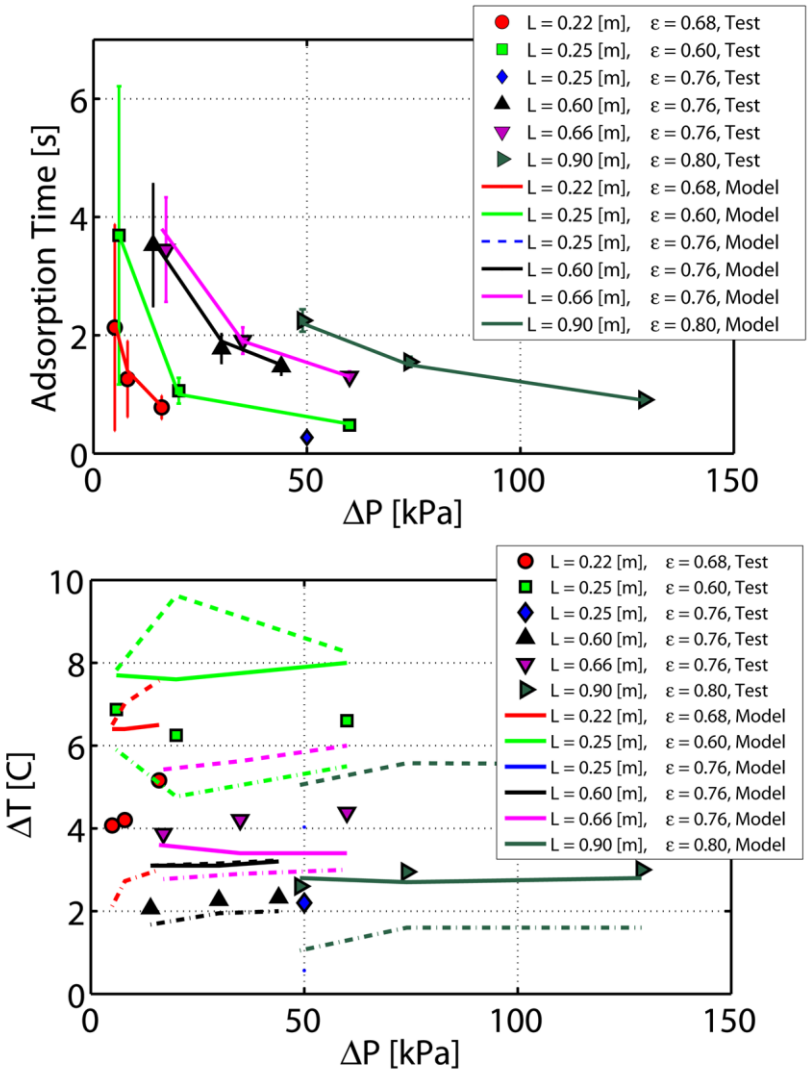

Figure 4.18. Test matrix model validation for adsorbent-coated microchannels for (a) adsorption time (b) ΔT. The dashed lines in ΔT validation represent ΔT_{Max} and the dash-dotted lines represent ΔT_{min} for the corresponding adsorbent-coated microchannel.

Figure 4.19 shows a comparison between model predictions and data for the adsorbent-coated microchannels for the three monitored variables: adsorption time, ΔT and ΔT_{Max}. As shown in Figure 4.19(a), all predicted adsorption times fall within ±20% of the observed adsorption times with an AAD of 4%, signifying very good agreement between the overall gas separation performance prediction and the observed performance.

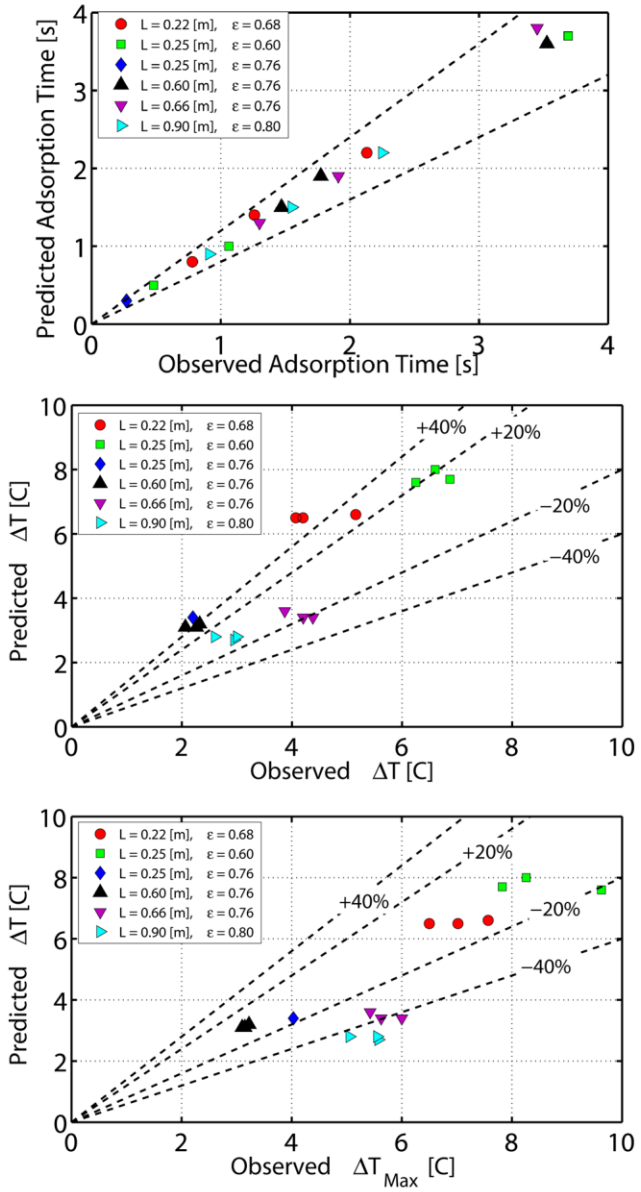

Figure 4.19. Comparison between predicted and measured values for adsorbent-coated microchannels for (a) Adsorption time (b) ΔT (c) ΔT_{Max}

However, the AADs for ΔT and ΔT_{Max} are 25% and 20%, respectively, as seen in Figure 4.19(b) and (c). For samples 1 and 2, the predicted ΔT values agree more closely with the observed ΔT_{Max} (AAD of 8%). Therefore, for samples 1 and 2, it can be inferred that the adsorbent loading is not uniform, as the estimated packing properties shown in Table 4.5 correspond to the maximum temperature peak height. The rest of the observed

thermocouple readings are lower than the maximum value, indicating that the thermocouples in the case of samples 1 and 2 make contact with the low adsorbent loading region, due to which the predicted adsorption times for samples 1 and 2 are in good agreement with those observed. If the adsorbent packing properties in the models match exactly with those in the experiments at any axial location, the predicted ΔT would match the observed ΔT_{Max} exactly. However, if there is a non-uniform adsorbent loading in the microchannel, then the observed temperature rise readings would be different for different axial locations, as seen in Figure 4.13. This local variation in the observed ΔTs in the experiments would result in a greater deviation of the predicted ΔT by the models from the average experimental ΔT. Samples 1 and 2 show this type of behavior, in which the observed ΔT_{Max} values in the experiments match closely with the predicted ΔT by the models. However, because of variations in observed local readings, the agreement between predicted ΔT and observed ΔT is not as good as that between predicted ΔT and observed ΔT_{Max}. The AAD for predicted ΔT for these two samples is 31%.

For samples 3 to 6, predicted ΔTs have slightly better agreement with the corresponding experimental results for average ΔT (AAD of 24%), as compared to samples 1 and 2. This behavior indicates that packing is somewhat more uniform in these samples, as compared with samples 1 and 2. The AAD for average experimental ΔT_{Max} for samples 3 to 6, is however 31%. For all six samples, the AADs for ΔT and ΔT_{Max} are 25% and 20%. These AAD values indicate that the error bands for ΔT decrease by a factor of ≈ 2, as compared with the results for the PLOT columns.

4.7 Conclusions

Gas separation in adsorbent-coated microchannels is studied experimentally and analytically. For preliminary validation, adsorption experiments are conducted on PLOT columns over a range of imposed ΔP and L. Trace water vapor adsorption is demonstrated to be interfering with dry CO_2 adsorption, affecting the repeatability of the adsorption tests. Installation of gas dryers in flow paths results in reliable and uniform adsorption time and ΔT data.

Additionally, fluid flow, heat and mass transfer models for the adsorption stage are developed. PLOT column packing properties are inferred from the measured values of adsorption times and temperature rises for the entire range of test matrix. With the properties established, the model predicts adsorption times with an AAD of 14%, ΔT with an AAD of 41%, and ΔT_{Max} with an AAD of 13%. The qualitative agreement between the model results and the data for adsorption times is good, while the differences between predicted and observed ΔTs are attributed to local variation in adsorbent packing, absence of adsorbent particles at some locations, and uneven adsorbent layer thickness. However, the observed ΔT_{Max} data agree closely with the predicted ΔTs. This is because, if the adsorbent packing properties in the models match exactly with those in the experiments at any axial location, the predicted ΔT would match with the observed ΔT_{Max} exactly.

Adsorption in customized adsorbent-coated microchannels with known adsorbent layer packing properties and adsorbent mass is also investigated to achieve improved validation. These channels result in greater ΔTs compared to those with the PLOT columns as a result of higher adsorbent volume fraction, which yields greater adsorption capacity. The model predictions for these channels agree very well with the data with an

AAD of 4% for adsorption time. Local fabrication variability appears to persist in some measure in these channels also, results in a 25% AAD for ΔT and 20% for ΔT_{Max}. The lower error margins for ΔTs are due to the more accurately known adsorbent layer properties in this case.

The heat and mass transfer analyses in the present work, combined with a composite binder-adsorbent matrix approach for modeling the adsorbent layer, describe the heat and mass transfer processes within the adsorbent layer and the microchannel during gas separation processes well. Such a combined modeling and test platform is applicable to a wide variety of gas separation scenarios, enabling their evaluation through the use of the appropriate isotherms and thermo-physical properties for the fluids of interest.

The PLOT columns used in the present work rely on silica as a binding agent, unlike rubbery or glassy polymers in case of MMMs. For all tests, after channels are saturated with water, they are regenerated (baked) in an oven for more than 10 hours at 225°C, and are simultaneously subjected to pressures lower than 10 Pa (absolute) to remove adsorbed water. These extreme baking conditions are necessitated by the very high affinity of water with zeolites. Trace water in the adsorbent reduces the adsorption capacity and adsorption time.

Figure 4.20 shows progressive decreases in adsorption times for the same channel and for the same flow conditions after it is baked in the oven and reused for testing. The decrease in adsorption time after baking is most likely due to the loss of adsorbent particles. It should be noted that readings shown as ‘baked’ in Figure 4.20 correspond to

the adsorption time observed after the channel is baked twice. The first baking is performed before the first tests to remove water that may have entered the channel before first use. The second baking corresponds to the test conducted after baking following the first test to assess its repeatability, with the results shown in Figure 4.20. Repetitive baking might affect the bonding of the adsorbent layer, which is coated on the inner wall of the fused silica support layer and may in turn worsen the separation performance. As shown in Figure 4.20, three channels are baked for the second time and a significant drop in adsorption time is observed for each of the cases. The flow conditions are kept the same for these experiments to analyze the effect of baking alone. For instance, for a 2 m long channel with a ΔP of 22 kPa, the adsorption time in the first breakthrough test is 12 s (Solid black line). For the same channel exposed to the same test conditions, the adsorption time in the first breakthrough test decreases to 9.5 s after the second baking. It must be noted that the gradual drop in adsorption time for each test condition is due to water adsorption, which is discussed in connection with Figure 4.3.

The decrease in adsorption time is expected to be due to repeated exposure of the test sections to harsh pressure and temperature conditions required for baking, and not chemical softening of the layer. Because PLOT columns and the custom adsorbent-coated channels are fabricated by the solution drying approach, a perfectly annular adsorbent layer with uniform thickness is unlikely. Due to the nonuniform thickness, it is possible that the particles dislodged due to shear at the wall. While reactions of the component gases with the adsorbent are taken into account in the adsorption equilibrium equations, those with the silica binder do not take place at temperatures of 400°C and lower, and pressures of 18 GPa and lower (Santoroa *et al.*, 2011; Wan *et al.*, 2013). The presence of

water in the gas stream affects the adsorption process as shown in Figure 4.20; however, it does not dislodge the adsorbent from the adsorbent layer.

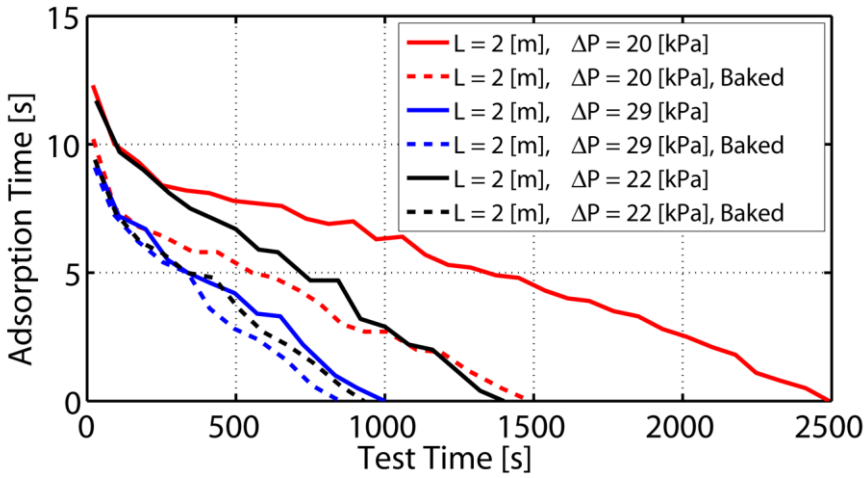

Figure 4.20. Drop in adsorption time with test time for repeated baking and because of water adsorption

Another concern identified in the present work is adsorbent layer manufacturing variability. When a coating and solution drying approach is used for making the adsorbent-coated channels, the layer is discontinuous and non-uniform, giving rise to variable temperature rise during adsorption. Figure 4.11 and Figure 4.12 demonstrate this variability. In large-scale installations, these variations would determine delivered product purities and overall process performance. The predicted adsorption times agree well (4% AAD) with observed adsorption times, and uniformity of the adsorbent layer is critical for accurate predictions of temperature rise. In the presence of a fast-moving liquid with high shear stress, adherence of such a layer to the covering support layer is also an important consideration that must be addressed.

Figure 4.20 showed the effect of gradual water adsorption on adsorption time. Compatibility of the adsorbent and the HTF fluid is an important factor in designing large-scale gas separation processes. Zeolites, such as the one used in the present work, are excellent CO_2 adsorbents; however, they show even greater affinities for water. Hence, ensuring completely dry incoming gas streams is a significant challenge. If the working fluids are different than those in the present work, a feasibility/compatibility study of adsorbent/working fluids/coupling fluids analogous to that detailed in Chapter 2 should be performed for the installation under consideration.

5 CONCLUSIONS AND RECOMMENDATIONS

A novel TSA cycle using adsorbent-coated microchannels for natural gas purification was proposed and analyzed. Comprehensive HT/MT/FD models were developed for the adsorption, desorption, cooling, and purge stages of the cycle to investigate species exchange and mass transfer phenomena in the adsorbent layer in a cyclic, steady-state process. Full process simulations were conducted and process performance maps in terms of ranges of gas processing capacity, product purity, CH_4 recovery, and operating energy requirements were presented. The process performance was then compared with that of conventional purification systems. Gas adsorption in adsorbent-coated microchannels was experimentally investigated and the adsorbent uptake capacity, adsorption time, and the temperature rise at the adsorption wave front were documented. Laboratory scale models were developed to replicate the experimental procedure. The adsorption time and temperature rise data from the experiments and models were compared to validate the modeling techniques and confirm the feasibility of the process investigated in the present work.

Based on these simulations, the times required for satisfactory completion of each of the stages in the cycle were estimated. The optimal adsorbent-coated microchannel geometry was selected after a parametric study on microchannel hydraulic diameter and adsorbent layer thickness. It was concluded that a hydraulic diameter of 530 μm, with an adsorbent layer thickness of 30 μm resulted in short cycle times of 203 s for the baseline case considered. With the adsorption, desorption and cooling stages executed within ~8 s, the purge stage for a silicalite-water pair was extended for 195 s, to completely dry the

adsorbent layer and make it ready for the next purification cycle. The performance of the silicalite-water pair was compared against that of the other adsorbent-HTF pair, zeolite 5A - PAO. Although zeolite 5A is a strong CO_2 adsorbent, the use of PAO as an HTF resulted in severe performance deterioration as a result of the high viscosity of the lubricant oil. Furthermore, once PAO enters the adsorbent layer, it cannot be removed in a practicable manner as a result of its low volatility. Therefore, silicalite, which has moderate affinity for CO_2, was deemed suitable as an adsorbent with water as the HTF, which offers excellent heat and mass transfer characteristics.

By simulating the full process model for a range of feed and product collection times and plotting the performance indicators against those of the existing processes, the present concept was predicted to yield up to 55 times greater process capacity as compared to bed-based PSA processes (Kapoor and Yang, 1989; Olajossy *et al.*, 2003) and up to four times greater capacity than a microchannel-based design with separate, parallel adsorbent-coated and HTF channels (Pahinkar *et al.*, 2016). A first stage product purity range of 87% - 99% predicted for the present concept is competitive with the bed-based processes. The CH_4 recovery from the present concept used in a single stage is up to 84% as a result of loss of the rest of the gas to the liquid water. By designing a two-stage purification system, the product purity could be enhanced to 99.9%. The multistage design could purify the product stream by subjecting it to successive purification stages; additionally, it also recovers gases from the desorption stream and separates impurities from it to create a CO_2 rich stream to be used for sequestration.

The operating energy requirement for the present concept was found to be 14% of the combustion potential of the product for the baseline case. The equivalent absolute

energy requirement amounted to 1.6 kWh kg-CH_4^{-1}, which is competitive with the reversible electrical input for the cryogenic separation process. Two avenues to reduce the energy requirement – reduction of desorption temperature and reduction of pressure drop across the microchannel – were considered. Desorption temperature reduction resulted in reduction of the adsorption capacity, thereby reducing the purity of the product and deterioration of overall performance of the process. However, reduction in the pressure drop across the microchannel reduced the total energy requirement by 53%, without any significant change in the cycle time. Additionally, about 97% of the total energy could be supplied as low-grade heat, making the present concept environmentally friendly and energy efficient. The improved energy requirement value, 0.725 kWh kg-CH_4^{-1}, is competitive with those for MEA absorption-based systems most commonly used for natural gas purification (Göttlicher and Pruschek, 1997). Furthermore, the maintenance costs associated with the present concept are expected to be smaller as solid adsorbent would require replacement less frequently. The use of microchannels with a small amount of adsorbent per microchannel in addition to convective transport within the microchannel increases the compactness and scalability of the system for a given adsorbent mass drastically over the conventional PSA-based systems. The process therefore yields very high process capacity, moderate CH_4 recovery, high product purities and moderate energy utilization.

Gas separation was studied by designing and constructing a test facility with a mass spectrometer and conducting batch adsorption tests on adsorbent-coated microchannels. The first phase of the experiments was conducted on PLOT columns, for which precise information on adsorbent mass and packing fraction was absent.

Laboratory scale models were simulated with void fraction, ε and adsorbent loading, *MF* values as parameters to match the adsorption time and temperature rise for a set of pressure drops and lengths. The selected values of ε and MF were then used to simulate the laboratory scale models for all other combinations of pressure drop and length. This exercise resulted in an AAD of 14% for adsorption time, 41% for ΔT, and 13% for ΔT_{Max}, indicating that maximum values of ΔT in tests correspond to the ideal adsorbent layer assumed in the models. From the qualitative temperature rise data and microscopic images of the PLOT columns, manufacturing variability and the absence of a continuous adsorbent layer were identified as the causes for the high value of AAD for ΔT.

To minimize the AAD and improve model validation and model reliability, custom adsorbent-coated microchannels, for which information on adsorbent loading and adsorbent mass was available, were procured. Void fractions were precisely calculated for each of the samples tested. Batch adsorption tests were conducted on the custom channels and adsorption times and temperature rise values were noted. The simulations of laboratory scale models were conducted with the known values of ε and *MF* for the same experimental conditions. The comparison resulted in excellent agreement of the mass transfer data with the model results, with an AAD of 4%, and better agreement for ΔT, with AAD = 26%. There appears to be some manufacturing variability in these channels also; nevertheless, the agreement between the model results and the data is much better. The agreement between mass transfer data and model predictions suggest that for a given adsorbent mass, the adsorption time for the adsorbent-coated microchannel can be predicted. The ΔT values, despite being averaged for ten thermocouples, are dependent

on local adsorbent layer packing properties. Therefore, the average ΔT value can be different for a different choice of thermocouple locations.

The present work investigated the optimum geometry, materials, and operating conditions for a TSA-based process by developing a full process model. While each of the stages, adsorption, desorption, cooling and purge, are analyzed computationally to predict the process performance, only the adsorption stage was considered in detail by conducting 2-D axisymmetric modeling, alternative process modeling, and experiments to understand factors affecting the adsorption of CO_2 in microchannels. It is recommended that gas-liquid-adsorbent interactions should also be studied experimentally for the desorption stage. In particular, the convective-diffusive flow early in the desorption stage and diffusive flow late in desorption stage can be studied by means of visual inspection and mass spectrometry. The selection of adsorbent and HTF materials for the experiments are critical due to measurability concerns. Silicalite, which can use water as the HTF, has moderate CO_2 selectivity and very low adsorption capacity at near-ambient pressures. This adsorbent is shown to offer excellent adsorption swing capacities at high pressures as seen in Chapters 2 and 3. Zeolite 5A and its variants have excellent CO_2 adsorption capacity at ambient pressure as discussed in Chapter 4; however, the design of the desorption stage experiments would be difficult if water were used as the HTF. The heavy lubricant oil, PAO, which does not interfere with CO_2 adsorption, has already been shown to be impractical for microchannel flows. Furthermore, the flammability of PAO poses additional constraints on the design of desorption stage experiments. Designing high pressure flow-visualization desorption experiments with silicalite-water pair is one of the feasible options. A 2-D axisymmetric

heat and mass transfer modeling exercise can be conducted to study a standalone desorption stage. The results from this model can be used to design the desorption stage experiments and the findings from the experiments can, in turn, be used to refine the stage-level model and full process model predictions. If the desorption stage experiments yield measurable results, pilot plant development to assess large-scale feasibility of the present concept can be initiated. The greatest benefit the present design is expected to offer to purification systems technology is its scalability. While performance of the process can be analyzed by merely modeling the fluid flow, heat and mass transfer in a single microchannel for selected boundary conditions, its output can be scaled depending on the output needed and footprint constraints. Therefore, it is expected to find application in small-scale to large-scale purification facilities. Furthermore, this framework is applicable to a variety of separation scenarios, subject to economic viability and lifecycle costs. For the optimal design configuration, this plant is estimated to operate primarily on heat input, with an electrical energy requirement of only 3.8% of the total energy input. Therefore, such a system could be implemented in remote locations, where electrical infrastructure is limited.

Once stage level models for all the processes involved in the purification cycle are validated experimentally, pilot plant development would require the following modeling steps: Identify purity, processing capacity demand and available energy requirement, conduct parametric studies to assess the feasibility of working and coupling fluids, optimize the microchannel geometry and determine boundary conditions and stage times that result in optimal process performance, simulate the process performance. Once

process performance is determined through simulations, the pilot plant could be built based on the specified geometry, boundary conditions and energy requirements.

Based on the total working and coupling fluid flow rates, headers and valves can be designed and installed. A vertically upward flow direction through the microchannels is recommended, which not only reduces system footprint, but also minimizes flow maldistribution. Flow distribution in headers of the microchannel monolith in these plants is an important topic of further investigation, as flow maldistribution can be a considerable challenge for the scaling up of the pilot plant. Additionally, the effect of mixing of hot and cold HTFs in the inlet headers should be analyzed so that efficient headers to minimize loss of hot HTF energy during desorption can be designed.

Another concern identified in the present work is the adsorbent layer manufacturing variability. It was observed that when a coating and solution drying approach was used for making the channels, the layer was discontinuous and non-uniform, giving rise to variable temperature rise during adsorption. Additionally, only gases were passed through the microchannels in the present work. Very high adsorbent mass fraction in the adsorbent layer, as was the case for the customized coated microchannels used in the present work, results in a high gas separation capacity; however, durability of such microchannels for use in continuous gas separation operations on a large scale is not fully established. In presence of fast-moving liquid, the resulting shear may pose challenges to the adherence of such a layer to the covering support. Adsorbent could be held in a fixed annular medium, such as a polymer matrix employed by Lively *et al.* (2009), to ensure that adsorbent volume fractions and adsorbent layer thickness are uniform throughout along the microchannel length.

Additionally, the adsorbent particles are less likely to be dislodged from the microchannel surface if they are firmly held in a polymer matrix. The hollow fiber spinning method reported by Lively *et al.* (2009) can be used for making hollow fibers with the adsorbent layer forming the outer coating of the microchannel, which was reported by them as having durable performance. With the possibility of fabricating a uniform adsorbent layer and attaching it to the inner surface of a supporting layer, the ideal adsorbent-coated microchannels can be used for pilot-scale tests and for substantiating the industrial viability with an enhanced gas separation capacity. If the adsorbent-coated microchannels are efficiently fabricated and do not require frequent replacement, adsorption-based gas separation processes can become competitive with the widely used absorption systems.

APPENDICES

A. 2-D AXISYMMETRIC HEAT AND MASS TRANSFER MODELING

A.1 Modeling methodology

For modeling heat and mass transfer within the adsorbent layer, a radially lumped approach is followed and described in Chapter 2. However, a 2-D axisymmetric model is developed to analyze heat and mass transfer accurately during the adsorption stage, and its results are compared with the radially lumped model. This investigation is not carried forward due to very long simulation times and difficulties associated with coupling the 2-D heat and mass transfer models with alternating gas and liquid columns in the microchannels. A comparison of adsorption stage performance from the 2-D model and those from the lumped model provides the rationale for the use of the lumped heat and mass transfer approach in the process model development.

The 2-D axisymmetric model utilizes the simulation parameters shown in Table 2.1. The thermo-physical properties of the adsorbent layer and the fluid mixtures are also the same as those used in the lumped model. The only difference in the execution of these two models is the variation of species concentration and energy in radial directions. The species and energy equations used in the 2-D axisymmetric model are shown in Equations (A.1) and (A.2). It must be noted that the boundary conditions from the microchannel side are not incorporated in the species and energy balance, because in this case, the boundary conditions are employed only at the microchannel and adsorbent layer interface.

$$\frac{\partial C_{w,i}}{\partial t}+\frac{\omega}{\varepsilon}\frac{\partial C_{A,i}}{\partial t}=\frac{D_{eff,i}}{r}\cdot\frac{\partial}{\partial r}\left(r\frac{\partial C_{w,i}}{\partial r}\right)+D_{eff,i}\frac{\partial}{\partial z}\left(\frac{\partial C_{w,i}}{\partial z}\right) \qquad \text{(A.1)}$$

$$\rho_w C_{p,w} \frac{\partial T_w}{\partial t} = \frac{k_w}{r} \cdot \frac{\partial}{\partial r}\left(r \frac{\partial T_w}{\partial r} \right) + k_w \frac{\partial}{\partial z}\left(\frac{\partial k_w}{\partial z} \right) + \sum \omega \cdot \Delta H_{ads,i} \frac{\partial C_{A,i}}{\partial t} \tag{A.2}$$

The boundary conditions at the side walls of the adsorbent layer are as used in the lumped model and are shown in Equations (A.3) and (A.4). In the radial direction, both the conservation equations need different boundary conditions. For species conservation, the fused silica layer attached with the adsorbent layer is impermeable to species; hence, a no-flux boundary condition as shown in Equation (A.5) is employed at the outer wall. The adsorbent layer interacts with the microchannel species; hence, the mass convection boundary condition as shown in Equation (A.6) is used.

The heat of adsorption released from the adsorbent layer is transferred to the adjacent gases in the microchannel as well as the fused silica layer; hence, the heat transfer boundary conditions involve heat conduction to the fused silica layer as shown in Equation (A.7), and heat convection to the microchannel as shown in Equation (A.8).

$$D_{eff,i} \left. \frac{\partial C_{w,i}}{\partial z} \right|_{z=0} = D_{eff,i} \left. \frac{\partial C_{w,i}}{\partial z} \right|_{z=L} = 0 \tag{A.3}$$

$$k_w \left. \frac{\partial T_w}{\partial z} \right|_{z=0} = k_w \left. \frac{\partial T_w}{\partial z} \right|_{z=L} = 0 \tag{A.4}$$

$$D_{eff,i} \left. \frac{\partial C_{w,i}}{\partial r} \right|_{r=r_{out}} = 0 \tag{A.5}$$

$$-D_{eff,i} \left. \frac{\partial C_{w,i}}{\partial r} \right|_{r=r_{in}} = h_m \left(C_{g,i} - C_{w,i}\big|_{r=r_{in}} \right) \tag{A.6}$$

$$k_w \left.\frac{\partial T_w}{\partial r}\right|_{r=r_{out}} = k_{FS} \left(\frac{T_w\big|_{r=r_{out}} - T_{FS}}{th_{FS}/2} \right) \tag{A.7}$$

$$-k_w \left.\frac{\partial T_w}{\partial r}\right|_{r=r_{in}} = h_T \left(T_{g,i} - T_{w,i}\big|_{r=r_{in}} \right) \tag{A.8}$$

For the simulation of the 2-D axisymmetric model, the adsorbent layer and the microchannel are assumed to be filled with CH_4-CO_2 mixture (99:1) at the start of the adsorption stage, while the temperature for all the calculation points is assumed to be 25°C. As in the case with the radially lumped model, CH_4:CO_2 (70:30) mixture enters the microchannel and saturates the adsorbent layer. The microchannel species, energy and momentum balance equations are the same as those used for the development of the radially lumped model. The adsorbent layer response predicted by the lumped model is compared with that predicted by the 2-D model to justify the use of lumped model. The assumed values of hydraulic diameter D_h and adsorbent layer thickness *th* for the microchannel are 200 µm and 100 µm, with a length of 1 m.

Figure A.1 shows the variation of the adsorbed CO_2 concentration along thickness of the adsorbent layer and that along the axis of the microchannel at different time instances. As CO_2 enters the microchannel, it enters the adsorbent layer after overcoming the convection resistance and then gradually diffuses outward in the adsorbent layer. Due the effective diffusion coefficient being of the order of 10^{-8} m^2 s^{-1} at 5500 kPa ($\approx 10^{-6}$ m^2 s^{-1} at 100 kPa), a slightly inclined CO_2 concentration front is seen in Figure A.1. The effect of such a pattern is marginal underutilization of the adsorbent layer (in the upper right corner, at the contour at 1.2 s), as the feed wave front reaches the microchannel outlet. After this instant in the process, the product purity starts to drop regardless of

whether the remaining volume of the adsorbent layer is saturated by incoming feed mixture or not.

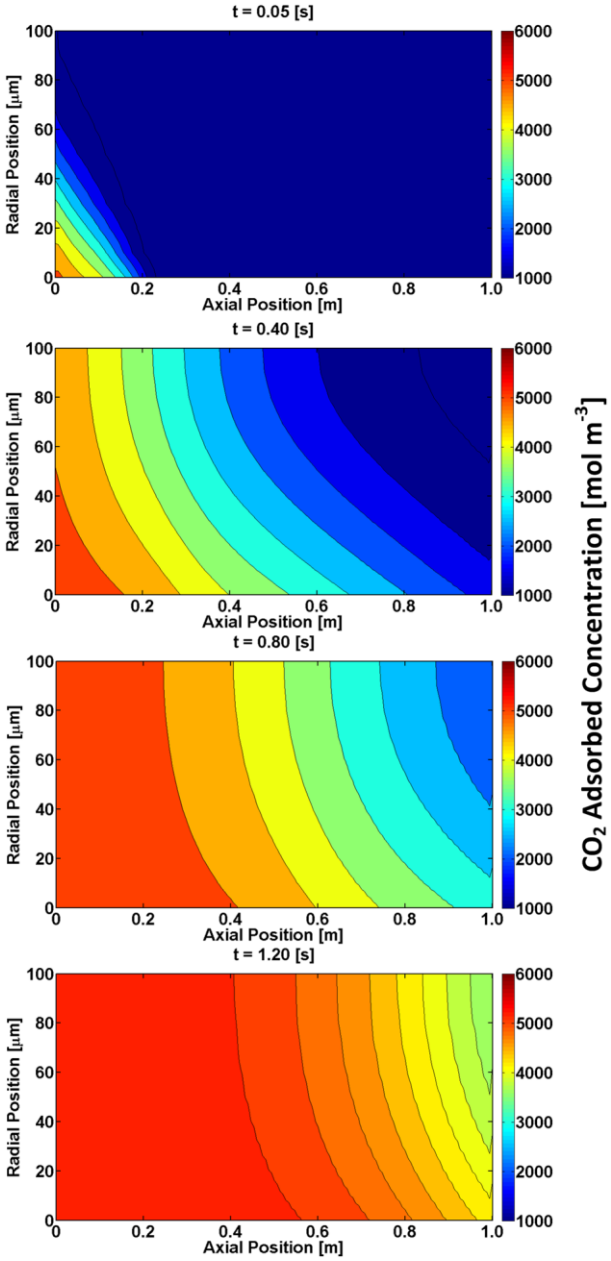

Figure A.1 Adsorbed CO_2 concentration contour plots during adsorption stage.

Figure A.2 represents the corresponding temperature contours during the adsorption stage. The heat of adsorption is released, raising the temperature of the adsorbent locally, where the rate of adsorption is the highest, i.e., at the concentration wave front. While the adsorbent layer temperature increases with the progressing concentration front, it drops in the upstream region as a result of influx of cold feed gas. The cold feed mixture carries the heat away in the upstream locations, while adsorption continues in the downstream locations. This simulation does not consider asymmetric operation of inlet and outlet valves discussed in Chapters 2 and 3 that involves hot water entering the microchannel well before the adsorbent layer is saturated with feed mixture. However, for the sake of comparison of the radially lumped model and 2-D axisymmetric model, only gas-phase simulation is considered and the adsorbent layer response is noted.

With the radially lumped model, it is assumed that the adsorbed concentration C_A represents a radially integrated value. The diffusion of gases outward in the adsorbent layer is governed by the overall mass transfer resistance, and is assumed to represent the diffusion lag for all the radial calculation points. Therefore, the concentration wave front would have appeared as straight vertical lines in Figure A.1. Figure A.3 shows the effect of using these two approaches on the product purity variation. It is assumed that the product collection starts at the instant the feed gas enters the microchannel and the reference starting point for purity calculation is the same.

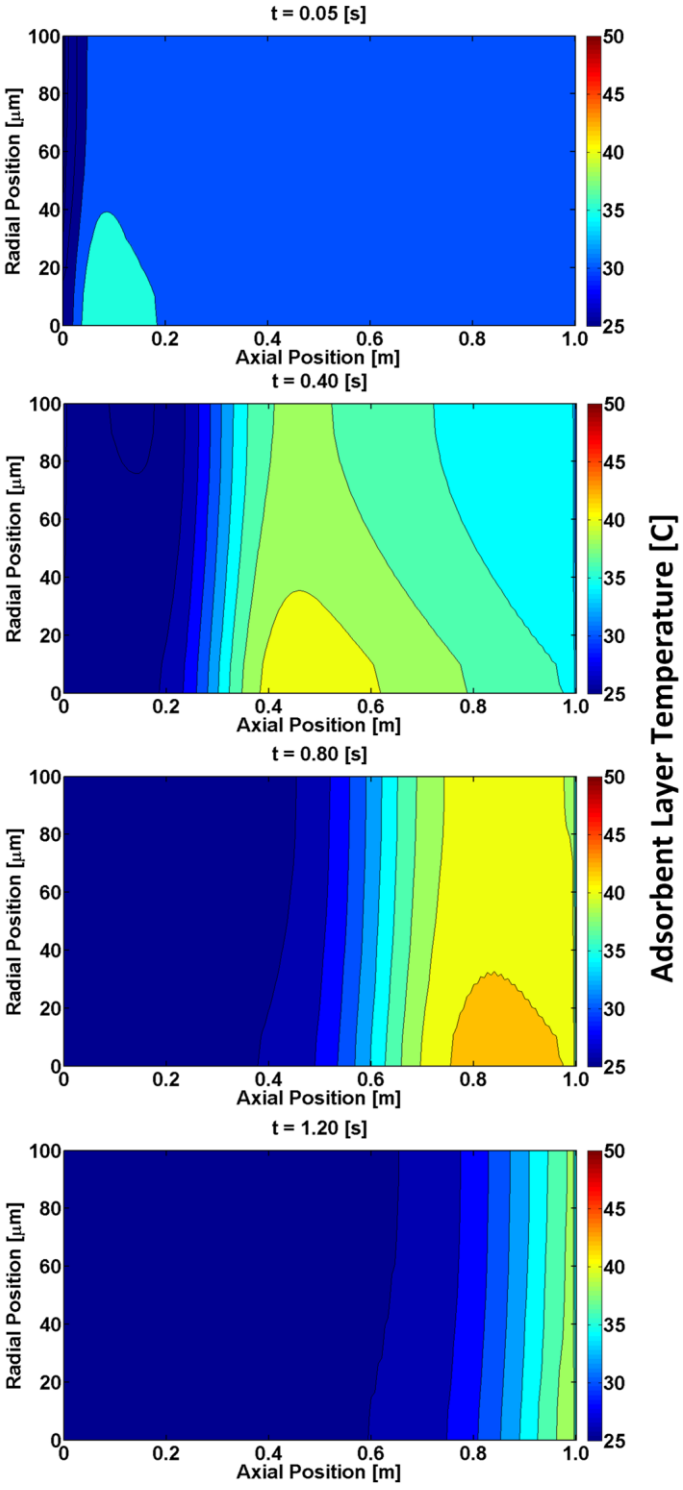

Figure A.2 Adsorbent layer temperature contour plots during adsorption stage.

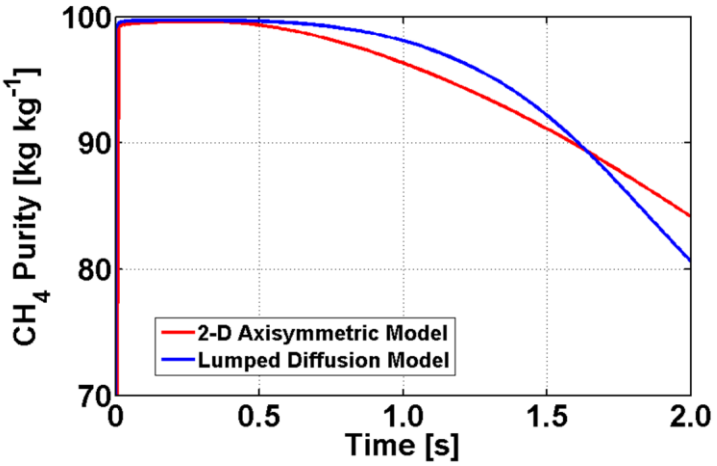

Figure A.3. Product purity variation with two heat and mass transfer modeling approaches.

From Figure A.3, it is clear that with the 2-D axisymmetric modeling approach, the product purity starts to drop gradually after 0.5 s, when the front end of the concentration front reaches the microchannel outlet. However, the lumped model overpredicts the adsorption capacity by a small margin as a result of the implicit assumption of saturation of all radial locations at the same time. Therefore, the product purity value for the case of the lumped model remains higher than that predicted by the axisymmetric model for 1.5 s. It starts to drop more rapidly than that with a 2-D model, as adsorbent particles located in the last microchannel nodes adsorb CO_2 at the same time in the lumped model. In contrast, in the 2-D axisymmetric model, the drop in CH_4 purity is decelerated as a part of the adsorbent layer still keeps accepting CO_2 as the remaining fraction exits the microchannel as shown in Figure A.1.

For the process performance prediction and model validation exercises, the radially lumped model is adopted due to the ease of modeling, very small computation time, and the reliability of coupling with the conservation equations for the microchannel

domain irrespective of the fluid phase present in the microchannel. The temporal error seen as a slight change of purity slopes as shown in Figure A.3, which is caused by radial lumping is negligible, as the process reaches cyclic steady state and the product tank contains substantial product. It must be noted that for the present comparison, it is assumed that product tank contains no product mass, which in turn augments the effects on instantaneous purities.

It must also be noted that the radially lumped model is validated against the adsorption tests in Chapter 4. The radially lumped model is expected to predict the adsorbent layer saturation time within 4% of the observed adsorption time. Therefore, although a radial variation of species and energy is not modeled, the radially lumped model is concluded to reproduce the overall heat and mass transfer phenomena accurately enough, enabling quick and reliable prediction of purification process performance.

B. DECOUPLED MOMENTUM APPROACH AND PROPERTY VARIATION

The use of a single set of coupled momentum, energy and species equations for the entire microchannel during displacement stages results in an inaccurate gas-liquid interface. This is because the liquid numerical property data are transferred across the interface to the gas region, and because of this numerical diffusion, as the time step progresses, the interface location becomes undetectable. This condition is depicted in Figure B.1, where there is no clear location across which the liquid density transitions quickly to the gas density, resulting in an unrealistic displacement scenario. This also poses difficulties in the timing of the stages, as the time instant when the interface reaches a specific axial location in the microchannel cannot be determined with certainty.

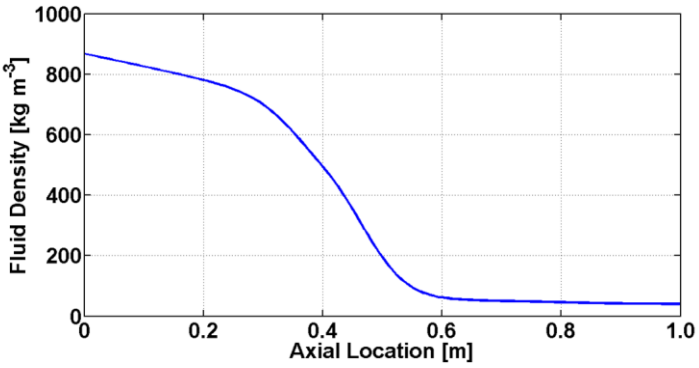

Figure B.1. Instantaneous density variation during displacement of gas assuming a homogeneous mixture.

Furthermore, from the experimental observations by Moore (2012) as shown in Figure B.2, gases in the microchannel are cleanly displaced by liquid. The decoupled momentum approach allows precise calculation of thermo-physical properties of working and coupling fluids, and tracking of the gas-liquid interface.

Figure B.2. Time lapse image of displacement of gas showing clean displacement showing a distinct gas-liquid interface (Moore, 2012).

Figure B.3 shows the density variation in the microchannel during the displacement of gas with the decoupled approach. Not only can the gas-liquid interface be distinctly tracked, but also the temperature dependence is properly resolved, which results in precise calculation of displacement times.

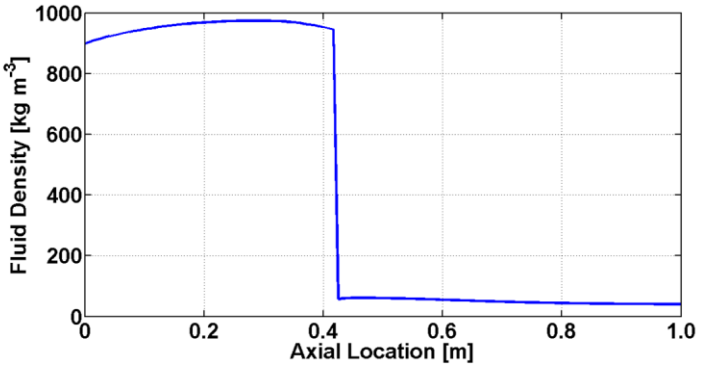

Figure B.3. Instantaneous density variation during displacement of gas with decoupled approach.

C. SAMPLE CALCULATIONS FOR PROCESS MODEL DATA POINT

Before, the sample calculation for the differential variables is reported, important geometry and important packing properties of the adsorbent layer are established. Figure C.1 shows a cross section of the microchannel with important geometrical parameters that are used as inputs for the calculation of the heat and mass transfer resistances.

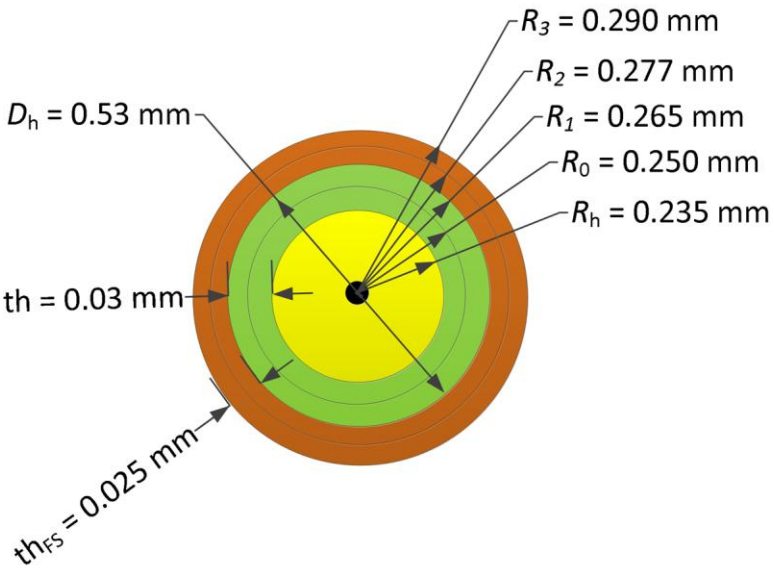

Figure C.1. Adsorbent-coated microchannel cross section showing geometrical parameters

Table C.1 Calculation of geometrical parameters (not iterative variables)

Input	**Equations**	**Output**
$D_h = 530 \times 10^{-6}$ [m] $th = 30 \times 10^{-6}$ [m] $th_{FS} = 25 \times 10^{-6}$ [m] Inlet pressure, $P = 55 \times 10^{-6}$ [Pa] Average molecular size, $d = 3.8495 \times 10^{-10}$ [m] Collision integral, $\Omega = 1.12$ Inlet temperature, $T = 298$ [K] CH_4 Molecular weight, $MW_{CH4} = 16.043$ CO_2 Molecular weight $MW_{CO2} = 44.01$	$R_h = \frac{D_h}{2} - th$ $R_0 = \frac{D_h}{2} - \frac{th}{2}$ $R_1 = \frac{D_h}{2}$ $R_2 = R_1 + \frac{th_{FS}}{2}$ $R_3 = R_2 + \frac{th_{FS}}{2}$	$R_h = 235 \times 10^{-6}$ [m] $R_0 = 250 \times 10^{-6}$ [m] $R_1 = 265 \times 10^{-6}$ [m] $R_2 = 277 \times 10^{-6}$ [m] $R_3 = 290 \times 10^{-6}$ [m]
	$A_g = \frac{\pi}{4}(D_h - 2 \times th)^2$ $A_w = \frac{\pi}{4}(D_h^{\,2} - (D_h - 2 \times th)^2)$ $Peri = \pi(D_h - 2 \times th)$ $Peri_{FS} = 2\pi R_1$ $A_{FS} = \pi(R_3^{\,2} - R_1^{\,2})$	Channel Cross sectional area, $A_g = 1.735 \times 10^{-7}$ [m^2] Adsorbent layer cross sectional area, $A_w = 4.712 \times 10^{-8}$ [m^2]Channel perimeter, $Peri = 1477 \times 10^{-6}$ [m] Fused silica cover inner perimeter, $Peri_{FS} = 1665 \times 10^{-6}$ [m] $A_{FS} = 4.359 \times 10^{-8}$ [m^2]

Table C.1 Calculation of geometrical parameters (not iterative variables)-continued

Void fraction, $\varepsilon = 0.55$ Tortuosity factor, $\tau = 2$ Zeolite density, $\rho_{ads} = 1600$ [kg m^{-3}] Fused silica density, $\rho_{FS} = 2200$ [kg m^{-3}]Silicalite density, $\rho_{ads,silicalite} = 1760$ [kg m^{-3}] Binder density, $\rho_{binder} = 1270$ [kg m^{-3}] Binder specific heat, $C_{p,binder} = 1461$ [J kg^{-1} K^{-1}] Adsorbent specific heat, $C_{p,ads} = 800$ [J kg^{-1} K^{-1}] Fused silica specific heat, $C_{p,FS} = 740$ [J kg^{-1} K^{-1}] Binder thermal conductivity, $k_{binder} = 0.22$ [W m^{-1} K^{-1}] Adsorbent thermal conductivity, $k_{ads} = 1.2$ [W m^{-1} K^{-1}] Fused silica thermal conductivity, $k_{FS} = 1.3$ [W m^{-1} K^{-1}] Insulation sheet thermal conductivity, $k_{ins} = 0.04$ [W m^{-1} K^{-1}]	$D_{AB} = \frac{1.858\times10^{-27}\cdot T^{1.5}}{Pd^2\Omega}\sum_i\left(\frac{1}{MW_i}\right)^{0.5}$ $D_{eff} = D_{AB}\cdot\frac{\varepsilon}{\tau}$ $\omega = \frac{\rho_{binder}\cdot MF_{ads}\cdot(1-\varepsilon)}{(\rho_{ads}+\rho_{binder}\cdot MF_{ads})}$ $\rho_w = \rho_{ads}\cdot\omega + \rho_{binder}\cdot(1-\omega-\varepsilon)$ $C_{P,w} = \frac{\left[C_{P,ads}\cdot\omega\cdot\rho_{ads} + C_{P,binder}\cdot(1-\omega-\varepsilon)\cdot\rho_{binder}\right]}{\rho_m}$ $k_w = k_{ads}\cdot\omega + k_{binder}\cdot(1-\omega-\varepsilon)$ (Hines and Maddox, 1985; Cussler, 1997; Pahinkar *et al.*, 2015)	Binary diffusion coefficient, $D_{AB} = 3.05\times10^{-7}$ [m^2 s^{-1}] Effective diffusion coefficient, $D_{eff} = 8.39\times10^{-8}$ [m^2 s^{-1}] Adsorbent volume fraction, $\omega = 0.1991$ Adsorbent layer density, $\rho_w = 637.2$ [kg m^{-3}] Adsorbent layer specific heat, $C_{p,w} = 1131$ [J kg^{-1} K^{-1}] Adsorbent layer thermal conductivity, $k_w = 0.2941$ [W m^{-1} K^{-1}]
	$R_{eq,FS} = \frac{\ln\left(\frac{R_1}{R_{w,mid}}\right)}{2\pi k_w} + \frac{\ln\left(\frac{R_2}{R_1}\right)}{2\pi k_{FS}}$	Heat transfer resistance between adsorbent layer and fused silica, $R_{eq,FS} = 0.0369$ [W^{-1} m K]

C.1 Instantaneous heat and mass transfer resistance calculation

For this section, an instant during displacement of gas by liquid is chosen, for a comprehensive demonstration of the modeling methodology. Calculations could also be shown at other instants, when a single phase occupies the entire length of the microchannel. The selected instant is 0.392 s, after the process is initialized and an adsorption stage of 0.19 s long is already completed. The calculation point under consideration is 0.5 m from both the ends of the microchannel. The displacing hot water has occupied the upstream node. At the current instant, gas-phase residual gases have occupied the node. At the following instant at 0.397 s, the displacing hot liquid occupies the same node. Figure C.2 shows the initial and final instants considered for the present sample calculation. The node at 0.5 m is shown to be occupied by component gases before the displacement of gas takes place and liquid occupies the same node.

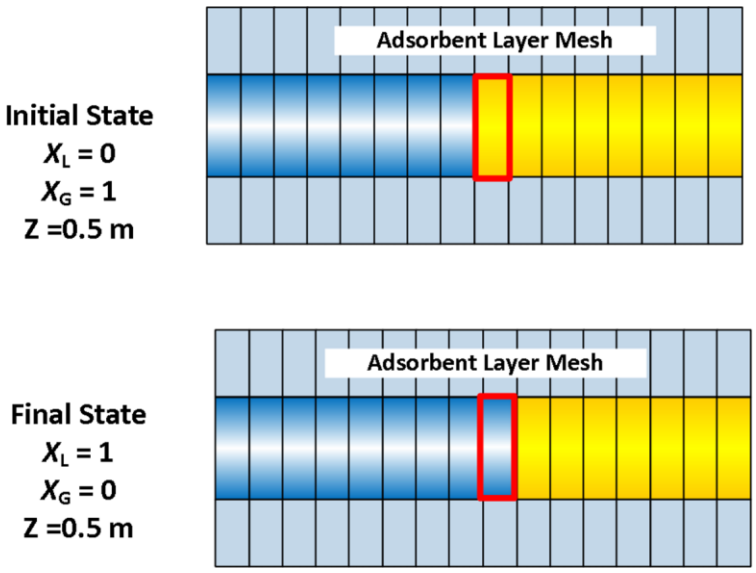

Figure C.2. Initial and final states of the displacement of gas used for the sample calculation.

As explained in Chapter 2, the equations are modified to account for the interface location. The time step is also decided based on how fast the interface reaches the next calculation point. Because the gas-liquid interface is monitored throughout the displacement, the calculation is performed as the interface crosses each node point. Hence, depending on the velocity of the interface, when the interface passes each node, the time step is automatically calculated and the results are reported. In this way, the time step is implicitly kept small (0.005 s, in this case, which is calculated by dividing the grid size of 0.01 m by the instantaneous interface velocity of 1.83 m s^{-1}, when the interface is at 0.5 m from the inlet) to keep track of the interface precisely during displacement. As more liquid occupies the channel, the displacement process slows down; therefore, the implicit time step becomes marginally larger.

Table C.2 Calculation of heat and mass transfer coefficients

Input	Equations	Output
This table shows calculation of heat and mass transfer coefficients and corresponding resistances in the microchannel for the initial and final states as shown in the schematic (Figure C.2)**.**		
Hydraulic radius, R_h = 235×10^{-6} [m] Binary diffusion coefficient, $D_{AB} = 3.05 \times 10^{-7}$ [$m^2\ s^{-1}$] Mixture diffusion coefficient in water, $D_{AB,water} = 2.23 \times 10^{-9}$ [$m^2\ s^{-1}$] Laminar Sherwood number, $Sh_0 = 4.01$ Gas Schmidt number, Sc = 0.72 (before liquid displaces gas) Liquid Schmidt number, Sc_L = 500 (after liquid displaces gas) Interface velocity, u = 1.83 [m s^{-1}] $\rho_G = 50.44$ [kg m^{-3}] $\rho_L = 951.68$ [kg m^{-3}] $\mu_G = 1.5 \times 10^{-5}$ [kg $m^{-3}\ s^{-1}$] $\mu_L = 7.37 \times 10^{-4}$ [kg $m^{-3}\ s^{-1}$] Liquid and gas velocity are the same for displacement phase.	**Mass transfer coefficient for gas phase** $$\left(\frac{2\times R_h h_m}{D_{AB}}\right)^{10} = (Sh_0)^{10} + \left[\frac{e^{\frac{(2200-Re)}{365}}}{(Sh_0)^2} + \left(\frac{1}{Sh_0 + \frac{0.079Re\sqrt{f}\,Sc_G}{\left(1+Sc^{4/5}\right)^{5/6}}}\right)^2\right]^{-5}$$ **Mass transfer coefficient for liquid phase** $$\left(\frac{2\times R_h h_{m,L}}{D_{AB,water}}\right)^{10} = (Sh_0)^{10} + \left[\frac{e^{\frac{(2200-Re)}{365}}}{(Sh_0)^2} + \left(\frac{1}{Sh_0 + \frac{0.079Re\sqrt{f}\,Sc_L}{\left(1+Sc^{4/5}\right)^{5/6}}}\right)^2\right]^{-5}$$ **Heat transfer coefficient for all scenarios** $$\left(\frac{2\times R_h h_T}{k_g}\right)^{10} = (Nu_0)^{10} + \left[\frac{e^{\frac{(2200-Re)}{365}}}{(Nu_0)^2} + \left(\frac{1}{Nu_0 + \frac{0.079Re\sqrt{f}\,\mathrm{Pr}_g}{\left(1+Pr^{4/5}\right)^{5/6}}}\right)^2\right]^{-5}$$ **(**Churchill, 1977a; Churchill, 1977b) **Single phase Reynolds number and friction factor** $$\mathrm{Re} = \frac{2\rho u R_h}{\mu}$$ $$f = 8\cdot\left(\left(\frac{8}{\mathrm{Re}}\right)^{12} + \left[\left(\frac{37530}{\mathrm{Re}}\right)^{16} + \left(-2.457\cdot\ln\left(\left[\frac{7}{\mathrm{Re}}\right]^{0.9} + 0.27\times\frac{eps}{2R_h}\right)\right)^{16}\right]^{(-1.5)}\right)^{\left(\frac{1}{12}\right)}$$	Reynolds numbers: Re = 2898 (before liquid displaces gas) Re = 1105 (after liquid displaces gas) Convection mass transfer coefficient for gas in channel, $h_{m,G} = 0.006$ [m s^{-1}] (before liquid displaces gas) Convection mass transfer coefficient for liquid in channel, $h_{m,L} = 0.002$ [m s^{-1}] (after liquid displaces gas) Convection heat transfer coefficient for gas in channel, $h_{T,G} = 800$ [W $m^{-2}\ K^{-1}$] (before liquid displaces gas) Convection heat transfer coefficient for liquid in channel, $h_{T,L} = 5767$ [W $m^{-2}\ K^{-1}$] (after liquid displaces gas) $f = 0.047$ (before liquid displaces gas) $f = 0.057$ (after liquid displaces gas)

Table C.2 Calculation of heat and mass transfer coefficients – continued

Effective diffusion coefficient, $D_{eff} = 8.39 \times 10^{-8}$ [m^2 s^{-1}] Channel perimeter, $Peri = 1477 \times 10^{-6}$ [m] Gas mass transfer coefficient, $h_{m,G} = 0.006$ [m s^{-1}] (before liquid displaces gas) Liquid mass transfer coefficient, $h_{m,L} = 0.002$ [m s^{-1}] (after liquid displaces gas) Channel hydraulic radius, $R_h = 235 \times 10^{-6}$ [m] $R_0 = 250 \times 10^{-6}$ [m] For gas occupied node $y_{g,CH4} = 0.45$ $y_{g,CO2} = 0.55$ For liquid occupied node ($y_{g,CH4} = 0.02$ $y_{g,CO2} = 0.024$, iteratively solved species equation, described later)	**Mass transfer resistance during gas flows** $$R_{eq,Mass,G} = \frac{1}{h_m \cdot Peri} + \frac{\ln\left(\frac{R_0}{R_h}\right)}{2\pi \frac{D_{eff}}{1-y_{g,i}}}$$ **Total mass transfer resistance in liquid filled region during bubbly flow (Pressure driven)** $$R_{eq,Mass,L} = \frac{\ln\left(\frac{R_0}{R_h}\right)}{2\pi \frac{D_{eff}}{1-y_{g,i}}}$$ **Total mass transfer resistance in liquid filled region during diffusive flow (diffusion driven)** $$R_{eq,Mass,L} = \frac{1}{h_{m,L} \cdot Peri} + \frac{\ln\left(\frac{R_0}{R_h}\right)}{2\pi \frac{D_{eff}}{1-y_{g,i}}}$$ **Total mass transfer resistance in liquid filled region during cooling (diffusion driven, after water enters the adsorbent layer)** $$R_{eq,Mass,L} = \frac{1}{h_{m,L} \cdot Peri} + \frac{\ln\left(\frac{R_0}{R_h}\right)}{2\pi \frac{D_{eff,L}}{1-y_{g,i}}}$$	**Mass transfer resistance during gas flows** $R_{eq,Mass,G,CH4} = 69696$ [m^{-2} s] $R_{eq,Mass,G,CO2} = 84558$ [m^{-2} s] (Not used after liquid occupies the node at 0.5 m) Pressure driven: $R_{eq,Mass,L,CH4} = 64773$ [m^{-2} s] $R_{eq,Mass,L,CO2} = 52496$ [m^{-2} s] Diffusion driven: $R_{eq,Mass,L,CH4} = 3.276 \times 10^7$ [m^{-2} s] $R_{eq,Mass,L,CO2} = 3.275 \times 10^7$ [m^{-2} s] Liquid filled diffusion driven: $R_{eq,Mass,L,CH4} = 3.514 \times 10^7$ [m^{-2} s] $R_{eq,Mass,L,CO2} = 3.467 \times 10^7$ [m^{-2} s]
	Total heat transfer resistance $$R_{eq,Heat} = \frac{1}{h_T \cdot Peri} + \frac{\ln\left(\frac{R_0}{R_h}\right)}{2\pi k_w}$$	$R_{eq,Heat,G} = 0.88$ [W^{-1} m K] (Before liquid displaces gas) $R_{eq,Heat,G} = 0.15$ [W^{-1} m K] (After liquid displaces gas)

C.2. Governing equations

The species and energy conservation equations are solved using the DASOLV mathematical solver in gPROMS ModelBuilder (Process Systems Enterprise, 1997-2015). The solver uses an implicit variable time backward differentiation formulation for discretizing the equations. Sample formulation of species and energy conservation is shown, with calculations for the process instance of 0.392 s and for calculation node at 0.5 m from each end of the microchannel after initialization. In the equations, *i* is the iterator for species, whereas *j* is the iterator for axial locations for node points. This is the exact instant shown schematically in Figure C.2.

For all the equations in the governing equations sections, the switches implemented for altering equations assume the following values.

1. $S_{ads} = 0$, feed supply is cut off.
2. $S_{LDG} = 1$, gas displacement by liquid in progress, product collection can continue.
3. $S_{deso} = 0$, desorption stage not activated yet.
4. $S_{cool} = 0$, desorption stage not activated yet.
5. $S_{GDL} = 0$, desorption stage not activated yet.
6. $S_{Purge} = 0$, desorption stage not activated yet.

For the considered sample data point, as gases are being displaced by liquid at an axial location of 0.5 m from both the ends of the microchannel, the switches maintain their value indicated above. However, the gas and liquid phase identifiers are switched as follows.

1. $X_G = 1$, $X_L = 1$, at time $t = t$. Node occupied by gas.
2. $X_G = 0$, $X_L = 0$, at time $t = t+\Delta t$. Node occupied by liquid.

This technique allows the model to select the appropriate set of equations for each of the stages in the process, without the need for a complex computational approach.

Table C.3 Sample calculations for the governing conservation equations

Input	Equations	Output
This table shows the calculation of all differential variables using a backward differencing scheme with implicit time stepping method for the microchannel node.		
$C^{t}_{g,CH_4,j} = 22.69$ [kg m^{-3}] $C^{t}_{g,CO_2,j} = 27.74$ [kg m^{-3}] $\Delta t = 0.005$ [s] $u^{t+\Delta t}_{j} = 1.83$ [m s^{-1}] $C^{t+\Delta t}_{g,CH_4,j-1} = 18.30$ [kg m^{-3}] $C^{t+\Delta t}_{g,CO_2,j-1} = 22.51$ [kg m^{-3}] $\Delta z = 0.01$ [m] $D^{t+\Delta t}_{A,G,j} = 0.012$ [m^2 s^{-1}] $D^{t+\Delta t}_{A,L,j} = 2.23\times10^{-9}$ [m^2 s^{-1}] $C^{t+\Delta t}_{g,CH_4,j-2} = 16.21$ [kg m^{-3}] $C^{t+\Delta t}_{g,CO_2,j-2} = 20.31$ [kg m^{-3}] $\mathrm{R}^{t+\Delta t}_{eq,Mass,G,CH_4,j} = 76001$ [m^{-2} s] $\mathrm{R}^{t+\Delta t}_{eq,Mass,G,CO_2,j} = 90133$ [m^{-2} s] $\mathrm{R}^{t+\Delta t}_{eq,Mass,L,CH_4,j} = 2.72\times10^{6}$ [m^{-2} s] $\mathrm{R}^{t+\Delta t}_{eq,Mass,L,CO_2,j} = 2.73\times10^{6}$ [m^{-2} s] $C^{t+\Delta t}_{w,CH_4,j} = 23.68$ [kg m^{-3}] $C^{t+\Delta t}_{w,CO_2,j} = 29.18$ [kg m^{-3}] $A_g = 1.735\times10^{-7}$ [m^2]	**Microchannel species conservation equation** $\frac{\partial C_{g,i}}{\partial t} + u\frac{\partial C_{g,i}}{\partial z} -$ $\left[\begin{matrix}\left(S_{ads}+S_{LDG}\cdot X_G+S_{GDL}\cdot X_G+S_{purge}\right)D_{A,G}+\\ \left(S_{LDG}\cdot X_L+S_{deso}+S_{cool}+S_{GDL}\cdot X_L\right)D_{A,L}\end{matrix}\right]\cdot\frac{\partial^2 C_{g,i}}{\partial z^2}+$ $\left[\begin{matrix}\left(S_{ads}+S_{LDG}\cdot X_G+S_{GDL}\cdot X_G+S_{purge}\right)\frac{1}{\mathrm{R}_{eq,Mass,G,i}}+\\ \left(S_{LDG}\cdot X_L+S_{deso}+S_{cool}+S_{GDL}\cdot X_L\right)\frac{1}{\mathrm{R}_{eq,Mass,L,i}}\end{matrix}\right]\cdot\frac{\left(C_{g,i}-C_{w,i}\right)}{A_g}=0$ **Discretized form** $\frac{C^{t+\Delta t}_{g,i,j}-C^{t}_{g,i,j}}{\Delta t}+u^{t+\Delta t}_{j}\frac{C^{t+\Delta t}_{g,i,j}-C^{t+\Delta t}_{g,i,j-1}}{\Delta z}-$ $\left[\begin{matrix}\left(S_{ads}+S_{LDG}\cdot X_G+S_{GDL}\cdot X_G+S_{purge}\right)D^{t+\Delta t}_{A,G,i,j}+\\ \left(S_{LDG}\cdot X_L+S_{deso}+S_{cool}+S_{GDL}\cdot X_L\right)D^{t+\Delta t}_{A,L,i,j}\end{matrix}\right]\cdot\frac{C^{t+\Delta t}_{g,i,j-2}-2C^{t+\Delta t}_{g,i,j-1}+C^{t+\Delta t}_{g,i,j}}{\Delta z^2}+$ $\left[\begin{matrix}\left(S_{ads}+S_{LDG}\cdot X_G+S_{GDL}\cdot X_G+S_{purge}\right)\frac{1}{\mathrm{R}^{t+\Delta t}_{eq,Mass,G,i,j}}+\\ \left(S_{LDG}\cdot X_L+S_{deso}+S_{cool}+S_{GDL}\cdot X_L\right)\frac{1}{\mathrm{R}^{t+\Delta t}_{eq,Mass,L,i,j}}\end{matrix}\right]\cdot\frac{\left(C^{t+\Delta t}_{g,i,j}-C^{t+\Delta t}_{w,i,j}\right)}{A_g}=0$	$C^{t+\Delta t}_{g,CH_4,j} = 20.49$ [kg m^{-3}] $C^{t+\Delta t}_{g,CH_4,j} = 25.12$ [kg m^{-3}] (After iterations and implementing the switch procedure)

Table C.3 Sample calculations for the governing conservation equations – continued

$\rho_j^{t+\Delta t} = 651$ [kg m^{-3}] $c_{P,j}^{t+\Delta t} = 3867$ [kg m^{-3}] $T_{g,j}^{t} = 306.7$ [K] $\Delta t = 0.005$ [s] $u_j^{t+\Delta t} = 1.83$ [m s^{-1}] $T_{g,j-1}^{t+\Delta t} = 308.4$ [K] $\Delta z = 0.01$ [m] $k_{G,j}^{t+\Delta t} = 0.035$ [W m^{-1} K^{-1}] $k_{L,j}^{t+\Delta t} = 0.621$ [W m^{-1} K^{-1}] $T_{g,j-2}^{t+\Delta t} = 309.4$ [K] $\mathrm{R}_{eq,Heat,G,j}^{t+\Delta t} = 0.89$ [W^{-1}m K] $\mathrm{R}_{eq,Heat,L,j}^{t+\Delta t} = 0.15$ [W^{-1}m K] $T_{w,j}^{t+\Delta t} = 306.4$ [K] $A_g = 1.735\times10^{-7}$ [m^2]	**Microchannel energy conservation equation** $\frac{\partial(h_g)}{\partial t} + u\frac{\partial(h_g)}{\partial z} -$ $\left[\begin{matrix}(S_{ads} + S_{LDG}\cdot X_G + S_{GDL}\cdot X_G + S_{purge})k_G + \\ (S_{LDG}\cdot X_L + S_{deso} + S_{cool} + S_{GDL}\cdot X_L)k_L\end{matrix}\right]\cdot\frac{\partial^2 T_g}{\partial z^2} +$ $\left[\begin{matrix}(S_{ads} + S_{LDG}\cdot X_G + S_{GDL}\cdot X_G + S_{purge})\frac{1}{\mathrm{R}_{eq,Heat,G}} + \\ (S_{LDG}\cdot X_L + S_{deso} + S_{cool} + S_{GDL}\cdot X_L)\frac{1}{\mathrm{R}_{eq,Heat,L,i}}\end{matrix}\right]\cdot\frac{(T_g - T_w)}{A_g} = 0$ **Discretized form** $\rho_j^{t+\Delta t}c_{P,j}^{t+\Delta t}\frac{T_{g,j}^{t+\Delta t} - T_{g,j}^{t}}{\Delta t} + \rho_j^{t+\Delta t}c_{P,j}^{t+\Delta t}u_j^{t+\Delta t}\frac{T_{g,j}^{t+\Delta t} - T_{g,j-1}^{t+\Delta t}}{\Delta z} -$ $\left[\begin{matrix}(S_{ads} + S_{LDG}\cdot X_G + S_{GDL}\cdot X_G + S_{purge})k_{G,j}^{t+\Delta t} + \\ (S_{LDG}\cdot X_L + S_{deso} + S_{cool} + S_{GDL}\cdot X_L)k_{L,j}^{t+\Delta t}\end{matrix}\right]\cdot\frac{T_{g,j-2}^{t+\Delta t} - 2T_{g,j-1}^{t+\Delta t} + T_{g,j}^{t+\Delta t}}{\Delta z^2} +$ $\left[\begin{matrix}(S_{ads} + S_{LDG}\cdot X_G + S_{GDL}\cdot X_G + S_{purge})\frac{1}{\mathrm{R}_{eq,Heat,G,j}^{t+\Delta t}} + \\ (S_{LDG}\cdot X_L + S_{deso} + S_{cool} + S_{GDL}\cdot X_L)\frac{1}{\mathrm{R}_{eq,Heat,L,j}^{t+\Delta t}}\end{matrix}\right]\cdot\frac{(T_{g,j}^{t+\Delta t} - T_{w,j}^{t+\Delta t})}{A_g} = 0$	$T_{g,j}^{t} = 307.5$ [K] (After iterations and implementing the switch procedure)

Table C.3 Sample calculations for the governing conservation equations – continued

This table shows the calculation of all differential variables using a backward differencing scheme with implicit time stepping method for the adsorbent layer node.

$\varepsilon = 0.55$

$C^{t}_{w,CH_4,j} = 23.68$ [kg m^{-3}]

$C^{t}_{w,CO_2,j} = 29.18$ [kg m^{-3}]

$\Delta t = 0.005$ [s]

$\omega = 0.1991$

$C^{t}_{A,CH_4,j} = 1659$ [mol m^{-3}]

$C^{t}_{A,CO_2,j} = 5205$ [mol m^{-3}]

$D^{t+\Delta t}_{eff,G,j} = 8.39\times10^{-8}$ [m^2 s^{-1}]

$D^{t+\Delta t}_{eff,L,j} = 6.13\times10^{-10}$ [m^2 s^{-1}]

$C^{t+\Delta t}_{w,CH_4,j-2} = 23.17$ [kg m^{-3}]

$C^{t+\Delta t}_{w,CO_2,j-2} = 28.76$ [kg m^{-3}]

$C^{t+\Delta t}_{w,CH_4,j-1} = 23.41$ [kg m^{-3}]

$C^{t+\Delta t}_{w,CO_2,j-1} = 28.96$ [kg m^{-3}]

$\Delta z = 0.01$ [m]

$\mathrm{R}^{t+\Delta t}_{eq,Mass,G,CH_4,j} = 76001$ [m^{-2} s]

$\mathrm{R}^{t+\Delta t}_{eq,Mass,G,CO_2,j} = 90133$ [m^{-2} s]

$\mathrm{R}^{t+\Delta t}_{eq,Mass,L,CH_4,j} = 2.72\times10^{6}$ [m^{-2} s]

$\mathrm{R}^{t+\Delta t}_{eq,Mass,L,CO_2,j} = 2.73\times10^{6}$ [m^{-2} s]

$C^{t+\Delta t}_{g,CH_4,j} = 20.49$ [kg m^{-3}]

$C^{t+\Delta t}_{g,CO_2,j} = 25.12$ [kg m^{-3}]

$A_w = 4.712 \times 10^{-8}$ [m^2]

Adsorbent layer species conservation equations

$$\varepsilon\frac{\partial C_{w,i}}{\partial t}+\omega\frac{\partial C_{A,i}}{\partial t}-\left[\begin{array}{l}\left(S_{ads}+S_{LDG}\cdot X_G+S_{GDL}\cdot X_G+S_{purge}\right)D_{eff,G,i}+\\ \left(S_{LDG}\cdot X_L+S_{deso}+S_{cool}+S_{GDL}\cdot X_L\right)D_{eff,L,i}\end{array}\right]\cdot\frac{\partial^2 C_{w,i}}{\partial z^2}-\left[\begin{array}{l}\left(S_{ads}+S_{LDG}\cdot X_G+S_{GDL}\cdot X_G+S_{purge}\right)\dfrac{1}{\mathrm{R}_{eq,Mass,G,i}}+\\ \left(S_{LDG}\cdot X_L+S_{deso}+S_{cool}+S_{GDL}\cdot X_L\right)\dfrac{1}{\mathrm{R}_{eq,Mass,L,i}}\end{array}\right]\cdot\frac{\left(C_{g,i}-C_{w,i}\right)}{A_w}=0$$

Discretized form

$$\varepsilon\frac{\left(C^{t+\Delta t}_{w,i,j}-C^{t}_{w,i,j}\right)}{\Delta t}+\omega\frac{\left(C^{t+\Delta t}_{A,i,j}-C^{t}_{A,i,j}\right)}{\Delta t}-\left[\begin{array}{l}\left(S_{ads}+S_{LDG}\cdot X_G+S_{GDL}\cdot X_G+S_{purge}\right)D^{t+\Delta t}_{eff,G,j}+\\ \left(S_{LDG}\cdot X_L+S_{deso}+S_{cool}+S_{GDL}\cdot X_L\right)D^{t+\Delta t}_{eff,L,j}\end{array}\right]\cdot\frac{C^{t+\Delta t}_{w,i,j-2}-2C^{t+\Delta t}_{w,i,j-1}+C^{t+\Delta t}_{w,i,j}}{\Delta z^2}-\left[\begin{array}{l}\left(S_{ads}+S_{LDG}\cdot X_G+S_{GDL}\cdot X_G+S_{purge}\right)\dfrac{1}{\mathrm{R}^{t+\Delta t}_{eq,Mass,G,i,j}}+\\ \left(S_{LDG}\cdot X_L+S_{deso}+S_{cool}+S_{GDL}\cdot X_L\right)\dfrac{1}{\mathrm{R}^{t+\Delta t}_{eq,Mass,L,i,j}}\end{array}\right]\cdot\frac{\left(C^{t+\Delta t}_{g,i,j}-C^{t+\Delta t}_{w,i,j}\right)}{A_w}=0$$

$C^{t+\Delta t}_{w,CH_4,j} = 23.61$ [kg m^{-3}]

$C^{t+\Delta t}_{w,CO_2,j} = 29.13$ [kg m^{-3}]

$C^{t+\Delta t}_{A,CH_4,j} = 1654$ [mol m^{-3}]

$C^{t+\Delta t}_{A,CO_2,j} = 5200$ [mol m^{-3}]

(After iterations and implementing the switch procedure)

Table C.3 Sample calculations for the governing conservation equations – continued

$\rho_w = 637$ [kg m^{-3}] $c_{P,w} = 1131$ [J kg^{-1} K^{-1}] $T_{w,j}^{t} = 306$ [K] $\Delta t = 0.005$ [s] $k_w = 0.2941$ [W m^{-1} K^{-1}] $T_{w,j-2}^{t+\Delta t} = 307.5$ [K] $T_{w,j-1}^{t+\Delta t} = 306.9$ [K] $\Delta z = 0.01$ [m] $A_w = 4.71\times10^{-8}$ [m^2] $T_{g,j}^{t+\Delta t} = 308$ [K] $\mathrm{R}_{eq,Heat,j}^{t+\Delta t} = 0.89$ [W^{-1}m K] $\omega = 0.1991$ $\Delta H_{ads,CH_4} = 20400$ [J mol^{-1}] $\Delta H_{ads,CO_2} = 25000$ [J mol^{-1}] $C_{A,CH_4,j}^{t} = 1659$ [mol m^{-3}] $C_{A,CO_2,j}^{t} = 5205$ [mol m^{-3}] $\mathrm{R}_{eq,FS} = 0.0369$ $\left[\mathrm{W}^{-1}\mathrm{m\ K}\right]$ $\rho_{FS} = 2200$ [kg m^{-3}] $c_{P,FS} = 740$ [J kg^{-1} K^{-1}] $T_{FS,j}^{t} = 306$ [K] $k_{FS} = 1.3$ [W m^{-1} K^{-1}] $T_{FS,j-2}^{t+\Delta t} = 307.2$ [K] $T_{FS,j-1}^{t+\Delta t} = 306.6$ [K] $A_{FS} = 4.359\times10^{-8}$ [m^2]	**Energy conservation for adsorbent layer** $$\rho_w C_{p,w}\frac{\partial T_w}{\partial t} = k_w\frac{\partial^2 T_w}{\partial z^2} + \frac{T_g - T_w}{A_w\cdot \mathrm{R}_{eq,heat}} +$$ $$\sum_i \omega\cdot h_{ads,i}\frac{\partial C_{A,i}}{\partial t} - \frac{T_w - T_{FS}}{A_w\cdot \mathrm{R}_{eq,FS}}$$ **Discretized form** $$\rho_w C_{p,w}\frac{T_{w,j}^{t+\Delta t} - T_{w,j}^{t}}{\Delta t} = k_w\frac{T_{w,j-2}^{t+\Delta t} - 2T_{w,j-1}^{t+\Delta t} + T_{w,j}^{t+\Delta t}}{\Delta z^2} +$$ $$\frac{T_{g,j}^{t+\Delta t} - T_{w,j}^{t+\Delta t}}{A_w\cdot \mathrm{R}_{eq,Heat,j}} + \sum_i \omega\cdot\Delta H_{ads,i}\frac{\left(C_{A,i,j}^{t+\Delta t} - C_{A,i,j}^{t}\right)}{\Delta t} - \frac{T_{w,j}^{t+\Delta t} - T_{FS,j}^{t+\Delta t}}{A_w\cdot \mathrm{R}_{eq,FS}}$$ **Energy conservation for fused silica monolith wall** $$\rho_{FS} C_{p,FS}\frac{\partial T_{FS}}{\partial t} = k_{FS}\frac{\partial^2 T_{FS}}{\partial z^2} + \frac{T_w - T_{FS}}{A_{FS}\cdot \mathrm{R}_{eq,FS}}$$ **Discretized form** $$\rho_{FS} C_{p,FS}\frac{T_{FS,j}^{t+\Delta t} - T_{FS,j}^{t}}{\Delta t} =$$ $$k_{FS}\frac{T_{FS,j-2}^{t+\Delta t} - 2T_{FS,j-1}^{t+\Delta t} + T_{FS,j}^{t+\Delta t}}{\Delta z^2} + \frac{T_{w,j}^{t+\Delta t} - T_{FS,j}^{t+\Delta t}}{A_{FS}\cdot \mathrm{R}_{eq,FS}}$$	$T_{w,j}^{t+\Delta t} = 306.5$ [K] $T_{FS,j}^{t+\Delta t} = 306.3$ [K] (After iterations and implementing the switch procedure)

Table C.3 Sample calculations for the governing conservation equations – continued

$\Delta P = 10^5$ [Pa] $L = 1$ [m] $\rho_j^{t+\Delta t} = 951$ [kg m^{-3}] $u_j^t = 1.838$ [m s^{-1}] $u_{j+1}^{t+\Delta t} = 1.838$ [m s^{-1}] $u_{j-1}^{t+\Delta t} = 1.838$ [m s^{-1}] $\Delta z = 0.5$ [m] $C_{g,CH_4,j}^{t+\Delta t} = 20.49$ [kg m^{-3}] $C_{g,CH_4,j}^{t+\Delta t} = 25.12$ [kg m^{-3}] $C_{w,CH_4,j}^{t+\Delta t} = 23.61$ [kg m^{-3}] $C_{w,CO_2,j}^{t+\Delta t} = 29.13$ [kg m^{-3}] $A_g = 1.73\times10^{-7}$ [m^2] $\mathrm{R}_{eq,Mass,G,CH_4,j}^{t+\Delta t} = 76001$ [m^{-2} s] $\mathrm{R}_{eq,Mass,G,CO_2,j}^{t+\Delta t} = 90133$ [m^{-2} s] $\mathrm{R}_{eq,Mass,L,CH_4,j}^{t+\Delta t} = 2.72\times10^6$ [m^{-2} s] $\mathrm{R}_{eq,Mass,L,CO_2,j}^{t+\Delta t} = 2.73\times10^6$ [m^{-2} s] $\mu_j^{t+\Delta t} = 7.3\times10^{-4}$ [kg m^{-1} s^{-1}] $f_j^{t+\Delta t} = 0.057$ $R_h = 235\times10^{-6}$ [m] $f_{L,j}^{t+\Delta t} = 0.057$ $\rho_{L,j}^{t+\Delta t} = 951$ [kg m^{-3}] $z_{IF} = 0.5$ [m]	**Overall momentum equation** $$-\frac{\partial P}{\partial z} = \left(S_{ads} + S_{purge} + S_{deso} + S_{cool}\right)\left(\begin{array}{l}\rho\frac{\partial u}{\partial t} + \rho u\frac{\partial u}{\partial z} - \\ \sum_i \frac{C_{g,i} - C_{w,i}}{A_{cs}\cdot \mathrm{R}_{eq,Mass,i}} u - \mu\frac{\partial^2 u}{\partial z^2} + f\frac{\rho u^2}{2D_h}\end{array}\right)$$ $$+\left(S_{LDG}\right)\left[\begin{array}{l}\left(f_L\frac{\rho_L u^2}{2D_h} + \rho_L\frac{du}{dt}\right)z_{IF} + \\ \left(f_G\frac{\rho_G u^2}{2D_h} + \rho_G\frac{du}{dt}\right)\left(L - z_{IF}\right)\end{array}\right] + \left(S_{GDL}\right)\left[\begin{array}{l}\left(f_L\frac{\rho_L u^2}{2D_h} + \rho_L\frac{du}{dt}\right)\left(L - z_{IF}\right) + \\ \left(f_G\frac{\rho_G u^2}{2D_h} + \rho_G\frac{du}{dt}\right)\left(z_{IF}\right)\end{array}\right]$$ **Discretized and overall form used in the process model** $$-\frac{\Delta P}{L} = \left(S_{ads} + S_{purge} + S_{deso} + S_{cool}\right)$$ $$\left(\begin{array}{l}\rho_j^{t+\Delta t}\frac{u_j^{t+\Delta t} - u_j^t}{\Delta t} + \rho_j^{t+\Delta t}u_j^{t+\Delta t}\frac{u_{j+1}^{t+\Delta t} - u_{j-1}^{t+\Delta t}}{2\Delta z} - \\ \sum_i \frac{C_{g,i,j}^{t+\Delta t} - C_{w,i,j}^{t+\Delta t}}{A_g\cdot \mathrm{R}_{eq,Mass,i,j}^{t+\Delta t}} u_j^{t+\Delta t} - \mu_j^{t+\Delta t}\frac{u_{j+1}^{t+\Delta t} - 2u_j^{t+\Delta t} + u_{j-1}^{t+\Delta t}}{\Delta z^2} + f_j^{t+\Delta t}\frac{\rho_j^{t+\Delta t}\left(u_j^{t+\Delta t}\right)^2}{2D_h}\end{array}\right)$$ $$+\left(S_{LDG}\right)\left[\begin{array}{l}\left(f_{L,j}^{t+\Delta t}\frac{\rho_{L,j}^{t+\Delta t}\left(u_j^{t+\Delta t}\right)^2}{2D_h} + \rho_{L,j}^{t+\Delta t}\frac{u_j^{t+\Delta t} - u_j^t}{\Delta t}\right)z_{IF} + \\ \left(f_{G,j}^{t+\Delta t}\frac{\rho_{G,j}^{t+\Delta t}\left(u_j^{t+\Delta t}\right)^2}{2D_h} + \rho_{G,j}^{t+\Delta t}\frac{u_j^{t+\Delta t} - u_j^t}{\Delta t}\right)\left(L - z_{IF}\right)\end{array}\right]$$ $$+\left(S_{GDL}\right)\left[\begin{array}{l}\left(f_{L,j}^{t+\Delta t}\frac{\rho_{L,j}^{t+\Delta t}\left(u_j^{t+\Delta t}\right)^2}{2D_h} + \rho_{L,j}^{t+\Delta t}\frac{u_j^{t+\Delta t} - u_j^t}{\Delta t}\right)\left(L - z_{IF}\right) + \\ \left(f_{G,j}^{t+\Delta t}\frac{\rho_{G,j}^{t+\Delta t}\left(u_j^{t+\Delta t}\right)^2}{2D_h} + \rho_{G,j}^{t+\Delta t}\frac{u_j^{t+\Delta t} - u_j^t}{\Delta t}\right)z_{IF}\end{array}\right]$$	$u_j^{t+\Delta t} = 1.838$ [m s^{-1}] (Because displacement equations without convection terms are solved, axial dependence on velocity is absent)

Table C.3 Sample calculations for the governing conservation equations – continued

$r_{crystal} = 10^{-6}$ [m] $D_{crystal,CH_4} = 7.2\times10^{-12}$ [m^2 s^{-1}] $D_{crystal,CO_2} = 5.9\times10^{-11}$ [m^2 s^{-1}] $C^t_{A,CH_4,j} = 1659$ [mol m^{-3}] $C^t_{A,CO_2,j} = 5205$ [mol m^{-3}] $\Delta t = 0.005$ [s] $b_{0,CH_4} = 4.15\times10^{-12}$ [kPa^{-1}] $b_{0,CO_2} = 4.50\times10^{-12}$ [kPa^{-1}] $Q_{B,CH_4} = 20400$ [J mol^{-1}] $Q_{B,CH_4} = 25000$ [J mol^{-1}] $R = 8.314$ [J mol^{-1} K^{-1}] $T^{t+\Delta t}_{w,j} = 306.5$ [K] $M_{B,CH_4} = 3.918$ [mol kg^{-1}] $M_{D,CO_2} = 4.161$ [mol kg^{-1}] $\rho_{ads} = 1760$ [kg m^{-3}] $C^t_{w,CH_4,j} = 23.68$ [kg m^{-3}] $C^t_{w,CO_2,j} = 29.18$ [kg m^{-3}]	**LDF constant** $K_{LDF,i} = \frac{15\cdot D_{crystal,i}}{r_{crystal}^{\ 2}}$ **LDF Equation** $\frac{\partial C_{A,i}}{\partial t} = K_{LDF,i}\cdot\left(C_{A,Eq,i} - C_{A,i}\right)$ **Discretized form** $\frac{C^{t+\Delta t}_{A,i,j} - C^t_{A,i,j}}{\Delta t} = K^{t+\Delta t}_{LDF,i,j}\cdot\left(C^{t+\Delta t}_{A,Eq,i,j} - C^{t+\Delta t}_{A,i,j}\right)$ **Auxiliary parameters for adsorbent capacity determination** $B_i = b_{0i}\exp\left(\frac{-Q_{B,i}}{RT_w}\right)$ $B^{t+\Delta t}_{i,j} = b_{0i}\exp\left(\frac{-Q_{B,i}}{RT^{t+\Delta t}_{w,j}}\right)$ **Isotherm equation for silicalite** $C_{A,Eq,i} = \rho_{ads}\left(M_{B,i}\frac{B_i\cdot P_i}{1+\sum_i B_i\cdot P_i}\right)$ $C^{t+\Delta t}_{A,Eq,i,j} = \rho_{ads}\left(M_{B,i}\frac{B^{t+\Delta t}_{i,\ j}\cdot P^{t+\Delta t}_{i,j}}{1+\sum_i B^{t+\Delta t}_{i,\ j}\cdot P^{t+\Delta t}_{i,j}}\right)$ **Gas partial pressure** $P_i = \frac{C_{w,i}RuT_w}{MW_i}$ $P^{t+\Delta t}_{i,j} = \frac{C^{t+\Delta t}_{w,i,j}RT^{t+\Delta t}_{w,j}}{MW_i}$	$K_{LDF,CH_4} = 108$ [s^{-1}] $K_{LDF,CO_2} = 885$ [s^{-1}] $C^{t+\Delta t}_{A,CH_4,j} = 1654$ [mol m^{-3}] $C^{t+\Delta t}_{A,CO_2,j} = 5200$ [mol m^{-3}] $C^{t+\Delta t}_{A,Eq,H_4,j} = 1647$ [mol m^{-3}] $C^{t+\Delta t}_{A,Eq,CO_2,j} = 5198$ [mol m^{-3}] $B^{t+\Delta t}_{CH_4,j} = 1.2\times10^{-3}$ [kPa^{-1}] $B^{t+\Delta t}_{CO_2,j} = 8.0\times10^{-3}$ [kPa^{-1}] $P^{t+\Delta t}_{CH_4,j} = 3749$ [kPa] $P^{t+\Delta t}_{CO_2,j} = 1686$ [kPa]

C.3 – Fluid property calculations and process performance parameters

For this section, calculations are shown for the instant when liquid has displaced gases in the microchannel at 0.397 s after the start of the process at 0.5 m. Figure C.2 also applies here, where appropriate techniques to calculate fluid properties are shown for the final state of the considered instant**.**

Table C.4. Sample calculations for fluid property and process performance parameters

Input	**Equations**	**Output**
$\sum_i C_{g,i} = 45.61\ [\text{kg m}^{-3}]$ $\rho_L = 995.2\ [\text{kg m}^{-3}]$	**Two phase quality in the microchannel** $Quality = \dfrac{\sum_i C_{g,i}}{\rho_L}$ $Quality_j^{t+\Delta t} = \dfrac{\sum_i C_{g,i,j}^{t+\Delta t}}{\rho_{L,j}^{t+\Delta t}}$	Quality of desorbed gases in the HTF liquid present in the microchannel, *Quality* = 0.0458
$\sum_i C_{g,i} = 45.61\ [\text{kg m}^{-3}]$ $\rho_L = 995.2\ [\text{kg m}^{-3}]$ $Quality = 0.0458$	**Effective fluid density in the microchannel** $\rho_g = \left(S_{ads} + S_{LDG}\cdot X_G + S_{GDL}\cdot X_G + S_{purge}\right)\times \sum_i C_{g,i}$ $+\left(S_{LDG}\cdot X_L + S_{deso} + S_{cool} + S_{GDL}\cdot X_L\right)\times$ $\left(\sum_i C_{g,i}\times Quality + \rho_L \times (1 - Quality)\right)$ $\rho_{g,j}^{t+\Delta t} = \left(S_{ads} + S_{LDG}\cdot X_G + S_{GDL}\cdot X_G + S_{purge}\right)\times \sum_i C_{g,i,j}^{t+\Delta t}$ $+\left(S_{LDG}\cdot X_L + S_{deso} + S_{cool} + S_{GDL}\cdot X_L\right)\times$ $\left(\sum_i C_{g,i,j}^{t+\Delta t}\times Quality_j^{t+\Delta t} + \rho_L^{t+\Delta t}\times\left(1 - Quality_j^{t+\Delta t}\right)\right)$	Reduced HTF density due to suspended gases in the liquid, $\rho_g = 951.7\ [\text{kg m}^{-3}]$

Table C.4. Sample calculations for fluid property and process performance parameters – continued

$C_{g,CH_4} = 20.50$ [kg m^{-3}] $C_{g,CO_2} = 25.12$ [kg m^{-3}] $\sum_i C_{g,i} = 45.61$ [kg m^{-3}] $\rho_L = 995.2$ [kg m^{-3}]	**Effective gas mass fraction in the microchannel** $y_{i,g} = \left(S_{ads} + S_{LDG} \cdot X_G + S_{GDL} \cdot X_G + S_{purge}\right) \times \frac{C_{g,i}}{\sum_i C_{g,i}}$ $+\left(S_{LDG} \cdot X_L + S_{deso} + S_{cool} + S_{GDL} \cdot X_L\right) \times \frac{C_{g,i}}{\sum_i C_{g,i} + \rho_L}$ $y_{g,i,j}^{t+\Delta t} = \left(S_{ads} + S_{LDG} \cdot X_G + S_{GDL} \cdot X_G + S_{purge}\right) \times \frac{C_{g,i,j}^{t+\Delta t}}{\sum_i C_{g,i,j}^{t+\Delta t}}$ $+\left(S_{LDG} \cdot X_L + S_{deso} + S_{cool} + S_{GDL} \cdot X_L\right) \times \frac{C_{g,i,j}^{t+\Delta t}}{\sum_i C_{g,i,j}^{t+\Delta t} + \rho_{L,j}^{t+\Delta t}}$	Mass fractions of component gases in liquid HTF, $y_{g,CH_4} = 0.019$ $y_{g,CO_2} = 0.024$
$c_{P,G} = 1853$ [J kg^{-1} K^{-1}] $c_{P,L} = 3867$ [J kg^{-1} K^{-1}]	**Effective fluid specific heat in the microchannel** $c_{p,g} = \left(S_{ads} + S_{LDG} \cdot X_G + S_{GDL} \cdot X_G + S_{purge}\right) \times C_{p,G}$ $+\left(S_{LDG} \cdot X_L + S_{deso} + S_{cool} + S_{GDL} \cdot X_L\right) \times C_{p,L}$ $C_{p,g,j}^{t+\Delta t} = \left(S_{ads} + S_{LDG} \cdot X_G + S_{GDL} \cdot X_G + S_{purge}\right) \times C_{p,G,j}^{t+\Delta t}$ $+\left(S_{LDG} \cdot X_L + S_{deso} + S_{cool} + S_{GDL} \cdot X_L\right) \times C_{p,L,j}^{t+\Delta t}$	Fluid specific heat for the microchannel node, $c_{P,g} = 3867$ [J kg^{-1} K^{-1}]
$k_G = 0.035$ [W m^{-1} K^{-1}] $k_L = 0.621$ [W m^{-1} K^{-1}]	**Effective fluid thermal conductivity in the microchannel** $k_g = \left(S_{ads} + S_{LDG} \cdot X_G + S_{GDL} \cdot X_G + S_{purge}\right) \times k_G$ $+\left(S_{LDG} \cdot X_L + S_{deso} + S_{cool} + S_{GDL} \cdot X_L\right) \times k_L$ $k_{g,j}^{t+\Delta t} = \left(S_{ads} + S_{LDG} \cdot X_G + S_{GDL} \cdot X_G + S_{purge}\right) \times k_{G,j}^{t+\Delta t}$ $+\left(S_{LDG} \cdot X_L + S_{deso} + S_{cool} + S_{GDL} \cdot X_L\right) \times k_{L,j}^{t+\Delta t}$	Fluid thermal conductivity for the microchannel node, $k_g = 0.621$ [W m^{-1} K^{-1}]
$\mu_G = 1.5 \times 10^{-5}$ [kg m^{-1} s^{-1}] $\mu_L = 7.3 \times 10^{-4}$ [kg m^{-1} s^{-1}]	**Effective fluid viscosity in the microchannel** $\mu_g = \left(S_{ads} + S_{LDG} \cdot X_G + S_{GDL} \cdot X_G + S_{purge}\right) \times \mu_G$ $+\left(S_{LDG} \cdot X_L + S_{deso} + S_{cool} + S_{GDL} \cdot X_L\right) \times \mu_L$ $\mu_{g,j}^{t+\Delta t} = \left(S_{ads} + S_{LDG} \cdot X_G + S_{GDL} \cdot X_G + S_{purge}\right) \times \mu_{G,j}^{t+\Delta t}$ $+\left(S_{LDG} \cdot X_L + S_{deso} + S_{cool} + S_{GDL} \cdot X_L\right) \times \mu_{L,j}^{t+\Delta t}$	Fluid viscosity for the microchannel node, $\mu_g = 7.3 \times 10^{-4}$ [kg m^{-1} s^{-1}]

Table C.4. Sample calculations for fluid property and process performance parameters – continued

	Feed gas supplied $\frac{dM_{Feed,inlet,i}}{dt} = N_{ch} S_{ads} \left(C_{g,i} A_g u \right)\Big\|_{z=0}$ $\frac{M^{t+\Delta t}_{Feed,inlet,i} - M^{t}_{Feed,inlet,i}}{\Delta t} = N_{ch} S_{ads} \left(C^{t}_{g,i} A_g u^{t}_{g} \right)\Big\|_{z=0}$	Feed gas entering the channel in 0.19 s, $M^{t+\Delta t}_{Feed,inlet,CH_4} = 0.3708$ [kg kg^{-1}] $M^{t+\Delta t}_{Feed,inlet,CO_2} = 0.4532$ [kg kg^{-1}]
	Product gas collected $\frac{dM_{Prod,net}}{dt} = N_{ch} \begin{bmatrix} \left(S_{ads} + S_{collection} + S_{Purge} \right) \left(C^{t}_{g,i} A_g u \right)\Big\|_{z=L} \\ -\left(S_{GDL} + S_{Purge} \right) \left(C^{t}_{g,i} A_g u \right)\Big\|_{z=0} \end{bmatrix}$ $\frac{M^{t+\Delta t}_{Prod,net} - M^{t}_{Prod,net}}{\Delta t} = N_{ch} \begin{bmatrix} \left(S_{ads} + S_{collection} + S_{Purge} \right) \left(C^{t}_{g,i} A_g u^{t}_{g} \right)\Big\|_{z=L} \\ -\left(S_{GDL} + S_{Purge} \right) \left(C^{t}_{g,i} A_g u^{t}_{g} \right)\Big\|_{z=0} \end{bmatrix}$	Product gas collected $M^{t+\Delta t}_{Prod,net,CH_4} = 0.8708$ [kg kg^{-1}] $M^{t+\Delta t}_{Prod,net,CO_2} = 0.0061$ [kg kg^{-1}]
	Mass and molar purities of product gas $Purity_{kg} = \frac{M^{t+\Delta t}_{Prod,net,CH_4}}{M^{t+\Delta t}_{Prod,net,CH_4} + M^{t+\Delta t}_{Prod,net,CO_2}}$ $Purity_{Mole} = \frac{\left(Purity_{kg,i} / MW_i \right)}{\sum_i \left(Purity_{kg,i} / MW_i \right)}$ $Purity^{t+\Delta t}_{kg,i} = \frac{M^{t+\Delta t}_{i}}{M^{t+\Delta t}_{CH_4} + M^{t+\Delta t}_{CH_4}}$ $Purity^{t+\Delta t}_{Mole} = \frac{\left(Purity^{t+\Delta t}_{kg,i} / MW_i \right)}{\sum_i \left(Purity^{t+\Delta t}_{kg,i} / MW_i \right)}$	$Purity^{t+\Delta t}_{kg,CH_4} = 0.993$ $Purity^{t+\Delta t}_{kg,CO_2} = 0.007$ $Purity^{t+\Delta t}_{mole,CH_4} = 0.997$ $Purity^{t+\Delta t}_{mole,CO_2} = 0.003$

$M^{t}_{Feed,inlet,CH_4} = 0.3708$ [kg kg^{-1}] $M^{t}_{Feed,inlet,CO_2} = 0.4532$ [kg kg^{-1}] $M^{t}_{\mathrm{Prod},net,CH_4} = 0.8657$ [kg kg^{-1}] $M^{t}_{\mathrm{Prod},net,CO_2} = 0.0057$ [kg kg^{-1}] $\Delta t = 0.005$ [s] $N_{ch} = 75500$ $C_{g,CH_4,0} = 0.01$ [kg m^{-3}] $C_{g,CO_2,0} = 0.01$ [kg m^{-3}] $A_g = 1.73\times10^{-7}$ [m^2] $u_0 = u_L = 1.838$ [m s^{-1}] $C_{g,CH_4,L} = 39.2$ [kg m^{-3}] $C_{g,CO_2,L} = 2.8$ [kg m^{-3}] $MW_{CH_4} = 16.04$ [kg kmol^{-1}] $MW_{CO_2} = 44.01$ [kg kmol^{-1}]	**Instantaneous methane recovery** $\mathrm{Recovery}_{CH_4} = \frac{M_{CH_4,\mathrm{Prod}}}{M_{CH_4,Feed}}$ $\mathrm{Recovery}^{t+\Delta t}_{CH_4} = \frac{M^{t+\Delta t}_{\mathrm{Prod},net,CH_4}}{M^{t+\Delta t}_{Feed,inlet,CH_4}}$	$\mathrm{Recovery}^{t+\Delta t}_{CH_4} = 2.34$ (Recovery is greater than one because of collection of residual gas at the start of the cycle. The value will decrease below one, after product purge)

C.4 – Energy requirement calculation for overall process operation in cyclic steady state

This section describes the overall energy requirement calculation for the process, after the cyclic steady state of the process is attained. These calculations correspond to Figure 3.6 in Chapter 3. These variables represent an overall process performance and they do not correspond to a particular time instant, such as one in Figure C.2.

Table C.5. Sample calculations for energy requirement for the process operation.

Input	**Equations**	**Output**
$\dot{N}_{cyc} = 17.7$ [cycles hr^{-1}] $N_{ch} = 75500$ [channels kg^{-1}] $\rho_w = 637.2$ [kg m^{-3}] $c_{P,w} = 1131$ [J kg^{-1} K^{-1}] $A_w = 1.73\times10^{-7}$ [m^2] $\rho_{FS} = 2200$ [kg m^{-3}] $c_{P,FS} = 740$ [J kg^{-1} K^{-1}] $A_{FS} = 4.359\times10^{-8}$ [m^2] $L = 1$ [m] $\Delta T = 175$ [C]	**Sensible heat** $\dot{E}_{Sens} = \dot{N}_{cyc} \cdot N_{ch} \left(\rho_w \cdot c_{p,w} \cdot A_w + \rho_{FS} \cdot c_{FS} \cdot A_{FS} \right) \cdot L \cdot \Delta T$	$\dot{E}_{Sens} = 23842$ [kJ kg^{-1} hr^{-1}]

Table C.5. Sample calculations for energy requirement for the process operation – continued

$\dot{N}_{cyc} = 17.7$ [cycles hr^{-1}] $N_{ch} = 75500$ [channels kg^{-1}] $A_w = 1.73\times10^{-7}$ [m^2] $L = 1$ [m] $\omega = 0.1991$ $\Delta H_{ads,CH_4} = 20400$ [J mol^{-1}] $\Delta H_{ads,CO_2} = 25000$ [J mol^{-1}] $\Delta C_{A,CH_4} = 3600$ [mol m^{-3}] $\Delta C_{A,CO_2} = 4900$ [mol m^{-3}]	**Heat of desorption** $\dot{E}_{Deso} = \dot{N}_{cyc} \cdot N_{ch} A_w \cdot L \cdot \sum_i \omega \cdot \Delta H_{ads,i} \cdot \Delta C_{A,i}$	$\dot{E}_{Deso} = 2457$ [kJ kg^{-1} hr^{-1}]
$\dot{N}_{cyc} = 17.7$ [cycles hr^{-1}] $N_{ch} = 75500$ [channels kg^{-1}] $M_{HTF,cyc} = 1.12\times10^{-3}$ [kg cycle^{-1}] $v_{HTF} = 0.0011$ [m^3 kg^{-1}] $\Delta P = 100$ [kPa]	**HTF recirculation energy** $\dot{E}_{HTF,recir} = \dot{N}_{cyc} \cdot N_{ch} \cdot M_{HTF,cyc} \cdot v_{HTF} \cdot \Delta P$	$\dot{E}_{HTF,recir} = 172$ [kJ kg^{-1} hr^{-1}]
$\dot{N}_{cyc} = 17.7$ [cycles hr^{-1}] $N_{ch} = 75500$ [channels kg^{-1}] $\Delta H_{com} = 0.0229$ [kJ cycle^{-1}]	**Purge gas recirculation energy** $\dot{E}_{purge} = \dot{N}_{cyc} \cdot N_{ch} \cdot \Delta H_{Com}$	$\dot{E}_{purge} = 30600$ [kJ kg^{-1} hr^{-1}]

Table C.5. Sample calculations for energy requirement for the process operation.

$\dot{E}_{Sens} = 25383$ [kJ kg^{-1} hr^{-1}] $\dot{E}_{Deso} = 2457$ [kJ kg^{-1} hr^{-1}] $\dot{E}_{HTF,recir} = 172$ [kJ kg^{-1} hr^{-1}] $\dot{E}_{purge} = 30600$ [kJ kg^{-1} hr^{-1}] $Purity_{CH_4} = 0.867$ $\dot{M}_{prod} = 9.66$ [kg kg^{-1} hr^{-1}] $LHV = 50000$ [kJ kg^{-1}]	**Energy ratio** $Ratio_{Energy} = \frac{\dot{E}_{Deso} + \dot{E}_{Sens} + \dot{E}_{HTF,recir} + \dot{E}_{purge}}{Purity_{CH_4} \dot{M}_{prod} \cdot LHV}$	$Ratio_{Energy} = 0.136$

D. SAMPLE CALCULATIONS FOR LABORATORY SCALE MODELS

This section describes sample calculations for the laboratory scale models. The laboratory scale model calculations are shown for t = 2 s after the start of the adsorption stage, for the axial midpoint of the custom adsorbent-coated microchannel, where the adsorption wave front is approximately located. The length of the channel is 0.22 m, while the applied pressure drop is 16 kPa. The description of the algebraic and differential parameters in this section for the laboratory scale models is analogous to that for the full process model. Figure D.1 shows the cross section of the microchannel schematic considered for modeling, whereas Figure D.2 shows the longitudinal cross section of the channel showing the possible location of the adsorption thermal wave.

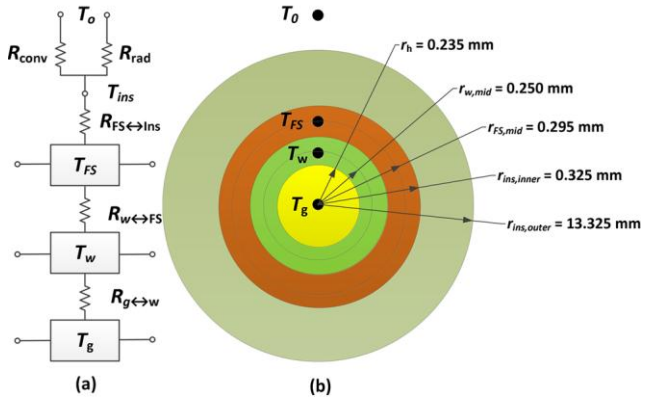

Figure D.1 Cross section of the microchannel assembly with surrounding insulation and temperature nodes.

Because of the adsorption experiments in these experiments involve only a gaseous medium, drastic changes in properties and other variables as seen in case of the displacement stage of the full process model are absent. Nevertheless, Figure D.2 shows an exaggerated schematic of the progression of the adsorption thermal wave, which is present at 0.11 m from the channel inlet for a 0.22 m long channel.

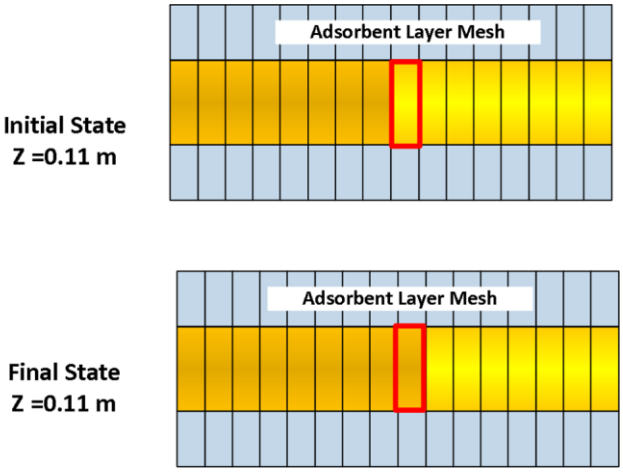

Figure D.2. A schematic showing initial and final states considered for sample calculations with a 0.22 m long channel with a ΔP of 16 kPa. The Orange region represents the impure gas; light yellow represents the pure gas.

.

Table D.1. Calculation of heat and mass transfer resistances.

Input	Equations	Output
$T = 298$ [K] $P = 1.15$ [bar] $d_{He,N_2} = 3.17\times10^{-10}$ [m] $d_{He,CO_2} = 3.24\times10^{-10}$ [m] $d_{N_2,CO_2} = 3.87\times10^{-10}$ [m] $\Omega_{He,N_2} = 0.742$ $\Omega_{He,CO_2} = 0.7972$ $\Omega_{N_2,CO_2} = 0.999$ $MW_{He} = 4.002$ [m] $MW_{N_2} = 28.01$ [m] $MW_{CO_2} = 44.01$ [m] $\varepsilon = 0.688$ $\tau = 2$ $x_{He} = 0.76$ $x_{N_2} = 0.14$ $x_{CO_2} = 0.10$ $d_{pore} = 10^{-6}$ [m]	**Diffusion coefficients** $D_{ij,eff,ordinary} = \frac{1.858\times10^{-27}\cdot T^{1.5}}{Pd^2\Omega}\sum_i\left(\frac{1}{MW_i}\right)^{0.5}\frac{\varepsilon}{\tau}$ $D_{i,mix,eff,ordinary} = \frac{1-x_i}{\sum_{j\neq i}\frac{x_j}{D_{ij,eff,ordinary}}}$ $D_{eff,Knudsen} = 48.5\times d_{pore}\frac{\sqrt{T}}{\tau MW_{He}}$ $\frac{1}{D_{i,eff,total}} = \frac{1}{D_{i,mix,eff,Ordinary}} + \frac{1}{D_{eff,Knudsen}}$	$D_{He-N_2,eff,ordinary} = 2.04\times10^{-5}$ [m^2 s^{-1}] $D_{He-CO_2,eff,ordinary} = 1.77\times10^{-5}$ [m^2 s^{-1}] $D_{N_2-CO_2,eff,ordinary} = 4.62\times10^{-6}$ [m^2 s^{-1}] $D_{He,mix,eff,ordinary} = 1.92\times10^{-5}$ [m^2 s^{-1}] $D_{N_2,mix,eff,ordinary} = 1.46\times10^{-5}$ [m^2 s^{-1}] $D_{CO_2,mix,eff,ordinary} = 1.23\times10^{-5}$ [m^2 s^{-1}] $D_{eff,Knudsen} = 1.04\times10^{-5}$ [m^2 s^{-1}] $D_{He,mix,eff,total} = 1.62\times10^{-5}$ [m^2 s^{-1}] $D_{N_2,mix,eff,total} = 1.28\times10^{-5}$ [m^2 s^{-1}] $D_{CO_2,mix,eff,total} = 1.11\times10^{-5}$ [m^2 s^{-1}]
$K_B = 1.38\times10^{-23}$ [J K^{-1}] $T = 298$ [K] $P = 10^5$ [Pa] $d_{molecule} = 3.43\times10^{-10}$ [m]	**Knudsen number and mean free path** $Kn = \frac{\lambda}{d_{pore}}$ $\lambda = \frac{K_B\cdot T}{\sqrt{2}\pi {d_{molecule}}^2\cdot P}$	$\lambda = 6.84\times10^{-8}$ [m] Kn = 0.06

Table D.1. Calculation of heat and mass transfer resistances – continued

$h_{m,He} = 0.178$ [m s^{-1}] $h_{m,N_2} = 0.136$ [m s^{-1}] $h_{m,CO_2} = 0.114$ [m s^{-1}] $Peri = 1.477 \times 10^{-3}$ [m] $R_{w,mid} = 250 \times 10^{-6}$ [m] $R_h = 235 \times 10^{-6}$ [m] $D_{He,mix,eff,total} = 1.62 \times 10^{-5}$ [m^2 s^{-1}] $D_{N_2,mix,eff,total} = 1.28 \times 10^{-5}$ [m^2 s^{-1}] $D_{CO_2,mix,eff,total} = 1.11 \times 10^{-5}$ [m^2 s^{-1}]	**Mass transfer resistance between microchannel and adsorbent layer** $\mathrm{R}_{Mass,i} = \frac{1}{h_{m,i} \cdot Peri} + \frac{\ln\left(\frac{R_{w,mid}}{R_h}\right)}{2\pi D_{i,eff,total}}$	$\mathrm{R}_{Mass,He} = 4411$ [s m^{-2}] $\mathrm{R}_{Mass,N_2} = 5748$ [s m^{-2}] $\mathrm{R}_{Mass,CO_2} = 6834$ [s m^{-2}]
$h_T = 751$ [W m^{-2} K^{-1}] $Peri = 1.477 \times 10^{-3}$ [m] $R_{w,mid} = 250 \times 10^{-6}$ [m] $R_h = 235 \times 10^{-6}$ [m] $k_w = 0.376$ [W m^{-1} K^{-1}]	**Heat transfer resistance between microchannel and adsorbent layer** $\mathrm{R}_{Heat,g\leftrightarrow w} = \frac{1}{h_T \cdot Peri} + \frac{\ln\left(\frac{R_{w,mid}}{R_h}\right)}{2\pi k_w}$	$\mathrm{R}_{Heat,g\leftrightarrow w} = 0.928$ [W^{-1} m K]
$th = 30 \times 10^{-6}$ [m] $R_{w,mid} = 250 \times 10^{-6}$ [m] $R_h = 235 \times 10^{-6}$ [m] $R_{FS,mid} = 295 \times 10^{-6}$ [m] $k_w = 0.376$ [W m^{-1} K^{-1}] $k_{FS} = 1.3$ [W m^{-1} K^{-1}]	**Heat transfer resistance between adsorbent layer and fused silica cover** $\mathrm{R}_{Heat,w\leftrightarrow FS} = \frac{\ln\left(\frac{R_h + th}{R_{w,mid}}\right)}{2\pi k_w} + \frac{\ln\left(\frac{R_{FS,mid}}{R_h + th}\right)}{2\pi k_{FS}}$	$\mathrm{R}_{Heat,w\leftrightarrow FS} = 0.049$ [W^{-1} m K]

Table D.1. Calculation of heat and mass transfer resistances – continued

$R_{FS,mid} = 295\times10^{-6}$ [m] $R_{Ins,inner} = 325\times10^{-6}$ [m] $k_{FS} = 1.3$ [W m^{-1} K^{-1}] $k_{air} = 0.02529$ [W m^{-1} K^{-1}] $D_{ins} = 0.0265$ [m] $Ra_D = 1948$ $\mathrm{Pr} = 0.728$ $Peri_{Ins} = 0.08325$ [m] $\varepsilon_r = 0.1$ $\sigma = 5.67\times10^{-8}$ [W m^{-2} K^{-4}]	**Heat transfer resistance between fused silica cover and ambient** $\mathrm{R}_{Heat,ins} = \dfrac{\ln\left(\dfrac{R_{FS,mid}}{R_{Ins,inner}}\right)}{2\pi k_{FS}}$ $h_{free} = \dfrac{k_{air}}{D_{ins}}\left[0.60 + \dfrac{0.387\times Ra_D^{\left(\frac{1}{6}\right)}}{\left[1+\left(\dfrac{0.559}{\mathrm{Pr}}\right)^{\left(\frac{9}{16}\right)}\right]^{\left(\frac{8}{27}\right)}}\right]^2$ $h_{rad} = 4\varepsilon_r\sigma T_0^3$ $\mathrm{R}_{Heat,conv} = \dfrac{1}{h_{free}Peri_{ins}}$ $\mathrm{R}_{Heat,rad} = \dfrac{1}{h_{rad}Peri_{ins}}$ **Total heat transfer resistance from fused silica cover to ambient** $\mathrm{R}_{Heat,FS\leftrightarrow\infty} = R_{Heat,ins} + \left(\dfrac{1}{\mathrm{R}_{Heat,conv}} + \dfrac{1}{R_{Heat,rad}}\right)^{-1}$	$\mathrm{R}_{Heat,ins} = 1.475$ [W^{-1} m K] $h_{free} = 2.841$ [W m^{-2} K^{-1}] $h_{rad} = 0.5832$ [W m^{-2} K^{-1}] $\mathrm{R}_{Heat,conv} = 4.22$ [W^{-1} m K] $\mathrm{R}_{Heat,rad} = 20.6$ [W^{-1} m K] $\mathrm{R}_{Heat,FS\leftrightarrow\infty} = 4.984$ [W^{-1} m K]

Table D.2. Sample calculations for governing equations in the laboratory scale models

Input	Equations	Output
$\rho_j^t = 0.302$ [kg m^{-3}] $\Delta t = 0.1$ [s] $\rho_{j+1}^{t+\Delta t} = 0.3175$ [kg m^{-3}] $u_{j+1}^{t+\Delta t} = 10.728$ [m s^{-1}] $\rho_{j-1}^{t+\Delta t} = 0.3181$ [kg m^{-3}] $u_{j-1}^{t+\Delta t} = 10.724$ [m s^{-1}] $\Delta z = 0.0003$ [m] $C_{g,He,j}^{t+\Delta t} = 0.1605$ [kg m^{-3}] $C_{g,N_2,j}^{t+\Delta t} = 0.0955$ [kg m^{-3}] $C_{g,CO_2,j}^{t+\Delta t} = 0.0703$ [kg m^{-3}] $C_{w,He,j}^{t+\Delta t} = 0.1605$ [kg m^{-3}] $C_{w,N_2,j}^{t+\Delta t} = 0.0955$ [kg m^{-3}] $C_{w,CO_2,j}^{t+\Delta t} = 0.05894$ [kg m^{-3}] $\mathrm{R}_{Mass,He} = 4411$ [s m^{-2}] $\mathrm{R}_{Mass,N_2} = 5748$ [s m^{-2}] $\mathrm{R}_{Mass,CO_2} = 6834$ [s m^{-2}] $A_g = 1.735\times10^{-7}$ [m^2]	**Microchannel total mass conservation equation** $\frac{\partial\rho}{\partial t}+\frac{\partial(\rho u)}{\partial z}=-\sum_i\frac{C_{g,i}-C_{w,i}}{A_g\cdot \mathrm{R}_{Mass,i}}$ $\frac{\rho_j^{t+\Delta t}-\rho_j^t}{\Delta t}+\frac{\rho_{j+1}^{t+\Delta t}u_{j+1}^{t+\Delta t}-\rho_{j-1}^{t+\Delta t}u_{j-1}^{t+\Delta t}}{2\Delta z}=-\sum_i\frac{C_{g,i,j}^{t+\Delta t}-C_{w,i,j}^{t+\Delta t}}{A_g\cdot \mathrm{R}_{Mass,i,j}^{t+\Delta t}}$ **Real gas equation of state** $P=\frac{RT}{V_m-b}-\frac{a\alpha}{V_m^{\,2}+2bV_m-b^2}$ $a=\frac{0.457235R^2T_c^{\,2}}{P_c}$ $\quad b=\frac{0.077796R\cdot T_c}{P_c}$ $\quad T_r=\frac{T}{T_c}$ $\alpha=\left(1+\kappa\left(1-T_r^{\,0.5}\right)\right)^2$ $\quad \kappa=0.37464+1.54226\omega-0.26992\omega^2$	$\rho_j^{t+\Delta t} = 0.3178$ [kg m^{-3}] $u_j^{t+\Delta t} = 10.726$ [m s^{-1}]

Table D.2. Sample calculations for governing equations in the laboratory scale models – continued

$\rho_j^{t+\Delta t} = 0.3178$ [kg m^{-3}] $\Delta t = 0.1$ [s] $y_{g,He,j}^{t} = 0.5437$ $y_{g,N_2,j}^{t} = 0.3056$ $y_{g,CO_2,j}^{t} = 0.1871$ $u_j^{t+\Delta t} = 10.726$ [m s^{-1}] $y_{g,He,j+1}^{t+\Delta t} = 0.5056$ $y_{g,N_2,j+1}^{t+\Delta t} = 0.3030$ $y_{g,CO_2,j+1}^{t+\Delta t} = 0.2204$ $y_{g,He,j-1}^{t+\Delta t} = 0.5041$ $y_{g,N_2,j-1}^{t+\Delta t} = 0.3006$ $y_{g,CO_2,j-1}^{t+\Delta t} = 0.2212$ $\Delta z = 0.0003$ [m] $C_{g,He,j}^{t+\Delta t} = 0.1605$ [kg m^{-3}] $C_{g,N_2,j}^{t+\Delta t} = 0.0955$ [kg m^{-3}] $C_{g,CO_2,j}^{t+\Delta t} = 0.0703$ [kg m^{-3}] $C_{w,He,j}^{t+\Delta t} = 0.1605$ [kg m^{-3}] $C_{w,N_2,j}^{t+\Delta t} = 0.0955$ [kg m^{-3}] $C_{w,CO_2,j}^{t+\Delta t} = 0.05894$ [kg m^{-3}] $\mathrm{R}_{Mass,He} = 4411$ [s m^{-2}] $\mathrm{R}_{Mass,N_2} = 5748$ [s m^{-2}] $\mathrm{R}_{Mass,CO_2} = 6834$ [s m^{-2}] $A_g = 1.735\times10^{-7}$ [m^2] $C_{g,He,j-1}^{t+\Delta t} = 0.1604$ [kg m^{-3}] $C_{g,N_2,j-1}^{t+\Delta t} = 0.0955$ [kg m^{-3}] $C_{g,CO_2,j-1}^{t+\Delta t} = 0.0706$ [kg m^{-3}] $C_{g,He,j+1}^{t+\Delta t} = 0.16056$ [kg m^{-3}] $C_{g,N_2,j+1}^{t+\Delta t} = 0.9556$ [kg m^{-3}] $C_{g,CO_2,j+1}^{t+\Delta t} = 0.0703$ [kg m^{-3}]	**Microchannel species conservation equation** $\rho\frac{\partial y_{g,i}}{\partial t} + \rho u\frac{\partial y_{g,i}}{\partial z} - y_{g,i}\sum_i \frac{C_{g,i}-C_{w,i}}{A_g\cdot \mathrm{R}_{Mass,i}} = D_{A,i}\frac{\partial}{\partial z}\left(\frac{\partial C_{g,i}}{\partial z}\right) + \frac{C_{g,i}-C_{w,i}}{A_g\cdot \mathrm{R}_{Mass,i}}$ $\rho_j^{t+\Delta t}\frac{y_{g,i,j}^{t+\Delta t}-y_{g,i,j}^{t}}{\Delta t} + \rho_j^{t+\Delta t}u_j^{t+\Delta t}\frac{y_{g,i,j+1}^{t+\Delta t}-y_{g,i,j-1}^{t+\Delta t}}{2\Delta z} - y_{g,i,j}^{t+\Delta t}\sum_i \frac{C_{g,i,j}^{t+\Delta t}-C_{w,i,j}^{t+\Delta t}}{A_g\cdot \mathrm{R}_{Mass,i,j}^{t+\Delta t}} =$ $D_{A,i,j}^{t+\Delta t}\frac{C_{g,i,j-1}^{t+\Delta t}-2C_{g,i,j}^{t+\Delta t}+C_{g,i,j+1}^{t+\Delta t}}{\Delta z^2} + \frac{C_{g,i,j}^{t+\Delta t}-C_{w,i,j}^{t+\Delta t}}{A_g\cdot \mathrm{R}_{Mass,i,j}^{t+\Delta t}}$ Dispersion coefficient $Pe_i = \frac{uD_h}{D_{AB,i}}$ $D_{A,i} = D_{AB,i}\left(1+\frac{Pe_i^{\,2}}{192}\right)$	$y_{g,He,j}^{t+\Delta t} = 0.5049$ $y_{g,N_2,j}^{t+\Delta t} = 0.3006$ $y_{g,CO_2,j}^{t+\Delta t} = 0.2212$ $D_{A,He,j}^{t+\Delta t} = 0.006$ [m^2 s^{-1}] $D_{A,N_2,j}^{t+\Delta t} = 0.009$ [m^2 s^{-1}] $D_{A,CO_2,j}^{t+\Delta t} = 0.010$ [m^2 s^{-1}]

Table D.2. Sample calculations for governing equations in the laboratory scale models – continued

$\rho_j^{t+\Delta t} = 0.3178$ [kg m^{-3}] $\Delta t = 0.1$ [s] $u_j^t = 10.940$ [m s^{-1}] $u_j^{t+\Delta t} = 10.726$ [m s^{-1}] $u_{j+1}^{t+\Delta t} = 10.728$ [m s^{-1}] $u_{j-1}^{t+\Delta t} = 10.724$ [m s^{-1}] $\Delta z = 0.0003$ [m] $C_{g,He,j}^{t+\Delta t} = 0.1605$ [kg m^{-3}] $C_{g,N_2,j}^{t+\Delta t} = 0.0955$ [kg m^{-3}] $C_{g,CO_2,j}^{t+\Delta t} = 0.0703$ [kg m^{-3}] $C_{w,He,j}^{t+\Delta t} = 0.1605$ [kg m^{-3}] $C_{w,N_2,j}^{t+\Delta t} = 0.0955$ [kg m^{-3}] $C_{w,CO_2,j}^{t+\Delta t} = 0.05894$ [kg m^{-3}] $\mathrm{R}_{Mass,He} = 4411$ [s m^{-2}] $\mathrm{R}_{Mass,N_2} = 5748$ [s m^{-2}] $\mathrm{R}_{Mass,CO_2} = 6834$ [s m^{-2}] $A_g = 1.735\times10^{-7}$ [m^2] $P_{j-1}^{t+\Delta t} = 109.768$ [kg m^{-3}] $P_{j+1}^{t+\Delta t} = 109.748$ [kg m^{-3}] $\mu_j^{t+\Delta t} = 1.7838\times10^{-5}$ [kg m^{-1} s^{-1}] $f = 0.712$ $D_h = 4.7\times10^{-4}$ [m] $L = 0.22$ [m]	**Microchannel momentum conservation equation** $$\rho\frac{\partial u}{\partial t}+\rho u\frac{\partial u}{\partial z}-\sum_i\frac{C_{g,i}-C_{w,i}}{A_g\cdot \mathrm{R}_{Mass,i}}u=-\frac{\partial P}{\partial z}+\mu\frac{\partial^2 u}{\partial z^2}-f\frac{\rho u^2}{2D_h}$$ $$\rho_j^{t+\Delta t}\frac{u_j^{t+\Delta t}-u_j^t}{\Delta t}+\rho_j^{t+\Delta t}u_j^{t+\Delta t}\frac{u_{j+1}^{t+\Delta t}-u_{j-1}^{t+\Delta t}}{2\Delta z}-u_j^{t+\Delta t}\sum_i\frac{C_{g,i,j}^{t+\Delta t}-C_{w,i,j}^{t+\Delta t}}{A_g\cdot \mathrm{R}_{Mass,i,j}^{t+\Delta t}}=$$ $$-\frac{P_{j+1}^{t+\Delta t}-P_{j-1}^{t+\Delta t}}{2\Delta z}+\mu_j^{t+\Delta t}\frac{u_{j-1}^{t+\Delta t}-2u_j^{t+\Delta t}+u_{j+1}^{t+\Delta t}}{\Delta z^2}-f_j^{t+\Delta t}\frac{\rho_j^{t+\Delta t}\left(u_j^{t+\Delta t}\right)^2}{2D_h}$$	$P_j^{t+\Delta t} = 109.758$ [kPa]

Table D.2. Sample calculations for governing equations in the laboratory scale models – continued

$U_j^t = -108052.69$ [J m^{-3}] $\Delta t = 0.1$ [s] $\dot{m}_{j+1}^{t+\Delta t} = 5.909\times10^{-7}$ [kg s^{-1}] $h_{g,j+1}^{t+\Delta t} = 6981$ [J kg^{-1}] $\dot{m}_{j-1}^{t+\Delta t} = 5.920\times10^{-7}$ [kg s^{-1}] $h_{g,j-1}^{t+\Delta t} = 7051$ [J kg^{-1}] $\Delta z = 0.0003$ [m] $A_g = 1.735\times10^{-7}$ [m^2] $k_{g,j}^{t+\Delta t} = 0.0809$ [W m^{-1} K^{-1}] $T_{g,j-1}^{t+\Delta t} = 300.3925$ [K] $T_{g,j+1}^{t+\Delta t} = 300.3645$ [K] $T_{w,j}^{t+\Delta t} = 300.3177$ [K] $\mathrm{R}_{Heat,g\leftrightarrow w}^{t+\Delta t} = 0.928$ [W^{-1} m K]	**Microchannel energy conservation equation** $$A_g \cdot \frac{\partial\left(U_g\right)}{\partial t} + \frac{\partial\left(\dot{m}\cdot h_g\right)}{\partial z} = A_g \cdot \frac{\partial}{\partial z}\left(k_g \frac{\partial T_g}{\partial z}\right) - \frac{T_g - T_w}{\mathrm{R}_{Heat,g\leftrightarrow w}}$$ $$A_g \cdot \frac{U_j^{t+\Delta t} - U_j^t}{\Delta t} + \frac{\left(\dot{m}_{j+1}^{t+\Delta t}\cdot h_{g,j+1}^{t+\Delta t}\right) - \left(\dot{m}_{j-1}^{t+\Delta t}\cdot h_{g,j-1}^{t+\Delta t}\right)}{2\Delta z} =$$ $$A_g \cdot k_{g,j}^{t+\Delta t} \frac{T_{g,j-1}^{t+\Delta t} - 2T_{g,j}^{t+\Delta t} + T_{g,j+1}^{t+\Delta t}}{\Delta z^2} - \frac{T_{g,j}^{t+\Delta t} - T_{w,j}^{t+\Delta t}}{\mathrm{R}_{Heat,g\leftrightarrow w}^{t+\Delta t}}$$	$U_j^{t+\Delta t} = -107527.72$ [J m^{-3}] $T_{g,j}^{t+\Delta t} = 300.3787$ [K]

Table D.2. Sample calculations for governing equations in the laboratory scale models – continued

$\varepsilon = 0.688$ $C^{t}_{w,He,j} = 0.1642$ [kg m^{-3}] $C^{t}_{w,N_2,j} = 0.0923$ [kg m^{-3}] $C^{t}_{w,CO_2,j} = 0.0394$ [kg m^{-3}] $\Delta t = 0.1$ [s] $\omega = 0.3012$ $C^{t}_{A,He,j} = 0$ [mol m^{-3}] $C^{t}_{A,N_2,j} = 13.825$ [mol m^{-3}] $C^{t}_{A,CO_2,j} = 2018.695$ [mol m^{-3}] $D^{t+\Delta t}_{He,mix,eff,total,j} = 1.62\times10^{-5}$ [m^2 s^{-1}] $D^{t+\Delta t}_{N_2,mix,eff,total,j} = 1.28\times10^{-5}$ [m^2 s^{-1}] $D^{t+\Delta t}_{CO_2,mix,eff,total,j} = 1.11\times10^{-5}$ [m^2 s^{-1}] $C^{t+\Delta t}_{w,He,j-1} = 0.1641$ [kg m^{-3}] $C^{t+\Delta t}_{w,N_2,j-1} = 0.0923$ [kg m^{-3}] $C^{t+\Delta t}_{w,CO_2,j-1} = 0.0393$ [kg m^{-3}] $C^{t+\Delta t}_{w,He,j+1} = 0.1643$ [kg m^{-3}] $C^{t+\Delta t}_{w,N_2,j+1} = 0.0923$ [kg m^{-3}] $C^{t+\Delta t}_{w,CO_2,j+1} = 0.03938$ [kg m^{-3}] $\Delta z = 0.0003$ [m] $R_{Mass,He} = 4411$ [s m^{-2}] $R_{Mass,N_2} = 5748$ [s m^{-2}] $R_{Mass,CO_2} = 6834$ [s m^{-2}] $C^{t+\Delta t}_{g,He,j} = 0.1604$ [kg m^{-3}] $C^{t+\Delta t}_{g,N_2,j} = 0.0955$ [kg m^{-3}] $C^{t+\Delta t}_{g,CO_2,j} = 0.07033$ [kg m^{-3}] $A_w = 4.712 \times 10^{-8}$ [m^2]	**Adsorbent layer species conservation equation** $\frac{\partial C_{w,i}}{\partial t} + \frac{\omega}{\varepsilon}\frac{\partial C_{A,i}}{\partial t} = \frac{\partial}{\partial z}\left(D_{eff,i}\frac{\partial C_{w,i}}{\partial z}\right) + \frac{C_{g,i} - C_{w,i}}{A_w \cdot R_{Mass,i}}$ $\varepsilon\frac{\left(C^{t+\Delta t}_{w,i,j} - C^{t}_{w,i,j}\right)}{\Delta t} + \omega\frac{\left(C^{t+\Delta t}_{A,i,j} - C^{t}_{A,i,j}\right)}{\Delta t} -$ $D^{t+\Delta t}_{i,mix,eff,total,j}\frac{C^{t+\Delta t}_{w,i,j-1} - 2C^{t+\Delta t}_{w,i,j} + C^{t+\Delta t}_{w,i,j+1}}{\Delta z^2} - \frac{\left(C^{t+\Delta t}_{g,i,j} - C^{t+\Delta t}_{w,i,j}\right)}{A_w \cdot R^{t+\Delta t}_{eq,Mass,i,j}} = 0$	$C^{t+\Delta t}_{w,He,j} = 0.1604$ [kg m^{-3}] $C^{t+\Delta t}_{w,N_2,j} = 0.0955$ [kg m^{-3}] $C^{t+\Delta t}_{w,CO_2,j} = 0.0589$ [kg m^{-3}] $C^{t+\Delta t}_{A,He,j} = 0$ [mol m^{-3}] $C^{t+\Delta t}_{A,N_2,j} = 12.35$ [mol m^{-3}] $C^{t+\Delta t}_{A,CO_2,j} = 2347$ [mol m^{-3}]

Table D.2. Sample calculations for governing equations in the laboratory scale models – continued

$\rho_w = 474$ [kg m^{-3}] $c_{P,w} = 802$ [J kg^{-1} K^{-1}] $T_{w,j}^{t} = 299.72$ [K] $\Delta t = 0.1$ [s] $k_w = 0.3765$ [W m^{-1} K^{-1}] $T_{w,j-1}^{t+\Delta t} = 300.333$ [K] $T_{w,j+1}^{t+\Delta t} = 300.301$ [K] $\Delta z = 0.0003$ [m] $A_w = 4.71\times10^{-8}$ [m^2] $T_{g,j}^{t+\Delta t} = 300.3787$ [K] $\mathrm{R}_{eq,Heat,j}^{t+\Delta t} = 0.928$ [W^{-1}m K] $\omega = 0.3012$ $\Delta H_{ads,He} = 0$ [J mol^{-1}] $\Delta H_{ads,N_2} = 17.14$ [J mol^{-1}] $\Delta H_{ads,CO_2} = 30790$ [J mol^{-1}] $C_{A,He,j}^{t} = 0$ [mol m^{-3}] $C_{A,N_2,j}^{t} = 13.825$ [mol m^{-3}] $C_{A,CO_2,j}^{t} = 2018.695$ [mol m^{-3}] $\mathrm{R}_{eq,FS} = 0.049$ $\left[\mathrm{W}^{-1}\mathrm{m\ K}\right]$ $\rho_{FS} = 2200$ [kg m^{-3}] $c_{P,FS} = 740$ [J kg^{-1} K^{-1}] $T_{FS,j}^{t} = 299.635$ [K] $k_{FS} = 1.3$ [W m^{-1} K^{-1}] $T_{FS,j-1}^{t+\Delta t} = 300.278$ [K] $T_{FS,j+1}^{t+\Delta t} = 300.244$ [K] $A_{FS} = 1.112\times10^{-7}$ [m^2]	**Adsorbent layer energy conservation equation** $$(1-\varepsilon)\rho_w c_{p,w}\frac{\partial T_w}{\partial t} = (1-\varepsilon)k_w\frac{\partial^2 T_w}{\partial z^2} + \frac{T_g - T_w}{A_w\cdot \mathrm{R}_{Heat,g\leftrightarrow w}} + \sum_i \omega\cdot h_{ads,i}\frac{\partial C_{A,i}}{\partial t} + \frac{T_{FS} - T_w}{A_w\cdot \mathrm{R}_{Heat,w\leftrightarrow FS}}$$ $$\rho_w c_{p,w}\frac{T_{w,j}^{t+\Delta t} - T_{w,j}^{t}}{\Delta t} = k_w\frac{T_{w,j-1}^{t+\Delta t} - 2T_{w,j}^{t+\Delta t} + T_{w,j+1}^{t+\Delta t}}{\Delta z^2} + \frac{T_{g,j}^{t+\Delta t} - T_{w,j}^{t+\Delta t}}{(1-\varepsilon)A_w\cdot \mathrm{R}_{eq,Heat,j}} + \sum_i \frac{\omega}{(1-\varepsilon)}\cdot\Delta H_{ads,i}\frac{\left(C_{A,i,j}^{t+\Delta t} - C_{A,i,j}^{t}\right)}{\Delta t} - \frac{T_{w,j}^{t+\Delta t} - T_{FS,j}^{t+\Delta t}}{(1-\varepsilon)A_w\cdot \mathrm{R}_{eq,FS}}$$ **Fused silica energy conservation equation** $$\rho_{FS} c_{p,FS}\frac{\partial T_{FS}}{\partial t} = k_{FS}\frac{\partial^2 T_{FS}}{\partial z^2} + \frac{T_w - T_{FS}}{A_{FS}\cdot \mathrm{R}_{Heat,w\leftrightarrow FS}} + \frac{T_\infty - T_{FS}}{A_{FS}\cdot \mathrm{R}_{Heat,FS\leftrightarrow\infty}}$$ $$\rho_{FS} c_{p,FS}\frac{T_{FS,j}^{t+\Delta t} - T_{FS,j}^{t}}{\Delta t} = k_{FS}\frac{T_{FS,j-1}^{t+\Delta t} - 2T_{FS,j}^{t+\Delta t} + T_{FS,j+1}^{t+\Delta t}}{\Delta z^2} + \frac{T_{w,j}^{t+\Delta t} - T_{FS,j}^{t+\Delta t}}{A_{FS}\cdot \mathrm{R}_{eq,w\leftrightarrow FS}} + \frac{T_\infty - T_{FS,j}^{t+\Delta t}}{A_{FS}\cdot \mathrm{R}_{Heat,FS\leftrightarrow\infty}}$$	$T_{w,j}^{t+\Delta t} = 300.3177$ [K] $T_{FS,j}^{t+\Delta t} = 300.2615$ [K]

Table D.2. Sample calculations for governing equations in the laboratory scale models – continued

$K_{LDF,N_2} = 10.10\ [s^{-1}]$ $K_{LDF,CO_2} = 92.87\ [s^{-1}]$ $C^t_{A,He,j} = 0\ [\text{mol m}^{-3}]$ $C^t_{A,N_2,j} = 13.825\ [\text{mol m}^{-3}]$ $C^t_{A,CO_2,j} = 2018.695\ [\text{mol m}^{-3}]$ $\Delta t = 0.005\ [\text{s}]$ $b_{0,N_2} = 3.73\times10^{-5}\ [\text{kPa}^{-1}]$ $b_{0,CO_2} = 3.32\times10^{-7}\ [\text{kPa}^{-1}]$ $d_{0,N_2} = 3.18\times10^{-5}\ [\text{kPa}^{-1}]$ $d_{0,CO_2} = 6.43\times10^{-7}\ [\text{kPa}^{-1}]$ $Q_{B,N_2} = -7528.1\ [\text{J mol}^{-1}]$ $Q_{B,CO_2} = -41077.1\ [\text{J mol}^{-1}]$ $Q_{D,N_2} = -7941.2\ [\text{J mol}^{-1}]$ $Q_{D,CO_2} = -29812\ [\text{J mol}^{-1}]$ $R = 8.314\ [\text{J mol}^{-1}\ \text{K}^{-1}]$ $T^{t+\Delta t}_{w,j} = 300.3177\ [\text{K}]$ $M_{B,N_2} = 1.4339\ [\text{mol kg}^{-1}]$ $M_{B,CO_2} = 0.9266\ [\text{mol kg}^{-1}]$ $M_{D,N_2} = 1.4339\ [\text{mol kg}^{-1}]$ $M_{D,CO_2} = 2.9791\ [\text{mol kg}^{-1}]$ $\rho_{ads} = 1480\ [\text{kg m}^{-3}]$ $P^{t+\Delta t}_{He,j} = 100.11\ [\text{kPa}]$ $P^{t+\Delta t}_{N_2,j} = 8.5197\ [\text{kPa}]$ $P^{t+\Delta t}_{CO_2,j} = 3.3444\ [\text{kPa}]$	**For zeolite 5A using DSL** $C_{A,Eq,i} = \rho_{ads}\left(M_{B,i}\frac{B_i\cdot P_i}{1+\sum_i B_i\cdot P_i} + M_{D,i}\frac{D_i\cdot P_i}{1+\sum_i D_i\cdot P_i}\right)$ $C^{t+\Delta t}_{A,Eq,i,j} = \rho_{ads}\left(M_{B,i}\frac{B^{t+\Delta t}_{i,\ j}\cdot P^{t+\Delta t}_{i,j}}{1+\sum_i B^{t+\Delta t}_{i,\ j}\cdot P^{t+\Delta t}_{i,j}} + M_{D,i}\frac{D^{t+\Delta t}_{i,\ j}\cdot P^{t+\Delta t}_{i,j}}{1+\sum_i D^{t+\Delta t}_{i,\ j}\cdot P^{t+\Delta t}_{i,j}}\right)$ **Auxiliary parameters for adsorbent capacity determination** $B_i = b_{0i}\exp\left(\frac{-Q_{B,i}}{RT_w}\right)\quad B^{t+\Delta t}_{i,j} = b_{0i}\exp\left(\frac{-Q_{B,i}}{RT^{t+\Delta t}_{w,j}}\right)$ $D_i = d_{0i}\exp\left(\frac{-Q_{d,i}}{RT_w}\right)\quad D^{t+\Delta t}_{i,j} = d_{0i}\exp\left(\frac{-Q_{D,i}}{RT^{t+\Delta t}_{w,j}}\right)$ **LDF Equation** $\frac{\partial C_{A,i}}{\partial t} = K_{LDF,i}\cdot\left(C_{A,Eq,i} - C_{A,i}\right)$ $\frac{C^{t+\Delta t}_{A,i,j} - C^t_{A,i,j}}{\Delta t} = K^{t+\Delta t}_{LDF,i,j}\cdot\left(C^{t+\Delta t}_{A,Eq,i,j} - C^{t+\Delta t}_{A,i,j}\right)$ **Heat of adsorption** $\Delta H_{ads,i} = \frac{-Q_{B,i}\cdot M_{B,i}\cdot B_i\cdot\left(1+D_i\cdot P_i\right)^2 - Q_{D,i}\cdot M_{D,i}\cdot D_i\cdot\left(1+B_i\cdot P_i\right)^2}{M_{B,i}\cdot B_i\cdot\left(1+D_i\cdot P_i\right)^2 + M_{D,i}\cdot D_i\cdot\left(1+B_i\cdot P_i\right)^2}$ $-Q_{B,i}\cdot M^{t+\Delta t}_{B,i}\cdot B^{t+\Delta t}_{i,j}\cdot\left(1+D^{t+\Delta t}_{i,j}\cdot P^{t+\Delta t}_{i,j}\right)^2$ $\Delta H^{t+\Delta t}_{ads,i} = \frac{-Q_{D,i}\cdot M^{t+\Delta t}_{D,i}\cdot D^{t+\Delta t}_{i,j}\cdot\left(1+B^{t+\Delta t}_{i,j}\cdot P^{t+\Delta t}_{i,j}\right)^2}{M^{t+\Delta t}_{B,i}\cdot B^{t+\Delta t}_{i,j}\cdot\left(1+D^{t+\Delta t}_{i,j}\cdot P^{t+\Delta t}_{i,j}\right)^2}$ $+M^{t+\Delta t}_{D,i}\cdot D^{t+\Delta t}_{i,j}\cdot\left(1+B^{t+\Delta t}_{i,j}\cdot P^{t+\Delta t}_{i,j}\right)^2$	$C^{t+\Delta t}_{A,N_2,j} = 12.35\ [\text{mol m}^{-3}]$ $C^{t+\Delta t}_{A,CO_2,j} = 2347\ [\text{mol m}^{-3}]$ $C^{t+\Delta t}_{A,Eq,N_2,j} = 11.18\ [\text{mol m}^{-3}]$ $C^{t+\Delta t}_{A,Eq,CO_2,j} = 2375\ [\text{mol m}^{-3}]$ $B^{t+\Delta t}_{N_2,j} = 7.6\times10^{-4}\ [\text{kPa}^{-1}]$ $B^{t+\Delta t}_{CO_2,j} = 4.63\ [\text{kPa}^{-1}]$ $D^{t+\Delta t}_{N_2,j} = 7.6\times10^{-4}\ [\text{kPa}^{-1}]$ $D^{t+\Delta t}_{CO_2,j} = 0.0985\ [\text{kPa}^{-1}]$ $\Delta H^{t+\Delta t}_{ads,He} = 0\ [\text{J mol}^{-1}]$ $\Delta H^{t+\Delta t}_{ads,N_2} = 17.14\ [\text{J mol}^{-1}]$ $\Delta H^{t+\Delta t}_{ads,CO_2} = 30790\ [\text{J mol}^{-1}]$

E. HEAT TRANSFER COEFFICIENTS IN THE TEST ENVIRONMENT

This section describes the estimation of heat losses during the transient adsorption process. During the experiments, as the fused silica temperature varies, the insulation surface temperature also changes in accordance with the rate of heat loss between the fused silica and the ambient. In the present work, in view of the low temperature differences between the test section and the ambient and the expected correspondingly low heat losses, a representative temperature difference of 1°C between the insulation surface temperature and is assumed for the heat loss estimation based on the resulting natural convection and radiative heat transfer coefficients. Rates of heat loss for the temperature extremes observed in the present work are analyzed here to support this assumption. For the batch adsorption tests on PLOT columns and adsorbent-coated microchannels, the fused silica temperature is observed to vary between 22°C to 32°C. (A fused silica temperature of 22°C implies that heat of adsorption at the concerned location is insignificant or no adsorbent is present at that location). Table E.1 shows the estimated relevant parameters for representative values of fused silica temperature of 23°C, 27°C and 32°C.

Table E.1. Variation of heat loss parameters for fused silica temperature extremes observed in the experiments

Case	T_{FS} [C]	T_{amb} [C]	T_{ins} [C]	Q_{gen} [W m^{-1}]	h_{free} [W m^{-2} K^{-1}]	h_r [W m^{-2} K^{-1}]	$R_{FS\leftrightarrow\infty}$ [K-m W^{-1}]	$Q_{loss,act}$ [W m^{-1}]	$Q_{loss,calc}$ [W m^{-1}]
1	23	22	22.23	4.25	2.088	0.584	0.447	2.23	2.86
2	27	22	23.00	24.62	2.835	0.588	0.349	14.32	14.32
3	32	22	23.77	52.28	3.217	0.593	0.313	31.68	28.64

For the smallest value of fused silica temperature of 23°C, the insulation surface temperature, h_{free}, and h_r are calculated as 22.23°C, 2.088 W m^{-2} K^{-1} and 0.5836 W m^{-2} K^{-}

[1], respectively. However, with an assumption of a fixed insulation surface temperature of 23°C, h_{free}, and h_r are estimated to be 2.835 W m^{-2} K^{-1} and 0.588 W m^{-2} K^{-1}; thereby overestimating the rate of heat loss by 28%, if the fused silica temperature indeed were 1°C. At the other end of the temperature spectrum for fused silica (32°C,) the calculated values of h_{free}, and h_r using a fixed surface temperature of 23°C results in under-prediction of the rate of heat loss by 9%. For both of these temperature extremes, the accuracy of h_r remains within 0.8% and variation in the natural convection coefficient is found to be the dominant factor in calculating the rate of heat loss. In these cases, however, the heat losses are 52.5% and 60.4% of the heat of adsorption, respectively. Because the fused silica temperature (T_{FS}) and not the rate of heat loss is used for the validation of the models, the effect of the assumption of a fixed temperature for the insulation surface (23°C) is assessed in greater detail by simulating the models for the case that were shown in Figure 4.16.

Figure E.1 shows the predicted temperature curves for the cases simulated with three overall heat transfer resistances shown in Figure E.1. The lowest heat transfer resistance corresponds to the case with the total temperature difference of 10°C (ΔT_{amb} of 1.77°C), while it is the maximum for the case with the total temperature difference of 1°C (ΔT_{amb} of 0.23°C) across the entire test matrix studied in the present work. The temperature variation for the case with a ΔT_{amb} of 1°C that was assumed for all the analyses is also shown, and it is the same set of temperature curves that were shown in Figure 16.

As shown in Figure E.1, the temperature curves predicted using a constant ΔT_{amb} of 1°C in the simulations are similar to those with ΔT_{amb} of 0.23°C and 1.77°C considered

here. The temperature peak heights and rate of increase of temperatures for all the heat loss conditions are almost identical. The maximum difference between temperature peak heights for a ΔT_{amb} of 0.23°C and ΔT_{amb} of 1°C is 0.035°C (1.1% error for 3°C peak height), whereas the difference between the temperature peak heights for a ΔT_{amb} of 1.77°C and ΔT_{amb} of 1°C is 0.02°C (0.6% error for 3°C peak height). As also seen in Figure A1, the temperature difference between the curves for a ΔT_{amb} of 0.23°C and those with a ΔT_{amb} of 1°C increases to 0.08°C after 5 s; however, this region is not monitored for model validation. These analyses support the assumption of a constant ΔT_{amb} assumption used in all the analyses, which offers some simplicity and computational savings in the analyses.

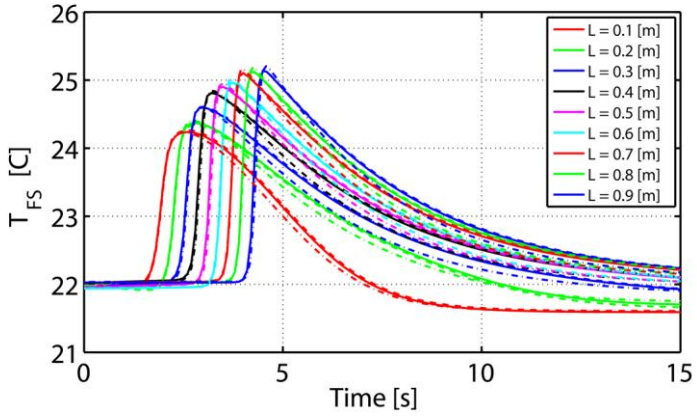

Figure E.1. Comparison of temperature curves predicted by models for a ΔT_{amb} of 1.77°C, 1°C and 0.23°C (Corresponding to the total temperature difference of 10°C, 5°C and 1°C between the fused silica cover and the ambient). Solid lines, dashed lines and dash-dotted lines represent these three cases, respectively.

REFERENCES

Aaron, D. and C. Tsouris (2005), "Separation of CO2 from Flue Gas: A Review," *Separation Science and Technology* Vol. 40(1-3) pp. 321-348 DOI: 10.1081/SS-200042244.

Askari, M. and T.-S. Chung (2013), "Natural gas purification and olefin/paraffin separation using thermal cross-linkable co-polyimide/ZIF-8 mixed matrix membranes," *Journal of Membrane Science* Vol. 444(0) pp. 173-183 DOI: http://dx.doi.org/10.1016/j.memsci.2013.05.016.

Babarao, R., Z. Hu, J. Jiang, S. Chempath and S. I. Sandler (2007), "Storage and Separation of CO2 and CH4 in Silicalite, C168 Schwarzite, and IRMOF-1: A Comparative Study from Monte Carlo Simulation," *Langmuir* Vol. 23(2) pp. 659-666 DOI: 10.1021/la062289p.

Baker, R. W. (2002), "Future Directions of Membrane Gas Separation Technology," *Industrial & Engineering Chemistry Research* Vol. 41(6) pp. 1393-1411 DOI: 10.1021/ie0108088.

Bernardo, P., E. Drioli and G. Golemme (2009), "Membrane Gas Separation: A Review/State of the Art," *Industrial & Engineering Chemistry Research* Vol. 48(10) pp. 4638-4663 DOI: 10.1021/ie8019032.

Bounaceur, R., N. Lape, D. Roizard, C. Vallieres and E. Favre (2006), "Membrane processes for post-combustion carbon dioxide capture: A parametric study," *Energy* Vol. 31(14) pp. 2556-2570 DOI: http://dx.doi.org/10.1016/j.energy.2005.10.038.

Brooks, R. E. (2013), "Modeling the North American Market for Natural Gas Liquids," *32nd USAEE/IAEE North American Conference* Anchorage, AK

Casas, N., J. Schell, R. Blom and M. Mazzotti (2013), "MOF and UiO-67/MCM-41 adsorbents for pre-combustion CO2 capture by PSA: Breakthrough experiments and process design," *Separation and Purification Technology* Vol. 112 pp. 34-48 DOI: http://dx.doi.org/10.1016/j.seppur.2013.03.042.

Cavenati, S., C. A. Grande and A. E. Rodrigues (2004), "Adsorption Equilibrium of Methane, Carbon Dioxide, and Nitrogen on Zeolite 13X at High Pressures," *Journal of Chemical & Engineering Data* Vol. 49(4) pp. 1095-1101 DOI: 10.1021/je0498917.

Cen, P. L., W. N. Chen and R. T. Yang (1985), "Ternary gas mixture separation by pressure swing adsorption: a combined hydrogen-methane separation and acid gas removal process," *Industrial & Engineering Chemistry Process Design and Development* Vol. 24(4) pp. 1201-1208 DOI: 10.1021/i200031a051.

Chevron (2008). *Safe Handling and Storage of Synfluid® Polyalphaolefins (PAO)*. C. P. C. C. Llc.

Chowdhury, P., S. Mekala, F. Dreisbach and S. Gumma (2012), "Adsorption of CO, CO2 and CH4 on Cu-BTC and MIL-101 metal organic frameworks: Effect of open metal sites and adsorbate polarity," *Microporous and Mesoporous Materials* Vol. 152(0) pp. 246-252 DOI: http://dx.doi.org/10.1016/j.micromeso.2011.11.022.

Churchill, S. W. (1977a), "Comprehensive Correlating Equations for Heat, Mass and Momentum Transfer in Fully Developed Flow in Smooth Tubes," *Industrial &*

Engineering Chemistry Fundamentals Vol. 16(1) pp. 109-116 DOI: 10.1021/i160061a021.

Churchill, S. W. (1977b), "Friction-Factor Equations Spans All Fluid Flow Regimes," *Chemical Engineering (New York)* Vol. 84(24) p. 2

Churchill, S. W. and H. H. S. Chu (1975), "Correlating equations for laminar and turbulent free convection from a horizontal cylinder," *International Journal of Heat and Mass Transfer* Vol. 18(9) pp. 1049-1053 DOI: http://dx.doi.org/10.1016/0017-9310(75)90222-7.

Clausse, M., J. Merel and F. Meunier (2011), "Numerical parametric study on CO2 capture by indirect thermal swing adsorption," *International Journal of Greenhouse Gas Control* Vol. 5(5) pp. 1206-1213 DOI: http://dx.doi.org/10.1016/j.ijggc.2011.05.036.

Coleman, H. W. and W. G. Steele (1989). *Experimentation and Uncertainty Analysis for Engineers*. New York, Wiley.

Cussler, E. L. (1997). *Diffusion Mass Transfer in Fluid Systems*, Cambridge University Press.

Dassault Systems, I. (2011). *Thermal Contact Resistance* D. Systems, Dassault Systems Vol. 2016.

Delgado, J. A., M. A. Uguina, J. L. Sotelo, V. I. Águeda, A. García and A. Roldán (2012), "Separation of ethanol–water liquid mixtures by adsorption on silicalite," *Chemical Engineering Journal* Vol. 180(0) pp. 137-144 DOI: http://dx.doi.org/10.1016/j.cej.2011.11.026.

Delgado, J. A., M. A. Uguina, J. L. Sotelo, B. Ruíz and M. Rosário (2007), "Carbon Dioxide/Methane Separation by Adsorption on Sepiolite," *Journal of Natural Gas Chemistry* Vol. 16(3) pp. 235-243 DOI: http://dx.doi.org/10.1016/S1003-9953(07)60054-1.

Determan, M. D., D. C. Hoysall and S. Garimella (2011), "Heat- and Mass-Transfer Kinetics of Carbon Dioxide Capture Using Sorbent-Loaded Hollow Fibers," *Industrial & Engineering Chemistry Research* Vol. 51(1) pp. 495-502 DOI: 10.1021/ie201380r.

EIA (2015). *Monthly Energy Review December 2015*. U. S. D. o. E. Office of Energy Statistics. Washington, DC 20585.

Gates, B. (2010). *Innovating to zero!* https://www.ted.com/talks/bill_gates/transcript?language=en.

GCA (2014). *Global Carbon Atlas*, Global Carbon Project 2015, Vol. 2016 p. http://www.globalcarbonatlas.org/?q=en/emissions.

Gholami, M. and M. R. Talaie (2009), "Investigation of Simplifying Assumptions in Mathematical Modeling of Natural Gas Dehydration Using Adsorption Process and Introduction of a New Accurate LDF Model," *Industrial & Engineering Chemistry Research* Vol. 49(2) pp. 838-846 DOI: 10.1021/ie901183q.

Gholami, M., M. R. Talaie and S. Roodpeyma (2010), "Mathematical modeling of gas dehydration using adsorption process," *Chemical Engineering Science* Vol. 65(22) pp. 5942-5949 DOI: http://dx.doi.org/10.1016/j.ces.2010.08.026.

Göttlicher, G. and R. Pruschek (1997), "Comparison of CO2 removal systems for fossil-fuelled power plant processes," *Energy Conversion and Management* Vol. 38,

Supplement(0) pp. S173-S178 DOI: http://dx.doi.org/10.1016/S0196-8904(96)00265-8.

Herm, Z. R., R. Krishna and J. R. Long (2012), "Reprint of: CO2/CH4, CH4/H2 and CO2/CH4/H2 separations at high pressures using Mg2(dobdc)," *Microporous and Mesoporous Materials* Vol. 157(0) pp. 94-100 DOI: http://dx.doi.org/10.1016/j.micromeso.2012.04.042.

Hines, A. and R. Maddox (1985). *Mass Transfer Fundamentals and Applications*. Upper Saddle River, NJ, USA, Prentice-Hall.

Incropera, F. P., T. L. Bergman, A. S. Lavine and D. P. DeWitt (2011). *Fundamentals of heat and mass transfer*, Wiley.

Kalyanaraman, J., Y. Fan, R. P. Lively, W. J. Koros, C. W. Jones, M. J. Realff and Y. Kawajiri (2015), "Modeling and experimental validation of carbon dioxide sorption on hollow fibers loaded with silica-supported poly(ethylenimine)," *Chemical Engineering Journal* Vol. 259 pp. 737-751 DOI: http://dx.doi.org/10.1016/j.cej.2014.08.023.

Kapoor, A. and R. T. Yang (1989), "Kinetic separation of methane—carbon dioxide mixture by adsorption on molecular sieve carbon," *Chemical Engineering Science* Vol. 44(8) pp. 1723-1733 DOI: http://dx.doi.org/10.1016/0009-2509(89)80014-4.

Klein, S. A. (2016). *Engineering Equation Solver*. Madison, F-Chart Software.

Koros, W. J. and R. Mahajan (2000), "Pushing the limits on possibilities for large scale gas separation: which strategies?," *Journal of Membrane Science* Vol. 175(2) pp. 181-196 DOI: http://dx.doi.org/10.1016/S0376-7388(00)00418-X.

Krishnamurthy, S., V. R. Rao, S. Guntuka, P. Sharratt, R. Haghpanah, A. Rajendran, M. Amanullah, I. A. Karimi and S. Farooq (2014), "CO2 capture from dry flue gas by vacuum swing adsorption: A pilot plant study," *AIChE Journal* Vol. 60 pp. 1830-1842 DOI: 10.1002/aic.14435.

Kulkarni, A. R. and D. S. Sholl (2012), "Analysis of Equilibrium-Based TSA Processes for Direct Capture of CO2 from Air," *Industrial & Engineering Chemistry Research* Vol. 51(25) pp. 8631-8645 DOI: 10.1021/ie300691c.

Lee, S. C. (2007), "Prediction of permeation behavior of CO2 and CH4 through silicalite-1 membranes in single-component or binary mixture systems using occupancy-dependent Maxwell–Stefan diffusivities," *Journal of Membrane Science* Vol. 306(1–2) pp. 267-276 DOI: http://dx.doi.org/10.1016/j.memsci.2007.09.003.

Lee, T. S., J. H. Cho and S. H. Chi (2015), "Carbon dioxide removal using carbon monolith as electric swing adsorption to improve indoor air quality," *Building and Environment* Vol. 92(0) pp. 209-221 DOI: http://dx.doi.org/10.1016/j.buildenv.2015.04.028.

Li, Z., G. Xiao, Q. Yang, Y. Xiao and C. Zhong (2014), "Computational exploration of metal–organic frameworks for CO2/CH4 separation via temperature swing adsorption," *Chemical Engineering Science* Vol. 120(0) pp. 59-66 DOI: http://dx.doi.org/10.1016/j.ces.2014.08.003.

Liang, Z., M. Marshall and A. L. Chaffee (2009), "Comparison of Cu-BTC and zeolite 13X for adsorbent based CO2 separation," *Energy Procedia* Vol. 1(1) pp. 1265-1271 DOI: http://dx.doi.org/10.1016/j.egypro.2009.01.166.

Liu, Z., C. A. Grande, P. Li, J. Yu and A. E. Rodrigues (2011), "Multi-bed Vacuum Pressure Swing Adsorption for carbon dioxide capture from flue gas," *Separation*

and Purification Technology Vol. 81(3) pp. 307-317 DOI: http://dx.doi.org/10.1016/j.seppur.2011.07.037.

Lively, R. P., R. R. Chance, B. T. Kelley, H. W. Deckman, J. H. Drese, C. W. Jones and W. J. Koros (2009), "Hollow Fiber Adsorbents for CO2 Removal from Flue Gas," *Industrial & Engineering Chemistry Research* Vol. 48(15) pp. 7314-7324 DOI: 10.1021/ie9005244.

Lively, R. P., R. R. Chance and W. J. Koros (2010), "Enabling Low-Cost CO2 Capture via Heat Integration," *Industrial and Engineering Chemistry Research* Vol. 49(16) pp. 7550-7562 DOI: 10.1021/ie100806g.

Lively, R. P., R. R. Chance, J. A. Mysona, V. P. Babu, H. W. Deckman, D. P. Leta, H. Thomann and W. J. Koros (2012), "CO2 sorption and desorption performance of thermally cycled hollow fiber sorbents," *International Journal of Greenhouse Gas Control* Vol. 10 pp. 285-294 DOI: http://dx.doi.org/10.1016/j.ijggc.2012.06.019.

Lively, R. P., D. P. Leta, B. A. DeRites, R. R. Chance and W. J. Koros (2011), "Hollow fiber adsorbents for CO2 capture: Kinetic sorption performance," *Chemical Engineering Journal* Vol. 171(3) pp. 801-810 DOI: http://dx.doi.org/10.1016/j.cej.2011.01.004.

Luis, P. (2016), "Use of monoethanolamine (MEA) for CO2 capture in a global scenario: Consequences and alternatives," *Desalination* Vol. 380 pp. 93-99 DOI: http://dx.doi.org/10.1016/j.desal.2015.08.004.

Mark, J. E. (1999). *Polymer Data Handbook*, Oxford University Press Inc. .

Mérel, J., M. Clausse and F. Meunier (2006), "Carbon dioxide capture by indirect thermal swing adsorption using 13X zeolite," *Environmental Progress* Vol. 25(4) pp. 327-333 DOI: 10.1002/ep.10166.

Moate, J. R. and M. D. LeVan (2010), "Temperature swing adsorption compression: Effects of nonuniform heating on bed efficiency," *Applied Thermal Engineering* Vol. 30(6–7) pp. 658-663 DOI: http://dx.doi.org/10.1016/j.applthermaleng.2009.11.013.

Moore, B. K. (2012). *Gas-Liquid Flows in Adsorbent Microchannels*. Mechanical Engineering. Atlanta, Georgia Institute of Technology Vol. Master of Science p. 202.

Moore, B. K., D. G. Pahinkar and S. Garimella (2016), "Experimental and Analytical Investigation of Displacement Flows in Microchannels," *International Journal of Multiphase Flows* Vol. In Review

Morishige, K. (2011), "Adsorption and Separation of CO2/CH4 on Amorphous Silica Molecular Sieve," *The Journal of Physical Chemistry C* Vol. 115(19) pp. 9713-9718 DOI: 10.1021/jp202572w.

Mulgundmath, V. P., F. H. Tezel, T. Saatcioglu and T. C. Golden (2012), "Adsorption and separation of CO2/N2 and CO2/CH4 by 13X zeolite," *The Canadian Journal of Chemical Engineering* Vol. 90(3) pp. 730-738 DOI: 10.1002/cjce.20592.

Olajossy, A., A. Gawdzik, Z. Budner and J. Dula (2003), "Methane Separation from Coal Mine Methane Gas by Vacuum Pressure Swing Adsorption," *Chemical Engineering Research and Design* Vol. 81(4) pp. 474-482 DOI: http://dx.doi.org/10.1205/026387603765173736.

Pahinkar, D. G., S. Garimella and T. R. Robbins (2015), "Feasibility of Using Adsorbent-Coated Microchannels for Pressure Swing Adsorption: Parametric Studies on

Depressurization," *Industrial & Engineering Chemistry Research* Vol. 54(41) pp. 10103-10114 DOI: 10.1021/acs.iecr.5b01023.

Pahinkar, D. G., S. Garimella and T. R. Robbins (2016), "Feasibility of Using Adsorbent Coated Microchannels for Temperature Swing Adsorption," *Industrial & Engineering Chemistry Research* Vol. In Review

Palomino, M., A. Corma, F. Rey and S. Valencia (2009), "New Insights on CO2−Methane Separation Using LTA Zeolites with Different Si/Al Ratios and a First Comparison with MOFs," *Langmuir* Vol. 26(3) pp. 1910-1917 DOI: 10.1021/la9026656.

Peng, X., D. Cao and W. Wang (2011), "Adsorption and separation of CH4/CO2/N2/H2/CO mixtures in hexagonally ordered carbon nanopipes CMK-5," *Chemical Engineering Science* Vol. 66(10) pp. 2266-2276 DOI: http://dx.doi.org/10.1016/j.ces.2011.02.044.

Pirngruber, G. D., F. Guillou, A. Gomez and M. Clausse (2013), "A theoretical analysis of the energy consumption of post-combustion CO2 capture processes by temperature swing adsorption using solid sorbents," *International Journal of Greenhouse Gas Control* Vol. 14(0) pp. 74-83 DOI: http://dx.doi.org/10.1016/j.ijggc.2013.01.010.

Process Systems Enterprise, I. (1997-2015). *gPROMS*, *www.psenterprise.com/gproms*.

Rattner, A. S. and S. Garimella (2011), "Energy harvesting, reuse and upgrade to reduce primary energy usage in the USA," *Energy* Vol. 36(10) pp. 6172-6183 DOI: http://dx.doi.org/10.1016/j.energy.2011.07.047.

Reid, R. C., J. M. Prausnitz and B. E. Poling (1986). *The Properties of Gases and Liquids*. Fourth Ed., The McGraw-Hill, Inc. .

Riemer, P. W. F., I. C. Webster, W. G. Ormerod and H. Audus (1994), "Results and full fuel cycle study plans from the IEA greenhouse gas research and development programme," *Fuel* Vol. 73(7) pp. 1151-1158 DOI: http://dx.doi.org/10.1016/0016-2361(94)90252-6.

Santoroa, M., F. Gorellia, J. Hainesc, O. Cambonc, C. Levelutd and G. Garbarinoe (2011), "Silicon carbonate phase formed from carbon dioxide and silica under pressure," *Proc Nat Acad Sci*, pp. 7689-7692.

Schaal, M. A. (2013). *International Energy Outlook 2013*. Office of Petroleum, Natural Gas and a. B. Analysis, U.S. Energy Information Administration.

Shao, X., Z. Feng, R. Xue, C. Ma, W. Wang, X. Peng and D. Cao (2011), "Adsorption of CO2, CH4, CO2/N2 and CO2/CH4 in novel activated carbon beads: Preparation, measurements and simulation," *AIChE Journal* Vol. 57(11) pp. 3042-3051 DOI: 10.1002/aic.12515.

Shen, C., J. Yu, P. Li, C. Grande and A. Rodrigues (2011), "Capture of CO2 from flue gas by vacuum pressure swing adsorption using activated carbon beads," *Adsorption* Vol. 17 pp. 179-188 DOI: 10.1007/s10450-010-9298-y.

Wan, X., G. Zhang, O. Ostrovski and H. Aral (2013), "Carbothermal reduction of silica in nitrogen and nitrogen-hydrogen mixture," *Proceedings of the Thirteenth International Ferroalloys Congress: Efficient Technologies in Ferroalloy Industry*, Karaganda, Kazakhstan, pp. 739-748.

Wang, Y. and M. D. LeVan (2009), "Adsorption Equilibrium of Carbon Dioxide and Water Vapor on Zeolites 5A and 13X and Silica Gel: Pure Components," *Journal*

of Chemical & Engineering Data Vol. 54(10) pp. 2839-2844 DOI: 10.1021/je800900a.

White, B. (2014). *Alaska LNG could have right heat content for Asia buyers*, Alaska Natural Gas Transportation Projects.

Xiang, S., Y. He, Z. Zhang, H. Wu, W. Zhou, R. Krishna and B. Chen (2012), "Microporous metal-organic framework with potential for carbon dioxide capture at ambient conditions," *Nat Commun* Vol. 3 p. 954 DOI: http://www.nature.com/ncomms/journal/v3/n7/suppinfo/ncomms1956_S1.html.

Yang, H., Z. Xu, M. Fan, R. Gupta, R. B. Slimane, A. E. Bland and I. Wright (2008), "Progress in carbon dioxide separation and capture: A review," *Journal of Environmental Sciences* Vol. 20(1) pp. 14-27 DOI: http://dx.doi.org/10.1016/S1001-0742(08)60002-9.

Zhang, J., P. Xiao, G. Li and P. A. Webley (2009), "Effect of flue gas impurities on CO2 capture performance from flue gas at coal-fired power stations by vacuum swing adsorption," *Energy Procedia* Vol. 1(1) pp. 1115-1122 DOI: http://dx.doi.org/10.1016/j.egypro.2009.01.147.